INSTITUTO SUPERIOR DE ENGENHARIA DO PORTO
MESTRADO EM ENGENHARIA MECÂNICA




Validação do critério ISSF aplicado a juntas adesivas usando métodos numéricos

JOÃO MANUEL MAIA DIONÍSIO
novembro de 2021

POLITÉCNICO
DO PORTO

Instituto Superior de Engenharia do Porto

VALIDATION OF THE ISSF CRITERION APPLIED TO BONDED JOINTS USING NUMERICAL METHODS

João Manuel Maia Dionísio

1160876

2021

ISEP – School of Engineering

Mechanical Engineering Department

POLITÉCNICO DO PORTO

Instituto Superior de Engenharia do Porto

VALIDATION OF THE ISSF CRITERION APPLIED TO BONDED JOINTS USING NUMERICAL METHODS

João Manuel Maia Dionísio

1160876

Dissertation presented to ISEP – School of Engineering to fulfil the requirements necessary to obtain a Master's degree in Mechanical Engineering, carried out under the guidance of PhD Raul Duarte Salgueiral Gomes Campilho and co-orientation of M.Sc. Luís Daniel Costa Ramalho, PhD Isidro de Jesús Sánchez-Arce and PhD Jorge Américo de Oliveira Pinto Belinha.

2021

ISEP – School of Engineering

Mechanical Engineering Department

POLITÉCNICO DO PORTO

JURY

President

PhD Sandra Cristina de Faria Ramos

Assistant professor, ISEP

Supervisor

PhD Raul Duarte Salgueiral Gomes Campilho

Assistant professor, ISEP

Second supervisor

MSc Luís Daniel Costa Ramalho

Research fellow, INEGI

PhD Isidro de Jesús Sánchez-Arce

Researcher, INEGI

PhD Jorge Américo de Oliveira Pinto Belinha

Assistant professor, ISEP

Examiner

PhD Ricardo José Alves Sousa

Assistant professor with habilitation, UA

ACKNOWLEDGEMENTS

Firstly, I want to thank my supervisor Dr Raul Campilho for the tireless support during this year, always ready to help and advise in every subject. I also want to thank him for the opportunity of participating in international conferences with this work and publishing it in international journals.

I am also extremely grateful to MSc Luís Ramalho, who was always available to help me with all the theoretical and numerical portions of this work, to Dr Isidro Sánchez-Arce, for his readiness and sense of humour during our weekly meetings, and to Dr Jorge Belinha, for his experienced reviews that helped to improve the work.

Finally, I want to thank my family, especially my parents and my godmother, for believing in me and supporting me throughout my life and certainly, for their support in my future endeavours. Without them, this wouldn't have been possible. A special thanks to my closest friends, especially Ricardo Sousa, who were also a part of this journey that is still starting.

KEYWORDS

Intensity of Singular Stress Fields Criterion, Composite Materials, Meshless Methods, Adhesive Joints, Radial Point Interpolation Method, Finite Element Method, Single-Lap Joints.

ABSTRACT

Due to the limitations presented by conventional joining techniques, like bolted and welded joints, the industry has turned attention to adhesively-bonded joints. The lower weight and decreased stress concentrations are some of the advantages made possible by this technique. Over the years, diverse analytical and numerical approaches to the failure of these joints were investigated.

The work presented in this report aims to propose and validate a fracture mechanics based approach to joint failure, named Intensity of Singular Stress Fields (ISSF). With this purpose, aluminium and composite single-lap joints bonded with a brittle adhesive were tested. Different overlap lengths (L_O) were also considered in order to evaluate this parameter influence in the final results. The experimental data was treated and the average maximum loads sustained by the joints were collected. Then, a numerical method for joint strength prediction was proposed, consisting of a combination of experimental and numerical information. The numerical data was obtained through simulations resorting to the Finite Element Method (FEM) and a meshless technique, the Radial Point Interpolation Method (RPIM). The validation of the approach was achieved by analysing the polar stress components and comparing the experimental and numerical results.

It was experimentally verified that increasing L_O leads to an increase in strength of the joints. The proposed technique was successfully applied for both aluminium and composite adherends even though they had different formulations. The results attained with the proposed method were promising given its simplicity compared with previously proposed methodologies. The method's application to meshless methods was also confirmed since the RPIM presented very similar results to the FEM, despite presenting some oscillations.

PALAVRAS CHAVE

Critério da Intensidade dos Campos de Tensões Singulares, Materiais Compósitos, Juntas Adesivas, *Radial Point Interpolation Method*, Método dos Elementos Finitos, Juntas de Sobreposição Simples.

RESUMO

Devido às limitações das técnicas de ligação convencionais, tais como as ligações aparafusadas e a soldadura, a indústria virou a sua atenção para as juntas adesivas estruturais. O baixo peso e a redução das concentrações de tensões são algumas das vantagens inerentes a esta técnica. Ao longo dos anos foram investigadas diversas abordagens analíticas e numéricas relativas à fratura deste tipo de juntas.

O presente trabalho tem como objetivo propor e validar um método baseado na mecânica da fratura para avaliar a falha destas juntas. Para o efeito, foram testadas juntas de sobreposição simples de alumínio e compósito ligadas por um adesivo frágil. Também foram considerados diferentes comprimentos de sobreposição (L_O) de forma a avaliar a influência deste parâmetro nos resultados finais. Os dados experimentais foram tratados e foram recolhidas as cargas máximas médias suportadas pelas juntas. Posteriormente, foi proposto um método numérico para prever a resistência das juntas, que consiste na combinação de informação analítica e numérica. Os dados numéricos foram obtidos através de simulações recorrendo ao Método dos Elementos Finitos (MEF) e a uma técnica *meshless*, o *Radial Point Interpolation Method* (RPIM). A validação da abordagem foi conseguida através da análise das componentes polares das tensões e por comparação entre os resultados experimentais e analíticos.

Verificou-se experimentalmente que um aumento do comprimento de sobreposição origina um aumento da resistência das juntas. A técnica foi aplicada com sucesso para aderentes de alumínio e de compósito mesmo apresentando formulações distintas. Os resultados obtidos com o método proposto foram promissores dada a simplicidade do mesmo quando comparado com metodologias previamente propostas. A aplicabilidade do método aos métodos sem malha também foi comprovada já que o RPIM apresentou resultados muito similares ao MEF, apesar de apresentar algumas oscilações.

LIST OF SYMBOLS AND ABBREVIATIONS

List of abbreviations

2D	Bidimensional
CNS	Critical Normal Strain
CZM	Cohesive Zone Model
DCB	Double cantilever beam
DEM	Diffuse Element Method
DLJ	Double-lap joint
DSJ	Double-strap joint
EFGM	Element Free Galerkin Method
FEM	Finite Element Method
FFM	Finite Fracture Mechanics
GSIF	Generalised Stress Intensity Factor
GY	Global yielding
ISSF	Intensity of Singular Stress Fields
MLPG	Meshless Local Petrov-Galerkin
MLS	Moving Least Square
NNRPIM	Natural Neighbour Radial Point Interpolation Method
PIM	Point Interpolation Method
RBF	Radial Basis Functions
RKPM	Reproducing Kernel Particle Method
RPIM	Radial Point Interpolation Method
ScF	Scarf joint
SIF	Stress Intensity Factor
SLJ	Single-lap joint
SJ	Strap joint
SPH	Smooth Particle Hydrodynamics
SSPH	Symmetric Smooth Particle Hydrodynamics
VCCT	Virtual Crack Closure Technique
XFEM	Extended Finite Element Method

List of symbols

$a_i(\mathbf{x}_I), b_j(\mathbf{x}_I)$	Non-constant coefficients
A_{SIi}	Voronoï sub-cell area
A_{VI}	Voronoï cell area
b	Joint width
E	Young's modulus
G	Energy release rate
G_{IC}	Critical energy release rate
G^{inc}	Incremental energy release rate
H	Intensity of singular stress field value
H_C	Critical intensity of singular stress field value
$\mathbf{J}$	Jacobian matrix
k	Stress intensity factor
K_{IC}	Critical stress intensity factor
l	Overlap length
m	Number of polynomial basis monomials
M_{Ii}	Voronoï cell middle point
$\boldsymbol{N}$	Set of nodes
n	Number of nodes
$N_i, \phi(\mathbf{x})$	Shape functions
P	Force
P_{Ii}	Interception point between Voronoï cells
$P_j(\mathbf{x}_I)$	Polynomial basis function
$\mathbf{P}_m$	Polynomial basis
$R_i(\mathbf{x}_I)$	Real basis function
r_{Ii}	Neighbour nodes distance
S_{Ii}	Voronoï sub-cells
V	Voronoï diagram
V_i	Node i sub-region
V_I	Voronoï cell
x_i, y_i	Cartesian coordenates of cell nodes
Ω	Problem domain

ε_e	Equivalent strain (von Mises)
ε_r	Tensile failure strain
σ	Peel stress
σ_r	Tensile strength
τ	Shear stress
γ	Shear strain
γ_p	Plastic shear failure strain

FIGURES INDEX

TABLES INDEX

INDEX

INTRODUCTION

1 INTRODUCTION

1.1 Framework

Due to the attractive characteristics of adhesive joints, their study and use has increased in recent years. They have several advantages over conventional joining techniques, such as the possibility of joining different kinds of materials, lower weight, and decreased stress concentrations. However, some disadvantages can be pointed out, like the lower resistance to extreme conditions of service.

This technology can be applied to a wide range of fields. The first ones to develop this technology were the aeronautical and space engineers in their pursuit to reduce the weight of aircraft and spaceships. Nowadays, its use goes from the different areas of engineering to medicine, amongst others.

These joints started to be studied in the late 1930s using analytical and numerical methods to predict their strength. Analytical methods are limited to initial design evaluations or simple problems. On the other hand, due to the improvement of the computer's capacity over the years, it became possible to analyse bonded joints with increasing complexity. Currently, there are a few different numerical methods to predict joint strength.

Typically, these criteria rely on the Finite Element Method (FEM) to be applied. Thus, this method's high dependency on the mesh led to the appearance of a different type of numerical method, known as meshless methods. The works with these methods are still scant, but the results obtained are auspicious. The Intensity of Singular Stress Fields (ISSF) criterion arose very recently, which can be evaluated with the FEM or meshless methods.

1.2 Objectives

The primary purpose of this work is to propose and validate a new fracture mechanics based approach to evaluate stress singularities and predict the strength of bonded joints. This validation was achieved through a comparison between experimental and numerical data, as well as an analysis of the polar stresses found around the corner tip of a Single-Lap Joint (SLJ). Therefore, SLJs made from aluminium and Carbon Fibre Reinforced Polymer (CFRP) and bonded with a brittle adhesive were experimentally tested. Different overlap lengths (L_O) were also considered in the joints to evaluate this parameter's influence in the final results.

The numerical study and strength prediction of adhesive joints was also an objective, including aluminium and composite adhesive joints. These studies were performed resorting to the FEM and the Radial Point Interpolation Method (RPIM), which was another interest of this work: analysing adhesive joints with meshless methods. The performed simulations were crucial to the proposed method since it relies on a combination of experimental and numerical data to work.

Concurrently to the described objectives, the developed work was destined to be transformed into scientific knowledge by creating four scientific papers to be published in specialised journals.

1.3 Thesis outline

The present report was divided into four sections.

The first section frames the subject of the work developed in this report. The objectives and the organisation of the report are also outlined.

Section 2 is reserved for a comprehensive review of the most important concepts and developments related to this thesis subject, necessary to better understand the developed work. This section is divided into three sub-sections. Firstly, the fundamentals of adhesive bonding are covered. Then, the most common joint configurations and industrial applications of this technique are presented. The second sub-section is dedicated to strength prediction methods for adhesive joints. The two main categories (analytical and numerical) are analysed, highlighting the pioneers and the most important concepts. The ISSF criterion is also analysed in detail. This sub-section ends with a state-of-the-art review of the most recent works developed in these fields. Finally, the third sub-section approaches the recently studied meshless methods. Once again, a state-of-the-art review related to these techniques is exposed.

In section 3, the developed work is presented. Initially, an introduction to the same is performed, covering the four scientific papers elaborated. Readily, each one of those scientific papers is exposed. The first two propose and investigate an ISSF formulation for isotropic materials relying on aluminium adhesive joints, using FEM and RPIM. The other two present a formulation suited for orthotropic materials, resorting to the same numerical methods to validate it.

Finally, the main conclusions are laid out and in annexe, the journal version of the four scientific papers is presented.

LITERATURE REVIEW

2 LITERATURE REVIEW

2.1 Adhesive joints

This chapter contains a brief introduction to the adhesive bonding fundamentals, exploring this technique's principles and its advantages and disadvantages over conventional joining methods. It also covers the most common joint configurations and the applications that this process has in the industry.

2.1.1 Fundamentals of adhesive bonding

Recent archaeological discoveries made in Italy showed that Neanderthals, living in Europe about 55000 to 40000 years ago, would leave their caves to collect resin from pine trees. They then used it to glue their stone tools to handles made of bones or wood [1]. This discovery shows how far the bonding technique exists. Nowadays, it is not easy to imagine a product that does not incorporate adhesive bonding [2].

There is not a single definition of adhesive bonding. However, in simple terms, it can be described as the process of joining two different surfaces. There are two types of adhesive bonding: structural and non-structural. The difference between them is the amount of stress that the bonded objects experience. Typically, a bond that resists shear strengths over 7 MPa is considered a structural bond [3].

The adhesion process does not rely exclusively on mechanical engineering knowledge. It is vital to understand other sciences like chemistry and physics, to fully comprehend this phenomenon. Two stages stand out from this process: before and after the adhesive contact with the surfaces to bond. Initially, the adhesive must be in liquid form to properly flow and wet the adherent surfaces, making intimate molecular contact. After the application, the adhesive must harden to bear with the joint's loads during service lifetime [4].

In recent times, the use of adhesively-bonded joints has grown exponentially over conventional joining methods such as riveting or welding. This growth is due to the advantages of this process. The method's primary evidence is the most uniform stress distribution along the bonded area's width, allowing higher stiffness and load transmission, reducing the weight and inherently the cost [2]. Figure 2.1.1 shows this evidence, comparing a riveted and a bonded joint.

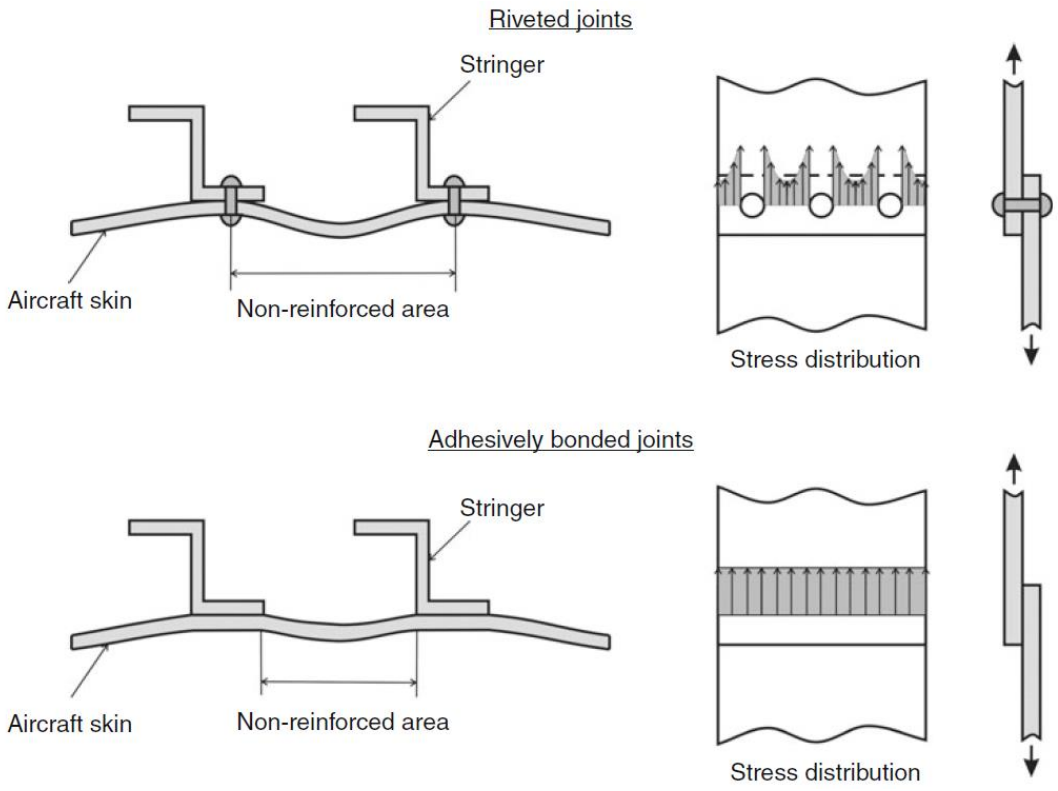

Figure 2.1.1 - Stress distribution in riveted and bonded joints [2]

Bonded joints also excel at damping vibrations, mainly because of the polymeric nature of the adhesive. Such characteristic enables higher fatigue strength [3]. This approach also empowers joining thick or thin surfaces of any shape and both similar or dissimilar materials (minimising galvanic corrosion, for example). Besides, production-wise, it allows for easy automation of the process, incrementing efficiency.

Nonetheless, this method has some handicaps that need attention. One of the most crucial problems to consider in joint design is the possibility of cleavage and peeling stresses. These are the worst enemies of bonded joints, and it is vital to reduce them as much as possible [2]. With this procedure, joints also have limited resistance to high temperatures and humidity conditions. They require careful preparation of the adherends' surfaces before the process and often high temperatures for the cure, thus increasing the overall operation cost. Another disadvantage is the quality control of the joint. However, in this matter, a few non-destructive inspection techniques were already developed.

2.1.2 Common joint configurations

In its essence, an adhesive joint has the components presented in Figure 2.1.2. The adherends are the surfaces/materials to be joined by the adhesive or sealant. The interphase region is the area that separates the adhesive and the adherends. This region's chemical and physical properties are different from either the bulk adhesive or

the adherend [4]. A primer improves the bond's performance and protects the adherends' surfaces until the adhesive is applied.

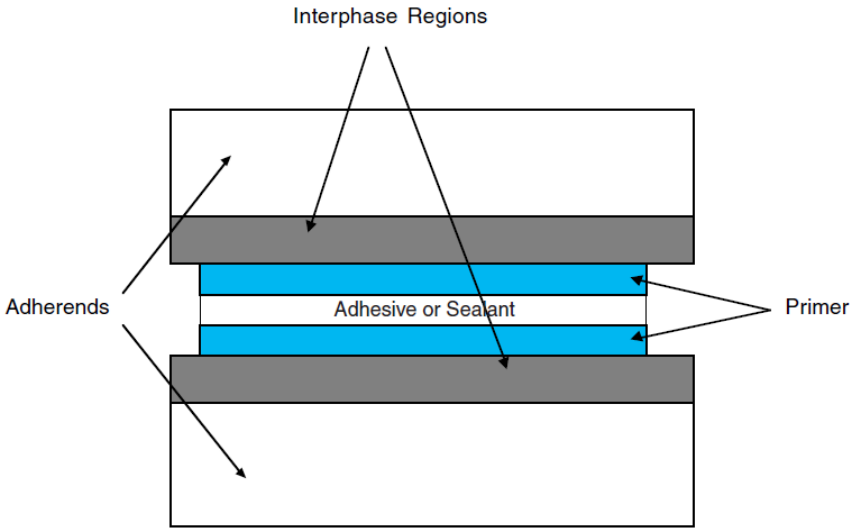

Figure 2.1.2 - Components of a typical adhesive joint [4]

These joints can have many different configurations. The most common ones are Single-Lap Joints (SLJ), Double-Lap Joints (DLJ), Strap Joints (SJ), Double-Strap Joints (DSJ), Scarf Joints (ScJ), Single-L Joints, T-joints, and T-peel joints, represented in Figure 2.1.3 [5].

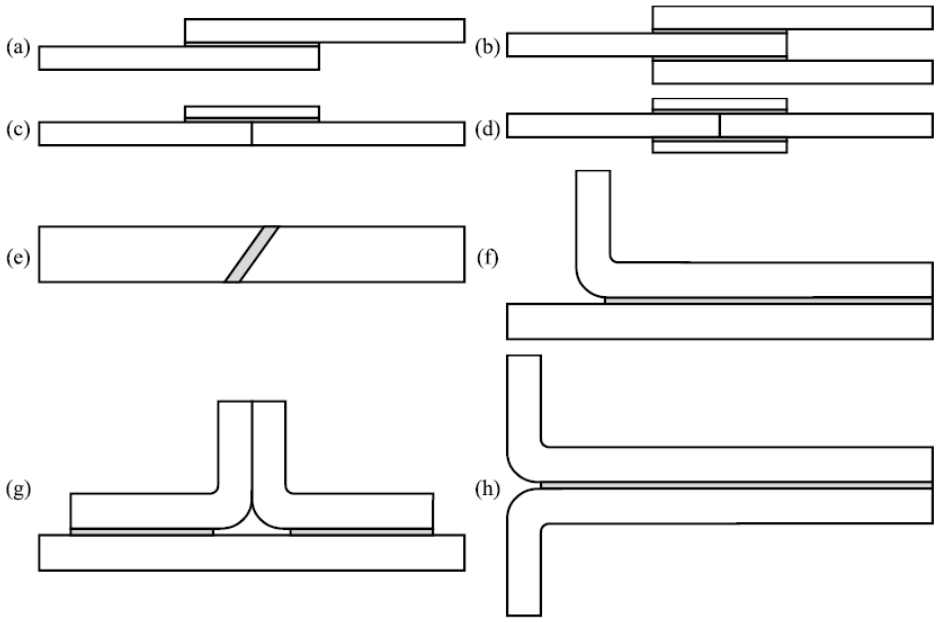

Figure 2.1.3 - Most common joint configurations: SLJ (a), DLJ (b), SJ (c), DSJ (d), ScF (e), Single-L joints (f), T-joints (g), and T-peel joints (h) [5]

Due to the ease of manufacture, the SLJ has been the most studied theoretically and experimentally [6].

2.1.3 Applications

Adhesive technology is a common feature in a wide range of industries. The Aeronautical Industry has been the main responsible for developing this technology, searching to reduce aircraft weight. Nowadays, the adhesives used in this industry are all based on synthetical polymers like epoxy, phenolic, or acrylic [6]. One of the most common applications is on the fuselage or the wings. Figure 2.1.4 shows a construction detail in the frame of a Cessna Citation III. It is possible to see the skin bonded to the waffle doubler, longerons, and the frame's outer half. This design's significance is that there are no weaknesses along the bonded area associated with traditional mouseholes in the frames [2].

If saving mass is an issue in an aircraft, it is even more so in a spacecraft. The energy required to escape gravity is directly related to the weight. In such a way, during the space conquest in the 1960s, the space industry applied aeronautical principles regarding composite materials. The problem with these materials was that drilling a composite part resulted in fibre discontinuities, triggering premature failures. In that matter, when structural adhesives became available, they were implemented to solve this issue [2]. Satellites and rocket launchers are examples of structures that resort to adhesive bonding.

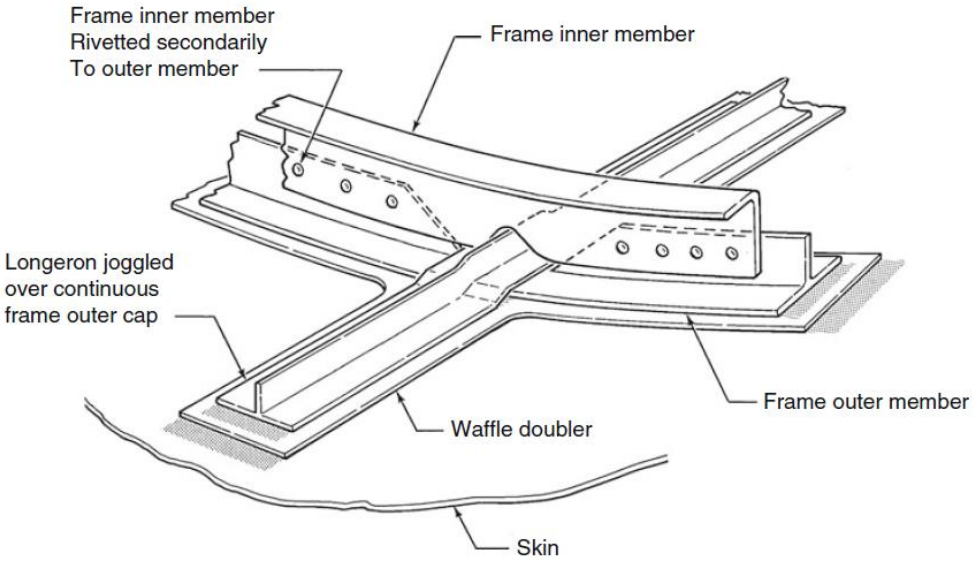

Figure 2.1.4 - Cessna Citation III bonded frame [2]

The advancements made in the industries mentioned above allowed other industries to start using this technology. One of the most benefited was the automotive industry. Initially, adhesives did not have a structural role in the car, as they were mainly used to bond windscreens. Nevertheless, when windscreens started to be a part of the structure, the adhesives used until then were no longer a solution. Therefore, engineers created high modulus adhesives to withstand the loads [7]. Nowadays, adhesives are an integral part of constructing a car, as shown in Figure 2.1.5.

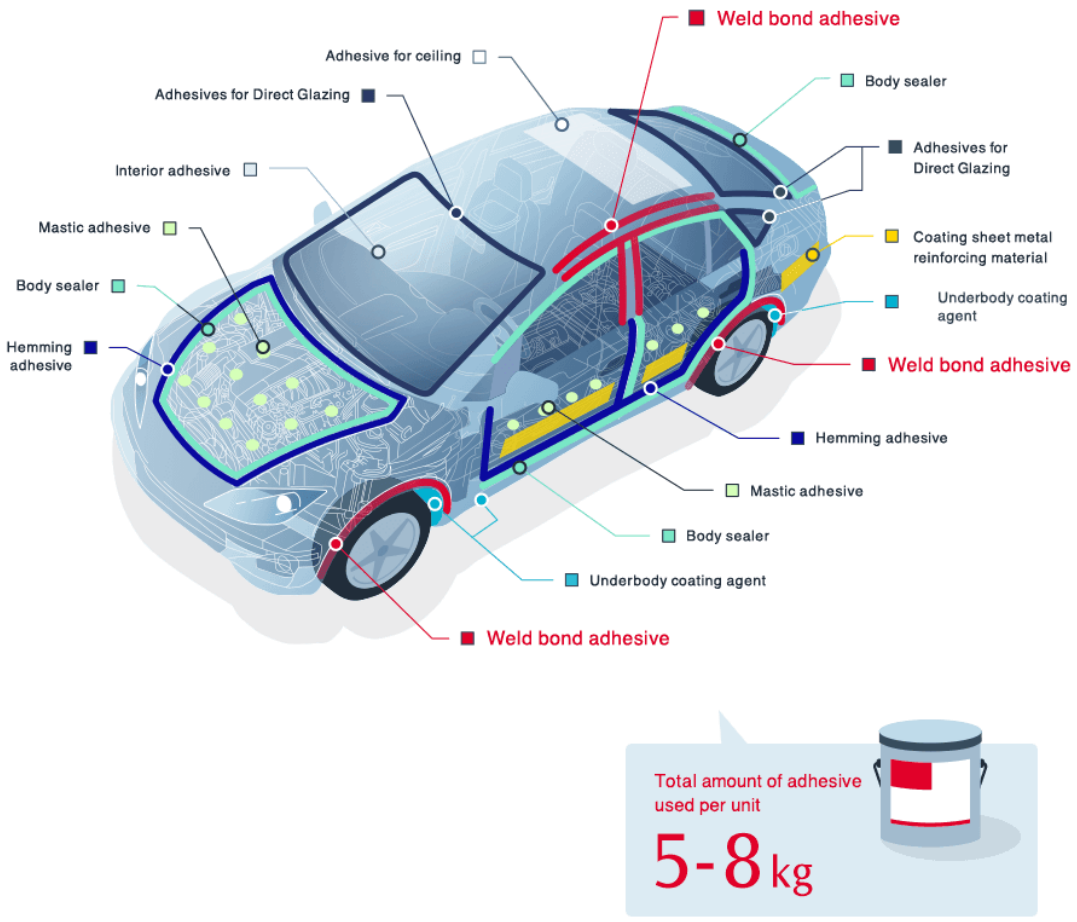

Figure 2.1.5 - Adhesive bonding in the construction of a car [8]

Like the automotive industry, nowadays, other industries depend more and more on adhesives. Examples are the naval, railway, and sports industries. Another significant business that has a long tradition in bonding technology is civil construction. As far as it goes, any mortar used actually can be considered an adhesive. The Porta Nigra construction in Trier, Germany, is an example where the designers tried to improve the mortars' resistance to frost by adding organic substances like milk, casein, or urine [9]. Electrotechnical, Medicine, and Bioengineering are also areas where the use of adhesives can have significant importance.

On top of the current technology is nanotechnology. The know-how and increased use of nanoparticles commercially led to the incorporation of this technology in structural adhesives. Nanoparticles can alter different adhesives' properties, emphasising the mechanical properties, like stiffness, and the electrical properties, like conductivity. The functional properties, such as permeability or glass transition temperature, and the fracture performance of thermoset polymers, are also characteristics that nanoparticles can change [2].

2.2 Strength prediction of adhesive joints

In the first half of the 20th century, the adhesively-bonded joint design relied on trial and error and much experimentation. Due to the non-existing optimisation techniques, joints were often over-dimensioned, increasing the process's overall cost and structures' weight. The pioneer of strength prediction models was Volkersen [10] in 1938.

The development of computers brought the capability to solve complex problems, allowing for a more detailed analysis before mass production. With accurate predictive methods, the use of adhesives can be more efficient. It is possible to distinguish two main categories of these methods: analytical and numerical. An analytical analysis relies on simple formulations. When the problem involves composite adherends, the adhesive layer's plasticisation, or an adhesive fillet at the bonding edges, these formulations become far too complicated [11]. In these cases, numerical methods emerge as an alternative. The FEM is the most commonly used technique to solve these complex problems. The first ones to use this method to study adhesively-bonded joints were Adams and Peppiatt [12].

2.2.1 Analytical methods

The study of analytical models started 80 years ago. Since then, numerous analytical models have been proposed. These methods allow for a fast and straightforward understanding of the adhesive joint behaviour. In the most superficial linear elastic analysis, the adhesive only deforms in shear, and the adherends are rigid [13]. Consequently, the adhesive shear stress (τ) does not change along the overlap length, as shown in Figure 2.2.1, and it is given by

$$\tau = \frac{P}{bl}, \tag{1}$$

where P represents the load applied, b is the joint width, and l is the overlap length. The resulting value is the average shear stress in the adhesive layer. This analysis has significant simplifications. However, it is the basis for stating adhesive shear strength.

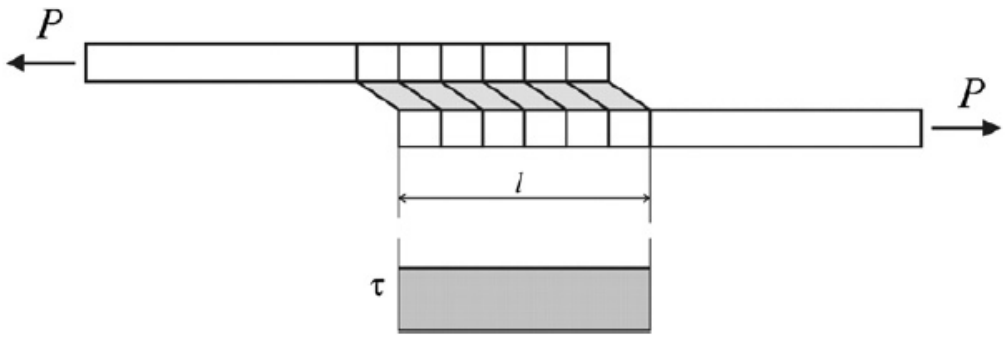

Figure 2.2.1 - Shear stress distribution in SLJs, considering rigid adherends [13]

The model of Volkersen [10] proposed the consideration of the adherend as elastic instead of rigid. This way, the adherends can deform in tension. This concept is known as *differential shear* [13].

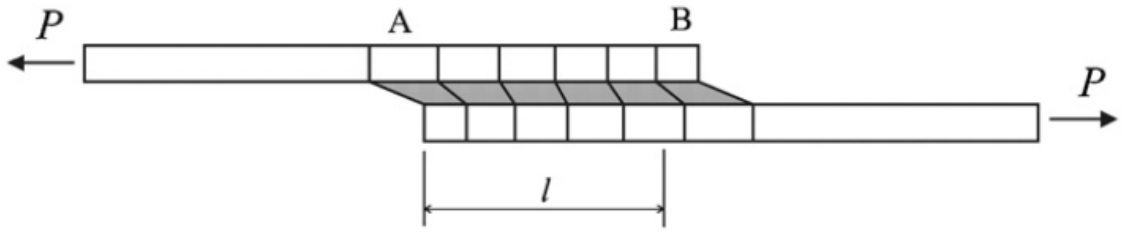

Figure 2.2.2 - Deformation in an adhesive joint, considering elastic adherends [13]

As shown in Figure 2.2.2, the adherend deformation reaches its maximum at A and its minimum at B. This phenomenon causes a non-uniform shear stress distribution in the adhesive layer, like the one presented in Figure 2.2.3.

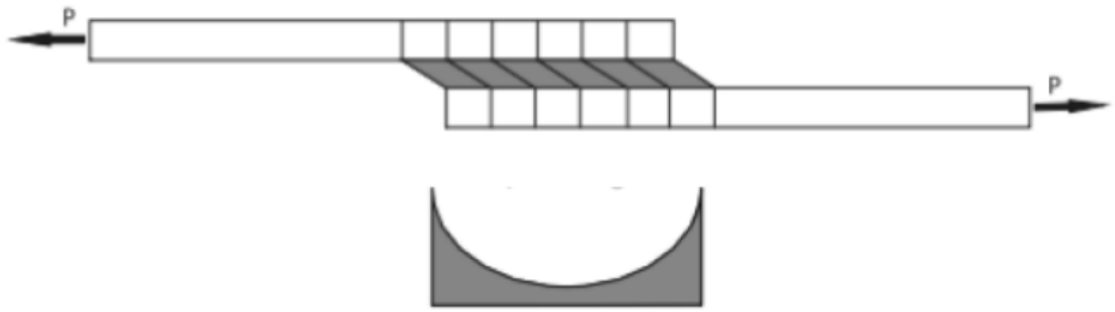

Figure 2.2.3 - Shear stress distribution in SLJs, considering elastic adherends [6]

However, the analysis of Volkersen does not take into account the bending effect caused by the non-collinearity of the load path in SLJs. This effect leads to a bending moment that causes the joint's rotation, originating large deflections of the adherends that need consideration. Goland and Reissner [14] were the first to consider these issues. This formulation is very similar to Volkersen's but allows estimating peel stresses as well.

In 1973, Hart-Smith [15] improved this method by considering plasticity in the adhesive layer.

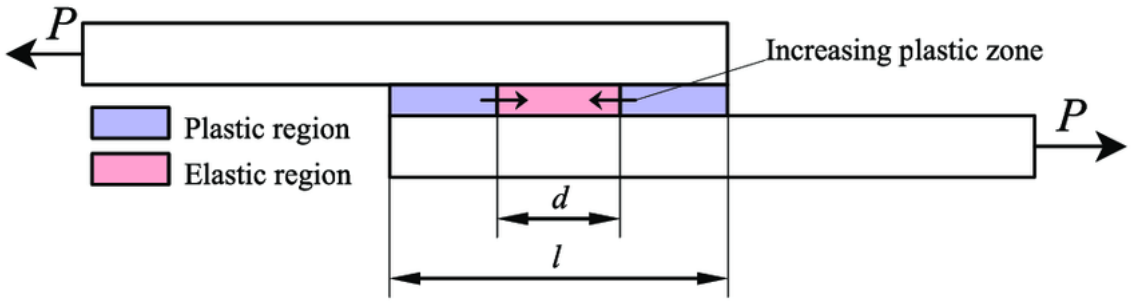

Figure 2.2.4 - Hart-Smith plastic regions [16]

As shown in Figure 2.2.4, the adhesive layer splits into three regions, two of them considered plastic. This proposal states that adhesive plasticity enhances the joint's strength [15]. When the material plasticises, it can support an additional force before failure, reducing shear deformation peaks. This consideration leads to a more accurate prediction of the joint's behaviour.

Although these developments were very significant in predicting the stress in an adhesive joint, they have several limitations. One of those is the fact that they do not consider the stresses throughout the thickness direction. Another constraint is considering the peak stress at the overlap ends, violating the stress-free condition, leading to more conservative failure load predictions [13], as shown in Figure 2.2.5. Lastly, these models assume the adherends as thin beams, ignoring the throughout-thickness shear.

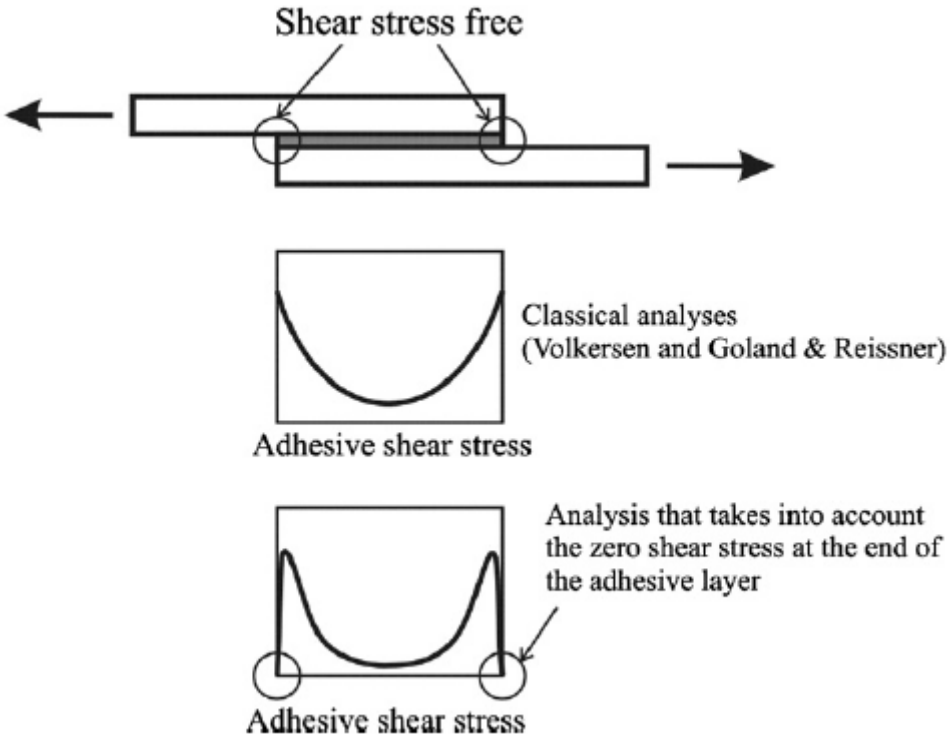

Figure 2.2.5 - Stress-free condition [13]

Over the years, other authors investigated these restrictions. Ojalvo and Eidinoff [17] studied the adherend thickness's influence, while Tsai et al. [18] investigated the shear and normal deformations in the adherends. Other theories, such as Allman's [19] and Cheng's [20], conjecture that the peak stress occurs near the joint ends.

Despite the presented limitations, these models are still the reference nowadays. However, they are relatively simple and do not require much computational power [13].

2.2.2 Numerical methods

The methods described in the previous chapter are often related to joints of simple complexity, like SLJs and DLJs. When the complexity of the joint increases, the classical models are not viable. Therefore, numerical methods are the solution. As mentioned before, FEM is the most implemented. With this method, there are different approaches to evaluate the failure of adhesive joints. Continuum mechanics, fracture mechanics, Cohesive Zone Modeling (CZM), damage mechanics, and the eXtended Finite Element Method (XFEM) are featured in this chapter.

2.2.2.1 Continuum mechanics

The first analyses of adhesives considered a continuum mechanics approach to predict the strength. For this method to work, it is necessary to have information about the stress or strain distributions inside the adhesive layer. This knowledge can be obtained by either an analytical method or FEM. In the presence of intricate geometries and material models, it is preferable to use FEM [11]. Then, the maximum values obtained for the joint are compared to the limit values for the material in question.

The use of continuum mechanics in the strength prediction is not very common nowadays due to the stress singularities at the interface corners, leading to increased stress in that area by increasing the mesh refinement [5]. This phenomenon does not allow for a convergence of results. Over the years, efforts have been made to improve the failure criteria considered in this method. However, the mesh problem is still unsolved.

2.2.2.2 Fracture mechanics

Fracture mechanics emerged to fill in the limitations left by continuum mechanics. In reality, a structure can have flaws resultant from manufacture or re-entrant corners at the adhesive-adherend interface. This model allows the study of these discontinuities [5]. The purpose is to evaluate if these defects can cause catastrophic failure or if their dimensions stay below the limit during the structure's lifetime.

Figure 2.2.6 (a) demonstrates the existence of these singularities. An infinitely large plate is shown with the stresses around the tip of a sharp crack. Palpably, the normal stresses, σ_y, at the crack's tip A must be finite instead of infinite as predicted by theory. However, far from the crack's tip and into the crack, the stresses are nil because of the free surfaces. Therefore, a discontinuity of σ_y arises at A unless the value is zero there [21]. This stress distribution is not acceptable in continuum mechanics, resulting in undefined stresses at the crack's tip (being infinite).

Diverse theories define these singularities' existence when the crack angle is below 180° [22]. This assumption is also viable for re-entrant corners (Figure 2.2.6 (b)). The discontinuity still exists, even though the free surfaces do not.

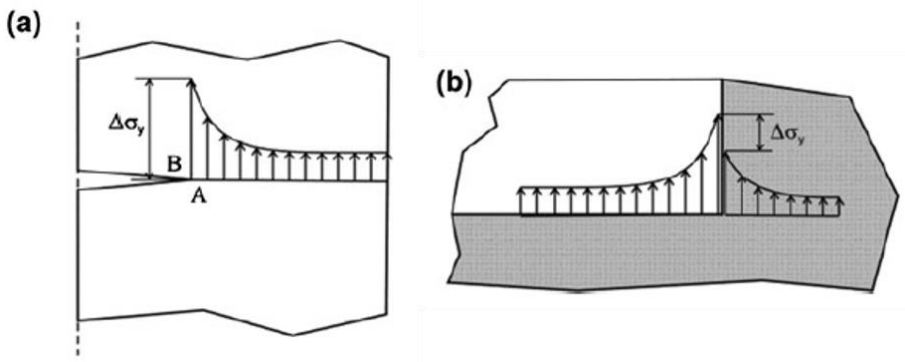

Figure 2.2.6 - Stress discontinuity around (a) a crack tip and (b) a re-entrant corner [21]

Fracture mechanics distinguishes three basic crack opening modes, as demonstrated in Figure 2.2.7.

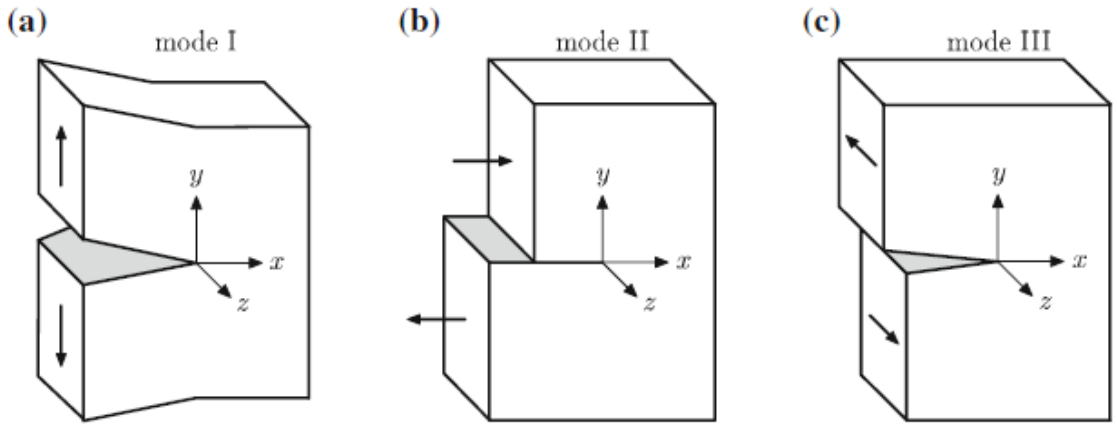

Figure 2.2.7 - Crack opening modes: (a) opening mode, (b) sliding mode, and (c) tearing mode [23]

Mode I or opening mode is characterised by an opening in the x-z plane. In Mode II or the sliding mode, the sliding occurs in the x-direction. Finally, in the out-of-plane shear (Mode III) or the tearing mode, relative displacements occur in the z-direction [23]. In reality, Mode I is considered the most relevant case.

Traditionally, fracture characterisation can be based on two approaches: the Stress Intensity Factor (SIF) or the energetic approach.

2.2.2.2.1 Stress intensity factors (SIF)

For a better understanding of this approach, an example is presented. Figure 2.2.8 shows an element near the tip of a crack in an elastic material and the in-plane element stresses.

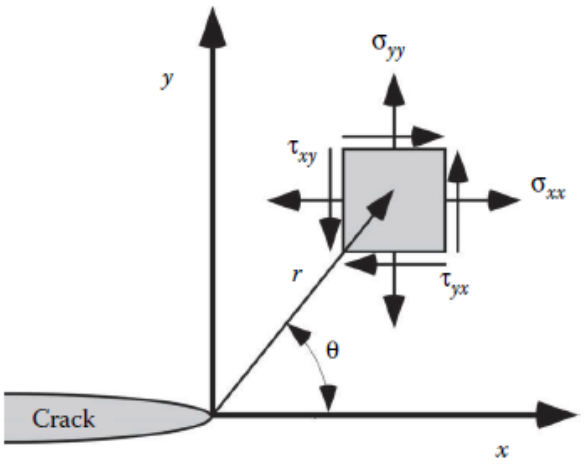

$$\sigma_{xx} = \frac{K_I}{\sqrt{2\pi r}}\cos\left(\frac{\theta}{2}\right)\left[1-\sin\left(\frac{\theta}{2}\right)\sin\left(\frac{3\theta}{2}\right)\right]$$

$$\sigma_{yy} = \frac{K_I}{\sqrt{2\pi r}}\cos\left(\frac{\theta}{2}\right)\left[1+\sin\left(\frac{\theta}{2}\right)\sin\left(\frac{3\theta}{2}\right)\right]$$

$$\tau_{xy} = \frac{K_I}{\sqrt{2\pi r}}\cos\left(\frac{\theta}{2}\right)\sin\left(\frac{\theta}{2}\right)\cos\left(\frac{3\theta}{2}\right)$$

Figure 2.2.8 - Stresses near the tip of the crack in an elastic material [24]

It is possible to observe a direct relationship between all the stresses: the constant K_I. Therefore, this constant is essential to the fracture's characterisation and is called the stress intensity factor [24]. This factor is given by

$$k_I = \sigma\sqrt{\pi a}\,, \tag{2}$$

where σ is the applied tensile stress, and a is half crack length. This concept arose from Irwin [25] in 1957. Assuming material failure at some critical combination of stress and strain, then it follows that fracture must occur at a critical stress intensity value, K_{IC} [24]. Therefore failure takes place when K_I=K_{IC}. These considerations and formulation are similar to the other crack opening modes. The fracture toughness K_{IC} of materials needs to be determined by an experimental procedure [26].

2.2.2.2.2 Energetic approach

The energetic approach affirms that the fracture occurs when the energy available for crack growth is sufficient to overcome the material's resistance [24]. Griffith [27] originally stated this proposal, later modified by Irwin [28].

Accordingly, the energy release rate, G, can be described as the rate of change in potential energy with the crack area for a linear elastic material. Thus, when failure occurs, G=G_{IC}, which represents the critical energy release rate [24]. Figure 2.2.9 contains an infinite plate with a crack of length 2a subjected to tensile stress. For this crack, the energy release rate is given by

$$G = \frac{\pi\sigma^2 a}{E}\,, \tag{3}$$

where E is Young's modulus.

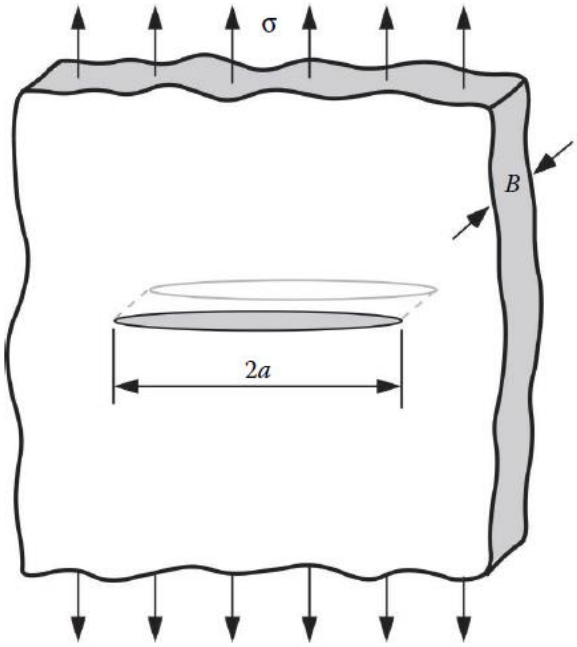

Figure 2.2.9 - Infinite plate with a crack subjected to tensile stress [24]

Comparing equations (2) and (3), a relationship between G and K_I emerges:

$$G = \frac{K_I^2}{E}. \tag{4}$$

This relationship is also viable for G_{IC} and K_{IC}. Consequently, the two approaches are essentially equivalent for elastic materials [24].

2.2.2.2.3 Virtual crack closure technique (VCCT)

The Virtual Crack Closure Technique (VCCT) is a numerical approach to determine the energy release rate seen in the previous chapter. It assumes that the energy required to create a new crack is the same required to close it back to its original state [29]. This method hinges on Irwin's crack closure integral [30].

Figure 2.2.10 illustrates this statement. The energy ΔE liberated when opening the crack from a to $a+\Delta a$ is equivalent to the energy necessary to close the crack from l to i [31]. This energy (ΔE), considering two-dimensional four-noded elements, can be calculated by

$$\Delta E = \frac{1}{2}\left[X_{1l} \times \Delta u_{2l} + Z_{1l} \times \Delta w_{2l}\right], \tag{5}$$

where X_{1l} and Z_{1l} correspond to the shear and opening forces at node l to be closed, and Δu_{2l} and Δz_{2l} are the differences in shear and opening nodal displacements at node l.

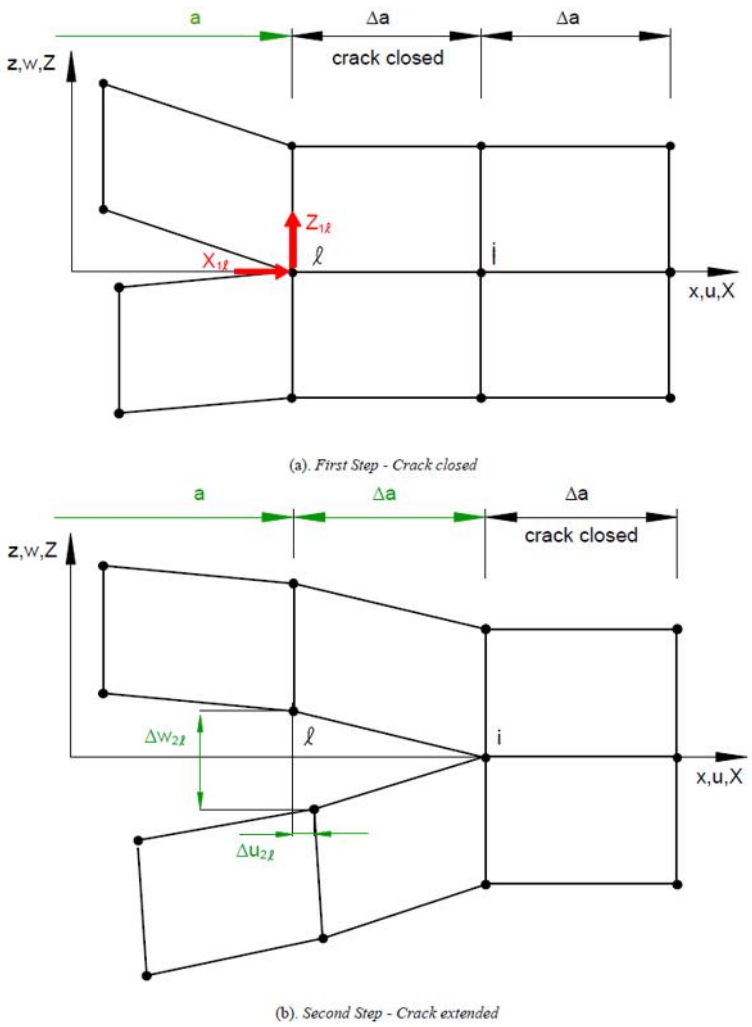

Figure 2.2.10 - Two-step process of VCCT [31]

As shown, this is a two-step process. The forces X_{1l} and Z_{1l} can be obtained from a first finite element analysis where the crack is closed. After that, the displacements Δu_{2l} and Δz_{2l} are calculated from a second finite element analysis where the crack is open.

Later on, a modified VCCT analysis was proposed. In this case, it is assumed that a crack extension of Δa from $a+\Delta a$ to $a+2\Delta a$ does not change the state considerably at the crack tip. Therefore, the displacements at node i are essentially the same as the displacements at node l [31]. Accordingly, the energy ΔE (considering two-dimensional four-noded elements) is given by

$$\Delta E = \frac{1}{2}\left[X_i \times \Delta u_l + Z_i \times \Delta w_l\right], \tag{6}$$

in which X_i and Z_i are the shear and opening forces at the nodal point i, and Δu_l and Δz_l are the shear and opening displacements at node l. This way, this energy only requires one finite element analysis to be determined (Figure 2.2.11).

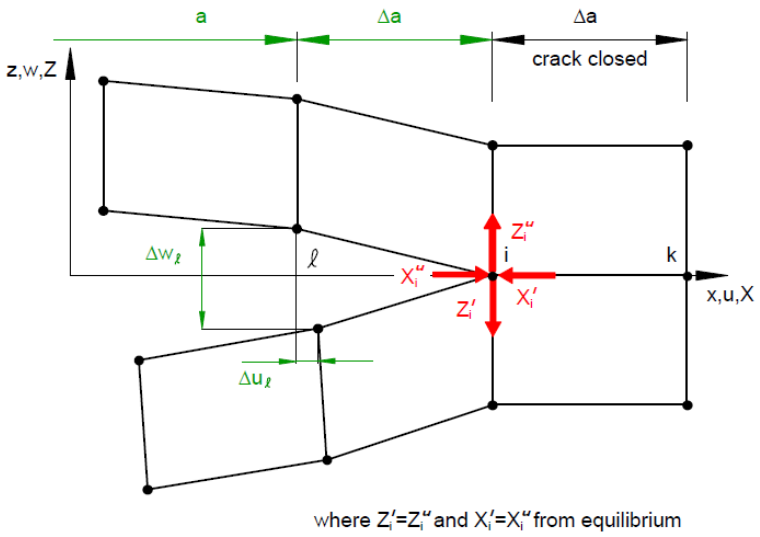

Figure 2.2.11 - One-step VCCT analysis [31]

With the energy necessary to open and close the crack, the strain energy release rate can be obtained by dividing ΔE by the area ΔA of the crack surface. Considering mixed-mode strain energy release rates using two-dimensional four-noded finite element, G_I and G_{II} are calculated by

$$G_I = -\frac{1}{2\Delta a} \times Z_i \times \left(w_l - w_{l^*} \right) \tag{7}$$

$$G_{II} = -\frac{1}{2\Delta a} \times X_i \times \left(u_l - u_{l^*} \right). \tag{8}$$

These equations consider a unitary thickness, as shown in Figure 2.2.12. Therefore, the area ΔA considered is $\Delta a \cdot 1$.

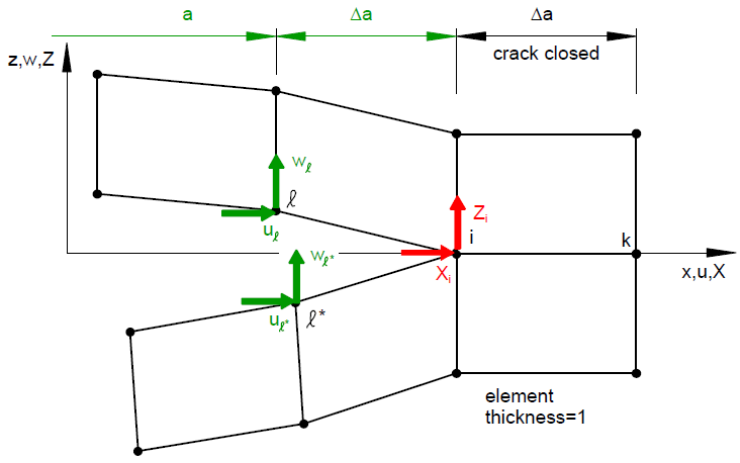

Figure 2.2.12 - VCCT for a four-noded finite element [31]

The work of Krueger [31] can be consulted for the formulation of three-dimensional solids and shell elements, as well as geometrically non-linear analysis.

2.2.2.2.4 Finite fracture mechanics

In 2002, Leguillon [32] introduced a new criterion based on fracture mechanics to predict crack initiation. This criterion was initially called the coupled stress-strain criterion and, more recently, became Finite Fracture Mechanics (FFM). Unlike classical fracture mechanics, this method does not require an initial crack, and it can determine that moment. For that, two criteria must be satisfied: an energetic criterion and a stress criterion [5]. The energetic approach limits the lower bound in crack initiation, and the stress approach the upper bound. Figure 2.2.13 shows this process.

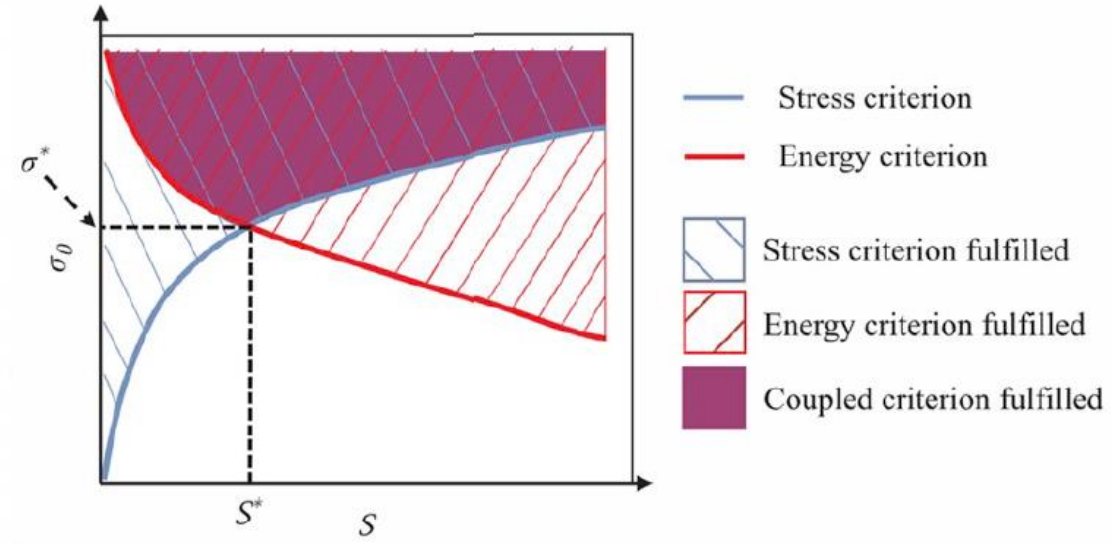

Figure 2.2.13 - Coupled criterion as a function of the crack area and imposed loading [33]

In simple terms, a certain amount of energy is necessary to open the crack and sufficient stress to damage the material. These two conditions can be expressed separately. The energy condition declares that the incremental energy release rate G^{inc} must be higher than the critical energy release rate G^{C}. The incremental release rate represents the proportion between the change in potential energy W due to the crack initiation and the newly created crack area S [33]. This statement is expressed in the following equation:

$$G^{inc}(S)=\frac{\Delta W}{S}=\frac{W(0)-W(S)}{S}=A(S)\times\sigma_0^2>G^C. \tag{9}$$

In this equation, A only depends on the geometry and properties of the material.

Relatively to stress condition, the crack surface must be overloaded to initiate. Therefore, a stress criterion f must be fulfilled. Assuming that stress is proportional to the applied load:

$$f(\underline{\sigma})=k(S)\times\sigma_0\geq\sigma_C. \tag{10}$$

In the case of *A* and *k* being a monotonic function of *S*, the configuration must be solved by combining and solving equations (9) and (10) [33], giving

$$\frac{A(S)}{k(S)^2} = \frac{G^C}{\sigma_C^2}. \tag{11}$$

This criterion is only applicable to brittle adhesives.

2.2.2.2.5 Intensity of singular stress fields (ISSF)

A method was recently proposed to determine the stress around the interface corner between an adhesive and adherend. The magnitude of this stress singularity is usually called ISSF. It is also known as the Generalised Stress Intensity Factor (GSIF). This method is identical to the SIF but does not require an initial crack [34]. The stress around this interface corner typically leads to crack initiation. The analysis of these singularities was already studied for scarf joints [35], butt joints [36], DLJ [37], and SLJ [38].

The scalar value of the ISSF is nominated *H*. There are two main ways of obtaining this parameter: an extrapolation method and the contour integral method. The first one considers that the asymptotic stress field developed at the vicinity of interface corners, when the body is subjected to a remote uniaxial load [36], in polar coordinates (r,θ), is given by

$$\sigma_{ij} = \sum_{n=1}^{\infty} H_n r^{\lambda_n - 1} f_{ij}(\lambda_n, \theta), \tag{12}$$

where r is the distance from the interface corner, H is the intensity of the stress singularity, and λ is the order of stress singularity. The displacement in the same region is given by

$$u_j = \sum_{n=1}^{\infty} H_n r^{\lambda_n} g_j(\lambda_n, \theta), \tag{13}$$

where n is the number of exponents that varies with the geometry of the interface corners.

The second method is based on Betti's reciprocal theorem [39]. In the absence of body forces, the reciprocal work contour integral is stated as

$$\oint_{\Sigma} \left(\sigma_{ij} u_i^* - \sigma_{ij}^* u_i \right) \cdot n_j ds = 0, \tag{14}$$

where σ_{ij} and u_i are the actual free-edge singular stress and displacement fields, and σ^*_{ij} and u^*_i are auxiliary fields satisfying the same boundary conditions as σ_{ij} and u_i. Since the auxiliary field must satisfy the same conditions as the actual field, the integral in equation (14) fades at the free edges of the materials adjacent to the interface corner, i.e., along C_1 and C_3, as shown in Figure 2.2.14.

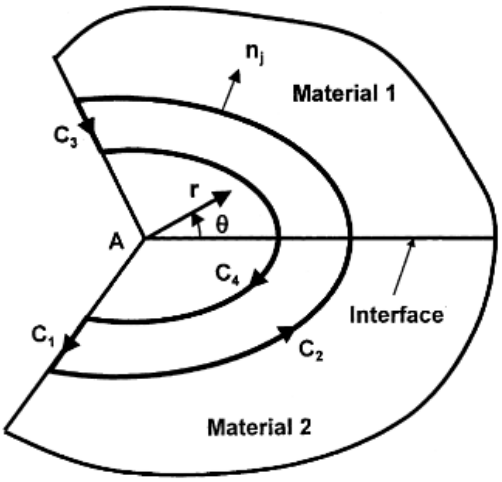

Figure 2.2.14 - Closed integration path around the interface corner [39]

Thus, equation (14) reduces to

$$\int_{C_4}\left(\sigma_{ij}u_i^* - \sigma_{ij}^* u_i\right)\cdot n_j ds = -\int_{C_2}\left(\sigma_{ij}u_i^* - \sigma_{ij}^* u_i\right)\cdot n_j ds\,. \tag{15}$$

Failure initiates when H at the interface corner exceeds the critical value H_C [36].

2.2.2.3 *Cohesive zone models*

One of the most studied strength prediction techniques for adhesively-bonded joints are the Cohesive Zone Models (CZM). This method's primary advantage is that it is not necessary to have an initial flaw in the material, unlike fracture mechanics [11]. The CZM approach includes continuum mechanics principles for damage initiation and fracture mechanics principles for crack propagation, establishing a softening relationship between stresses and strain, thus simulating gradual degradation of the material's mechanical properties. Therefore, it is the most recommended method for adhesive joint design. However, a limitation crops up with this process. It is usually required measurement of geometrically comparable adhesive properties [5]. The book of Campilho [11] explores this technique with more depth.

2.2.2.4 *Damage mechanics*

The procedure that guides damage mechanics analysis has in consideration a criterion in which the material stiffness decreases after a certain amount of strain/stress is achieved. The adhesive layer's cohesive failure and adherend failure can be accounted for with this formulation, including composite laminates. This approach also simulates different types of crack propagation, giving rigorous strength predictions [5]. Nonetheless, the adjustment of the parameter that controls the decrease of material stiffness is intricate. Given that energetic principles are not considered in this technique, it leads to little use of the method for predicting adhesive joints behaviour.

2.2.2.5 *Extended finite element method*

The eXtended Finite Element Method (XFEM) is a recent development of the common FEM to model damage extension. XFEM can let the crack propagate freely, unlike CZM where it has to follow a predetermined path [11]. This propagation relies on fracture mechanic principles. In fact, it transcends fracture mechanics by including continuum mechanics criterium for damage initiation and algorithms to partition solid elements and stimulate crack nucleation and growth. Still, the crack often grows from the adhesive to the adherend when the joint has large deformations or the adhesive layer rotates [5]. This characteristic is not consistent with real behaviour. A recent development allows crack deviation when the material's stiffness where the crack is present is lower than the one of the materials to where the crack is supposed to propagate. Even so, this development is not revolutionary or extremely important in the strength prediction of adhesive joints. Thus, the method does not present major advantages over CZM.

2.2.3 Failure criteria

René Quispe Rodríguez and co-workers' paper presents a review of the main failure criteria [16]. For the authors, failure criteria can be divided into five categories: maximum stress or strain criteria, critical stress or strain at a distance over a zone, limit state criteria, fracture mechanics, and damage mechanics criteria.

The maximum stress or strain criteria is the most popular to perform strength prediction analysis. With this approach, different characteristics can be evaluated to predict the strength of an adhesive joint. Peel stresses should be minimised in design. Hart-Smith [40] considered this characteristic as a failure criterion. The maximum principal tensile stress and strain criteria [41], the maximum von Mises stress [42], and the maximum shear strain criteria [43] are also acceptable variations of this approach.

The critical stress or strain at a distance over a zone emerged due to the necessity of considering singularities [16]. The criteria presented above have a high dependency on the mesh in this analysis.

In 1989, Crocombe [44] proposed the limit state criteria. In his paper, it is declared that a line of adhesive along the overlap region reaches the state of failure when it can not withstand an increase in the applied load. This concept is also known as global yielding.

Failure criteria is a long and complicated theme, and there are many approaches to the subject. The work of René and co-workers has a more extensive review of these concepts. Table 2.2.1 presents some of the most crucial failure criteria [45].

Table 2.2.1 - Failure criteria [45] (τ shear stress, σ peel stress, σ_R tensile strength, γ shear strain, γ_P plastic shear failure strain, ε_e equivalent strain (von Mises), ε_R tensile failure strain, GY global yielding – all in the adhesive)

Model	Analysis	Failure Criterion
Volkersen [10]	Linear	$\tau>\tau_R$
Goland and Reissner [14]	Linear	$\tau>\tau_R$ or $\sigma>\sigma_R$
Hart-Smith[40]	Linear	$\tau>\tau_R$ or $\sigma>\sigma_R$
	Non-linear	$\gamma>\gamma_P$ or GY
Bigwood and Crocombe [46]	Linear	$\tau>\tau_R$ or $\sigma>\sigma_R$
	Non-linear	$\varepsilon_e>\varepsilon_R$ or GY
Frostig et al. [47]	Linear	$\tau>\tau_R$ or $\sigma>\sigma_R$
Adams and Mallick [48]	Linear	$\tau>\tau_R$ or $\sigma>\sigma_R$
	Non-linear	$\varepsilon_e>\varepsilon_R$ or GY
	'Effective modulus'	$\varepsilon_e>\varepsilon_R$
	Composite transverse failure	$\sigma_{comp}>\sigma_{r\ comp}$
Adams et al. [49]	Elastic adherend and ductile adhesive	GY
	Elasto-plastic adherend	Adherend yielding

2.2.4 State-of-the-art review

This chapter is reserved for a state-of-the-art review of strength prediction techniques related to adhesive joints, presented in Table 2.2.2.

Table 2.2.2 - State of the art review related to techniques of strength prediction

References	Description
A strain-based criterion for failure load prediction of steel/CFRP double strap joints [50]	This work employed strain-based failure criteria, namely the critical normal strain (CNS) criterion, to predict the failure load of adhesively-bonded double-strap joints made of steel plates reinforced with CFRP as externally-bonded sheets. Following the approach, the adhesive joint fails when the normal strain along the adhesive mid-line reaches a critical value at a critical distance. The authors concluded that CFRP sheets are an effective method to overhaul the damaged steel structures. This criterion successfully predicted two series of experimental results with different bonded lengths compared to theoretical results. It was also shown the method's accuracy, giving estimates with average discrepancies of about 5% over experimental results.

Applicability of VCCT in mode I loading of yielding adhesively bonded joints – a case study [51]	Jokinen and co-workers studied the applicability of VCCT for crack growth analyses of adhesively-bonded joints with self-similar crack growth. They used Double Cantilever Beam (DCB) specimens with an epoxy adhesive. First, they analysed the pre-crack cycle considering a linear elastic behaviour. The force-displacement curves obtained experimentally were very similar to those obtained numerically. Then a non-linear analysis was performed. They combined the non-linear and linear analysis data with experimental data to evaluate the adhesive's critical energy release rate. It was concluded that this evaluation could be performed with this technique. However, several parameters can affect the result, like the applied model and element mesh. They also pointed out the possibility of numerical problems.
Failure load prediction of a tubular bonded structures using a coupled criterion [52]	In this paper, the authors resorted to tubular bonded joints to validate the coupled criterion (FFM). To consider the loading rate effect on the failure load, the authors proposed modifying the criterion. The adhesive strength was estimated with a modified Arcan test. Then they compared the numerical results with experimental data. They concluded that the method presents a good agreement between the two types of results for different configurations. The modification proposed was able to predict the evolution of the loading rate.
Intensity of singular stress fields in single lap joints using a meshless method and the finite element method [34]	This report presents a study of singularity in aluminium SLJ bonded with a brittle adhesive (Araldite RAV138) and four different overlap lengths, proposing a method to verify joint strength using the ISSF. This analysis was performed using the FEM and a meshless method, the Radial Point Interpolation Method (RPIM). A comparison between the predictions and experimental results was made. To determine the magnitude of the stress singularity, the author relayed on an extrapolation method. He concluded that this method was an advantage because it showed independence from the discretisation and that the two numerical methods provided similar results in every aspect, which validates the use of the ISSF in meshless methods.

An adaptation of mixed-mode I+II continuum damage model for prediction of fracture characteristics in adhesively bonded joint [53]	The work developed in this article focused on a variation of a continuum mixed-mode I+II damage model consenting to the simulation of different paths of crack propagation. The model was based on an exponential damage evolution. They studied the effect of the adhesive end fillet on the load-carrying capacity of the SLJs. The method's performance was evaluated by comparing it with previous models based on CZM, VCCT, and XFEM. Related to the methods, they observed that VCCT results differed from the others, confirming the method's non-appropriacy for predicting failure in ductile adhesives. Therefore, the presented approach was capable of improving the simulation of failure.
Experimental and numerical analysis of hybrid adhesively-bonded scarf joints [54]	Using hybrid scarf joints (composite and aluminium adherends) and varying the scarf angle, the authors performed a numerical analysis with FEM obtaining peel and shear stresses and a CZM analysis to predict the joint strength. The CZM showed that the adhesive layer's damage started at the bond edges and grew towards the adhesive layer up to complete failure. From the FEM analysis, a natural asymmetry was observed when plotting peel and shear stresses due to the different stiffness of the adherends. They also detected a variation of the joint behaviour depending on the scarf angle, directly linked to the stresses developed in the adhesive layer during loading.
Numerical modelling of adhesively-bonded double-lap joints by the eXtended Finite Element Method [55]	Santos and Campilho presented an investigation of DLJ using an XFEM analysis. Different adhesives were studied, from brittle to ductile. The adherends were from aluminium, and distinct overlap lengths were considered. The XFEM analysis contemplated damage initiation criteria based on stresses and strains and an energy criterion for damage propagation. Different values of the parameter α (exponent of the energy criterion) were tested. The authors concluded that, in brittle adhesives, α=1 provided the best results, while in ductile adhesives, this parameter does not have much influence.

2.3 Meshless methods

The use of FEM implies the creation of a mesh to discretise the studied object. For that, its geometry is divided into elements. However, the dependency of the mesh leads to several analysis limitations. For example, an object with large deformations originates accuracy loss in the results obtained due to distortions in the elements [56]. These constraints compelled the development of methods that do not rely on a mesh, designated as meshless methods. The first ones to present a meshless method were Gingold and Monaghan [57] in 1977, proposing a Smooth Particle Hydrodynamics (SPH) method. They used it to model astrophysical phenomena without boundaries, like exploding stars and dust clouds [58].

This chapter is dedicated to these methods, focusing on two approaches: the Radial Point Interpolation Method (RPIM) and the Natural Neighbour Radial Point Interpolation Method (NNRPIM).

2.3.1 General analysis procedure

The first step in a meshless analysis establishes the solid domain and contour (Figure 2.3.1 (a)). Then, the essential and natural boundary conditions have to be identified [59]. The nodal discretisation of the studied object can be performed in two ways: using a regular or an irregular distribution, as shown in Figure 2.3.1 (b) and (c), respectively.

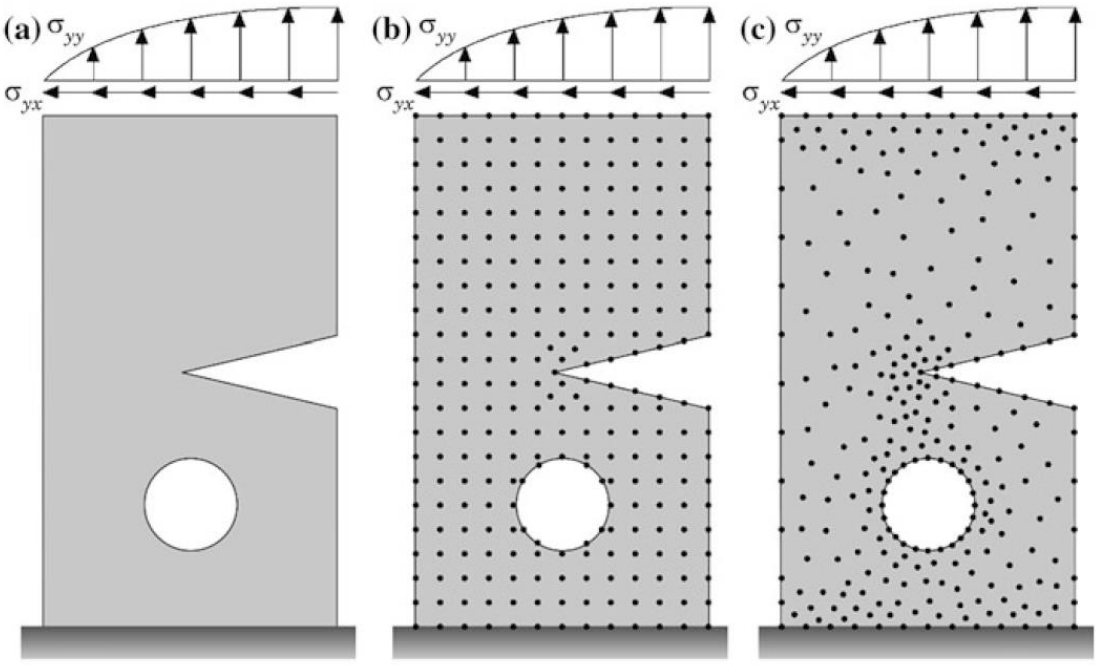

Figure 2.3.1 - (a) Solid domain and contour, (b) regular nodal discretization, and (c) irregular nodal discretization [59]

Thus, the only information required by meshless methods is each node's spatial location discretising the problem domain [59]. Therefore, meshing is not necessary.

A similarity arises between these methods and mesh dependent numerical methods: a fine nodal distribution leads to more accurate results, also valid with a mesh. Moreover, the computational cost also commonly rises with an increase in the total number of nodes [59]. Irregular distribution of the nodes, like in Figure 2.3.1 (c), originates lower accuracy. Nonetheless, predictable stress concentration locations should have a higher nodal density [60].

After securing nodal discretisation, a background integration mesh is formed. This mesh can be nodal dependent or independent. The nodal independent mesh leads to more accurate results, while the nodal dependent mesh requires a stabilisation method. Afterwards, the nodal connectivity can be enforced. With the FEM, this step is assured by the elements. With meshless methods, concentric areas or volumes are defined for each interest point of the problem domain, and the nodes inside those belong to the point's influence domain [59]. The final stage is the establishment of the equation system.

2.3.2 RPIM formulation

Liu and Gu [56] proposed the RPIM formulation to overcome singularity issues that occurred in earlier methods, such as the Element Free Galerkin Method (EFGM) [61], the Diffuse Element Method (DEM) [62], the Moving Least Square (MLS) [63], the Reproducing Kernel Particle Method (RKPM) [64] and the Meshless Local Petrov-Galerkin (MLPG) [65]. This method is more stable and robust for arbitrary nodal distributions. RPIM uses radial basis functions (RBF), but the shape parameters require careful selection [56]. This approach is an evolution of the Point Interpolation Method (PIM) that uses polynomials as base functions.

2.3.2.1 Influence domains and nodal connectivity

As mentioned before, in FEM, the nodal connectivity is guaranteed by the elements forming the mesh, where the nodes belonging to the same element interact with each other. With meshless methods, there is no predefined nodal interdependency. Hence, connectivity is established after the nodal distribution [59]. This association is obtained by overlapping the influence domain of each node. However, care must be taken with the size and shape of these influence domains along the problem domain. All the influence domains must contain roughly the same number of nodes because irregular domain boundaries could lead to unstable influence domains.

The most typical approach to assure nodal connectivity is to fix the size of the influence domains. Two sorts of fixed-size domains are recommended in two-dimensional problems: the rectangular and the circular shapes [59]. Nonetheless, this technique leads to a numerical accuracy loss. Therefore, flexible influence-domain sizes are a superior solution and avoid numerical problems. Figure 2.3.2 (a) to (c) shows the three described procedures.

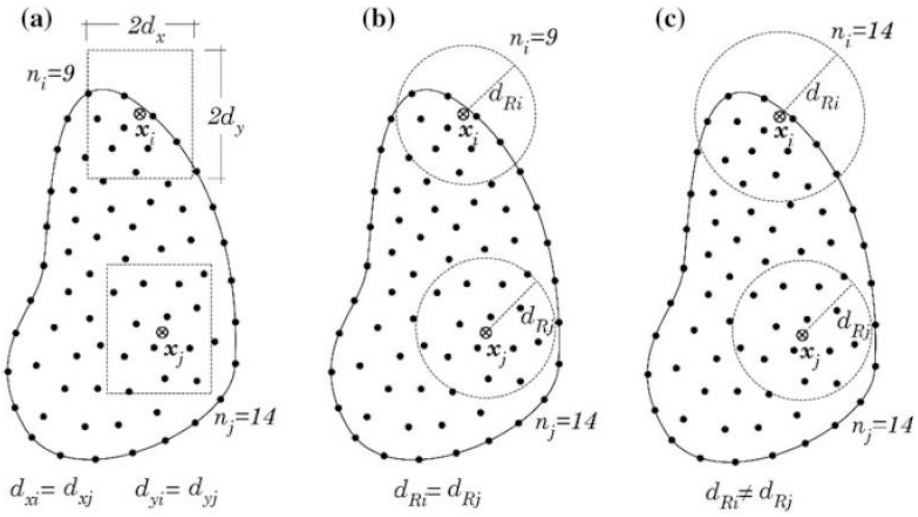

Figure 2.3.2 - (a) Fixed rectangular-shaped influence-domain, (b) fixed circular-shaped influence-domain, and (c) variable circular-shaped influence-domain [59]

2.3.2.2 Numerical integration

In most numerical methods using a variational formulation, the numerical integration process, obligatory to determine the system of equations based on the integrodifferential equations commanding the studied physical phenomenon, represents a substantial percentage of the computational cost [59]. In FEM, the element mesh is coincident with the integration mesh. In meshless methods, that is not the case. Thus, the background integration mesh cannot be defined a priori. With these methods, it is essential to establish the optimal relationship between the field nodes' density and the background integration mesh density, as shown in Figure 2.3.3.

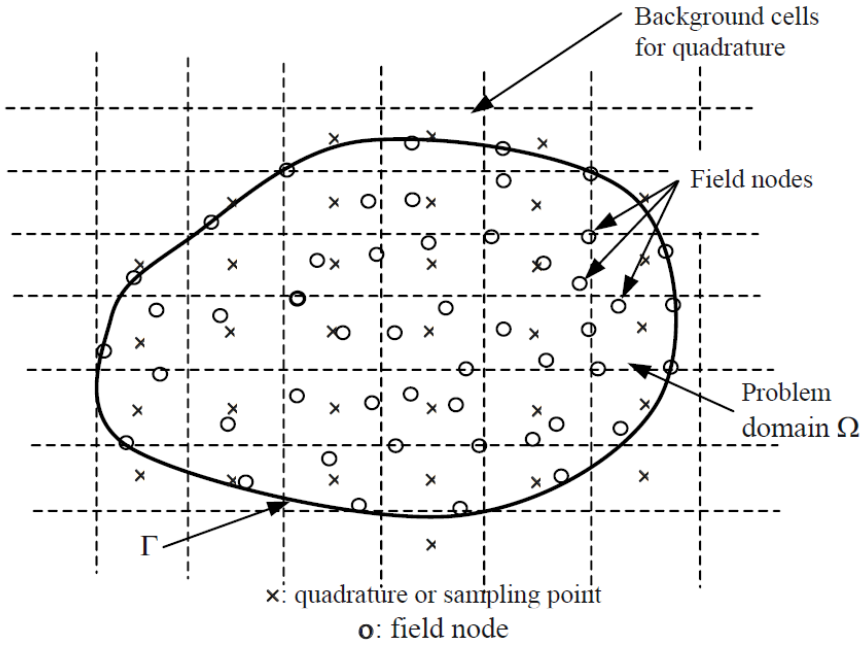

Figure 2.3.3 - Background integration mesh in meshless methods [56]

With the problem domain (Ω) discretised, global integration is given by the sum of integrals over the cells [56]

$$\int_{\Omega} \boldsymbol{G} \cdot d\Omega = \sum_{k}^{n_c} \int_{\Omega_k} \boldsymbol{G} \cdot d\Omega , \tag{16}$$

where n_c is the number of background cells, G represents the integrand, and Ω_k is the k^{th} background cell domain.

The most commonly applied scheme to execute these numerical integrations is the Gauss quadrature, also used in FEM. Considering n_g Gauss points in each background cell, equation (16) becomes [56]

$$\int_{\Omega} G \cdot d\Omega = \sum_{k}^{n_c} \int_{\Omega_k} G \cdot d\Omega = \sum_{k}^{n_c} \sum_{i=1}^{n_g} w_i G(x_{Qi}) \left| \boldsymbol{J}_{ik}^{D} \right| , \tag{17}$$

where w_i is the Gauss weighting factor for the i^{th} Gauss point at x_{Qi}, and J_{ik}^{D} is the Jacobian matrix for the area integration of the background cell k, at which the Gauss point x_{Qi} is located.

2.3.3 NNRPIM formulation

The NNRPIM formulation is a recent approach that combines the RPIM with the concept of natural neighbours. This method considers the concept of “influence-cells” instead of “influence-domain” to impose the nodal connectivity [59]. For the definition of the influence-cells, Voronoï diagrams and Delaunay tessellation are used. The exclusive dependency of the integration mesh on the nodal distribution makes the NNRPIM a genuinely meshless method. With this technique, a random node distribution for discretising the problem is possible. The interpolation functions are very similar to the ones of RPIM. However, some differences exist that change the method performance.

2.3.3.1 Natural neighbours

Sibson [66] firstly introduced the concept of natural neighbour in 1980. This concept is applied to obtain the Voronoï diagram. The theory applies to a d-dimensional space, but only a two-dimension example is presented [67]. Considering a set $\boldsymbol{N}$ of n distinct nodes

$$\boldsymbol{N} = \{ n_1, n_2, \ldots, n_n \} \in \mathbb{R}^2 , \tag{18}$$

discretising the problem domain Ω with

$$\boldsymbol{X} = \{ x_1, x_2, \ldots, x_n \} \in \Omega , \tag{19}$$

the Voronoï diagram of $\boldsymbol{N}$ is the partition of the function space discretised by $\boldsymbol{X}$ in sub-regions V_i. V_i is the geometric place where all points are closer to node n_i than any other node n_j [67]. The set of Voronoï cells $\boldsymbol{V}$ define the Voronoï diagram

$$\boldsymbol{V} = \{V_1, V_2, \ldots, V_n\}. \tag{20}$$

Each Voronoï cell is defined by

$$V_i = \left\{ x_l \in \mathbb{R}^2 : \|x_l - x_i\| < \|x_l - x_j\|, \forall i \neq j \right\}, \tag{21}$$

where x_l is an interesting point of the domain and $\|\cdot\|$ is the Euclidian metric norm.

Figure 2.3.4 (a) shows the construction of the sub-region V_l, starting with a set of potential neighbours.

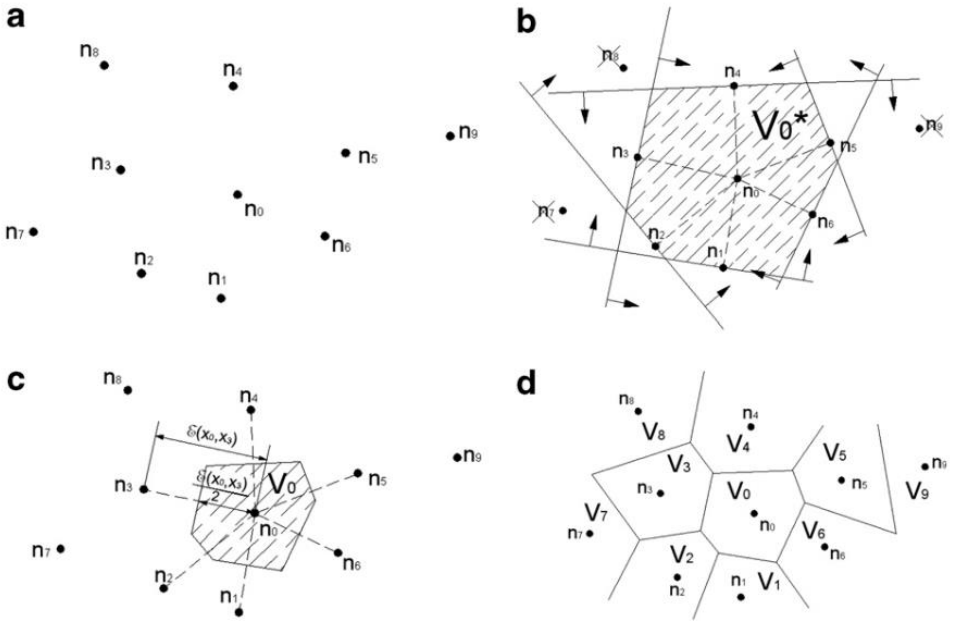

Figure 2.3.4 - (a) Initial nodal set of potential nodes, (b) final cell containing only neighbours nodes, (c) Voronoï cell, and (d) Voronoï diagram [67]

The objective is to determine the Voronoï cell V_0 of node n_0. Thus, potential neighbours need to be selected [59]. Choosing, as an example, node n_4, vector u_{40} is determined

$$u_{40} = \frac{(x_0 - x_4)}{\|x_0 - x_4\|}, \tag{22}$$

where u_{40} = (u_{40},v_{40},w_{40}). With the normal vector u_{40}, the plane π_{40} is defined (Figure 2.3.4 (b))

$$u_{40}x + v_{40}y + w_{40}z = (u_{40}x_4 + v_{40}y_4 + w_{40}z_4). \tag{23}$$

After this definition, all the nodes that do not respect the condition

$$u_{40}x + v_{40}y + w_{40}z \geq (u_{40}x_4 + v_{40}y_4 + w_{40}z_4) \tag{24}$$

are excluded as natural neighbours of node n_0 (Figure 2.3.4 (c)). Subsequently, the process is repeated for each one of the initial node-set (Figure 2.3.4 (d)) [59]. The Voronoï cell V_0 is the homothetic form of the auxiliary domain V_0^*.

By joining the nodes whose Voronoï cells have shared boundaries, Delaunay triangulations are constructed (Figure 2.3.5 (b)). These are the geometrical dual of the Voronoï diagram [67]. An essential attribute of the Delaunay triangles is the empty circumcircle criterion. If a set of three nodes forms a Delaunay triangle, then the triangle's circumcircle does not contain any other node of the global nodal set (Figure 2.3.5 (c)). The circles are known as natural neighbours circumcircles.

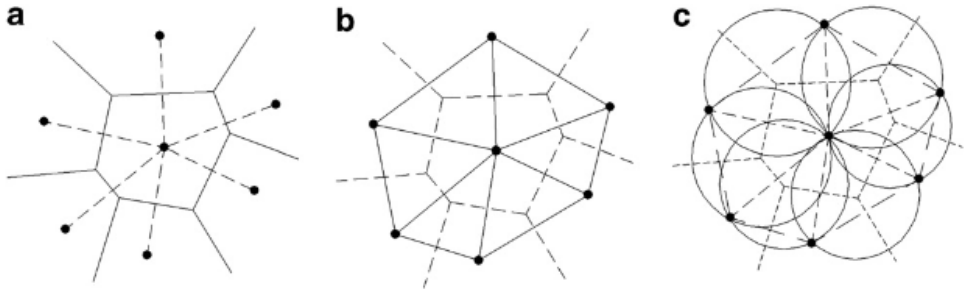

Figure 2.3.5 - (a) Initial Voronoi diagram, (b) Delaunay triangulation and (c) natural neighbours circumcircles [67]

2.3.3.2 Numerical integration

Based on the Voronoï cells' construction and the Delaunay triangles, small areas are considered, that can be quadrilaterals or triangles with an irregular or a regular mesh, respectively. Then, with the Voronoï cells, the interception points (P_{Ii}) of the cell's neighbour edges can be established (Figure 2.3.6 (a)). After that, the middle points (M_{Ii}) between node *I* and its neighbour nodes are attained (Figure 2.3.6 (b)) [67]. Therefore, the Voronoï cells are split into *n* quadrilateral sub-cells (S_{Ii}) (Figure 2.3.6 (c)) [67]. Within the context of a regular mesh, the middle points are coinciding with the edge intersection points (Figure 2.3.6 (d) and (e)). In that manner, triangles are formed instead of quadrilaterals (Figure 2.3.6 (f)).

As described, it is possible to divide the Voronoï cells into *n* sub-cells. Accordingly, the size of the Voronoï cell (V_I) is obtained with the sizes of the sub-cells (S_{Ii})

$$A_{V_I} = \sum_{i=1}^{n} A_{S_{Ii}} \forall A_{S_{Ii}} \geq 0\,, \tag{25}$$

being A_{VI} the size of the Voronoï cell V_I and A_{SIi} the size of the sub-cells S_{Ii}.

With the two shapes of sub-cells, various integration schemes can be composed. In the book of Belinha [59], diverse schemes are presented, such as a basic integration scheme, the Gauss-Legendre quadrature integration scheme, or the nodal integration scheme.

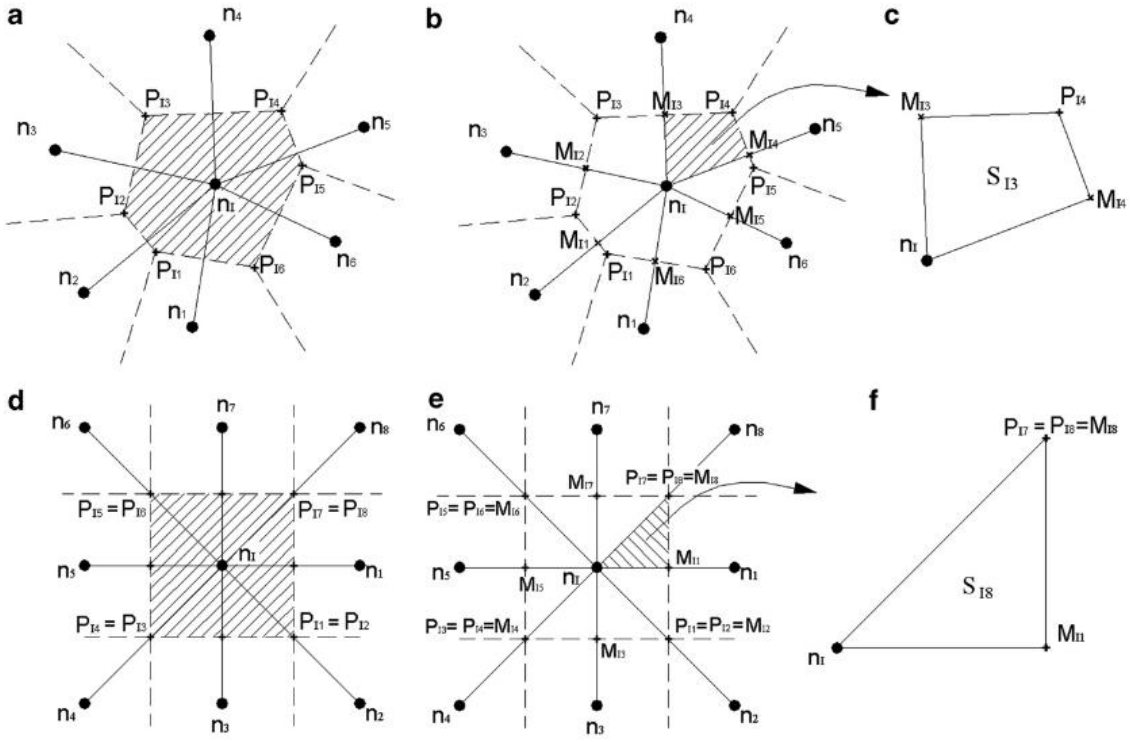

Figure 2.3.6 - For the irregular mesh: (a) Voronoï cells and interception points, (b) middle points, and (c) quadrilateral. For regular mesh: (d) Voronoï cells and interception points, (e) middle points, and (f) triangles [67]

2.3.4 Shape functions

Methods like the EFGM, RKPM, and MLPG resort to approximation functions to obtain the shape functions [67]. However, the delta Kronecker property is not present in this approach, making it complicated to impose the essential and natural boundary conditions.

The formulation presented here is based on the Moving Least-Square approximants (MLS) [63] and the Radial Point Interpolators (RPI) [68]. Considering a function $u(x)$ defined in a particular domain, discretised by a nodal set of N nodes and assuming that only the nodes within the influence-cell affect the function $u(x_I)$, it is possible to obtain the value of the function in a specific point x_I by

$$\boldsymbol{u}(\boldsymbol{x}_I)=\sum_{i=1}^{n}R_i(\boldsymbol{x}_I)\cdot a_i(\boldsymbol{x}_I)+\sum_{j=1}^{m}p_j(\boldsymbol{x}_I)\cdot b_j(\boldsymbol{x}_I)=\left\{\boldsymbol{R}^T(\boldsymbol{x}_I),\boldsymbol{p}^T(\boldsymbol{x}_I)\right\}\cdot\begin{Bmatrix}\boldsymbol{a}\\\boldsymbol{b}\end{Bmatrix}, \tag{26}$$

where $R_i(x_I)$ is the RBF and n is the number of nodes inside the influence-cell of x_I [67]. The coefficients $a_i(x_I)$, and $b_j(x_I)$ are non-constant coefficients of $R_i(x_I)$ and $p_j(x_i)$, respectively.The $p_j(x_i)$ function is of polynomial basis, and m is the number of polynomial basis monomials. Equation (19) vectors are:

$$\boldsymbol{R}^T(\boldsymbol{x}_I)=\left\{R_1(\boldsymbol{x}_I),R_2(\boldsymbol{x}_I),\ldots,R_n(\boldsymbol{x}_I)\right\}; \tag{27}$$

$$\boldsymbol{p}^T(\boldsymbol{x}_I) = \{p_1(\boldsymbol{x}_I), p_2(\boldsymbol{x}_I), \ldots, p_m(\boldsymbol{x}_I)\}; \tag{28}$$

$$\boldsymbol{a}^T(\boldsymbol{x}_I) = \{a_1(\boldsymbol{x}_I), a_2(\boldsymbol{x}_I), \ldots, a_n(\boldsymbol{x}_I)\}; \tag{29}$$

$$\boldsymbol{b}^T(\boldsymbol{x}_I) = \{b_1(\boldsymbol{x}_I), b_2(\boldsymbol{x}_I), \ldots, b_m(\boldsymbol{x}_I)\}. \tag{30}$$

In the RBF, the variable r_{Ii} is given by the distance between node x_I and the neighbour node x_i, being calculated by

$$r_{Ii} = \sqrt{(x_i - x_I)^2 + (y_i - y_I)^2 + (z_i - z_I)^2}\,. \tag{31}$$

The RBF multi quadratic proposed by Hardy [69] is given by

$$R(r_{Ii}) = \left(r_{Ii}^2 + c^2\right)^P, \tag{32}$$

in which c and p are two form parameters. These parameters directly affect the results of RBF. Therefore, they need optimisation recurring to numerical tests [67]. In the case of a 2D analysis, the polynomial basis are:

- Null basis

$$\boldsymbol{x}^T = \{x, y\}; \boldsymbol{p}^T(\boldsymbol{x}) = \{0\}; m = 0\,, \tag{33}$$

- Constant basis

$$\boldsymbol{x}^T = \{x, y\}; \boldsymbol{p}^T(\boldsymbol{x}) = \{1\}; m = 1\,, \tag{34}$$

- Liner basis

$$\boldsymbol{x}^T = \{x, y\}; \boldsymbol{p}^T(\boldsymbol{x}) = \{1, x, y\}; m = 3\,, \tag{35}$$

- Quadratic basis

$$\boldsymbol{x}^T = \{x, y\}; \boldsymbol{p}^T(\boldsymbol{x}) = \{1, x, y, x^2, xy, y^2\}; m = 6\,. \tag{36}$$

In order to obtain a unique solution, the polynomial basis has to satisfy the following requirement:

$$\sum_{i=1}^{n} p_j(\boldsymbol{x}_i) \cdot a_i(\boldsymbol{x}_i) = 0, \quad j = 1, 2, \ldots, m\,. \tag{37}$$

Thus, a new equation matrix is written

$$\begin{Bmatrix} \boldsymbol{u}_s \\ 0 \end{Bmatrix} = \begin{bmatrix} \boldsymbol{R}_Q & \boldsymbol{P}_m \\ \boldsymbol{P}_m^T & 0 \end{bmatrix} \begin{Bmatrix} a \\ b \end{Bmatrix} = \boldsymbol{G} \begin{Bmatrix} a \\ b \end{Bmatrix}, \tag{38}$$

where

$$\boldsymbol{u}_s = \{u_1, u_2, \ldots, u_n\}^T, \tag{39}$$

and

$$\boldsymbol{R_Q} = \begin{bmatrix} R(r_{11}) & R(r_{21}) & .. & R(r_{1n}) \\ R(r_{21}) & R(r_{22}) & .. & R(r_{2n}) \\ : & : & & : \\ R(r_{n1}) & R(r_{n2}) & .. & R(r_{nn}) \end{bmatrix}. \tag{40}$$

The constant polynomial basis is characterised by

$$\boldsymbol{P_m} = \begin{bmatrix} 1 & 1 & \dots & 1 \end{bmatrix}^T, \tag{41}$$

in which the polynomial basis for a 2D problem is

$$\boldsymbol{P_m} = \begin{bmatrix} 1 & 1 & \dots & 1 \\ x_1 & x_2 & \dots & x_n \\ y_1 & y_2 & \dots & y_n \end{bmatrix}^T. \tag{42}$$

Noticing that the *G* matrix is symmetric because the distance is independent of the direction. By solving equation (38)

$$\begin{Bmatrix} a \\ b \end{Bmatrix} = \boldsymbol{G}^{-1} \cdot \begin{Bmatrix} \boldsymbol{u_s} \\ 0 \end{Bmatrix}, \tag{43}$$

and replacing it in equation (26), it is obtained

$$\boldsymbol{u}(\boldsymbol{x_I}) = \left\{ \boldsymbol{R}^T(\boldsymbol{x_I}), \boldsymbol{p}^T(\boldsymbol{x_I}) \right\} \cdot \boldsymbol{G}^{-1} \cdot \begin{Bmatrix} \boldsymbol{u_s} \\ 0 \end{Bmatrix} = \left\{ \varphi_1(\boldsymbol{x_I}), \varphi_2(\boldsymbol{x_I}), \dots, \varphi_n(\boldsymbol{x_I}) \right\}, \tag{44}$$

where $\varphi(x)$ is the shape function.

In order to a variable ξ, the partial derivative of $\varphi(x)$ is defined as

$$\varphi_{,\xi} = \left\{ \boldsymbol{R}^T_{,\xi}(x_I), \boldsymbol{p}^T_{,\xi}(x_I) \right\} \cdot \boldsymbol{G}^{-1}. \tag{45}$$

The partial derivatives of the MQ-RBF in order to *x* and *y* are

$$\boldsymbol{R}_{,x}(r_{ij}) = 2p\left(r_{ij}^2 + c^2\right)^{p-1}(x_j - x_i), \tag{46}$$

$$\boldsymbol{R}_{,y}(r_{ij}) = 2p\left(r_{ij}^2 + c^2\right)^{p-1}(y_j - y_i). \tag{47}$$

These shape functions proved to possess the delta Kronecker property,

$$\varphi_i(\boldsymbol{x_j}) = \delta_{ij} = \begin{cases} 1(i=j) \\ 0(i \neq j) \end{cases}, i, \quad j = 1, \dots, n, \tag{48}$$

and the partition of unity is satisfied,

$$\sum_{i=1}^{n} \varphi_i(\boldsymbol{x}_i) = 1. \quad (49)$$

2.3.5 State-of-the-art applied to bonded joints

Table 2.3.1 presents a state-of-the-art review of the most recent works that applied meshless methods to bonded joints. Since these are recently developed methods, the applied works to bonded joints are scarce.

Table 2.3.1 - State-of-the-art review of meshless methods work applied to bonded joints

Reference	Description
Analysis of cohesive failure in adhesively bonded joints with SSPH meshless method [70]	This work uses a numerical approach to simulate crack initiation and propagation. The authors implemented CZM in the meshless method using the Symmetric Smoothed Particle Hydrodynamics (SSPH) basis functions. The experiments relied on a double cantilever beam under mode I and mixed-mode in-plane loadings. They concluded that the computed results agreed well with the experimental results in mode I, with a maximum difference between peak loads of less than 7%. The deformations attained were close to the corresponding experimental results for mixed-mode loadings, but only for mode mixity angles less than 50°.
Strength prediction and stress analysis of adhesively bonded composite joints using meshless methods [71]	This paper uses the RPIM to study the stress distributions and predict the strength of composite adhesive SLJ. In that manner, a brittle adhesive was tested in composite joints with different overlap lengths. To overcome the difficulty of using the RPIM in bi-materials problems, Ramalho and co-workers restricted the influence-domains in the interface region between materials. With this, the stresses obtained with RPIM were very similar to the ones of FEM. The authors also checked the applicability of the Critical Longitudinal Strain (CLS) criterion to SLJ with composite substrates. It was concluded that, although this criterion can give accurate strength predictions, its applicability is limited because the predictions can show significant variations depending on the chosen overlap length.

Analysing single-lap joints bonded with brittle adhesive by an elastic meshless method [72]	Sánchez-Arce and co-authors resorted to the NNRPIM to analyse adhesive joints. They measured experimental data of SLJ corresponding to four different overlap lengths with a brittle adhesive. Then, they simulated the geometries utilising the FEM and NNRPIM. By comparing the results, it was concluded that the results were very similar between the two methods, with a maximum observed difference in the strength of 2 %, proving that the NNRPIM is suitable for this analysis. The stresses also showed promising results, with a maximum peak shear stress difference of 6,6% between numerical and analytical results.
Material non-linearity in the numerical analysis of SLJ bonded with ductile adhesives: A meshless approach [73]	The work developed by Sánchez and co-workers implements a yielding criterion, the Exponent Drucker-Prager (EDP), in the NNRPIM. The NNRPIM elastic-plastic parametric analysis of SLJ with aluminium substrates was then performed for four overlap lengths and two different ductile adhesives. The results revealed a promising implementation of the method. They concluded that the EDP, combined with NNRPIM, can predict joint strength, joint extension, and stresses in the adhesive layer and analyse adhesively-bonded joints involving very ductile adhesives. To date, this was the first time that this combination was applied.

2.4 References

[1] Degano, I., S. Soriano, P. Villa, L. Pollarolo, J.J. Lucejko, Z. Jacobs, K. Douka, S. Vitagliano and C. Tozzi, *Hafting of Middle Paleolithic tools in Latium (central Italy): new data from Fossellone and Sant'Agostino caves.* PLoS One, 2019. **14**(6): p. e0213473.

[2] Da Silva, L.F., A. Öchsner and R.D. Adams, *Handbook of adhesion technology*. 2011, Berlin, Germany: Springer Science & Business Media.

[3] Ebnesajjad, S. and A.H. Landrock, *Adhesives technology handbook*. 2014, London, UK: William Andrew.

[4] Petrie, E.M., *Handbook of adhesives and sealants*. 2000, U.S: McGraw-Hill.

[5] Ramalho, L.D.C., R.D.S.G. Campilho, J. Belinha and L.F.M. da Silva, *Static strength prediction of adhesive joints: A review.* International Journal of Adhesion and Adhesives, 2020. **96**: p. 102451.

[6] da Silva, L.F.M., A.G. de Magalhaes and M.F.S. de Moura, *Juntas adesivas estruturais*. 2007, Porto, Portugal: Publindústria Portugal.

[7] Adams, R.D., *Adhesive bonding: science, technology and applications*. 2005, Boca Raton, North America: Elsevier.

[8] SUNSTAR. *Supporting global automotive innovation with adhesive technology*. [Accessed in 2020]; Available from: https://www.sunstar.com/healthy-thinking/weld-bonding/.

[9] Geiß, P.L., *Klebtechnik übernimmt tragende Rolle im Bauwesen.* adhäsion KLEBEN DICHTEN, 2006. **50**(1): p. 14-18.

[10] Volkersen, O., *Die Nietkraftverteilung in zugbeanspruchten Nietverbindungen mit konstanten Laschenquerschnitten.* Jahrbuch der Deutschen Luftfahrtforschung, 1938. **15**: p. 41-47.

[11] Campilho, R.D., *Strength prediction of adhesively-bonded joints*. 2017, Boca Raton, U.S.: CRC Press.

[12] Adams, R. and N. Peppiatt, *Stress analysis of adhesive-bonded lap joints.* Journal of strain analysis, 1974. **9**(3): p. 185-196.

[13] da Silva, L.F., P.J. das Neves, R. Adams and J. Spelt, *Analytical models of adhesively bonded joints—Part I: Literature survey.* International Journal of Adhesion and Adhesives, 2009. **29**(3): p. 319-330.

[14] Goland, M. and E. Reissner, *The stresses in cemented joints.* Journal of Applied Mechanics, 1944. **66**: p. A17-A27.

[15] Hart-Smith, L.J., *Adhesive-bonded single-lap joints*. 1973: Citeseer.

[16] Rodríguez, R.Q., W.P. De Paiva, P. Sollero, M.R.B. Rodrigues and É.L. De Albuquerque, *Failure criteria for adhesively bonded joints.* International Journal of Adhesion and Adhesives, 2012. **37**: p. 26-36.

[17] Ojalvo, I. and H. Eidinoff, *Bond thickness effects upon stresses in single-lap adhesive joints.* AIAA journal, 1978. **16**(3): p. 204-211.

[18] Tsai, M., D. Oplinger and J. Morton, *Improved theoretical solutions for adhesive lap joints.* International Journal of Solids Structures, 1998. **35**(12): p. 1163-1185.

[19] Allman, D., *A theory for elastic stresses in adhesive bonded lap joints.* The quarterly journal of mechanics applied mathematics, 1977. **30**(4): p. 415-436.

[20] Chen, D. and S. Cheng, *An analysis of adhesive-bonded single-lap joints.* Journal of Applied Mechanics, 1983. **50**: p. 109-115.

[21] Da Silva, L.F.M. and R.D.S.G. Campilho, *Advances in numerical modelling of adhesive joints*. Advances in numerical modeling of adhesive joints. 2012, Heidelberg: Springer.

[22] Williams, M.L., *The stresses around a fault or crack in dissimilar media.* Bulletin of the Seismological Society of America, 1959. **49**(2): p. 199-204.

[23] Öchsner, A., *Continuum damage mechanics*, in *Continuum Damage and Fracture Mechanics*. 2016, Springer. p. 65-84.

[24] Anderson, T.L., *Fracture mechanics: fundamentals and applications*. 2017, Boca Raton, U.S.: CRC press.

[25] Irwin, G.R., *Analysis of stresses and strains near the end of a crack transversing a plate.* Trans. ASME, Ser. E, J. Appl. Mech., 1957. **24**: p. 361-364.

[26] Kuna, M., *Finite elements in fracture mechanics*. Vol. 10. 2013, Wiesbaden, Germany: Springer.

[27] Griffith, A.A., *VI. The phenomena of rupture and flow in solids.* Philosophical transactions of the royal society of london. Series A, containing papers of a mathematical or physical character, 1921. **221**(582-593): p. 163-198.

[28] Irwin, G.R., *Onset of fast crack propagation in high strength steel and aluminum alloys*. 1956, Naval Research Lab Washington DC.

[29] Donough, M., A. Gunnion, A. Orifici and C. Wang. *Critical assessment of failure criteria for adhesively bonded composite repair design*. in *International Council of the Aeronautical Sciences*. 2012. ICAS.

[30] Irwin, G., *Fracture.* Handbuch der Physik, 1958. **6**: p. 551-590.

[31] Krueger, R., *Virtual crack closure technique: history, approach, and applications.* Appl. Mech. Rev., 2004. **57**(2): p. 109-143.

[32] Leguillon, D., *Strength or toughness? A criterion for crack onset at a notch.* European Journal of Mechanics-A/Solids, 2002. **21**(1): p. 61-72.

[33] Doitrand, A. and D. Leguillon, *Comparison between 2D and 3D applications of the coupled criterion to crack initiation prediction in scarf adhesive joints.* International Journal of Adhesion and Adhesives, 2018. **85**: p. 69-76.

[34] Ramalho, L.D.C., *Intensity of singular stress fields in single lap joints using a meshless method and the finite element method*. 2020, Faculty of Engineering of the University of Porto - Course Unit: Computational Methods in Plasticity and Fracture Mechanics.

[35] Wu, Z., S. Tian, Y. Hua and X. Gu, *On the interfacial strength of bonded scarf joints.* Engineering Fracture Mechanics, 2014. **131**: p. 142-149.

[36] Afendi, M., M.A. Majid, R. Daud, A.A. Rahman and T. Teramoto, *Strength prediction and reliability of brittle epoxy adhesively bonded dissimilar joint.* International Journal of Adhesion and Adhesives, 2013. **45**: p. 21-31.

[37] Mintzas, A. and D. Nowell, *Validation of an Hcr-based fracture initiation criterion for adhesively bonded joints.* Engineering Fracture Mechanics, 2012. **80**: p. 13-27.

[38] Rastegar, S., M.R. Ayatollahi, A. Akhavan-Safar and L.F.M. da Silva, *Prediction of the critical stress intensity factor of single-lap adhesive joints using a coupled ratio method and an analytical model.* Proceedings of the Institution of Mechanical Engineers, Part L: Journal of Materials: Design Applications, 2018. **233**(7): p. 1393-1403.

[39] Qian, Z. and A. Akisanya, *Wedge corner stress behaviour of bonded dissimilar materials.* Theoretical and Applied Fracture Mechanics, 1999. **32**(3): p. 209-222.

[40] Hart-Smith, L.J., *Adhesive-bonded single-lap joints*, in *NASA Contract Report, NASA CR-112236*. 1973.

[41] Harris, J. and R. Adams, *Strength prediction of bonded single lap joints by non-linear finite element methods.* International Journal of Adhesion and Adhesives, 1984. **4**(2): p. 65-78.

[42] Ikegami, K., T. Takeshita, K. Matsuo and T. Sugibayashi, *Strength of adhesively bonded scarf joints between glass fibre-reinforced plastics and metals.* International Journal of Adhesion and Adhesives, 1990. **10**(3): p. 199-206.

[43] Lee, S.J. and D.G. Lee, *Development of a failure model for the adhesively bonded tubular single lap joint.* The Journal of Adhesion, 1992. **40**(1): p. 1-14.

[44] Crocombe, A., *Global yielding as a failure criterion for bonded joints.* International Journal of Adhesion and Adhesives, 1989. **9**(3): p. 145-153.

[45] da Silva, L.F., P.J. das Neves, R. Adams, A. Wang and J. Spelt, *Analytical models of adhesively bonded joints—Part II: Comparative study.* International Journal of Adhesion and Adhesives, 2009. **29**(3): p. 331-341.

[46] Bigwood, D.A. and A.D. Crocombe, *Elastic analysis and engineering design formulae for bonded joints.* International Journal of Adhesion and Adhesives, 1989. **9**(4): p. 229-242.

[47] Frostig, Y., O.T. Thomsen and F. Mortensen, *Analysis of adhesive-bonded joints, square-end, and spew-fillet—high-order theory approach.* Journal of Engineering Mechanics, 1999. **125**(11): p. 1298-1307.

[48] Adams, R., J. Coppendale, V. Mallick and H. Al-Hamdan, *The effect of temperature on the strength of adhesive joints.* International Journal of Adhesion and Adhesives, 1992. **12**(3): p. 185-190.

[49] Adams, R.D., J. Comyn and W.C. Wake, *Structural adhesive joints in engineering*. 2nd ed. 1997, London: Chapman & Hall.

[50] Razavi, S.M.J., M.R. Ayatollahi, H.R. Majidi and F. Berto, *A strain-based criterion for failure load prediction of steel/CFRP double strap joints.* Composite Structures, 2018. **206**: p. 116-123.

[51] Jokinen, J., M. Wallin and O. Saarela, *Applicability of VCCT in mode I loading of yielding adhesively bonded joints—a case study.* International Journal of Adhesion and Adhesives, 2015. **62**: p. 85-91.

[52] Le Pavic, J., T. Bonnemains, É. Lolive, G. Stamoulis, D. Da Silva and D. Thévenet, *Failure load prediction of a tubular bonded structures using a coupled criterion.* Theoretical and Applied Fracture Mechanics, 2020: p. 102531.

[53] Kim, M.-H. and H.-S. Hong, *An adaptation of mixed-mode I+ II continuum damage model for prediction of fracture characteristics in adhesively bonded joint.* International Journal of Adhesion and Adhesives, 2018. **80**: p. 87-103.

[54] Alves, D., R. Campilho, R. Moreira, F. Silva and L. Da Silva, *Experimental and numerical analysis of hybrid adhesively-bonded scarf joints.* International Journal of Adhesion and Adhesives, 2018. **83**: p. 87-95.

[55] Santos, T. and R. Campilho, *Numerical modelling of adhesively-bonded double-lap joints by the eXtended Finite Element Method.* Finite Elements in Analysis Design, 2017. **133**: p. 1-9.

[56] Liu, G.-R. and Y.-T. Gu, *An introduction to meshfree methods and their programming*. 2005, Dordrecht, The Netherlands: Springer Science & Business Media.

[57] Gingold, R.A. and J.J. Monaghan, *Smoothed particle hydrodynamics: theory and application to non-spherical stars.* Monthly notices of the royal astronomical society, 1977. **181**(3): p. 375-389.

[58] Chen, Y., J. Lee and A. Eskandarian, *Meshless methods in solid mechanics*. 2006, New York, U.S.: Springer Science & Business Media.

[59] Belinha, J., *Meshless methods in biomechanics: Bone tissue remodelling analysis*. Vol. 16. 2014, Switzerland: Springer.

[60] Belinha, J., R.M.N. Jorge and L.M. Dinis, *A meshless microscale bone tissue trabecular remodelling analysis considering a new anisotropic bone tissue material law.* Computer Methods in Biomechanics and Biomedical Engineering, 2013. **16**(11): p. 1170-1184.

[61] Belytschko, T., Y.Y. Lu and L. Gu, *Element-free Galerkin methods.* International Journal for Numerical Methods in Engineering, 1994. **37**(2): p. 229-256.

[62] Nayroles, B., G. Touzot and P. Villon, *Generalizing the finite element method: diffuse approximation and diffuse elements.* Computational Mechanics, 1992. **10**(5): p. 307-318.

[63] Lancaster, P. and K. Salkauskas, *Surfaces generated by moving least squares methods.* Mathematics of Computation, 1981. **37**(155): p. 141-158.

[64] Liu, W.K., S. Jun, S. Li, J. Adee and T. Belytschko, *Reproducing kernel particle methods for structural dynamics.* International Journal for Numerical Methods in Engineering, 1995. **38**(10): p. 1655-1679.

[65] Atluri, S.N. and T. Zhu, *A new meshless local Petrov-Galerkin (MLPG) approach in computational mechanics.* Computational mechanics, 1998. **22**(2): p. 117-127.

[66] Sibson, R. *A vector identity for the Dirichlet tessellation*. in *Mathematical Proceedings of the Cambridge Philosophical Society*. 1980. Cambridge University Press.

[67] Dinis, L., R.N. Jorge and J. Belinha, *Analysis of 3D solids using the natural neighbour radial point interpolation method.* Computer Methods in Applied Mechanics and Engineering, 2007. **196**(13-16): p. 2009-2028.

[68] Wang, J. and G. Liu, *A point interpolation meshless method based on radial basis functions.* International Journal for Numerical Methods in Engineering, 2002. **54**(11): p. 1623-1648.

[69] Hardy, R.L., *Theory and applications of the multiquadric-biharmonic method 20 years of discovery 1968–1988.* Computers & Mathematics with Applications, 1990. **19**(8-9): p. 163-208.

[70] Tsai, C., Y. Guan, D. Ohanehi, J. Dillard, D. Dillard and R. Batra, *Analysis of cohesive failure in adhesively bonded joints with the SSPH meshless method.* International Journal of Adhesion and Adhesives, 2014. **51**: p. 67-80.

[71] Ramalho, L., I. Sánchez-Arce, R. Campilho, J. Belinha and F. Silva, *Strength prediction and stress analysis of adhesively bonded composite joints using meshless methods.* Procedia Manufacturing, 2020. **51**: p. 904-911.

[72] Sánchez-Arce, I., L. Ramalho, R. Campilho and J. Belinha, *Analyzing single-lap joints bonded with a brittle adhesive by an elastic meshless method.* Procedia Structural Integrity, 2020. **28**: p. 1084-1093.

[73] Sánchez-Arce, I., L. Ramalho, R. Campilho and J. Belinha, *Material non-linearity in the numerical analysis of SLJ bonded with ductile adhesives: A meshless approach.* International Journal of Adhesion and Adhesives, 2021. **104**: p. 102716.

DEVELOPMENT

3 DEVELOPMENT

The work developed in this thesis was part of an ongoing investigation in collaboration with the Mechanical and Industrial Engineering for Science and Innovation Institute (INEGI). Since one of the investigation objectives was to publish the developed works in scientific journals, they were reported in the scientific paper format. Therefore, this report contains the developed work in the same format. Four scientific papers were elaborated. The manufacture of the joints and substrates was described in detail in previous work [1]. Therefore, the procedures and details of these steps were not widely described in the papers. With that in mind, in Chapter 5, a more comprehensive analysis is carried out, and the published journal editions of the papers are attached.

Promptly, the title, authors, the journal in which the papers were published, and the abstracts and keywords are the following:

Paper 1: Fracture mechanics approach to stress singularity in adhesive joints

Authors: J.M.M. Dionísio[*], L.D.C. Ramalho[**], I.J. Sánchez-Arce[**], R.D.S.G. Campilho[*,**], J. Belinha[*]

[*]Departamento de Engenharia Mecânica, Instituto Superior de Engenharia do Porto, Instituto Politécnico do Porto, Rua Dr. António Bernardino de Almeida, 431, 4200-072 Porto, Portugal

[**]INEGI – Pólo FEUP, Rua Dr. Roberto Frias, s/n, 4200-465 Porto, Portugal

Published in: International Journal of Fracture

Abstract: Adhesives offer significant advantages when joining materials since they do not create discontinuities in the material, unlike bolting or riveting. Another interest of adhesive joints is the possibility of joining different materials and the lower weight. The analysis of the stress singularity in adhesive joints can provide a better understanding of joint behaviour, and it is mesh independent. The ISSF is based on a fracture mechanics concept, the Stress Intensity Factor (SIF). However, generally, the SIF is only applicable to cracks in a single material, while the ISSF is applicable to multi-material corners and does not require a crack. This work aims to study the stress singularity of aluminium adhesive joints bonded with a brittle adhesive with four different overlap lengths (L_O) by determining the singularity's exponents and its intensity. A method for joint strength prediction using the ISSF is also proposed. Additionally, the interface corner's stress is studied, with the different singularity components presented separately to assess their influence on the overall stress. These predictions are also compared with the

experimental strength to verify this strength prediction criterion's accuracy when applied to brittle adhesives. In conclusion, the ISSF criterion provides accurate results and can be utilised for further studies in this area.

Keywords: ISSF criterion, Adhesive Joints, Finite Element Method, Single-Lap Joints

Paper 2: Analysis of stress singularity in adhesive joints using meshless methods

Authors: L.D.C. Ramalho[**], J.M.M. Dionísio[*], I.J. Sánchez-Arce[**], R.D.S.G. Campilho[*,**], J. Belinha[*]

[*]Departamento de Engenharia Mecânica, Instituto Superior de Engenharia do Porto, Instituto Politécnico do Porto, Rua Dr. António Bernardino de Almeida, 431, 4200-072 Porto, Portugal

[**]INEGI – Pólo FEUP, Rua Dr. Roberto Frias, s/n, 4200-465 Porto, Portugal

Under review: Engineering Analysis with Boundary Elements

Abstract: Recent years saw a rise in the application of bonding techniques in the engineering industry. This fact is due to the various advantages of this technique when compared to traditional joining methods, such as riveting or bolting. The growth of bonding methods demands faster and more powerful tools to analyse the behaviour of products. For that reason, adhesive joints have been the subject of intensive investigation over the past few years. Recently, a fracture mechanics-based approach emerged with great potential to evaluate joint behaviour, called Intensity of Singular Stress Fields (ISSF), similar to the Stress Intensity Factor (SIF) concept. However, it allows the study of multi-material corners and does not require an initial crack. This approach was not yet tested with meshless methods. The present work intends to fill this gap, resorting to the Radial Point Interpolation Method (RPIM). With this purpose, adhesive joints with four different overlap lengths (L_O) bonded with a brittle adhesive were studied. The interface corner's stresses were also evaluated. The predicted strengths were compared with the experimental data to assess the accuracy of the applied methods. In conclusion, the ISSF criterion proved to be applicable to meshless methods, namely the RPIM, opening good prospects to pursue further studies in this area.

Keywords: ISSF criterion, RPIM, Adhesive Joints, Single Lap Joints, Meshless Methods

Paper 3: Fracture mechanics approach to stress singularity in composite adhesive joints

Authors: J.M.M. Dionísio[*], L.D.C. Ramalho[**], I.J. Sánchez-Arce[**], R.D.S.G. Campilho[*,**], J. Belinha[*]

[*]Departamento de Engenharia Mecânica, Instituto Superior de Engenharia do Porto, Instituto Politécnico do Porto, Rua Dr. António Bernardino de Almeida, 431, 4200-072 Porto, Portugal

[**]INEGI – Pólo FEUP, Rua Dr. Roberto Frias, s/n, 4200-465 Porto, Portugal

Published in: Composite Structures

Abstract: Structural design has significantly changed over the years driven by the weight's reduction goal. In that sense, composite materials established themselves as the material of excellence in most engineering areas, replacing wood, steel and aluminium. Connection processes also experienced a transformation, with adhesive bonding standing out. Those new materials and techniques require deep research until they could be applied to structures. These studies led to the appearance of different methods for evaluating material and bond performance. Fracture mechanics is an approach based on material discontinuities or defects. Recently, a new fracture mechanics-based technique arose called Intensity of Singular Stress Fields (ISSF). It hinges on the Stress Intensity Factors (SIF) approach but does not require an initial crack. This investigation aims to evaluate the applicability of this technique to composite materials. For that, Single-Lap Joints (SLJ) made from Carbon Fibre Reinforced Polymer (CFRP) bonded with a brittle adhesive and eight different overlap lengths (L_O) are analysed. The numerical simulations and strength predictions are performed through the Finite Element Method (FEM) and MATLAB software. Finally, the numerical predictions are compared to the experimental data. It can be concluded that the ISSF is applicable to orthotropic materials.

Keywords: ISSF criterion, Adhesive Joints, Composite Materials, Finite Element Method, Single-Lap Joints

Paper 4: Meshless analysis of the stress singularity in composite adhesive joints

Authors: L.D.C. Ramalho[**], J.M.M. Dionísio[*], I.J. Sánchez-Arce[**], R.D.S.G. Campilho[*,**], J. Belinha[*]

*Departamento de Engenharia Mecânica, Instituto Superior de Engenharia do Porto, Instituto Politécnico do Porto, Rua Dr. António Bernardino de Almeida, 431, 4200-072 Porto, Portugal

**INEGI – Pólo FEUP, Rua Dr. Roberto Frias, s/n, 4200-465 Porto, Portugal

Published in: Composite Structures

Abstract: Adhesives are an exceptionally well-suited method for joining composites. Unlike other methods, such as bolting or riveting, adhesives do not introduce holes in their joining material. This is a significant advantage in the case of composites because the holes required by bolting or riveting induce stress concentrations and can also lead to tears, burrs or delamination. A point of concern in adhesive joints is the adhesive/adherend interface corner where a stress singularity occurs, and failure usually initiates. Thus, it is crucial to study this stress singularity to better understand adhesive joints' mechanical behaviour.

The goal of this work is to validate the application of the Intensity of Singular Stress Fields (ISSF) criterion to meshless methods, in this case, the Radial Point Interpolation Method (RPIM). With this purpose, eight overlap lengths (L_O) in single-lap joints (SLJ) composed of Carbon Fibre Reinforced Polymer (CFRP) and bonded with a brittle adhesive were experimentally and numerically tested. Furthermore, an extrapolation-based method is implemented to determine the critical stress singularity components (H_c) necessary for the strength predictions. In the end, the experimental and numerical results are compared to assess the suitability of the method. It was found that the ISSF criterion can be accurately applied to meshless methods and composite materials successfully, given the simplicity of the method applied.

Keywords: Composite Materials, ISSF Criterion, RPIM, Adhesive Joints, Meshless Methods

Reference

[1] Nunes, S.L.S., R.D.S.G. Campilho, F.J.G. Da Silva, C.C.R.G. De Sousa, T.A.B. Fernandes, M.D. Banea and L.F.M. Da Silva, *Comparative failure assessment of single and double lap joints with varying adhesive systems.* The Journal of Adhesion, 2016. **92**(7-9): p. 610-634.

PAPER 1

FRACTURE MECHANICS APPROACH TO STRESS SINGULARITY IN ADHESIVE JOINTS

J.M.M. DIONÍSIO, L.D.C. RAMALHO, I.J. SÁNCHEZ-ARCE, R.D.S.G. CAMPILHO, J. BELINHA

3.1 Paper 1

3.1.1 Introduction

Optimal structural design is intrinsically associated with multi-component structures since it is possible to optimise the specific strength and stiffness by combining different materials, each one tailored for its function within the structure [1], and also to expedite fabrication and reduce the associated costs in structures with complex shapes, which can benefit from division in simpler shapes joined together [2]. Depending on the application and design restrictions, varying joining techniques can be applied. A significant body of knowledge exists in the literature, including a comparison between joining technologies for selected purposes [3]. The most relevant joining methods for industrial applications are riveting, bolting, welding, brazing, and adhesive bonding. Although adhesive joints are used historically, their structural use was only widely developed in the first half of the 20th century by the aeronautical field. With the advancements in the adhesives' formulations, resulting in ever-increasing adhesive and joint performance, and design tools, consisting of simulation packages and suitable criteria for strength prediction, adhesive bonding is now essential in structural applications including aerospace, aeronautical, automotive, sports, civil engineering structures and electronics [4]. This option became possible due to a set of characteristics (over conventional techniques) such as the unnecessity of drilling or damaging the parent materials to be joined, saving weight, improving stresses across the bonding regions, and ease of joining different materials. Possible limitations are the typical impossibility to disassemble after joining, required curing time, lack of confidence in the design, especially for fatigue and long-term analyses, and large scatter in experimental testing [5].

Since the use of adhesive joints has been increasing in several industries in recent times [6], it is important to use design tools that accurately model and predict the behaviour of adhesive joints to reduce the amount of experimental tests needed, which are, usually, costlier and take more time than numerical simulations. In the early stages of adhesive joint analysis, analytical methods were used to determine the stress distributions at the adhesive layer, namely the Volkersen [7] model, the Goland and Reissner [8] model or the Hart-Smith [9] model. However, these models have severe limitations since, for some, the formulation is difficult, while for others, the formulation is simple, but many assumptions are made, rendering the resulting stress distribution less accurate. These limitations mean that in recent years most literature focuses on numerical methods to analyse adhesive joints, although examples of analytical models developed in recent times can still be found, like the work by Carbas et al. [10] for graded adhesive joints. A literature review by Ramalho et al. [11] found that the most commonly used method to predict the strength of adhesive joints is Cohesive Zone Models (CZM), used together with the Finite Element Method (FEM) [12]. CZM generally provide

accurate strength predictions, as long as the cohesive law shape/formulation and the respective parameters are appropriate. A simple triangular law can be used for brittle adhesives, but ductile adhesives generally require more complex laws, such as the trapezoidal law or an exponential law [13]. Campilho et al. [14] evaluated the CZM accuracy of adhesive layers modelled with different law shapes in predicting the strength of composite single-lap joints (SLJ) under different geometries. The obtained results showed that triangular CZM models are most suitable for brittle adhesives, while ductile adhesives can be accurately dealt with trapezoidal CZM laws that capture the high-stress levels after damage onset. Despite this fact, the relative errors of these two law shapes were always under 10%, reinforcing that CZM, which is based on an area concept for crack propagation, i.e., mainly depending on the fracture energies, which gives satisfactory results even with less adequate models. Even though the strength predictions with CZM are accurate, these models have a significant drawback in that they require extensive experimental testing because the cohesive law parameters change with the adhesive thickness (t_A) and other geometric parameters affecting the damage zone in the adhesive in the advent of crack propagation. The t_A effect in CZM modelling with a triangular law was addressed by Xu and Wei [15] by simulating SLJ with different t_A, particularly showing that smaller t_A increases the joint strength. Additionally, the proposed CZM yielded accurate strength predictions for the brittle adhesive, although the ductile adhesive joint performance with the smallest t_A is underestimated. Demiral and Kadioglu [16] also showed the t_A influence on strength by CZM, namely SLJ strength reduction by increasing t_A, although this effect was much smaller than that of the overlap length (L_O), whose increase highly benefited the joint strength. Therefore, authors have also experimented with other methods to predict joint strength, such as the eXtended FEM (XFEM) [17], sometimes also combined with CZM [18], or even the common FEM using failure criteria based on continuum mechanics [19], fracture mechanics [20] or damage mechanics [21]. Some authors have also used the previous criteria with meshless methods [22] or meshless methods combined with CZM [23] to predict joint strength.

Fracture mechanics, in particular, can assess stress or strain singularities due to material discontinuities [24], which in bonded joints are usually related to the sharp corners at the overlap edges at the interface between an adherend and the adhesive layer. Conventionally, fracture mechanics can rely on stress intensity factors [25, 26] or energetic approaches [27], depending on the materials' fracture toughness. In the last option, the most widespread techniques are the J-integral [28] and the Virtual Crack Closure Technique (VCCT) [29]. More recently, Finite Fracture Mechanics (FFM) was proposed by Leguillon [30], consisting of a coupled stress-energy criterion for crack initiation and accounting for published work on adhesive joints [31]. FFM does not require an initial crack and, for crack initiation, both a stress and an energetic criterion should be fulfilled. However, it is essentially applicable to brittle adhesives. In adhesive joints, as previously discussed, there exists a stress singularity at the adhesive/adherend interface corners, whose magnitude is usually called Intensity of Singular Stress Fields

(ISSF) or Generalised Stress Intensity Factor (GSIF). The first published works trying to characterise this singularity date back to the mid-20th century [32, 33].

This singularity analysis has been performed in many different types of adhesive joints, including scarf joints [34], butt joints [35], Double Lap Joints (DLJ) [36] and SLJ [37]. Zhang et al. [38] proposed a new method to calculate the ISSF in bonded butt joints under tension and bending due to the known difficulties in using the FEM because of the existing singularity. The new method only considers stresses of the first elements at the end of the interface between the adhesive and adherend materials. Different combinations of materials and values of t_A were analysed and positively validated against experiments from previous works. It was also found that the ISSF was dependent on the joint materials and that the ISSF increased with t_A until t_A reached the joint width. Interactions between the singular stress fields at the two adhesive/adherend interfaces were also found, although this issue was remitted to future works. In the work of Li et al. [39], SLJ and DLJ bonded joints were used to investigate the adhesive strength by evaluating and minimising the ISSF at the interface end. It was shown that the ISSF diminishes by increasing the adherends' thickness (t_P) and that the minimum ISSF is achieved for a sufficiently high adherend thickness. Due to the DLJ having twice the bonding area and suppressing peel stresses and transverse deflection, the equivalent strength condition between identical material SLJ and DLJ was evaluated by the ISSF, leading to an equal strength between a SLJ with an adherend thickness of 7 mm and a DLJ with 1.5 mm. Galvez et al. [40] applied the ISSF concept to analyse mixed adhesive joints, i.e., with two adhesives in the bond line (with different stiffness and mechanical properties), to achieve strength optimisation. Four adhesive combinations were tested, including the two with a single use of each of the adhesives. The proposed approach was based on the Reciprocal Work Contour Integral Method (RWCIM), and it involved estimating the ISSF for the reference models (joints with the single adhesive), which were then applied for the unknown solution (mixed-adhesive joints). A clear improvement was found for one of the mixed-adhesive joint configurations, with a 36% reduction in the ISSF, when compared to the single-adhesive solutions.

The present work aims at studying the singularity in SLJ, with different L_O, bonded with a brittle adhesive and proposing a method to determine joint strength using the ISSF. The ISSF analysis and the strength predictions are performed using the FEM. This analysis is done to a material combination that was never previously studied using the ISSF. The stress around the interface corner is also studied, with the different singularity components presented separately to assess their influence on the overall stress. Additionally, a comparison between the stress obtained with the ISSF formula and the stress extracted from the FEM for the different L_O is compared to validate the formulation used to obtain the ISSF. The mesh independence of this approach is also assessed by studying two different mesh refinement levels. Finally, these predictions are also compared with the experimental strength to verify this strength prediction criterion's accuracy when applied to brittle adhesives.

3.1.2 Experimental work

3.1.2.1 Joint geometry

In this work, SLJ made of aluminium adherends bonded with the adhesive Araldite® AV138 were studied. The geometry and boundary conditions of the numerical model are shown in Figure 3.1.1. The SLJ was fixed at the left boundary, and a displacement (δ) was imposed at the right boundary. Four different L_O were tested, from 12.5 to 50 mm, in increments of 12.5 mm. The other relevant geometrical properties are the adherend thickness t_P=3 mm, the adhesive thickness t_A=0.2 mm, the total joint length L_T=180 mm and the joint width B=25 mm.

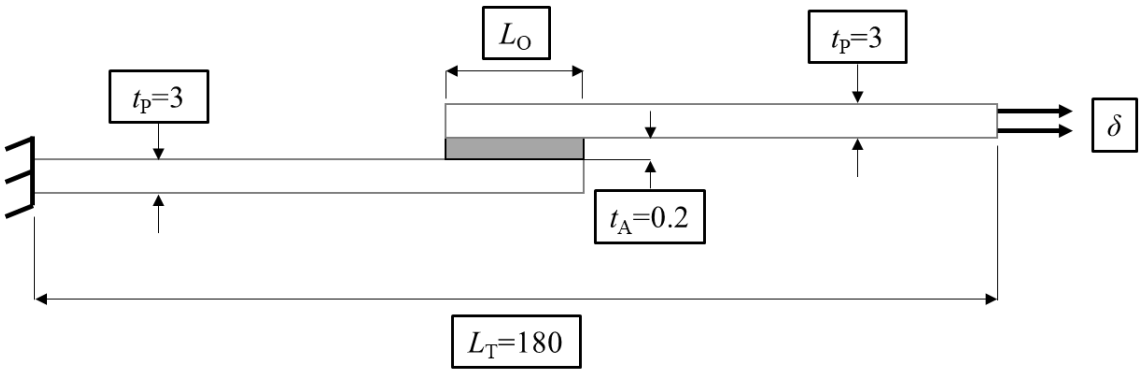

Figure 3.1.1 - Geometry and boundary conditions of the SLJ (dimensions in mm)

3.1.2.2 Materials

The SLJ were fabricated from Al6082-T651 aluminium alloy adherends. The adherend material is commonly used for structural appliances since it has good strength and ductility. Full characterisation of this aluminium is presented in previous works [41, 42], consisting of tensile bulk testing and subsequent data analysis of the load-displacement (P-δ) curves. The collected data is presented in (E is Young's modulus, ν the Poisson coefficient, σ_y the tensile yield stress, σ_f the tensile strength and ε_f the tensile failure strain).

Table 3.1.1 - Mechanical properties of the aluminium adherends [41, 42]

Property	Value
E (GPa)	70.1±0.83
ν	0.30
σ_y (MPa)	261.67±7.65
σ_f (MPa)	324.00±0.16
e_f (%)	21.70±4.24

Application of the ISSF to bonded joints was assessed by SLJ bonded with the Araldite® AV138, a strong but brittle epoxy adhesive. This adhesive has a tensile strength of approximately 40 MPa, which is significant for modern adhesives, but its brittleness highly limits the associated bonded joints' performance, especially for high L_O. For short L_O, in which stresses in the bond line tend to be more uniform due to smaller shear-lag and rotation effects, this adhesive still manages to compete with ductile adhesives, but it quickly fails to work for high L_O, in which stress gradients become significant. These findings were reported in reference [41]. This adhesive was evaluated by different testing architectures to acquire the required data to input into the models. The tensile mechanical properties (E, σ_y, σ_f and ε_f) were acquired from tensile tests to bulk specimens, considering the French standard NF T 76-142 indications for the geometry and fabrication process. The mechanical shear properties (shear modulus - G, shear yield stress – τ_y, shear strength – τ_f and shear failure strain – γ_f) were obtained from Thick Adherend Shear Tests (TAST). For this test, the 11003-2:1999 ISO standard was followed regarding the fabrication and testing procedures. Thus, all specimens were cured in a rigid mould to ensure the proper adherends' longitudinal alignment, and DIN C45E steel adherends were used to minimise adherend-induced deformations affecting the obtained results. Table 3.1.2 collects all data for the adhesive. It should be mentioned that Hooke's law relationship for isotropic materials (between E and G), and also the expected σ_y/τ_y relationship by Tresca or von Mises criteria, are not met in the obtained data due to different restraint conditions (unrestrained adhesive in the bulk tests vs. restrained adhesive in the TAST tests).

Table 3.1.2 - Mechanical properties of the adhesive [43]

Property	AV138
E (GPa)	4.89±0.81
ν	0.35[1]
σ_y (MPa)	36.49±2.47
σ_f (MPa)	39.45±3.18
ε_f (%)	1.21±0.10
G (GPa)	1.56±0.01
τ_y (MPa)	25.1±0.33
τ_f (MPa)	30.2±0.40
γ_f (%)	7.8±0.7

[1] Data from the manufacturer.

3.1.2.3 Fabrication and testing

For the joint fabrication, it was initially necessary to prepare the bonding surfaces. This process consisted of the adherends sandblasting with corundum sand followed by cleaning the surface with acetone until no traces of contaminants exist that can prevent a good bond. After the surface preparation, it was necessary to prepare the joints for bonding. With this purpose, the adherends should be aligned in a bonding jig and, to assure the designated t_A for the joints, calibrated nylon wires with 0.2 mm diameter were attached to the adherends at the overlap ends to stop the adherends' from entering contact when pressed and acquire t_A=0.2 mm. The adherends were then bonded together by applying adhesive to one of the elements and subsequent position the other adherend correctly. Then, pressure was applied with grips to reach the required thickness and cast out the excess adhesive, which was later removed after its cure. Due to the low pressure applied to the joints (minimum to expel the excess adhesive and promote the adherend/wire/adherend contact), it was assumed that the associated wires' deformation was negligible, and that t_A would be accurately achieved by this process. Moreover, the t_A accuracy was checked after adhesive curing by direct measurements. The removal of the excess adhesive is done after its cure to achieve the joint's theoretical layout without adhesive flaws at the joint boundaries. For testing, the joints were placed between the Universal Testing Machine (UTM) clamps using L_T=180 mm for all L_O. All the joints were experimentally tested using a UTM Shimadzu AG-X 100 with a 100 kN load cell. The tests were performed with a constant speed of 1 mm/min. The average failure load from each set was considered as the experimental maximum load (P_m).

3.1.3 Numerical work

3.1.3.1 ISSF technique

The SIF is mainly used to characterise the stress fields of sharp cracks. However, the ISSF also allows the evaluation of multi-material corners from the most diverse geometries. Figure 3.1.2 presents an example of these corners for the geometry used in this work, i.e., SLJ.

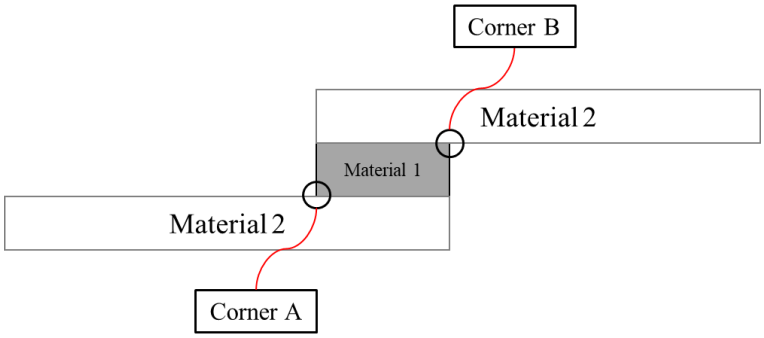

Figure 3.1.2 - Example of multi-material corners in SLJ that the ISSF can evaluate

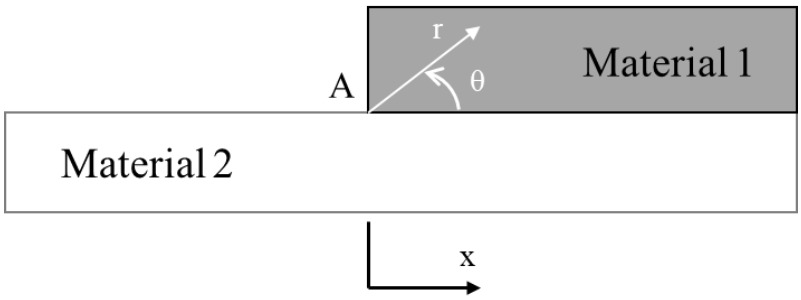

Figure 3.1.3 - Polar coordinates system

The stress near the interface corner can be described, in polar coordinates (r,θ), such as those presented in Figure 3.1.3, using the interface singularity as:

$$\sigma_{ij} = \sum_{n=1}^{\infty} H_n r^{\lambda_n - 1} f_{ij}(\lambda_n, \theta). \quad (1)$$

Additionally, the displacement in the same region, using the same coordinate system, can be described as:

$$u_j = \sum_{n=1}^{\infty} H_n r^{\lambda_n} g_j(\lambda_n, \theta), \quad (2)$$

where n is the number of exponents (λ), which varies with the geometry of the interface corner, and H_n is a scalar value representing the ISSF. The exponents are determined by finding the solution for the following equation [44]:

$$0 = e^2 + b^2 - (\lambda c)^2 - (\lambda d)^2, \quad (3)$$

where the equations to determine the parameters e, b, c and d can be found in Appendix 1. In these equations, θ_1 and θ_2 are the angles of the material interface corner, and α and β are the Dundurs parameters [45], defined as follows:

$$\alpha = \frac{G_1(\kappa_2 + 1) - G_2(\kappa_1 + 1)}{G_1(\kappa_2 + 1) + G_2(\kappa_1 + 1)}, \quad (4)$$

$$\beta = \frac{G_1(\kappa_2 - 1) - G_2(\kappa_1 - 1)}{G_1(\kappa_2 + 1) + G_2(\kappa_1 + 1)}, \quad (5)$$

where κ_m=3-4ν_m for plane strain cases and G_m is the shear modulus of material m. The subscripts 1 and 2 in κ and μ represent the two materials. Having determined λ using equation (3), it is then possible to calculate the $f_{ij}(\lambda_n, \theta)$ and $g_j(\lambda_n, \theta)$ by solving the following system of equations:

$$\left\{ g_{rr}^m \quad g_{\theta}^m \quad f_{rr}^m \quad f_{\theta\theta}^m \quad f_{\theta}^m \right\}^T = \boldsymbol{N_m X_m Y}, \quad (6)$$

where m indicates the material and the matrices $\boldsymbol{N}_m$ and $\boldsymbol{X}_m$, and vector $\boldsymbol{Y}$, are defined as [44]:

$$N_m = \begin{bmatrix} \frac{(\kappa_m-\lambda)\cos([\lambda-1]\theta)}{2G_m} & \frac{(-\kappa_m+\lambda)\sin([\lambda-1]\theta)}{2G_m} & -\frac{\cos([\lambda+1]\theta)}{2G_m} & \frac{\sin([\lambda+1]\theta)}{2G_m} \\ \frac{(\kappa_m+\lambda)\sin([\lambda-1]\theta)}{2G_m} & \frac{(\kappa_m+\lambda)\cos([\lambda-1]\theta)}{2G_m} & \frac{\sin([\lambda+1]\theta)}{2G_m} & \frac{\cos([\lambda+1]\theta)}{2G_m} \\ -(\lambda^2-3\lambda)\cos([\lambda-1]\theta) & (\lambda^2-3\lambda)\sin([\lambda-1]\theta) & -\lambda\cos([\lambda+1]\theta) & \lambda\sin([\lambda+1]\theta) \\ (\lambda^2+\lambda)\cos([\lambda-1]\theta) & -(\lambda^2+\lambda)\sin([\lambda-1]\theta) & \lambda\cos([\lambda+1]\theta) & -\lambda\sin([\lambda+1]\theta) \\ (\lambda^2-\lambda)\sin([\lambda-1]\theta) & (\lambda^2-\lambda)\cos([\lambda-1]\theta) & \lambda\sin([\lambda+1]\theta) & \lambda\cos([\lambda+1]\theta) \end{bmatrix} \quad (7)$$

$$\boldsymbol{X}_1 = \begin{bmatrix} 1 & 0 \\ 0 & 1 \\ \chi_{31} & \chi_{32} \\ \chi_{41} & \chi_{42} \end{bmatrix}; \quad \boldsymbol{X}_2 = \begin{bmatrix} \chi_{51} & \chi_{52} \\ \chi_{61} & \chi_{62} \\ \chi_{71} & \chi_{72} \\ \chi_{81} & \chi_{82} \end{bmatrix}; \quad \boldsymbol{Y} = \begin{Bmatrix} y_1 \\ y_2 \end{Bmatrix}; \quad (8)$$

the components of $\boldsymbol{X}_m$ and $\boldsymbol{Y}$ given by the equations in Appendix 2 [44].

There are several ways to determine the H_n using numerical methods. A popular method is performing an integration over a line, or area, encircling the interface corner as Qian and Akisanya [44] did. Alternately, the H_n values can also be determined by extrapolating to the corner the H_n from values near the corner [46]. This was the method used in this work. For a n number of λ, a n number of points at different angles (θ) is needed to determine the H_n values at a fixed radius (r), by solving the following system of equations for the $\boldsymbol{H}$ vector:

$$\begin{bmatrix} r^{\lambda_1-1} f_{\theta\theta}(\lambda_1,\theta_{n+1}) & \cdots & r^{\lambda_n-1} f_{\theta\theta}(\lambda_n,\theta_{n+1}) \\ \vdots & \ddots & \vdots \\ r^{\lambda_1-1} f_{\theta\theta}(\lambda_1,\theta_{n+n}) & \cdots & r^{\lambda_n-1} f_{\theta\theta}(\lambda_n,\theta_{n+n}) \end{bmatrix} \begin{Bmatrix} H_1 \\ \vdots \\ H_n \end{Bmatrix} = \begin{Bmatrix} \sigma_{\theta\theta}(r,\theta_{n+1}) \\ \vdots \\ \sigma_{\theta\theta}(r,\theta_{n+n}) \end{Bmatrix}. \quad (9)$$

The solution of equation (9) is obtained for several different r, and it is then extrapolated to r=0 mm, from an r interval where it is stable, to obtain $\boldsymbol{H}$ at the interface corner.

3.1.3.2 Modelling conditions

A FEM analysis was performed to validate the ISSF criterion. For that, a MATLAB based tool was used, where the finite element discretisation was created, and the natural and essential boundary conditions were imposed. A script was added to this tool with the previously described ISSF formulation. The SLJ was modelled accordingly to Figure 3.1.1. The left boundary was considered fixed (U_x=U_y=U_z=0), while δ was imposed in the right boundary. The simulations were executed considering plane strain, linear elastic material behaviour and small deformations. For these simulations, four-node quadrilateral elements were chosen to describe the whole model. Two different refinements near the interface corner were applied to discretise the interface corner in order to evaluate the mesh's influence on the results of the ISSF analysis. These discretisations near the corner were the same for all the studied L_O. The more refined

mesh had approximately double the number of nodes when compared with the baseline mesh in this region. The radial region of the two discretisations used in the ISSF analysis is presented in Figure 3.1.4 a) and b), with Figure 3.1.4 c) showing the dimensions and the number of nodes in the region near the corner that was discretized in the same manner for all L_O.

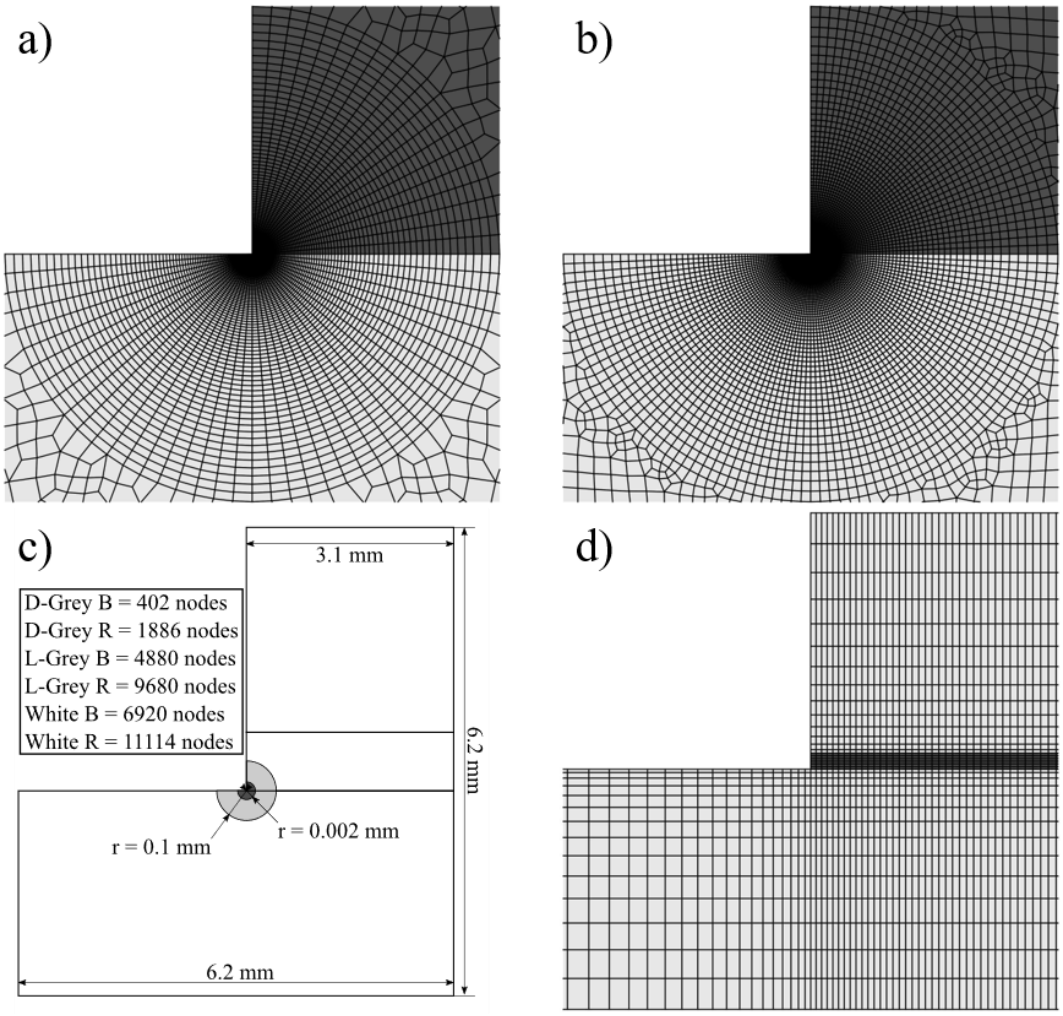

Figure 3.1.4 - Baseline (a) and refined (b) discretisation near the interface corner, dimensions and the number of nodes in the region near the corner (c) and discretization for the stress analysis (d)

After these simulations were solved, the P_m values were determined through the ISSF criterion and then compared to the experimental data. An analysis of the stress in the mid-thickness line of the adhesive was also performed. To do this, a new set of discretisations for each L_O was needed. An example of this discretization at the left end of the overlap for the joint with L_O=25 mm is shown in Figure 3.1.4 d). For the other L_O, the discretisations are similar. This discretization has 14 elements along the adherend thickness and 6 elements along the adhesive thickness. These simulations were performed under the same assumptions as the ISSF simulations, namely plane strain, linear elastic material behaviour and small deformations.

3.1.4 Results

3.1.4.1 Experimental data and analysis

Every single one of the SLJ tested presented cohesive failure in the adhesive layer. On top of that, none of the adherends displayed plastic deformation, as it can be proved by the load-displacement curves from Figure 3.1.5, considering the sample cases of L_O=12.5 (a) and 50 mm (b).

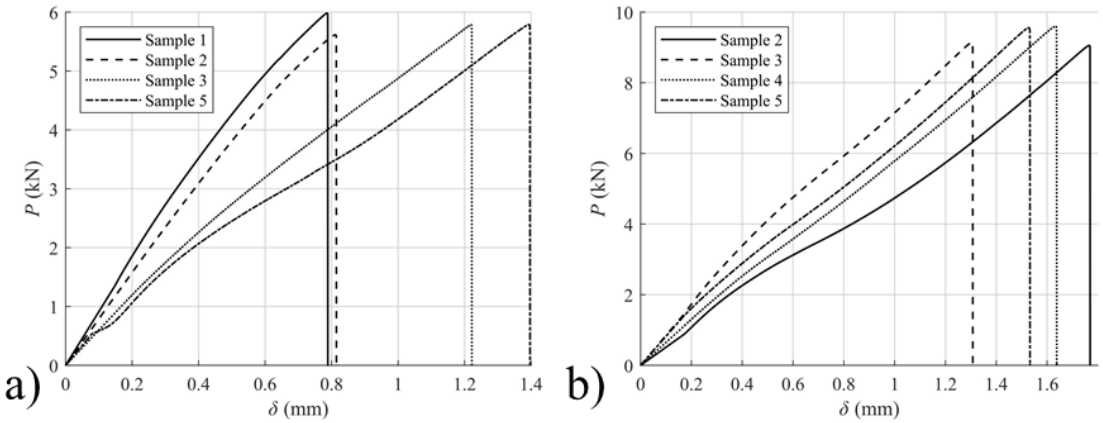

Figure 3.1.5 - Load-displacement curves for the SLJ bonded with the Araldite® AV138: L_O=12.5 (a) and 50 mm

All curves show a small loss of linearity between 3-4 kN, but this issue was experimentally identified as a minor gripping problem in the testing machine. In all cases, failure takes place without visible plasticization. This, allied to the experimental data's low variation, proves that the specimens were correctly prepared. Figure 3.1.6 presents the average P_m sustained by the joints for each L_O tested.

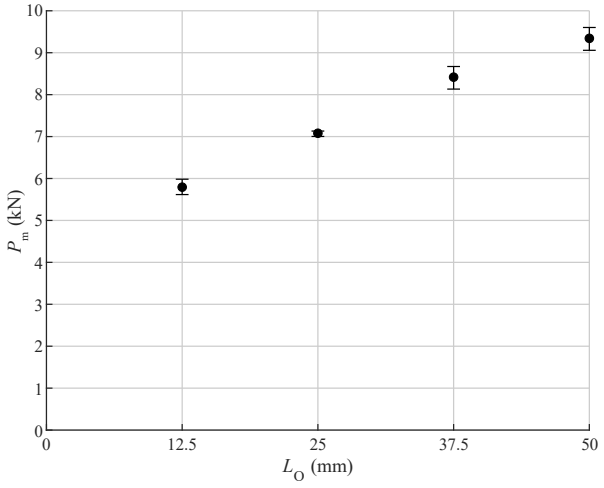

Figure 3.1.6 - Average P_m sustained by the joints for each L_O tested

From the observation of this graph, it is perceptible that the joint strength increases with each increment of L_O. This fact is in line with previous works where different adhesive

types were tested, including the one used in this analysis [43]. However, although the curve is nearly linear, P_m is not proportional to L_O, in the sense that the P_m/L_O ratio markedly diminishes for higher L_O, thus emphasizing the joints' performance reduction. This behaviour is due to the adhesive's brittleness, which does not accommodate the increasing peak stresses with L_O and fails prematurely, and contrasts with that of ductile adhesives, which usually manage to produce proportional P_m-L_O curves up to some extent [47].

3.1.4.2 Stress analysis in the adhesive layer mid-thickness

The stress distributions along the adhesive layer are also crucial in this analysis. Figure 3.1.7 shows the peel (σ_{yy}) (a) and shear (τ_{xy}) (b) stresses along the adhesive layer mid-thickness, marked in red in the diagram of Figure 3.1.7 a). The adhesive length was normalised by L_O to allow an easier comparison.

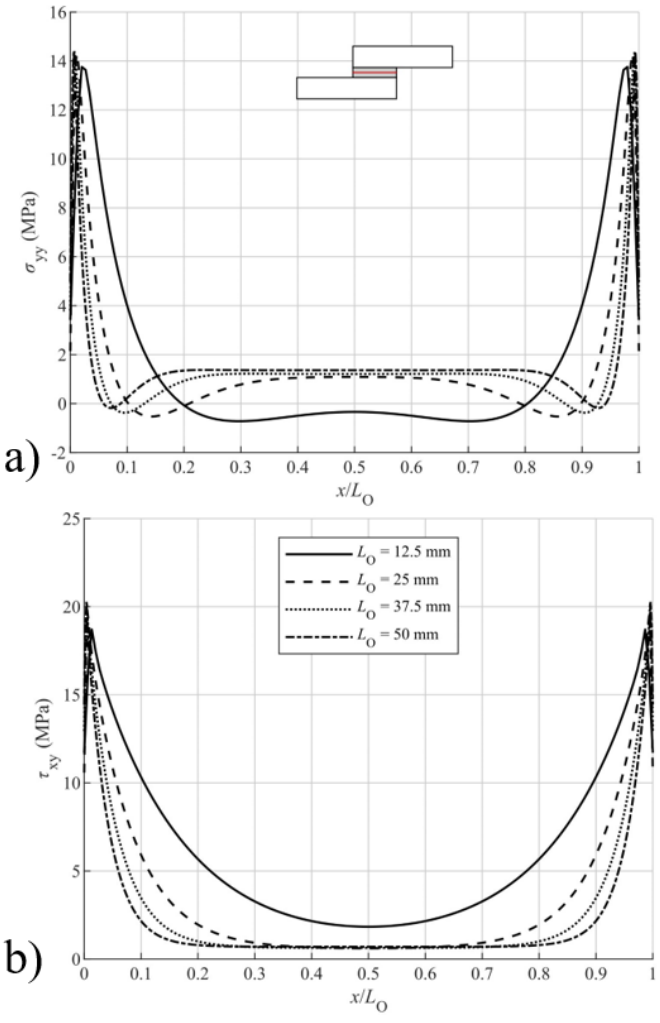

Figure 3.1.7 - σ_{yy} (a) and τ_{xy} (b) stresses along the adhesive layer

The mesh used to obtain these stresses had to be different from the radial mesh because this mesh cannot provide a steady set of nodes along the mid-thickness of the adhesive.

Thus, a structured mesh was considered for this analysis only (Figure 3.1.4 d)), while the other conditions remain equal. In this work, significant σ_{yy} stresses were observed at the overlap ends, mainly due to the joint rotation during the experimental tests. In fact, this is a common problem found in SLJ, and it arises since the overall joint deformation is ruled by the stiffer adherends, while the compliant adhesive is forced to follow the adherends separation at the overlap edges due to their opposed curvature. Owing to the same effect, compressive stresses are found towards the centre of the overlap [48]. The singularity effect should also be considered, but it was numerically found that this effect was negligible since stresses were taken at the adhesive mid-thickness. Analysing the stress variation with L_O, it was concluded that incrementing this parameter led to higher σ_{yy} peak stresses. As a result, P_m averaged to the bonded area reduces by increasing L_O. τ_{xy} stresses are also present in this joint type. The characteristic distribution consists of a small load towards the centre of the overlap, while in the ends, τ_{xy} stresses increase. This distribution is related to each adherend's varying longitudinal strains along the overlap [49]. Similarly to σ_{yy} stresses, τ_{xy} peak stresses increase with L_O. This fact is again related to the higher longitudinal strains of the adherends for bigger L_O [41]. Based on this analysis, higher L_O should affect the joint strength, especially for this type of adhesive.

3.1.4.3 ISSF calculation

The SLJ geometry presents anti-symmetry, shown in Figure 3.1.8, allowing the ISSF calculation for only one interface corner.

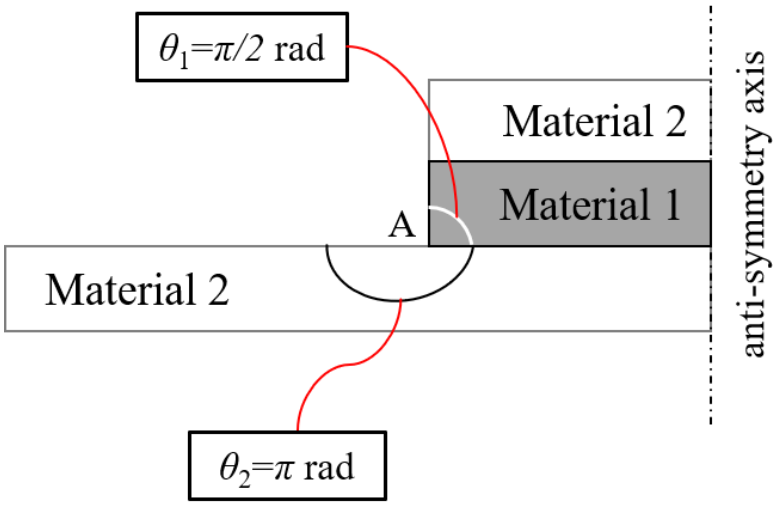

Figure 3.1.8 - Anti-symmetry of the SLJ and corner geometry

The ISSF calculation was performed using the extrapolation method described in Section 3.1.3.1. The procedure started with the determination of the eigenvalues (λ_n) following equation (3). Considering the combination of materials and geometry of the joints tested, as presented in Figure 3.1.8, with $\theta_1=\pi/2$ rad and $\theta_2=\pi$ rad, two different exponents were found: $\lambda_1=0.6539$ and $\lambda_2=0.9984$. Therefore, according to equation (9),

two different angles are needed to perform the extrapolation, equal to the number of exponents. The angles chosen were: $\theta_3=\pi/4$ rad and $\theta_4=-3\pi/4$ rad, because this way the determination of H_1 and H_2 is based on nodes in the two materials, being one in the ascending part of the $\sigma_{\theta\theta}$ curve (θ_4) and the other in the descending part of the $\sigma_{\theta\theta}$ curve (θ_3).

Considering L_O=37.5 mm as an example, the values of H_1 and H_2 were extrapolated to r=0 mm from the values in the interval 0.01<r<0.02 mm, which are close enough to the corner tip to be influenced by other singularities. This extrapolation was performed when the reaction forces equalled the experimental failure at the joint end where δ was imposed. The process is the same for the other L_O. Figure 3.1.9 presents the H_1 extrapolations with the baseline discretization (a) and the refined discretization (b) for the L_O=37.5 mm case.

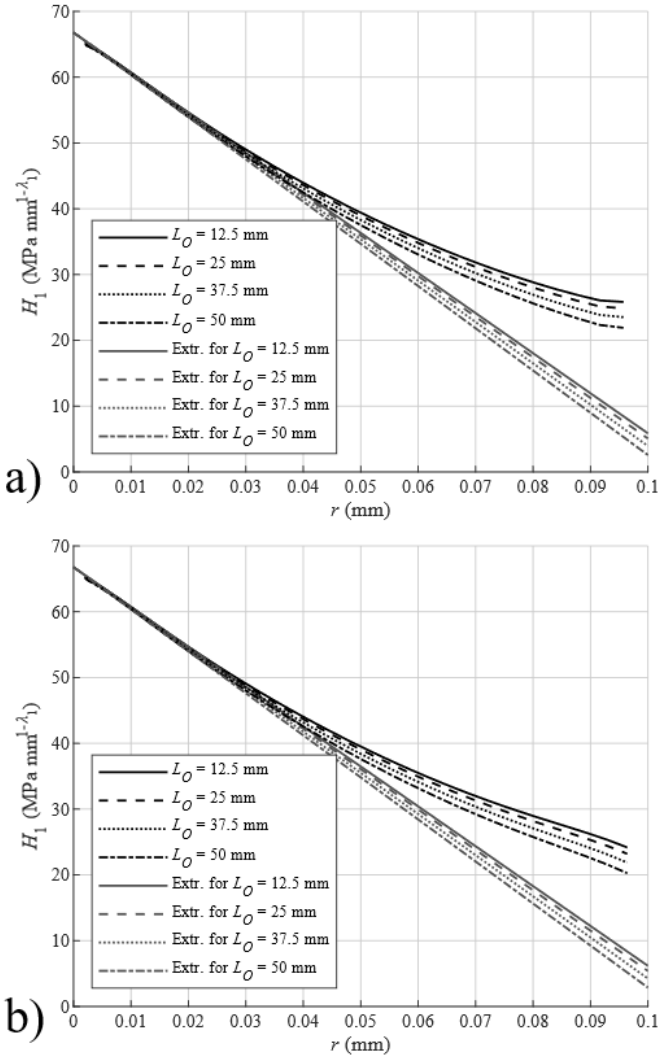

Figure 3.1.9 - H_1 extrapolation for the L_O=37.5 mm SLJ using the FEM with the baseline discretisation (a) and the refined discretisation (b)

This figure only presents the first singularity (H_1) component since it is the most important. However, the same extrapolation can be used to obtain the second singularity (H_2) component. The comparison between the discretisations in Figure 3.1.9 reveals that this calculation is discretisation independent. The graphs also show the H_1 extrapolations for the other L_O. These were performed at an imposed δ where H_1 would be the same as the H_1 of L_O=37.5 mm at failure displacement. The comparison between the different L_O shows a more pronounced slope in the extrapolation for larger L_O.

Figure 3.1.10 compares the stresses obtained from the numerical simulations and the ones predicted by the analytical formulae. The numerical stresses were obtained at r=0.02 mm from the interface corner and when H_1 was the same for all L_O.

In Figure 3.1.10, it can be observed that the analytical stress is very similar to the numerical stress, thus proving that the analytical functions obtained with equation (6) fit well the numerical stresses for the three different components and showing that the stress singularity dominates this region. The comparison of the numerical results shows that the stress components are almost the same for all L_O, which would be expected in a case where H_1 was the same for all L_O.

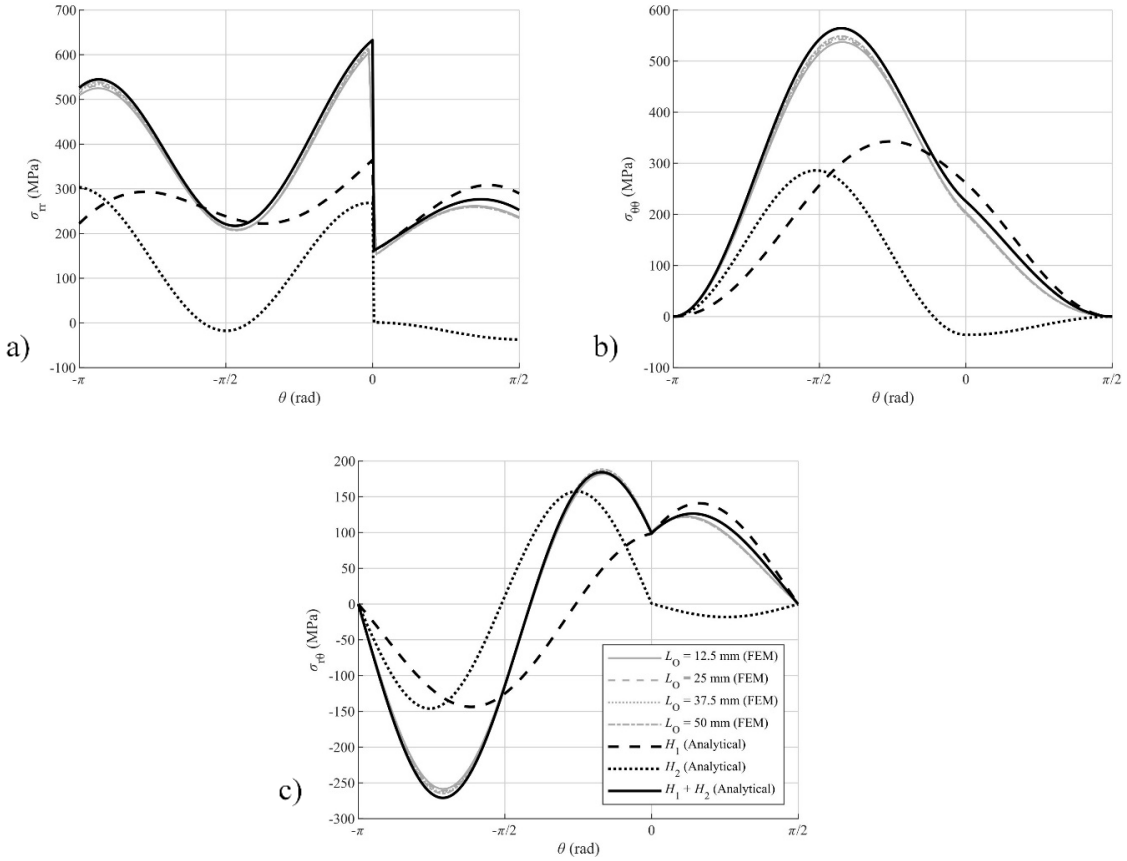

Figure 3.1.10 - Stress components using the FEM with the refined discretisation compared to the analytical stress

3.1.4.4 Strength prediction

In order to predict the joint strength, it is necessary to determine the critical ISSF (H_c). However, there is no standardized purely experimental test that allows this determination. The widespread methods to obtain this parameter are usually based on integrals and their implementation is often considerably intricate. Therefore, a combination of numerical simulations and experimental data was used. This type of hybrid experimental/numerical approach to determine failure criteria has been used previously for other criteria, such as the CLS criterion [50], but also to determine H_c [51]. The method proposed here consists of experimentally testing a SLJ of a given L_O and determining its P_m. Afterwards, a numerical simulation of the same joint is to be performed using the previously determined P_m as the imposed load. Then, the extracted singularity (H_n) components (n=1 or n=2) were used as the critical ISSF for both singularities (H_{nc}), which make possible the P_m prediction for different L_O. Since H_1 component is the most significant one, this method was used to obtain the H_{1c} estimates for each experimentally tested L_O.

Figure 3.1.11 shows that the H_{1c} values predicted using the two different discretisations present differences below 1%.

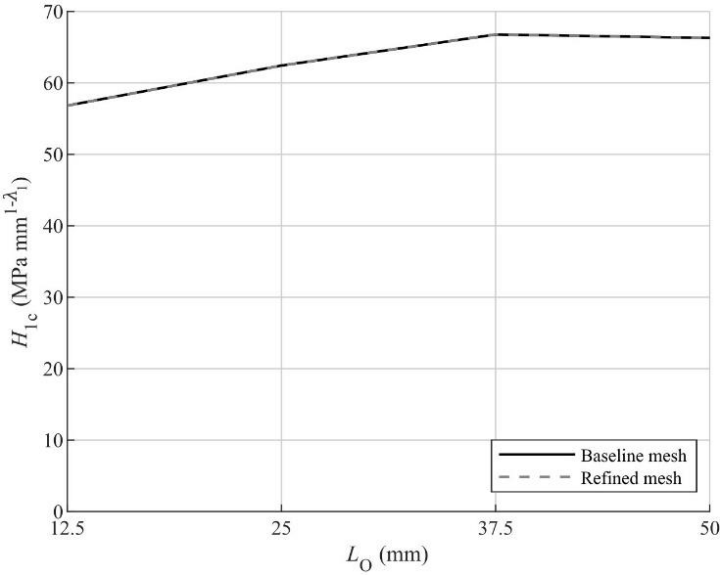

Figure 3.1.11 - Comparison of the predicted H_{1c} values for the different L_O and discretisations

It also shows that the H_{1c} estimated using L_O=37.5 mm and L_O=50 mm are similar, but for smaller L_O, the H_{1c} estimates are lower. This occurs because even an adhesive as brittle as this has a small amount of plasticity in longer L_O, which means that some energy would have to be spent in plasticizing the adhesive before a crack would form. Furthermore, in longer L_O, the crack can propagate stably for a few moments, but for shorter L_O, the joints fail as soon as there is a crack. Finally, P_m was predicted using each one of those H_{1c}. For example, using the H_{1c} obtained with the experiments and

numerical simulations of L_O=12.5 mm, P_m was numerically predicted for the other L_O (25, 37.5 and 50 mm). The same procedure was done for the H_{1c} obtained with the other L_O.

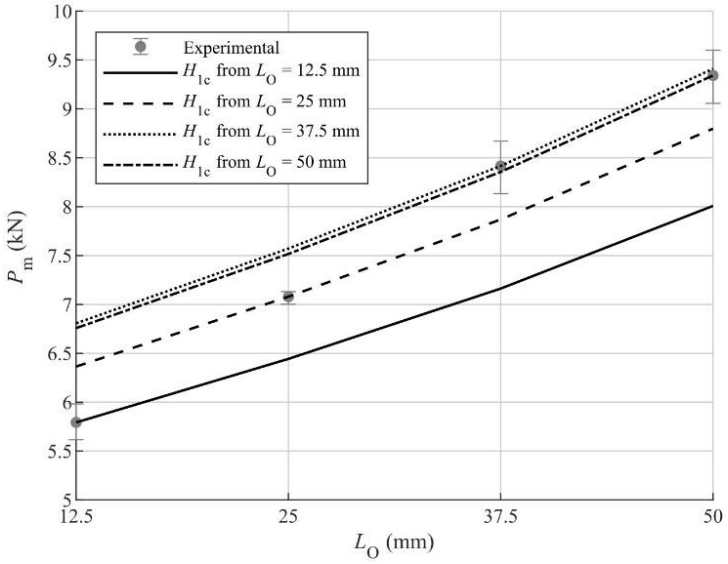

Figure 3.1.12 - Strength predictions using the FEM with the refined discretisation

Figure 3.1.12 presents the strength predictions only for the refined mesh since the results are similar to those obtained with the baseline mesh. On the other hand, it is observable that, as L_O increases, the curve slopes also increase. This fact is contrary to the experimental results where, for larger L_O, increasing L_O diminishes the returns in strength. However, this slope increase is minimal, and it is not a significant issue in the L_O range tested. For the largest L_O, the predicted strength increase is in line with what was verified experimentally, i.e., approximately a 1 kN strength increase between L_O=37.5 mm and L_O=50 mm. For the two shortest L_O, the predicted strength increases when L_O increases are smaller than those found experimentally, i.e., the strength prediction increase between L_O=12.5 mm and L_O=25 mm is smaller than 1 kN, while the experimental strength increase was over 1 kN.

By analysing the strength predictions for the L_O=12.5 mm, it is perceptible that the nearest prediction (beyond its own H_{1c} curve) is the curve of H_{1c} determined with L_O=25 mm. However, the joint strength is overpredicted, and the percentual deviation between this prediction and the experimental data is 9.75%, which can be considered high. The other two predictions are also higher than the experimental value, being the L_O=37.5 mm case the furthest away with a percentual deviation of 17.33%. For L_O=25 mm, similar behaviour is observed for the two highest L_O. Nonetheless, for the L_O=12.5 mm prediction case, the joint strength is underpredicted with a percentual deviation of 8.92%. For the largest L_O, it is clear that the predictions are identical, with a percentual deviation of 0.84% when a L_O=50 mm was used to predict the strength of the L_O=37.5 mm joint and the same percentual deviation on the contrary case. For both these cases, the worst-case scenario is predicting the strength with a L_O=12.5 mm, where percentual deviations over 16% were found.

3.1.5 Conclusions

The present work focused on the ISSF criterion, comparing the numerical analysis performed through FEM with experimental data. This work's geometry and material combination lead to the existence of two components that characterise the stress singularity at the adhesive/adherend interface corner, being the first singularity the most significant one. The extrapolation method used to determine H_1 showed independence from the discretisation. This is a major advantage when compared to the stress, which is affected by the stress singularity in the corner, meaning that finer discretisations lead to higher stress levels in this region. The method proposed to determine H_{1c} showed some variance depending on which L_O is used, except when comparing the H_{1c} obtained with L_O=37.5 mm with the one obtained with L_O=50 mm, which were similar. The strength predictions were lower than the experiments when the H_{1c} determined with a smaller L_O was used to predict a larger L_O's joint strength. However, joint strength was over predicted when an L_O smaller than the L_O with which H_{1c} was determined was used. The only exceptions to this rule are the two largest L_O, because the H_{1c} predicted with those two L_O are similar, meaning that the strength predictions for L_O=37.5 mm using the H_{1c} determined with L_O=50 mm, and vice-versa, are identical to the experimental P_m. Since it is better to have conservative P_m predictions due to safety reasons, it would be advisable to only predict P_m of joints with L_O larger than the L_O used to determine H_{1c}. The results found in this work revealed to be very promising, with very accurate results achieved, considering the simplicity of the method applied to determine H_{1c}. Although the method's validity was only checked for a specific adhesive system, this technique can be further studied in the field of adhesive joints and applied to different systems/joint types, provided that further validation is accomplished.

3.1.6 Appendixes

3.1.6.1 Appendix 1

$$e=(\alpha-\beta)\left(\cos\left[2\lambda\theta_1\right]-\cos\left[2\lambda\theta_1-2\lambda\theta_2\right]+\lambda^2\left[\cos\left(2\theta_1\right)-\cos\left(2\theta_1+2\theta_2\right)-1+\cos\left(2\theta_2\right)\right]\right) \\ +(1+\alpha)\left(1-\cos\left[2\lambda\theta_1\right]\right)-(1-\beta)\left(1-\cos\left[2\lambda\theta_2\right]\right) \tag{10}$$

$$b=(\alpha-\beta)\left(\sin\left[2\lambda\theta_1\right]-\sin\left[2\lambda\theta_1-2\lambda\theta_2\right]-\lambda^2\left[\sin\left(2\theta_1\right)-\sin\left(2\theta_1+2\theta_2\right)+\sin\left(2\theta_2\right)\right]\right) \\ -(1+\alpha)\sin\left(2\lambda\theta_1\right)-(1-\beta)\sin\left(2\lambda\theta_2\right) \tag{11}$$

$$c=(\alpha-\beta)\left(\cos\left[2\lambda\theta_1\right]-\cos\left[2\lambda\theta_1+2\theta_2\right]+\cos\left[2\lambda\theta_2\right]-\cos\left(2\lambda\theta_2-2\theta_1\right)-1+\cos\left(2\theta_1\right)\right) \\ +(1+\alpha)\left(1-\cos\left[2\theta_1\right]\right)-(1-\beta)\left(1-\cos\left[2\theta_2\right]\right) \tag{12}$$

$$d=(\alpha-\beta)\left(\sin\left[2\theta_1\right]+\sin\left[2\lambda\theta_2-2\theta_1\right]-\sin\left[2\lambda\theta_1\right]+\sin\left(2\lambda\theta_1+2\theta_2\right)-\sin\left(2\theta_2\right)\right) \\ -(1+\alpha)\sin\left(2\theta_1\right)-(1-\beta)\sin\left(2\theta_2\right) \tag{13}$$

3.1.6.2 Appendix 2

$$\chi_{31}=-\cos\left(2\lambda\theta_1\right)-\lambda\cos\left(2\theta_1\right) \tag{14}$$

$$\chi_{32}=\sin\left(2\lambda\theta_1\right)-\lambda\sin\left(2\theta_1\right) \tag{15}$$

$$\chi_{41}=\sin\left(2\lambda\theta_1\right)+\lambda\sin\left(2\theta_1\right) \tag{16}$$

$$\chi_{42}=\cos\left(2\lambda\theta_1\right)-\lambda\cos\left(2\theta_1\right) \tag{17}$$

$$\chi_{51}=\frac{1-\beta+(\alpha-\beta)\left(\lambda-\cos\left(2\lambda\theta_1\right)-\lambda\cos\left(2\theta_1\right)\right)}{1+\alpha} \tag{18}$$

$$\chi_{52} = \frac{(\alpha-\beta)\left(\sin(2\lambda\theta_1) - \lambda\sin(2\theta_1)\right)}{1+\alpha} \tag{19}$$

$$\chi_{61} = -\frac{(\alpha-\beta)\left(\sin(2\lambda\theta_1) + \lambda\sin(2\theta_1)\right)}{1+\alpha} \tag{20}$$

$$\chi_{62} = \frac{1-\beta-(\alpha-\beta)\left(\lambda+\cos(2\lambda\theta_1) - \lambda\cos(2\theta_1)\right)}{1+\alpha} \tag{21}$$

$$\begin{aligned}\chi_{71} = &\frac{(\alpha-\beta)\left(\sin[2\lambda\theta_1] + \lambda\sin[2\theta_1]\right)\left(\sin[2\lambda\theta_2] - \lambda\sin[2\theta_2]\right)}{1+\alpha} \\ -&\frac{\left(1-\beta+[\alpha-\beta]\left[\lambda-\cos(2\lambda\theta_1) - \lambda\cos(2\theta_1)\right]\right)\left(\cos[2\lambda\theta_2] + \lambda\cos[2\theta_2]\right)}{1+\alpha}\end{aligned} \tag{22}$$

$$\begin{aligned}\chi_{72} = &-\frac{(\alpha-\beta)\left(\sin[2\lambda\theta_1] - \lambda\sin[2\theta_1]\right)\left(\cos[2\lambda\theta_2] + \lambda\cos[2\theta_2]\right)}{1+\alpha} \\ -&\frac{\left(1-\beta-[\alpha-\beta]\left[\lambda+\cos(2\lambda\theta_1) - \lambda\cos(2\theta_1)\right]\right)\left(\sin[2\lambda\theta_2] - \lambda\sin[2\theta_2]\right)}{1+\alpha}\end{aligned} \tag{23}$$

$$\begin{aligned}\chi_{81} = &-\frac{(\alpha-\beta)\left(\sin[2\lambda\theta_1] + \lambda\sin[2\theta_1]\right)\left(\cos[2\lambda\theta_2] - \lambda\cos[2\theta_2]\right)}{1+\alpha} \\ -&\frac{\left(1-\beta+[\alpha-\beta]\left[\lambda-\cos(2\lambda\theta_1) - \lambda\cos(2\theta_1)\right]\right)\left(\sin[2\lambda\theta_2] + \lambda\sin[2\theta_2]\right)}{1+\alpha}\end{aligned} \tag{24}$$

$$\begin{aligned}\chi_{82} = &-\frac{(\alpha-\beta)\left(\sin[2\lambda\theta_1] - \lambda\sin[2\theta_1]\right)\left(\sin[2\lambda\theta_2] + \lambda\sin[2\theta_2]\right)}{1+\alpha} \\ -&\frac{\left(1-\beta-[\alpha-\beta]\left[\lambda+\cos(2\lambda\theta_1) - \lambda\cos(2\theta_1)\right]\right)\left(\cos[2\lambda\theta_2] - \lambda\cos[2\theta_2]\right)}{1+\alpha}\end{aligned} \tag{25}$$

$$y_1 = \frac{c-e}{\lambda\left(\left[\lambda+1-\cos\left(2\lambda\theta_1\right)-\lambda\cos\left(2\theta_1\right)\right]\left[c-e\right]+b+d\right)} \tag{26}$$

$$y_2 = \frac{b+d}{\lambda\left(\left[\lambda+1-\cos\left(2\lambda\theta_1\right)-\lambda\cos\left(2\theta_1\right)\right]\left[c-e\right]+b+d\right)} \tag{27}$$

3.1.7 References

[1] Jairaja, R. and G.N. Naik, *Single and dual adhesive bond strength analysis of single lap joint between dissimilar adherends.* International Journal of Adhesion and Adhesives, 2019. **92**: p. 142-153.

[2] Jeevi, G., S.K. Nayak and M. Abdul Kader, *Review on adhesive joints and their application in hybrid composite structures.* Journal of Adhesion Science and Technology, 2019. **33**(14): p. 1497-1520.

[3] Garrido, M., D. António, J.G. Lopes and J.R. Correia, *Performance of different joining techniques used in the repair of bituminous waterproofing membranes.* Construction and Building Materials, 2018. **158**: p. 346-358.

[4] Gui, C., J. Bai and W. Zuo, *Simplified crashworthiness method of automotive frame for conceptual design.* Thin-Walled Structures, 2018. **131**: p. 324-335.

[5] Du, J., F.T. Salmon and A.V. Pocius, *Modeling of cohesive failure processes in structural adhesive bonded joints.* Journal of Adhesion Science and Technology, 2004. **18**(3): p. 287-299.

[6] Konstantakopoulou, M., A. Deligianni and G. Kotsikos, *Failure of dissimilar material bonded joints.* Physical Sciences Reviews, 2016. **1**(3).

[7] Volkersen, O., *Die Nietkraftverteilung in zugbeanspruchten Nietverbindungen mit konstanten Laschenquerschnitten.* Jahrbuch der Deutschen Luftfahrtforschung, 1938. **15**: p. 41-47.

[8] Goland, M. and E. Reissner, *The stresses in cemented joints.* Journal of Applied Mechanics, 1944. **66**: p. A17-A27.

[9] Hart-Smith, L.J., *Adhesive-bonded single-lap joints*, in *NASA Contract Report, NASA CR-112236*. 1973.

[10] Carbas, R.J.C., L.F.M. Da Silva and G.W. Critchlow, *Adhesively bonded functionally graded joints by induction heating.* International Journal of Adhesion and Adhesives, 2014. **48**: p. 110-118.

[11] Ramalho, L.D.C., R.D.S.G. Campilho, J. Belinha and L.F.M. da Silva, *Static strength prediction of adhesive joints: A review.* International Journal of Adhesion and Adhesives, 2020. **96**: p. 102451.

[12] Blackman, B.R.K., H. Hadavinia, A.J. Kinloch and J.G. Williams, *The use of a cohesive zone model to study the fracture of fibre composites and adhesively-bonded joints.* International Journal of Fracture, 2003. **119**(1): p. 25-46.

[13] Carvalho, U.T.F. and R.D.S.G. Campilho, *Validation of pure tensile and shear cohesive laws obtained by the direct method with single-lap joints.* International Journal of Adhesion and Adhesives, 2017. **77**(Supplement C): p. 41-50.

[14] Campilho, R.D.S.G., M.D. Banea, J.A.B.P. Neto and L.F.M. da Silva, *Modelling adhesive joints with cohesive zone models: effect of the cohesive law shape of the adhesive layer.* International Journal of Adhesion and Adhesives, 2013. **44**: p. 48-56.

[15] Xu, W. and Y. Wei, *Influence of adhesive thickness on local interface fracture and overall strength of metallic adhesive bonding structures.* International Journal of Adhesion and Adhesives, 2013. **40**: p. 158-167.

[16] Demiral, M. and F. Kadioglu, *Failure behaviour of the adhesive layer and angle ply composite adherends in single lap joints: A numerical study.* International Journal of Adhesion and Adhesives, 2018. **87**: p. 181-190.

[17] Stein, N., S. Dölling, K. Chalkiadaki, W. Becker and P. Weißgraeber, *Enhanced XFEM for crack deflection in multi-material joints.* International Journal of Fracture, 2017. **207**(2): p. 193-210.

[18] Stuparu, F., D.M. Constantinescu, D.A. Apostol and M. Sandu, *A combined cohesive elements—XFEM approach for analyzing crack propagation in bonded joints.* The Journal of Adhesion, 2016. **92**(7-9): p. 535-552.

[19] Sánchez-Arce, I., L. Ramalho, R. Campilho and J. Belinha, *Material non-linearity in the numerical analysis of SLJ bonded with ductile adhesives: A meshless approach.* International Journal of Adhesion and Adhesives, 2021. **104**: p. 102716.

[20] Jiang, Z., Z. Fang, L. Yan, S. Wan and Y. Fang, *Mixed-mode I/II fracture criteria for adhesively-bonded pultruded GFRP/steel joint.* Composite Structures, 2021. **255**: p. 113012.

[21] Sugiman, S. and H. Ahmad, *Comparison of cohesive zone and continuum damage approach in predicting the static failure of adhesively bonded single lap joints.* Journal of Adhesion Science and Technology, 2017. **31**(5): p. 552-570.

[22] Ramalho, L.D.C., R.D.S.G. Campilho and J. Belinha, *Predicting single-lap joint strength using the natural neighbour radial point interpolation method.* Journal of the Brazilian Society of Mechanical Sciences and Engineering, 2019. **41**(9): p. 362.

[23] Tsai, C., Y. Guan, D. Ohanehi, J. Dillard, D. Dillard and R. Batra, *Analysis of cohesive failure in adhesively bonded joints with the SSPH meshless method.* International Journal of Adhesion and Adhesives, 2014. **51**: p. 67-80.

[24] Da Silva, L.F.M. and R.D.S.G. Campilho, *Advances in numerical modelling of adhesive joints*. Advances in numerical modeling of adhesive joints. 2012, Heidelberg: Springer.

[25] Parks, D.M., *A stiffness derivative finite element technique for determination of crack tip stress intensity factors.* International Journal of Fracture, 1974. **10**(4): p. 487-502.

[26] Matos, P.P.L., R.M. McMeeking, P.G. Charalambides and M.D. Drory, *A method for calculating stress intensities in bimaterial fracture.* International Journal of Fracture, 1989. **40**(4): p. 235-254.

[27] Lazzarin, P. and R. Zambardi, *A finite-volume-energy based approach to predict the static and fatigue behavior of components with sharp V-shaped notches.* International Journal of Fracture, 2001. **112**(3): p. 275-298.

[28] Rice, J.R., *A path independent integral and the approximate analysis of strain concentration by notches and cracks.* Journal of Applied Mechanics, 1968. **35**(2): p. 379-386.

[29] Rybicki, E.F. and M.F. Kanninen, *A finite element calculation of stress intensity factors by a modified crack closure integral.* Engineering Fracture Mechanics, 1977. **9**(4): p. 931-938.

[30] Leguillon, D., *Strength or toughness? A criterion for crack onset at a notch.* European Journal of Mechanics-A/Solids, 2002. **21**(1): p. 61-72.

[31] Hell, S., P. Weißgraeber, J. Felger and W. Becker, *A coupled stress and energy criterion for the assessment of crack initiation in single lap joints: a numerical approach.* Engineering Fracture Mechanics, 2014. **117**: p. 112-126.

[32] Williams, M.L., *The stresses around a fault or crack in dissimilar media.* Bulletin of the Seismological Society of America, 1959. **49**(2): p. 199-204.

[33] Bogy, D.B., *Edge-bonded dissimilar orthogonal elastic wedges under normal and shear loading.* Journal of Applied Mechanics, 1968. **35**(3): p. 460-466.

[34] Wu, Z., S. Tian, Y. Hua and X. Gu, *On the interfacial strength of bonded scarf joints.* Engineering Fracture Mechanics, 2014. **131**: p. 142-149.

[35] Afendi, M., M.A. Majid, R. Daud, A.A. Rahman and T. Teramoto, *Strength prediction and reliability of brittle epoxy adhesively bonded dissimilar joint.* International Journal of Adhesion and Adhesives, 2013. **45**: p. 21-31.

[36] Mintzas, A. and D. Nowell, *Validation of an Hcr-based fracture initiation criterion for adhesively bonded joints.* Engineering Fracture Mechanics, 2012. **80**: p. 13-27.

[37] Rastegar, S., M.R. Ayatollahi, A. Akhavan-Safar and L.F.M. da Silva, *Prediction of the critical stress intensity factor of single-lap adhesive joints using a coupled ratio method and an analytical model.* Proceedings of the Institution of Mechanical Engineers, Part L: Journal of Materials: Design Applications, 2018. **233**(7): p. 1393-1403.

[38] Zhang, Y., P. Wu and M. Duan, *A mesh-independent technique to evaluate stress singularities in adhesive joints.* International Journal of Adhesion and Adhesives, 2015. **57**: p. 105-117.

[39] Li, R., N.-A. Noda, R. Takaki, Y. Sano, Y. Takase and T. Miyazaki, *Most suitable evaluation method for adhesive strength to minimize bend effect in lap joints in terms of the intensity of singular stress field.* International Journal of Adhesion and Adhesives, 2018. **86**: p. 45-58.

[40] Galvez, P., N.-A. Noda, R. Takaki, Y. Sano, T. Miyazaki, J. Abenojar and M.A. Martínez, *Intensity of singular stress field (ISSF) variation as a function of the Young's modulus in single lap adhesive joints.* International Journal of Adhesion and Adhesives, 2019. **95**: p. 102418.

[41] Campilho, R.D.S.G., M.D. Banea, A.M.G. Pinto, L.F.M. da Silva and A.M.P. De Jesus, *Strength prediction of single-and double-lap joints by standard and extended finite element modelling.* International Journal of Adhesion and Adhesives, 2011. **31**(5): p. 363-372.

[42] Campilho, R.D.S.G., A.M.G. Pinto, M.D. Banea, R.F. Silva and L.F.M. da Silva, *Strength improvement of adhesively-bonded joints using a reverse-bent geometry.* Journal of Adhesion Science and Technology, 2011. **25**(18): p. 2351-2368.

[43] De Sousa, C.C.R.G., R.D.S.G. Campilho, E.A.S. Marques, M. Costa and L.F.M. da Silva, *Overview of different strength prediction techniques for single-lap bonded joints.* Proceedings of the Institution of Mechanical Engineers, Part L: Journal of Materials: Design Applications, 2017. **231**: p. 210-223.

[44] Qian, Z. and A. Akisanya, *Wedge corner stress behaviour of bonded dissimilar materials.* Theoretical and Applied Fracture Mechanics, 1999. **32**(3): p. 209-222.

[45] Dundurs, J., *Discussion:"Edge-bonded dissimilar orthogonal elastic wedges under normal and shear loading".* Journal of Applied Mechanics, 1969. **35**: p. 460-466.

[46] Klusák, J., T. Profant and M. Kotoul, *Various methods of numerical estimation of generalized stress intensity factors of bi-material notches.* Applied and Computational Mechanics, 2009. **3**(2).

[47] Nunes, S.L.S., R.D.S.G. Campilho, F.J.G. da Silva, C.C.R.G. de Sousa, T.A.B. Fernandes, M.D. Banea and L.F.M. da Silva, *Comparative failure assessment of single and double-lap joints with varying adhesive systems.* The Journal of Adhesion, 2016. **92**: p. 610-634.

[48] Fernandes, T.A.B., R.D.S.G. Campilho, M.D. Banea and L.F.M. da Silva, *Adhesive selection for single lap bonded joints: Experimentation and advanced techniques for strength prediction.* The Journal of Adhesion, 2015. **91**(10-11): p. 841-862.

[49] Jiang, W. and P. Qiao, *An improved four-parameter model with consideration of Poisson's effect on stress analysis of adhesive joints.* Engineering Structures, 2015. **88**: p. 203-215.

[50] Ramalho, L.D.C., I.J. Sánchez-Arce, R.D.S.G. Campilho and J. Belinha, *Strength prediction of composite single lap joints using the critical longitudinal strain criterion and a meshless method.* International Journal of Adhesion and Adhesives, 2021. **108**: p. 102884.

[51] Akhavan-Safar, A., M.R. Ayatollahi, S. Rastegar and L.F.M. da Silva, *Impact of geometry on the critical values of the stress intensity factor of adhesively bonded joints.* Journal of Adhesion Science and Technology, 2017. **31**(18): p. 2071-2087.

PAPER 2

ANALYSIS OF STRESS SINGULARITY IN ADHESIVE JOINTS USING MESHLESS METHODS

L.D.C. RAMALHO, J.M.M. DIONÍSIO, I.J. SÁNCHEZ-ARCE, R.D.S.G. CAMPILHO, J. BELINHA

3.2 Paper 2

3.2.1 Introduction

Recent centuries brought adhesive technology to the engineering panorama. However, this technique goes back to the time of the Neandertals, where they used resin collected from pine trees to glue their tools. Nowadays, it is applied to a wide range of industries, and it is hard to imagine a product that does not incorporate adhesive bonding [1]. The spread of adhesive bonding technology is mainly due to the aeronautical industry that introduced the concept of structural bonding. This notion highlighted several advantages of this joining process. The primary profit is in terms of the bonding weight. For the aeronautical industry, this characteristic is vital. Another distinctive quality is the more uniform stress distribution along the bonded area's width, allowing higher stiffness and improved load transmission [2]. Also, the non-necessity of drilling or damaging the adherends (including composites) for the joining process is highly convenient. Even so, like any other technology, this procedure has some associated issues. The most significant ones are the typical disassembly impossibility and the required curing time [3]. Nonetheless, the benefits of this technology are far more important than its weaknesses. For that reason, this technique is nowadays widely spread throughout a wide range of engineering fields, namely aeronautical, automotive, aerospace, civil and electronics [4].

When this technology emerged, computational resources were limited. Thus, the first analyses were performed through analytical models. Volkersen [5] was a pioneer in this area and developed the first model to analyse the stress distributions along the adhesive layer. He introduced the concept of differential shear [6], in which the adherends are considered elastic instead of rigid. Other researchers improved Volkersen's work, namely Goland and Reissner [7] and Hart-Smith [8]. However, these models had complex formulations or were very simple, but many simplifications were considered. De Sousa et al. [9] studied different analytical models and performed a comparison between them. The results showed that the Hart-Smith plastic model accurately predicts the strength increase with the overlap length (L_O) when dealing with brittle adhesives. When analysing ductile adhesives, the global yielding failure criterion [10] was the only one to accurately predict the joint strength for different L_O. The limitations of the analytical models meant that problems with a higher degree of complexity were impossible to solve. These limitations paved the way for the appearance of numerical methods. The most widespread numerical technique is the Finite Element Method (FEM) [11]. With this method, there are different approaches to evaluate the failure of adhesive joints, like continuum mechanics [12], damage mechanics [13], or the eXtended Finite Element Method (XFEM) [14]. Nonetheless, the most frequent method employed is Cohesive Zone Modeling (CZM) [15]. This approach is usually characterised by paired nodes that behave accordingly to a cohesive law. The CZM approach includes

continuum mechanics principles for damage initiation and fracture mechanics principles for crack propagation, establishing a softening relationship between stresses and strains, thus simulating gradual degradation of the material's mechanical properties. The cohesive law can assume different shapes, such as triangular, linear-parabolic, polynomial, exponential and trapezoidal [16]. The most basic shape is the triangular shape and it produces excellent results when treating brittle adhesives. Zhang et al. [17] examined different law shapes in Double-Cantilever Beam (DCB) and butt-joints, bonded with brittle and ductile adhesives. The results showed a significant influence of the law shape in the butt joint strength predictions, while for DCB the influence was smaller but still important. As expected, the triangular shape presented the best results for the brittle adhesives. For the ductile adhesives, the exponential law showed more suitability for the butt joints and the trapezoidal law for the DCB joints.

Another relevant approach to adhesive joint failure is fracture mechanics. Usually, two concepts are used in fracture mechanics: the Stress Intensity Factor (SIF) and the Strain Energy Release Rate (SERR). These techniques allow the evaluation of discontinuities in materials, such as re-entrant corners at the adhesive-adherend interface or defects. The determination of the SIF or the SERR can be performed through routines like the J-integral [18] or the Virtual Crack Closure Technique (VCCT) [19]. More recently, a new fracture mechanics based model arose that combines stress and energy criteria, called Finite Fracture Mechanics (FFM) [20]. In this model, an energetic and a stress criterion must be concurrently fulfilled for crack initiation.

The fracture mechanics approaches include the Intensity of Singular Stress Fields (ISSF) or General Stress Intensity Factor (GSIF). This approach can determine the singularity exponent in sharp material interface corners present in many adhesive joints and its intensity. Williams [21] and Bogy [22] published the first works dealing with this singularity. Many authors use the ISSF to only study the stresses and displacements around the interface corners of adhesive joints. Such is the case of Noda et al. [23], which studied the ISSF in single-lap joints (SLJ) and butt joints. In SLJ, they experimented with different L_O and adhesive thicknesses (t_A). It was shown that assuming an equal loading force, the ISSF remains almost constant for different t_A, but L_O affected the ISSF. Actually, for L_O<15 mm, the ISSF increased with increasing L_O, while for L_O≥15 mm, the ISSF decreased with increasing L_O. Goglio and Rossetto [24] proposed a purely numerical method to determine the singularity exponent (λ) and its intensity (H). This approach has the advantage that only a simple numerical simulation is needed, but it is not as precise. Moreover, depending on the stress component and angle used to perform this estimation, differences in the theoretical values of λ can be found. Thus, the choice of these parameters has to be careful. In addition to studying the stresses and displacements around an adhesive joint's corner, the ISSF has also been used to predict the strength of adhesive joints. Askarinejad et al. [25] used the ISSF to predict the strength of Thick Adherend Shear Tests (TAST) specimens without an initial crack and also used the conventional SIF for TAST specimens with initial cracks with different

lengths. In both cases, the strength predictions were in line with the experimental strength. Akhavan-Safar et al. [26] proposed that the critical ISSF (H_c) could be determined by performing numerical simulations with the experimental failure loads imposed. In that work, they tested SLJ with varying geometrical parameters, including L_O, t_A, substrate thickness and free length. The authors proposed that H_c depends on those geometrical parameters and recommended a function that could take these parameters into account to determine the maximum load (P_m). This function predicted the strength of the joints with good accuracy.

All the approaches mentioned before are generally applied through the FEM. However, a new class of discrete numerical techniques has been gaining prominence: meshless methods. The necessity of discretising the studied object into elements constrains the use of FEM. For example, an object with large deformations generates accuracy loss in the obtained results due to distortions in the elements [27]. Thence, the rise of meshless methods that do not rely on a structured mesh. One of the most studied meshless approaches is the Radial Point Interpolation Method (RPIM) [28]. The Natural Neighbour Radial Point Interpolation Method (NNRPIM) is a recent approach that combines the RPIM with the concept of natural neighbours [29]. This method considers the concept of "influence-cells" instead of "influence-domain" to impose nodal connectivity [30]. For the definition of the influence-cells, Voronoï diagrams and Delaunay tessellation are used. These methods have been applied to the study of adhesive joints in recent years. In 2017, Farahani et al. [31] used FEM and RPIM to determine the SIF for a compact tension specimen (CT) after determining these parameters experimentally with a fatigue crack growth test with Thermoelastic Stress Analysis (TSA). The two numerical methods presented similar results that agreed very well with the experimental data. Ramalho and co-workers [32] also applied this approach to composite adhesive SLJ with a brittle adhesive and different L_O. They overcame the difficulty of applying RPIM to bi-material problems by restricting the influence domains in the interface region between materials. With this procedure, the stresses obtained with the RPIM were very similar to the ones of FEM. Sánchez-Arce and co-authors [33] resorted to the NNRPIM to analyse adhesive joints. They measured experimental data of SLJ corresponding to four different L_O with a brittle adhesive. Then, they simulated the geometries resorting to the FEM and NNRPIM. By comparing the results, it was concluded that the results were very similar between the two methods, with a maximum difference observed in the strength of 2%, proving that the NNRPIM is suitable for this analysis. The maximum peak shear stress difference between FEM and NNRPIM predictions was 6.6%, indicating the method's suitability. The Boundary Element Method (BEM) is another discrete technique alternative to the FEM. Very recently, Wen et al. [34] resorted to BEM to analyse curved cracks. Until today, BEM has been applied to investigate the most diverse areas, such as composite materials [35-37].

The present work aims to evaluate the applicability of the ISSF criterion to meshless methods. In that regard, SLJ with different L_O bonded with a brittle adhesive were

studied. The influence of L_O in the experimental results was analysed. To predict the joint strength, the ISSF criterion was used. This method was numerically applied through the RPIM. The different steps necessary for these applications are also covered. In order to evaluate the influence of the discretization in the final results, two meshes with different levels of refinement were assessed. A comparison between the analytically obtained stresses and the ones determined numerically using RPIM was performed. Finally, the predicted strengths were compared with the experimental data to validate the applicability of the ISSF criterion to meshless methods, namely the RPIM. The proposed criterion is still an under-researched matter, with few research papers using this method to predict joint strength. Moreover, there is no standardised method to measure the critical singularities of a bi-material interface and a literature survey indicates the proposed combination of numerical simulations and experiments to estimate the strength is novel, especially for adhesive joints.

3.2.2 Experimental setup

3.2.2.1 SLJ geometry and dimensions

The meshless ISSF technique for strength prediction was validated with experiments, considering aluminium adherend SLJs bonded with a strong and brittle adhesive (Araldite® AV138). Figure 3.2.1 overviews the base geometry, dimensions (L_O was varied between 12.5 and 50 mm) and boundary conditions (BC). The applied BC aimed to emulate experimental testing under displacement control, and thus they involved clamping the left joint end, while a displacement (δ) was applied to the right end. Contrarily to L_O, the other base dimensions were kept constant: adherends' thickness t_P=3 mm, adhesive thickness t_A=0.2 mm, total joint length L_T=180 mm and joint width B=25 mm (B is not shown in the figure).

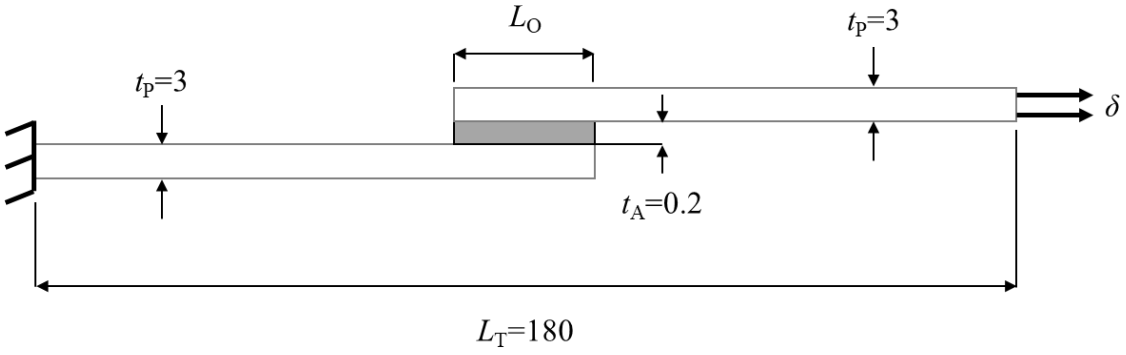

Figure 3.2.1 - SLJ geometry and dimensions in mm (L_O was varied between 12.5 and 50 mm)

3.2.2.2 Adherend and adhesive materials

The AW6082-T651 aluminium alloy was selected as the base material for the adherends. This aluminium alloy has medium strength and ductility and is used in structural

applications in the naval, automotive, and railroad industries. The unidirectional tensile behaviour of this material was acquired from former works [38, 39] by dogbone bulk tests leading to the characterisation up to failure by means of the stress-strain (σ-ε) curves. Data analysis led to the properties defined in Table 3.2.1, including the Young's modulus (E), the Poisson coefficient (ν), the tensile yield stress (σ_y), the tensile strength (σ_f) and the tensile failure strain (ε_f).

Table 3.2.1 - Tensile properties of the AW6082-T651 aluminium alloy [38, 39]

Property	Value
E (GPa)	70.1±0.83
ν	0.30
σ_y (MPa)	261.67±7.65
σ_f (MPa)	324.00±0.16
e_f (%)	21.70±4.24

The SLJs were bonded with a strong yet brittle epoxy adhesive: the Araldite® AV138 from Huntsman®. Actually, the AV138 has σ_f≈40 MPa, which can be considered a high standard for epoxy adhesives, although it is brittle. As a result, the performance can be poor when applied to bonded joints, typically experiencing large peak stresses due to the sharp corners and compliance difference between adjacent materials. Previous studies [38] showed that adhesives that fail to enter the plastic regime give usually worse results than less strong but ductile adhesives, particularly for large L_O, due to the associated peak stresses arising at the overlap edges. This statement is also valid for small L_O, but to a smaller extent, since the stress distributions in the adhesive layer flatten, thus decreasing the relevance of ductility. Thus, brittle adhesives can compete with ductile ones for small L_O. The Araldite® AV138 was properly characterised in a former work by De Sousa et al. [9] to obtain the necessary input properties for strength prediction. The mechanical tests included bulk tensile and TAST testing. The bulk tests were executed following the NF T 76-142 French standard, which gives the specimens' geometry and recommended manufacturing method, leading to estimations of E, σ_y, σ_f and ε_f. On the other hand, the TAST tests led to the shear elastic modulus (G), shear yield stress (τ_y), shear strength (τ_f) and shear failure strain (γ_f). These tests followed the 11003-2:1999 ISO standard (for manufacturing and test protocols). The TAST specimens were thus assembled, aligned and cured in a jig with side pins to assure the longitudinal alignment. The adherend material for these specimens was steel (DIN C45E), whose stiffness manages to almost eliminate adherend strains that affect the stiffness calculations. All the obtained properties of this adhesive are presented in Table 3.2.2.

Table 3.2.2 - Properties of the Araldite® AV138 [9]

Property	AV138
E (GPa)	4.89±0.81
ν	0.35[1]
σ_y (MPa)	36.49±2.47
σ_f (MPa)	39.45±3.18
ε_f (%)	1.21±0.10
G (GPa)	1.56±0.01
τ_y (MPa)	25.1±0.33
τ_f (MPa)	30.2±0.40
γ_f (%)	7.8±0.7

[1] Data from the manufacturer.

3.2.2.3 Joint production and testing

Joint manufacturing and testing is a highly relevant step of numerical validation works to be able to produce reliable and repeatable results for comparison with the output of the numerical simulations for a clear assessment. Thus, these procedures should be carefully planned and executed, following the current standards and practices. The initial step consisted of cutting the adherends with dimensions of 140×25 mm^2. Before bonding, the adherends were sandblasted with corundum sand particles to remove the oxide layer and dirt/contaminants, which could prevent a good bond and trigger premature adhesive (interfacial) failures. Following, before bonding the adherends in a steel jig, preparation was required. Actually, for the fabricated joints to achieve t_A=0.2 mm, it was necessary to place Teflon® wire, having a diameter of 0.2 mm, between adherends during the curing process. These stoppers were placed between 1 and 2 mm inside the overlap region to provide the minimum disruption to stress distributions in the adhesive layer but keeping the surfaces separated apart by 0.2 mm when applying pressure to the joints. To help with this process, the adherends were inserted in the jig with lateral guidance to prevent misalignments. After applying the adhesive to the lower adherend in the jig, the top adherend was slowly set in position and manually pressured against each other, such that the excess adhesive could flow out of the bonding length without the creation of voids. The specimens were then pressured at the overlap with grips and left to cure at room temperature. After curing, the excess adhesive was removed by milling to achieve the geometry of Figure 3.2.1 as closely as possible. The joints were tested in a Universal Testing Machine (UTM), considering L_T=180 mm for all joint configurations. A Shimadzu AG-X 100 UTM, equipped with a 100 kN load cell, was used. Loading was performed under displacement control, with a constant velocity of 1 mm/min. Each joint configuration gave at least 4 valid tests,

which enabled calculating the average failure load and considering it the experimental P_m for numerical model validation.

3.2.3 Numerical analysis

3.2.3.1 RPIM formulation

The implementation of the RPIM is similar to the FEM, representing an advantage to adapt existing FEM software to RPIM. It all starts with the discretization of a domain Ω into a nodal set $\mathbf{N}=\{n_1, n_2, \ldots, n_N\}$ with coordinates $\mathbf{X}=\{x_1, x_2, \ldots, x_N\} \in \Omega$. Afterwards, it is necessary to define a background integration grid used to create the integration points. For instance, one can use the finite element mesh as the RPIM integration grid. The integration technique used to perform the numerical integration of the stiffness matrix was the Gauss-Legendre quadrature. Within this technique, the grid-cells created are filled with integration points, following the Gauss-Legendre quadrature rule. Thus, inside each integration cell, 2x2 integration points were inserted, as Figure 3.2.2 shows. The procedure applied within this rule can be found in detail in the book of Bathe [40]. Then, the influence domain of each integration point is determined. The FEM counterpart of influence domains is how the elements are organized in a matrix. The influence domain of an integration point consists of a set of nodes used to construct the RPIM shape functions. There are several different techniques to determine the influence domains, but each influence domain should possess a similar number of nodes. Due to that, in the simulations performed in this work, the influence domains of each integration point are composed of the 16 nodes closest to it, which is within the advised number of nodes per influence domain found in the literature [30, 41]. It is important to note that any given node possibly belongs to several influence domains. This concept (called domain overlapping) allows imposing the nodal connectivity [30]. The concepts described previously are presented in Figure 3.2.2 for two example integration points.

In addition to the influence domains vs elements, the RPIM and the FEM also differ in how the shape functions are determined, which is described in detail in section 3.2.3.1.1. Apart from that, the implementation of the RPIM is very similar to the FEM implementation. A global stiffness matrix is assembled from all the local stiffness matrices obtained using the shape functions and material properties. The natural (imposed forces) and essential (displacement constraints/imposition) boundary conditions are imposed, and the global system of equations is solved. These steps are performed in the same manner as in the FEM.

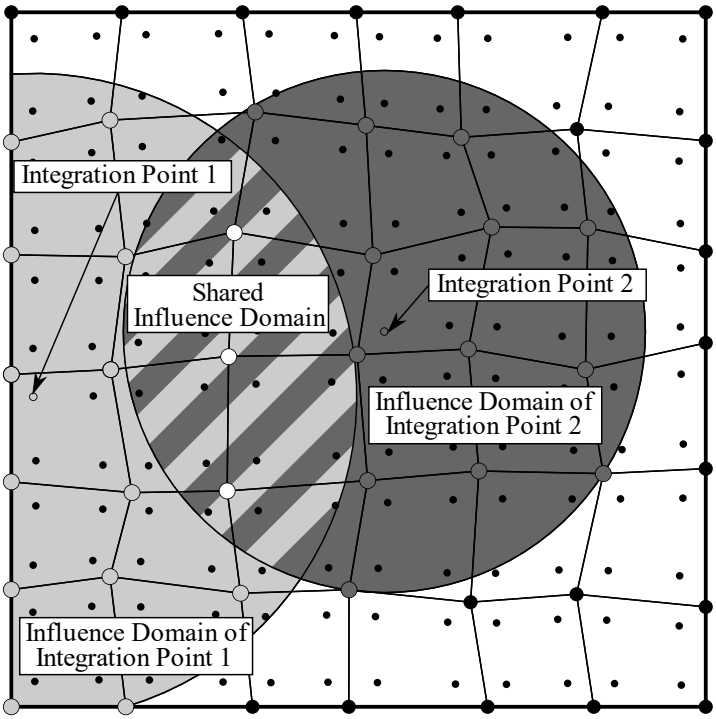

Figure 3.2.2 - Representation of RPIM concepts

3.2.3.1.1 Shape functions

For an integration point $\boldsymbol{x}_I \subset \mathbb{R}^d$, in the domain Ω, presented in section 3.2.3.1, any field variable $u(\boldsymbol{x})$ can be interpolated using the radial point interpolation technique[30]. Thus, the interpolated value of an integration point $\boldsymbol{x}_I$, $u(\boldsymbol{x}_I)$, can be obtained with:

$$u(\boldsymbol{x}_I) = \boldsymbol{r}(\boldsymbol{x}_I)^T \boldsymbol{a}(\boldsymbol{x}_I) + \boldsymbol{p}(\boldsymbol{x}_I)^T \boldsymbol{b}(\boldsymbol{x}_I), \quad (1)$$

Being $\boldsymbol{r}(\boldsymbol{x}_I)$ the radial basis function vector, $\boldsymbol{p}(\boldsymbol{x}_I)$ the polynomial basis function vector and $\boldsymbol{a}(\boldsymbol{x}_I)$ and $\boldsymbol{b}(\boldsymbol{x}_I)$ the non-constant coefficients of $\boldsymbol{r}(\boldsymbol{x}_I)$ and $\boldsymbol{p}(\boldsymbol{x}_I)$, respectively. While $\boldsymbol{a}(\boldsymbol{x}_I)$ and $\boldsymbol{r}(\boldsymbol{x}_I)$ will have a size equal to [n x 1], $\boldsymbol{b}(\boldsymbol{x}_I)$ and $\boldsymbol{p}(\boldsymbol{x}_I)$ will have a size equal to [m x 1]. The total number of nodes in the influence domain of $\boldsymbol{x}_I$ is denoted by n, while the number of monomials of the complete polynomial basis, defined according to Pascal's triangle, by m.

In this work, a linear polynomial basis was used in the RPI formulation ($p(\boldsymbol{x}) = \{1\ x\ y\}^T, m = 3$), since a higher polynomial basis results in longer computational times and the results did not change significantly with them. The Radial Basis Function (RBF) used in this work was the multi-quadrics (MQ) RBF, but there are other alternatives such as the Gaussian RBF or the thin plate spline RBF [30]. The MQ-RBF is defined as $r_i(x_I) = \left(d_{iI}^2 + (\gamma d_a)^2\right)^p$ [30], being γ and p the MQ-RBF shape parameters, d_a the integration weight of the interest point $\boldsymbol{x}_I$ and d_{iI} the Euclidean norm between node i and the integration point I. For the RPIM, the parameters that provide the best results are γ=1.03 and p=1.42, as suggested by Wang and Liu [42]. Thus, these values are used

in this work. Applying equation (1) to each node inside the influence domain of $\boldsymbol{x}_I$,leads to the following system of equations [30]:

$$\boldsymbol{R}\boldsymbol{a}\left(\boldsymbol{x}_I\right)+\boldsymbol{P}\boldsymbol{b}\left(\boldsymbol{x}_I\right)=\boldsymbol{u}_s\,, \tag{2}$$

where $\boldsymbol{u}_s^T=\{u_1 \quad u_2 \quad \dots \quad u_n\}$ is a vector with the field function values at each node inside the influence domain of $\boldsymbol{x}_I$, which can be the displacement, velocity, temperature or another variable, depending on the problem under analysis. The MQ-RBF moment matrix, $\boldsymbol{R}$, will have a size equal to $n \times n$, while the polynomial moment matrix, $\boldsymbol{P}$, will have a size equal to $m \times n$. To obtain a unique solution it is necessary to add another set of equations [30]:

$$\boldsymbol{P}^T\boldsymbol{a}\left(\boldsymbol{x}_I\right)=\boldsymbol{z}\,, \tag{3}$$

being $\boldsymbol{z}$ a null vector with size $[m \times 1]$. The combination of equations (2) and (3) leads to the final set of equations [30]:

$$\begin{bmatrix}\boldsymbol{R} & \boldsymbol{P}\\ \boldsymbol{P}^T & \boldsymbol{Z}\end{bmatrix}\begin{Bmatrix}\boldsymbol{a}\left(\boldsymbol{x}_I\right)\\ \boldsymbol{b}\left(\boldsymbol{x}_I\right)\end{Bmatrix}=\boldsymbol{M}_T\begin{Bmatrix}\boldsymbol{a}\left(\boldsymbol{x}_I\right)\\ \boldsymbol{b}\left(\boldsymbol{x}_I\right)\end{Bmatrix}=\begin{Bmatrix}\boldsymbol{u}_s\\ \boldsymbol{z}\end{Bmatrix}, \tag{4}$$

being $\boldsymbol{Z}$ a null matrix with size $[m \times m]$. [30]. Then, $\boldsymbol{a}(\boldsymbol{x}_I)$ and $\boldsymbol{b}(\boldsymbol{x}_I)$ can be obtained:

$$\begin{Bmatrix}\boldsymbol{a}\left(\boldsymbol{x}_I\right)\\ \boldsymbol{b}\left(\boldsymbol{x}_I\right)\end{Bmatrix}=\boldsymbol{M}_T^{-1}\begin{Bmatrix}\boldsymbol{u}_s\\ \boldsymbol{z}\end{Bmatrix}. \tag{5}$$

By substituting $\boldsymbol{M}_T^{-1}\{\boldsymbol{u}_s \quad \boldsymbol{z}\}^T$ into equation (1), the following is obtained:

$$u\left(\boldsymbol{x}_I\right)=\left\{\boldsymbol{r}\left(\boldsymbol{x}_I\right)^T \quad \boldsymbol{p}\left(\boldsymbol{x}_I\right)^T\right\}\boldsymbol{M}_T^{-1}\begin{Bmatrix}\boldsymbol{u}_s\\ \boldsymbol{z}\end{Bmatrix}. \tag{6}$$

The field function value for an interest point $\boldsymbol{x}_I$ is interpolated using the shape function values at the nodes inside the influence domain of $\boldsymbol{x}_I$, which can be identified in equation (6) [30]:

$$u\left(\boldsymbol{x}_I\right)=\left\{\boldsymbol{\Phi}\left(\boldsymbol{x}_I\right)^T \quad \boldsymbol{\Psi}\left(\boldsymbol{x}_I\right)^T\right\}\boldsymbol{M}_T^{-1}\begin{Bmatrix}\boldsymbol{u}_s\\ \boldsymbol{z}\end{Bmatrix}, \tag{7}$$

being $\boldsymbol{\Psi}\left(\boldsymbol{x}_I\right)=\{\psi_1(\boldsymbol{x}_I) \quad \psi_2(\boldsymbol{x}_I) \quad \dots \quad \psi_n(\boldsymbol{x}_I)\}^T$ and $\boldsymbol{\Phi}\left(\boldsymbol{x}_I\right)=\{\varphi_1(\boldsymbol{x}_I) \quad \varphi_2(\boldsymbol{x}_I) \quad \dots \quad \varphi_n(\boldsymbol{x}_I)\}^T$ a by-product vector with no relevant meaning and the interpolation shape function, respectively. A more complete formulation of the RPIM, including the derivatives of the shape functions needed to solve the $\boldsymbol{K}\boldsymbol{u}=\boldsymbol{f}$ system of equations, can be found in the literature [30].

3.2.3.2 ISSF approach

The ISSF, a fracture mechanics-based approach, intends to study discontinuities in materials, as explained in section 3.2.1. The present work uses the ISSF to analyse bi-material interface corners in SLJ, such as those in Figure 3.2.3.

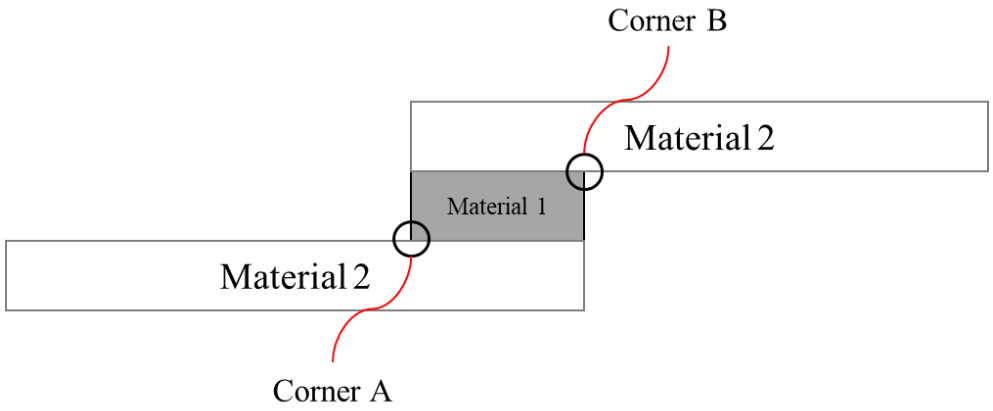

Figure 3.2.3 - Discontinuities in SLJ

The basis of the ISSF is the description of the stress, in polar coordinates (shown in Figure 3.2.4), around an interface singularity based on the following equation:

$$\sigma_{ij} = \sum_{n=1}^{\infty} H_n r^{\lambda_n - 1} f_{ij}(\lambda_n, \theta). \quad (8)$$

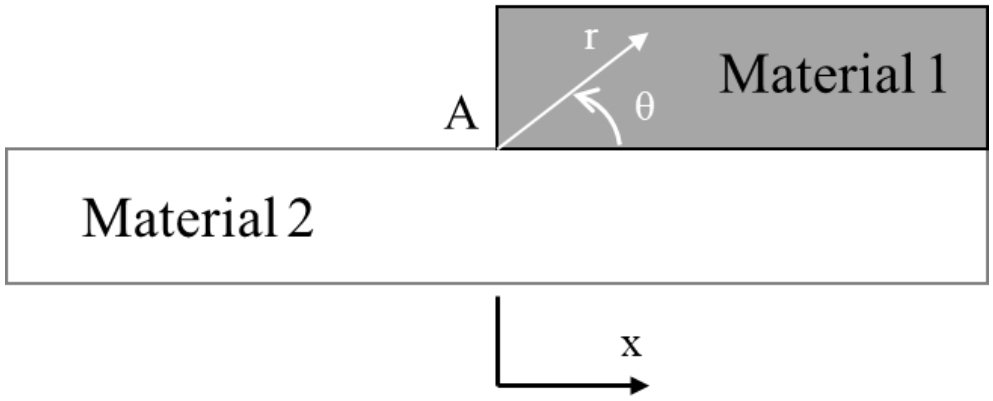

Figure 3.2.4 - Polar coordinates in a bi-material interface corner

It can also be used to describe the displacement, also in polar coordinates, in the same region:

$$u_j = \sum_{n=1}^{\infty} H_n r^{\lambda_n} g_j(\lambda_n, \theta), \quad (9)$$

being n the number of singularity exponents (λ), which depends on the interface corner's geometry and materials. H_n is the ISSF, or GSIF, which is a scalar value. The first

step to solve this equation is the determination of λ, which are obtained by solving the following equation [43]:

$$0 = e^2 + b^2 - \left(\lambda c\right)^2 - \left(\lambda d\right)^2 . \tag{10}$$

Equations *e*, *b*, *c* and *d* can be found in Appendix 1. The angles θ_1 and θ_2 in those equations are the angles of the materials in the interface corner, and α and β are the Dundurs parameters [44], which are material dependent and relate the properties of the interface corner materials, have the following definition:

$$\alpha = \frac{G_1\left(\kappa_2 + 1\right) - G_2\left(\kappa_1 + 1\right)}{G_1\left(\kappa_2 + 1\right) + G_2\left(\kappa_1 + 1\right)} \tag{11}$$

$$\beta = \frac{G_1\left(\kappa_2 - 1\right) - G_2\left(\kappa_1 - 1\right)}{G_1\left(\kappa_2 + 1\right) + G_2\left(\kappa_1 + 1\right)}, \tag{12}$$

being κ_m=3-4ν_m in plane strain cases and G_m the shear modulus of material *m*. The subscripts 1 and 2 in this equation represent the two different materials of the interface corner. With λ determined, the next step is the calculation of the displacement and stress functions, $f_{ij}(\lambda_n, \theta)$ and $g_j(\lambda_n, \theta)$ respectively, by solving the following system of equations:

$$\left\{ g_{rr}^m \quad g_{\theta}^m \quad f_{rr}^m \quad f_{\theta\theta}^m \quad f_{\theta}^m \right\}^T = \boldsymbol{N_m X_m Y} . \tag{13}$$

Here, *m* indicates the material and the matrices $\boldsymbol{N}_m$ and $\boldsymbol{X}_m$, and vector $\boldsymbol{Y}$ are defined as [43]:

$$N_m = \begin{bmatrix} \frac{\left(\kappa_m - \lambda\right)\cos\left(\left[\lambda - 1\right]\theta\right)}{2G_m} & \frac{\left(-\kappa_m + \lambda\right)\sin\left(\left[\lambda - 1\right]\theta\right)}{2G_m} & -\frac{\cos\left(\left[\lambda + 1\right]\theta\right)}{2G_m} & \frac{\sin\left(\left[\lambda + 1\right]\theta\right)}{2G_m} \\ \frac{\left(\kappa_m + \lambda\right)\sin\left(\left[\lambda - 1\right]\theta\right)}{2G_m} & \frac{\left(\kappa_m + \lambda\right)\cos\left(\left[\lambda - 1\right]\theta\right)}{2G_m} & \frac{\sin\left(\left[\lambda + 1\right]\theta\right)}{2G_m} & \frac{\cos\left(\left[\lambda + 1\right]\theta\right)}{2G_m} \\ -\left(\lambda^2 - 3\lambda\right)\cos\left(\left[\lambda - 1\right]\theta\right) & \left(\lambda^2 - 3\lambda\right)\sin\left(\left[\lambda - 1\right]\theta\right) & -\lambda\cos\left(\left[\lambda + 1\right]\theta\right) & \lambda\sin\left(\left[\lambda + 1\right]\theta\right) \\ \left(\lambda^2 + \lambda\right)\cos\left(\left[\lambda - 1\right]\theta\right) & -\left(\lambda^2 + \lambda\right)\sin\left(\left[\lambda - 1\right]\theta\right) & \lambda\cos\left(\left[\lambda + 1\right]\theta\right) & -\lambda\sin\left(\left[\lambda + 1\right]\theta\right) \\ \left(\lambda^2 - \lambda\right)\sin\left(\left[\lambda - 1\right]\theta\right) & \left(\lambda^2 - \lambda\right)\cos\left(\left[\lambda - 1\right]\theta\right) & \lambda\sin\left(\left[\lambda + 1\right]\theta\right) & \lambda\cos\left(\left[\lambda + 1\right]\theta\right) \end{bmatrix} \tag{14}$$

$$\boldsymbol{X}_1 = \begin{bmatrix} 1 & 0 \\ 0 & 1 \\ \chi_{31} & \chi_{32} \\ \chi_{41} & \chi_{42} \end{bmatrix}; \quad \boldsymbol{X}_2 = \begin{bmatrix} \chi_{51} & \chi_{52} \\ \chi_{61} & \chi_{62} \\ \chi_{71} & \chi_{72} \\ \chi_{81} & \chi_{82} \end{bmatrix}; \quad \boldsymbol{Y} = \begin{Bmatrix} y_1 \\ y_2 \end{Bmatrix}. \tag{15}$$

The components of $\boldsymbol{X}_m$ and $\boldsymbol{Y}$ are given by the equations in Appendix 2 [43].

After the two previous steps are completed, it is possible to determine H_n with the aid of a numerical simulation. In this work, this simulation was performed using the RPIM, and H_n was determined by performing an extrapolation to the corner, i.e. *r*=0 mm, from

values near it. However, there are other alternatives, such as performing a line or area integration encircling the interface corner, as in the work of Qian and Akisanya [43]. The extrapolation method requires a *n* number of points at different angles (θ) and at a fixed radius, equal to the number of λ, to determine H_1 to H_n using the following system of equations:

$$\begin{bmatrix} r^{\lambda_1-1} f_{\theta\theta}(\lambda_1,\theta_{n+1}) & \cdots & r^{\lambda_n-1} f_{\theta\theta}(\lambda_n,\theta_{n+1}) \\ \vdots & \ddots & \vdots \\ r^{\lambda_1-1} f_{\theta\theta}(\lambda_1,\theta_{n+n}) & \cdots & r^{\lambda_n-1} f_{\theta\theta}(\lambda_n,\theta_{n+n}) \end{bmatrix} \begin{Bmatrix} H_1 \\ \vdots \\ H_n \end{Bmatrix} = \begin{Bmatrix} \sigma_{\theta\theta}(r,\theta_{n+1}) \\ \vdots \\ \sigma_{\theta\theta}(r,\theta_{n+n}) \end{Bmatrix}. \quad (16)$$

With equation (16), ***H*** is determined for several different *r*, and then it is extrapolated to *r*=0 mm from an interval where the *r* vs ***H*** relationship is approximately linear to obtain the true ***H*** at the interface corner.

3.2.3.3 Numerical setup

As already stated, this work aims to validate the ISSF criterion through a meshless method, in this case, the RPIM. For this purpose, a developed meshless program running in MATLAB was used. At this stage, all the necessary modelling conditions to perform the numerical analysis were defined and input into the program. The first step was the creation of the geometries. Initially, a background integration grid (equivalent to a FEM mesh) was used to create the integration points, as previously described in section 3.2.3.1. The grid was constructed through quadrilateral elements characterised by the four points' coordinates corresponding to the vertices and the number of divisions along each dimension. These coordinates have to be precise to prevent the adherends and adhesive layer to overlap. Four geometries were created to evaluate the different L_O. Afterwards, the material properties were specified. These were described in section 3.2.2.2 for both the aluminium and the Araldite® AV138. For this analysis, the materials were considered linear elastic. Then, the essential BC were detailed. In this manner, the left side of the SLJ was considered fixed (U_x=U_y=U_z=0), as shown in Figure 3.2.1. On the contrary, on the right side, a prescribed displacement was imposed (U_x=δ; U_y=U_z=0).

The set of nodes that describe the geometries was assigned to finish the pre-processing for the numerical analysis. Unlike in the FEM, it was not necessary to define the type of elements that describe the geometry at this stage because, for RPIM, only the nodes are necessary. The selected nodal distribution applied intended to find a balance between resolution and computational cost. As mentioned in section 3.2.3.1, the size of each influence domain implemented was 16 nodes. Two different refinement levels were applied to evaluate the discretization's influence in the ISSF criterion, as shown in Figure 3.2.5 a) and b).

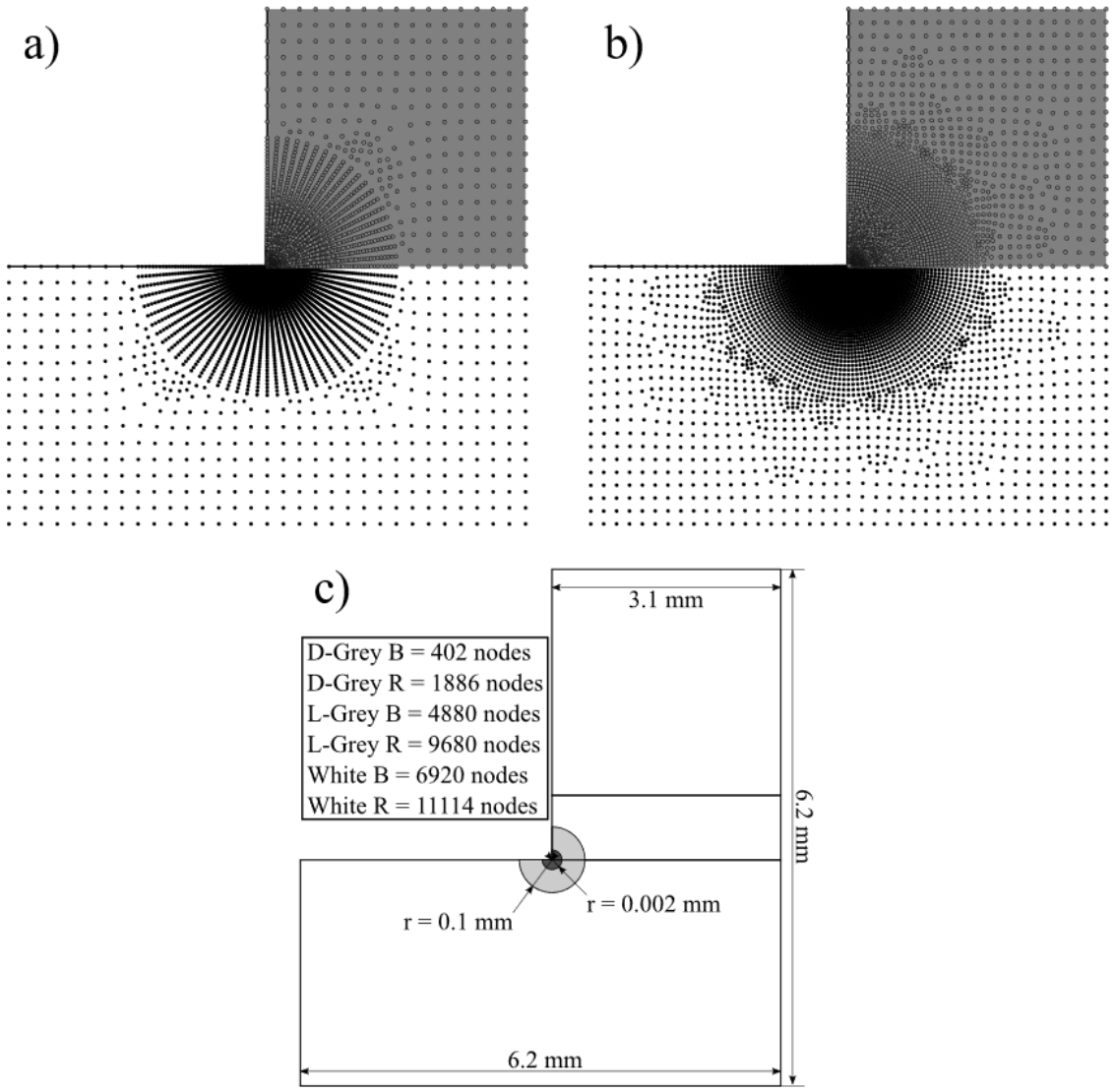

Figure 3.2.5 - Baseline (a) and refined discretisations (b) at the overlap end and mesh detail around the interface corner (c)

The baseline discretisation has approximately half the number of nodes of the refined discretization at the interface corners (Figure 3.2.5 c)). Material interfaces can be problematic in meshless methods like the RPIM. The influence domains of an integration point on a material can significantly penetrate the other material, influencing the numerical results. Several authors have proposed solutions to this problem [45-47]. They consist of limiting the interaction between different materials' influence domains to the interface's node layer. In summary, when the influence domain of a given integration point near the material interface is determined, the algorithm considers the interface as a separation zone. So, if the integration point is in the adherend, it will only look for nodes in the adherend or the interface, while if the integration point is in the adhesive, it will only look for nodes in the adhesive or the interface. This ensures that there is still connectivity between the materials since the nodes in the interface will belong to both materials' influence domains and that there is no influence domain

penetration. An example of the influence domains near the interface with this restriction is shown in Figure 3.2.6. All the simulations were performed under the following conditions: two-dimensional plane strain conditions, small deformations and linear elastic material behaviour. After these simulations were concluded, the ISSF criterion was tested through a script implemented in MATLAB that contained the previously presented formulation in section 3.2.3.2.

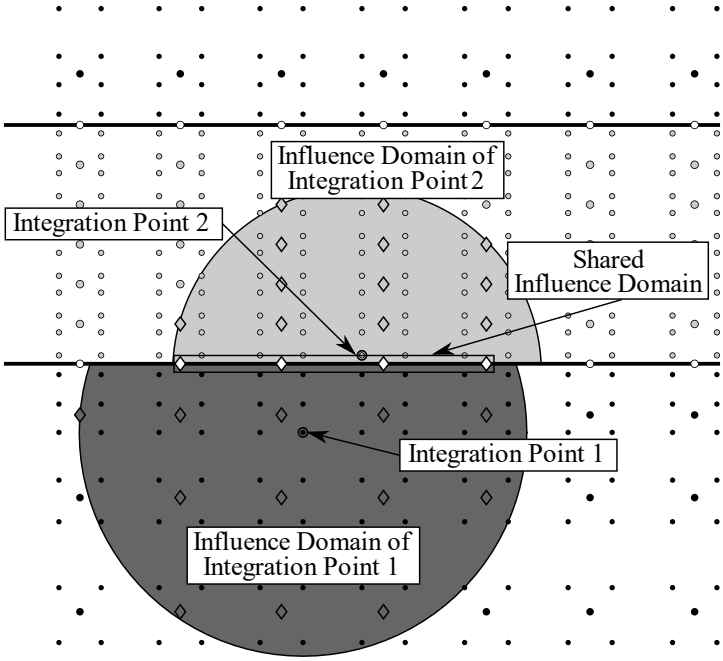

Figure 3.2.6 - Influence domains at the material interface

3.2.4 Results

3.2.4.1 Experimental results

After concluding the experimental tests, it was possible to analyse the type of fracture developed in the joints. A close inspection revealed that all the joints presented failure along the adhesive layer, with a visible and continuous adhesive layer on both failed adherends. These are signs of cohesive failure, indicating that joint preparation was accomplished correctly. Also, none of the joints presented plastic deformation in the adherends. The maximum sustained load (P_m) values were extracted from the load-displacement curves of every joint tested. Then, for each L_O, the average P_m was obtained along with the corresponding standard deviation, leading to the P_m vs L_O plot shown in Figure 3.2.7. This curve presents an almost linear behaviour, accompanied by a steady increase of P_m with L_O, although with a reduction of the increasing slope of P_m for higher L_O. Additionally, the P_m-L_O curve is largely non-proportional with respect to the plot origin. The reason for this phenomenon is the adhesive's brittleness or lack of ductility, which does not allow the joint to sustain the increasingly higher peel (σ_y) and

shear (τ_{xy}) peak stresses developing at both ends of the adhesive layer for higher L_O. Actually, this phenomenon is widely addressed in the literature [9] and it contrasts with the behaviour of joints bonded with ductile adhesives, where a close to proportional curve can be obtained if the adhesive is sufficiently ductile. Figure 3.2.7 also shows low standard deviations (maximum of 2.98% for L_O=50 mm), corroborating the good specimen preparation and repeatability of results.

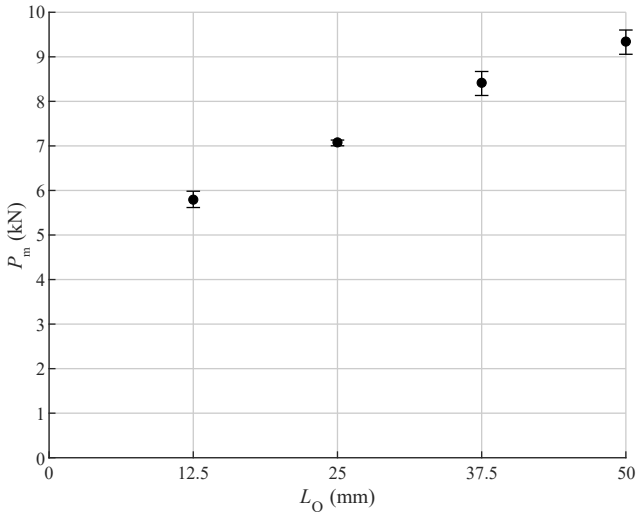

Figure 3.2.7 - P_m vs L_O plot with standard deviation

Although the scope of the present work is restricted to the L_O analysis and ISSF validation by changing this parameter, by comparison with available experimental data, other material and geometrical variables affect P_m.

- Geometrically, apart from L_O, the main parameters to be considered are t_A and t_P. Firstly, t_A is a controversial issue in the literature regarding the associated phenomena leading to the modification of the adhesive performance with this parameter, although there is generally a consensus that higher t_A reduce P_m. Some hypotheses are the higher interfacial shear stresses [48], the poorer adhesive quality due to the introduction of micro-cracks and voids [49], or even the reduction of the cohesive stresses at the crack tip [50]. On the other hand, higher t_P is often associated with improved strength, especially in joints bonded with brittle adhesives, due to more uniform stress distributions in the adhesive layer [51].
- The effect of the adhesive and adherends' material properties is also documented in the literature. Typically, and due to major stress gradients occurring in thin adhesive layers in bonded joints, strong and brittle adhesives perform well only for short L_O, for which the stress variations are smaller while failing to compete with less strong ductile adhesives for larger L_O. Actually, under these conditions, the peak stresses in the brittle adhesive are quickly reached at the overlap ends, and the joint fails prematurely. This issue was carefully assessed in the work of Nunes et al. [52], showing that the brittle Araldite® AV138

can compete with a less strong but ductile adhesive (Araldite® 2015) for short L_O (12.5 mm), while not accomplishing so for larger L_O (over 25 mm). The adherend material effect is closely related to the formerly introduced t_P discussion since higher adherend stiffness decreases peak stresses [53], and higher strength prevents adherend yielding, which can induce localized straining in the adhesive layer and lead to premature failures [54].

3.2.4.2 Determination of the stress singularities

The first step of the ISSF estimation process was to evaluate the corner geometry.

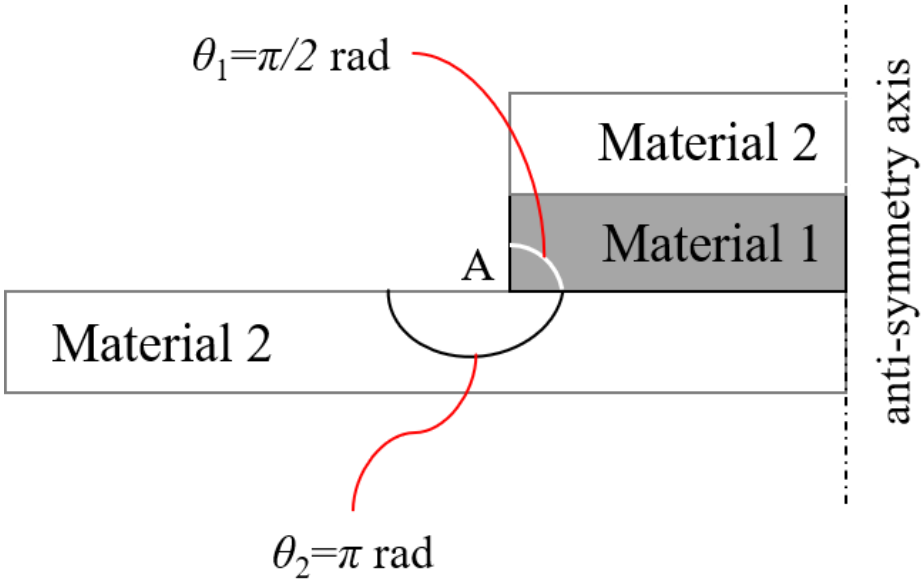

Figure 3.2.8 - SLJ corner geometry and anti-symmetry axis considered

Analysing Figure 3.2.8 and considering point A as the centre of the polar coordinate system, the angle θ_1 is associated with the adhesive layer geometry. In contrast, the angle θ_2 defines the adherend geometry. Therefore $\theta_1=\pi/2$ rad and $\theta_2=\pi$ rad. This corner geometry, alongside this material combination, leads to the existence of two exponents characterising the stress singularity at the adhesive/adherend interface corner (λ_1 and λ_2). Solving equation (10), λ_1=0.6539 and λ_2=0.9984 are obtained. As mentioned before, in this work, an interpolation method is applied. For that, two different angles are needed to perform the extrapolation, according to equation (16). In this case, the following angles were chosen: $\theta_3=\pi/4$ rad and $\theta_4=-\pi/4$ rad. These angles were not randomly chosen. They are the angles that allow a nodal based H_1 and H_2 determination in the two materials. Thus, one angle is in the ascending part of the $\sigma_{\theta\theta}$ curve (θ_4) and the other one in the descending part of the same curve (θ_3).

The determination of the eigenvalues (λ_n) allowed the calculation of the parameter $f_{\theta\theta}$ for the chosen interpolation angles (θ_3 and θ_4), by equation (13). This parameter completes the first matrix of equation (16). The matrix on the right side of this equation

is obtained through numerical analysis. This equation system was repeated for different radii from the interface corner. The stress singularities (H_1 and H_2) were finally calculated for the different radii considered. This calculation was performed when the reaction forces equal the experimental failure at the end where the displacement was imposed. By plotting the values from the different radii, it was perceptible that they are stable in the interval 0.01<r<0.02 mm (close enough to the corner tip to be influenced by other corners singularities). Thus, the values of H_1 and H_2 were extrapolated by a linear function to r=0 mm from the values in this interval. This process was performed for the joint with L_O=37.5 mm. To determine the stress singularities for the other L_O, the extrapolations were performed at an imposed displacement where H_n (where n=1 or n=2) would be the same as the H_n of L_O=37.5 mm at failure displacement.

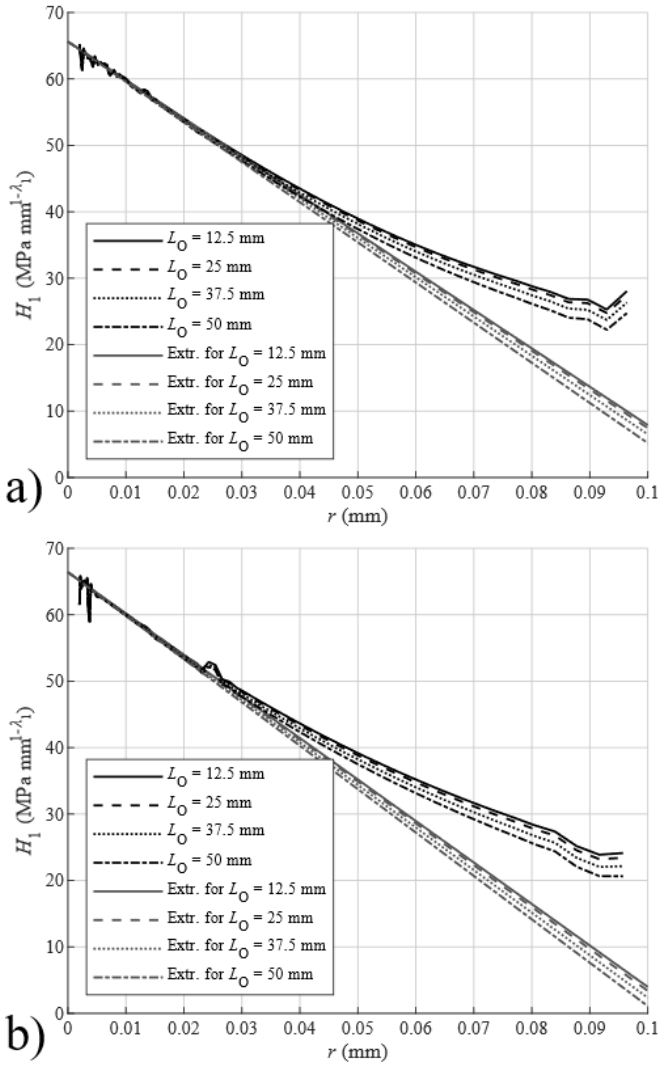

Figure 3.2.9 - Extrapolation of H_1 using the (a) baseline discretization and the (b) refined discretization

Figure 3.2.9 shows the extrapolations for the different L_O with the two considered discretisations. The obtained data reveals that the results are discretization-independent since the difference between the baseline and the refined mesh is below

1%. The comparison between the different L_O shows a more pronounced slope in extrapolation for larger L_O. The RPIM approach also leads to slight oscillations in the results because of the proximity to the singularity region. However, these do not affect the results since they occur outside the r interval considered to perform the extrapolations. All the presented results concern only the first singularity (H_1) since it is the most significant. Nonetheless, the determination of the second singularity component follows the same procedure. A comparison between the stress components obtained from the numerical simulations and the ones predicted by the analytical formulae was also performed, as shown in Figure 3.2.10. These were obtained at r=0.01 mm, and when H_1 was the same for all the L_O. From this figure, a considerable similarity is found between the numerical and analytical stresses, confirming the implemented formulation's suitability. As expected, the stress components for the different L_O are identical since the H_1 was the same for all L_O.

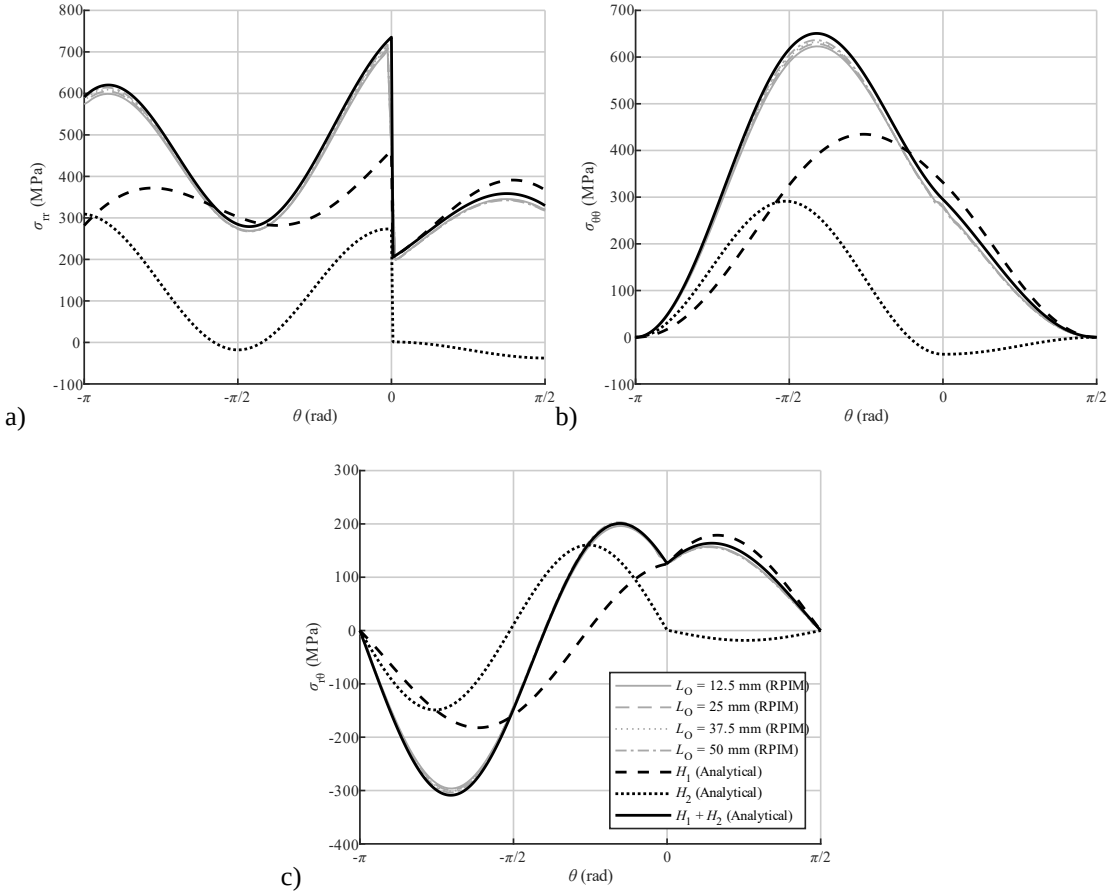

Figure 3.2.10 - Comparison between the analytical and numerical stress components: σ_{rr} (a), $\sigma_{\theta\theta}$ (b) and $\sigma_{r\theta}$ (c)

3.2.4.3 *Numerical predictions*

The last stage of the ISSF criterion validation was the strength prediction and comparison with the experimental results. For this purpose, it was necessary to know the critical singularity components (H_c) to compare them with the singularity

components determined in the previous section. This process can be carried out through different approaches, such as the Reciprocal Work Contour Integral Method (RWCIM) [55]. However, they usually are very complicated to implement. For that reason, an inverse technique was considered, consisting of a combination between numerical simulations and experimental data. In this case, the experimentally determined failure load was used as the imposed load in a numerical simulation with a given L_O. These simulations allowed the determination of the H_n values, which were then used as the H_{nc} values for the other L_O, leading to P_m estimation for all L_O. Since H_{nc} can be inferred for all L_O, this process can be repeated for the four experimentally tested L_O, giving four P_m vs L_O prediction curves.

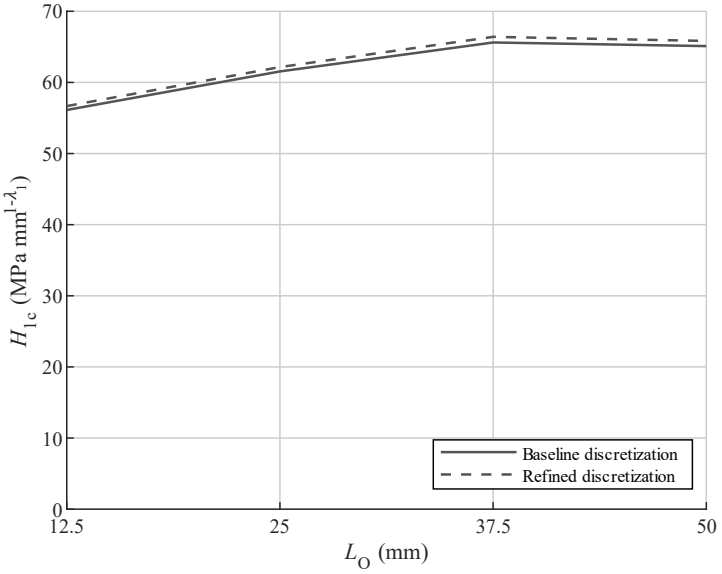

Figure 3.2.11 - H_{1c} comparison between the different L_O

The H_{1c} attained with this method are presented in Figure 3.2.11 for the different L_O and the two discretisations. As previously discussed, only the H_1 singularity component is presented due to its greater relevance to the predictions' outcome. Moreover, the H_{1c} values can be considered discretization-independent since the differences between the baseline and refined meshes are at most 1%. It was also found that the H_{1c} estimates using L_O=37.5 mm and L_O=50 mm are very similar. Nonetheless, for smaller L_O, the H_{1c} results are lower. This behaviour is because there is a small amount of plasticity in longer L_O, even in this brittle adhesive. Thus, some energy would have to be spent in plasticizing the adhesive before creating a crack. Additionally, the crack can propagate stably for a few moments in longer L_O, while for smaller L_O, the whole joint fails as soon as there is a crack.

Finally, Figure 3.2.12 features the strength predictions where P_m was predicted using each H_{1c}. These results concern the refined mesh since they are identical to those of the baseline mesh. By analysing the P_m vs L_O plots, a slope increase is detected with each increment of L_O. This observation contradicts the experimental results, where an L_O

increment leads to a slope decrease. Yet, this slope increase is minimal and does not affect the results in the L_O range tested. The strength increases with L_O for the two largest L_O are perfectly in line with the experimental results (approximately a 1 kN increase), contrary to the lower strength increases of the smaller L_O. While experimentally, a 1 kN strength increase (slightly over 1 kN) was verified, numerically, this increase was smaller than 1 kN.

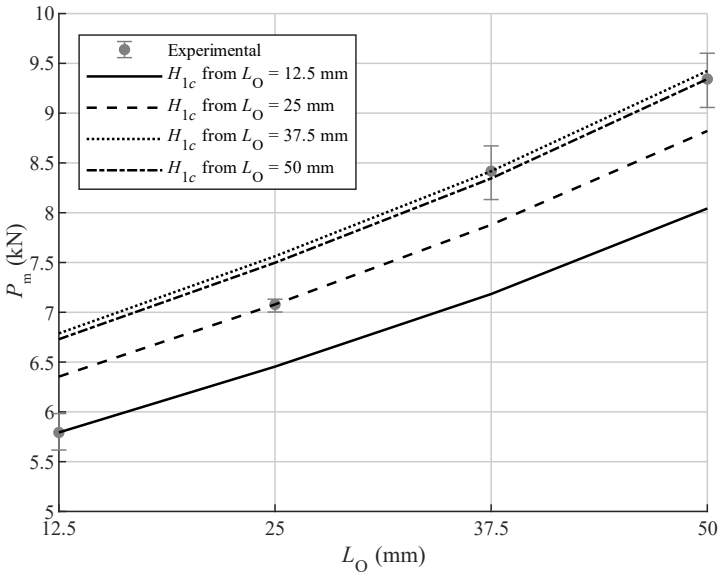

Figure 3.2.12 - Comparison between experimental and numerical P_m vs L_O

Regarding the method's accuracy, it is perceptible that the strength predictions are very similar for the two largest L_O, justified by a 0.87% percentual deviation when using L_O=37.5 mm to predict the strength of the L_O=50 mm joint. The same variation was verified when L_O=50 mm was used to predict the strength of the L_O=37.5 mm joint. For these two L_O, predicting the strength with L_O=12.5 mm is the least recommended procedure, given that percentual deviations of up to 14.66% were found. Predicting the strength of the highest L_O with L_O=25 mm leads to discrepancies around 5.58%. In the L_O=12.5 mm case, the nearest prediction is when L_O=25 mm was used. However, this originates an overprediction divergence of around 9.68%. Finally, for the L_O=25 mm case, the closest prediction was found when using L_O=50 mm, with a percentual deviation of 5.91%. These differences are only verified when the strength prediction of a given L_O is attained with a different L_O since each curve is based on the experimental failure load verified for that L_O.

3.2.5 Conclusions

This work's primary purpose was the implementation and validation of the ISSF criterion by a meshless method, in this case, the RPIM, for the strength prediction of multi-material corners in adhesively bonded joints. Initially, experimental tests were performed on aluminium SLJ with different L_O, and the resulting strength data was collected to validate the proposed approach. In terms of the ISSF criterion, its implementation started with defining the interface corner's geometry, which led to two exponents characterising it (λ_1 and λ_2). Then, to determine H_n, an extrapolation method was applied, which consisted of determining these parameters for different radii and then extrapolating them to the interface corner. The results obtained in this work allow the following conclusions:

- the numerical simulations showed that this technique does not depend on the discretization density, which constitutes a significant advantage in bonded joint design. Nonetheless, the RPIM results showed some oscillations of H_1 that were not significant since they were not in the extrapolation interval;
- an inverse method was applied to determine the critical singularity components (H_{nc}) necessary for the strength prediction. This approach combined numerical simulations with experimental data and led to good results for higher L_O;
- the obtained H_{nc} values with smaller L_O showed lower strength predictions when a smaller L_O was used to predict the strength of a larger L_O. For this reason, it is advisable to only predict the strength with L_O larger than the one used to determine H_{nc}. This way, a more conservative strength prediction is attained, which is recommended due to safety reasons;
- the two highest L_O presented incredibly similar strength predictions with a percentual deviation of only 0.83%. The maximum percentual deviation was found when the H_{1c} determined with L_O=12.5 mm was used to predict the strength of the L_O=37.5 mm joint (14.66%);
- the results obtained in this work validated the use of the ISSF criterion together with meshless methods for mixed-mode bonded joint analysis;
- the proposed method for determining the H_{nc} values showed exciting results when considering its simplicity against other widespread approaches.

3.2.6 Appendixes

3.2.6.1 Appendix 1

$$e=(\alpha-\beta)\left(\cos\left[2\lambda\theta_1\right]-\cos\left[2\lambda\theta_1-2\lambda\theta_2\right]+\lambda^2\left[\cos\left(2\theta_1\right)-\cos\left(2\theta_1+2\theta_2\right)-1+\cos\left(2\theta_2\right)\right]\right) \\ +(1+\alpha)\left(1-\cos\left[2\lambda\theta_1\right]\right)-(1-\beta)\left(1-\cos\left[2\lambda\theta_2\right]\right) \tag{17}$$

$$b=(\alpha-\beta)\left(\sin\left[2\lambda\theta_1\right]-\sin\left[2\lambda\theta_1-2\lambda\theta_2\right]-\lambda^2\left[\sin\left(2\theta_1\right)-\sin\left(2\theta_1+2\theta_2\right)+\sin\left(2\theta_2\right)\right]\right) \\ -(1+\alpha)\sin\left(2\lambda\theta_1\right)-(1-\beta)\sin\left(2\lambda\theta_2\right) \tag{18}$$

$$c=(\alpha-\beta)\left(\cos\left[2\lambda\theta_1\right]-\cos\left[2\lambda\theta_1+2\theta_2\right]+\cos\left[2\lambda\theta_2\right]-\cos\left(2\lambda\theta_2-2\theta_1\right)-1+\cos\left(2\theta_1\right)\right) \\ +(1+\alpha)\left(1-\cos\left[2\theta_1\right]\right)-(1-\beta)\left(1-\cos\left[2\theta_2\right]\right) \tag{19}$$

$$d=(\alpha-\beta)\left(\sin\left[2\theta_1\right]+\sin\left[2\lambda\theta_2-2\theta_1\right]-\sin\left[2\lambda\theta_1\right]+\sin\left(2\lambda\theta_1+2\theta_2\right)-\sin\left(2\theta_2\right)\right) \\ -(1+\alpha)\sin\left(2\theta_1\right)-(1-\beta)\sin\left(2\theta_2\right) \tag{20}$$

3.2.6.2 Appendix 2

$$\chi_{31}=-\cos\left(2\lambda\theta_1\right)-\lambda\cos\left(2\theta_1\right) \tag{21}$$

$$\chi_{32}=\sin\left(2\lambda\theta_1\right)-\lambda\sin\left(2\theta_1\right) \tag{22}$$

$$\chi_{41}=\sin\left(2\lambda\theta_1\right)+\lambda\sin\left(2\theta_1\right) \tag{23}$$

$$\chi_{42}=\cos\left(2\lambda\theta_1\right)-\lambda\cos\left(2\theta_1\right) \tag{24}$$

$$\chi_{51}=\frac{1-\beta+(\alpha-\beta)\left(\lambda-\cos\left(2\lambda\theta_1\right)-\lambda\cos\left(2\theta_1\right)\right)}{1+\alpha} \tag{25}$$

$$\chi_{52} = \frac{(\alpha-\beta)\left(\sin(2\lambda\theta_1)-\lambda\sin(2\theta_1)\right)}{1+\alpha} \tag{26}$$

$$\chi_{61} = -\frac{(\alpha-\beta)\left(\sin(2\lambda\theta_1)+\lambda\sin(2\theta_1)\right)}{1+\alpha} \tag{27}$$

$$\chi_{62} = \frac{1-\beta-(\alpha-\beta)\left(\lambda+\cos(2\lambda\theta_1)-\lambda\cos(2\theta_1)\right)}{1+\alpha} \tag{28}$$

$$\begin{aligned}\chi_{71} = &\frac{(\alpha-\beta)\left(\sin[2\lambda\theta_1]+\lambda\sin[2\theta_1]\right)\left(\sin[2\lambda\theta_2]-\lambda\sin[2\theta_2]\right)}{1+\alpha} \\ &-\frac{\left(1-\beta+[\alpha-\beta]\left[\lambda-\cos(2\lambda\theta_1)-\lambda\cos(2\theta_1)\right]\right)\left(\cos[2\lambda\theta_2]+\lambda\cos[2\theta_2]\right)}{1+\alpha}\end{aligned} \tag{29}$$

$$\begin{aligned}\chi_{72} = &-\frac{(\alpha-\beta)\left(\sin[2\lambda\theta_1]-\lambda\sin[2\theta_1]\right)\left(\cos[2\lambda\theta_2]+\lambda\cos[2\theta_2]\right)}{1+\alpha} \\ &-\frac{\left(1-\beta-[\alpha-\beta]\left[\lambda+\cos(2\lambda\theta_1)-\lambda\cos(2\theta_1)\right]\right)\left(\sin[2\lambda\theta_2]-\lambda\sin[2\theta_2]\right)}{1+\alpha}\end{aligned} \tag{30}$$

$$\begin{aligned}\chi_{81} = &-\frac{(\alpha-\beta)\left(\sin[2\lambda\theta_1]+\lambda\sin[2\theta_1]\right)\left(\cos[2\lambda\theta_2]-\lambda\cos[2\theta_2]\right)}{1+\alpha} \\ &-\frac{\left(1-\beta+[\alpha-\beta]\left[\lambda-\cos(2\lambda\theta_1)-\lambda\cos(2\theta_1)\right]\right)\left(\sin[2\lambda\theta_2]+\lambda\sin[2\theta_2]\right)}{1+\alpha}\end{aligned} \tag{31}$$

$$\begin{aligned}\chi_{82} = &-\frac{(\alpha-\beta)\left(\sin[2\lambda\theta_1]-\lambda\sin[2\theta_1]\right)\left(\sin[2\lambda\theta_2]+\lambda\sin[2\theta_2]\right)}{1+\alpha} \\ &-\frac{\left(1-\beta-[\alpha-\beta]\left[\lambda+\cos(2\lambda\theta_1)-\lambda\cos(2\theta_1)\right]\right)\left(\cos[2\lambda\theta_2]-\lambda\cos[2\theta_2]\right)}{1+\alpha}\end{aligned} \tag{32}$$

$$y_1 = \frac{c-e}{\lambda\left(\left[\lambda+1-\cos\left(2\lambda\theta_1\right)-\lambda\cos\left(2\theta_1\right)\right]\left[c-e\right]+b+d\right)} \tag{33}$$

$$y_2 = \frac{b+d}{\lambda\left(\left[\lambda+1-\cos\left(2\lambda\theta_1\right)-\lambda\cos\left(2\theta_1\right)\right]\left[c-e\right]+b+d\right)} \tag{34}$$

3.2.7 References

[1] Da Silva, L.F., A. Öchsner and R.D. Adams, *Handbook of adhesion technology*. 2011, Berlin, Germany: Springer Science & Business Media.

[2] Ebnesajjad, S. and A.H. Landrock, *Adhesives technology handbook*. 2014, London, UK: William Andrew.

[3] Du, J., F.T. Salmon and A.V. Pocius, *Modeling of cohesive failure processes in structural adhesive bonded joints.* Journal of Adhesion Science and Technology, 2004. **18**(3): p. 287-299.

[4] Gui, C., J. Bai and W. Zuo, *Simplified crashworthiness method of automotive frame for conceptual design.* Thin-Walled Structures, 2018. **131**: p. 324-335.

[5] Volkersen, O., *Die Nietkraftverteilung in zugbeanspruchten Nietverbindungen mit konstanten Laschenquerschnitten.* Jahrbuch der Deutschen Luftfahrtforschung, 1938. **15**: p. 41-47.

[6] da Silva, L.F., P.J. das Neves, R. Adams and J. Spelt, *Analytical models of adhesively bonded joints—Part I: Literature survey.* International Journal of Adhesion and Adhesives, 2009. **29**(3): p. 319-330.

[7] Goland, M. and E. Reissner, *The stresses in cemented joints.* Journal of Applied Mechanics, 1944. **66**: p. A17-A27.

[8] Hart-Smith, L.J., *Adhesive-bonded single-lap joints*, in *NASA Contract Report, NASA CR-112236*. 1973.

[9] De Sousa, C.C.R.G., R.D.S.G. Campilho, E.A.S. Marques, M. Costa and L.F.M. da Silva, *Overview of different strength prediction techniques for single-lap bonded joints.* Proceedings of the Institution of Mechanical Engineers, Part L: Journal of Materials: Design Applications, 2017. **231**: p. 210-223.

[10] Crocombe, A., *Global yielding as a failure criterion for bonded joints.* International Journal of Adhesion and Adhesives, 1989. **9**(3): p. 145-153.

[11] Campilho, R.D., *Strength prediction of adhesively-bonded joints*. 2017, Boca Raton, U.S.: CRC Press.

[12] Razavi, S.M.J., M.R. Ayatollahi, H.R. Majidi and F. Berto, *A strain-based criterion for failure load prediction of steel/CFRP double strap joints.* Composite Structures, 2018. **206**: p. 116-123.

[13] Kim, M.-H. and H.-S. Hong, *An adaptation of mixed-mode I+ II continuum damage model for prediction of fracture characteristics in adhesively bonded joint.* International Journal of Adhesion and Adhesives, 2018. **80**: p. 87-103.

[14] Santos, T. and R. Campilho, *Numerical modelling of adhesively-bonded double-lap joints by the eXtended Finite Element Method.* Finite Elements in Analysis Design, 2017. **133**: p. 1-9.

[15] Ramalho, L.D.C., R.D.S.G. Campilho, J. Belinha and L.F.M. da Silva, *Static strength prediction of adhesive joints: A review.* International Journal of Adhesion and Adhesives, 2020. **96**: p. 102451.

[16] Da Silva, L.F.M. and R.D.S.G. Campilho, *Advances in numerical modelling of adhesive joints*. Advances in numerical modeling of adhesive joints. 2012, Heidelberg: Springer.

[17] Zhang, J., J. Wang, Z. Yuan and H. Jia, *Effect of the cohesive law shape on the modelling of adhesive joints bonded with brittle and ductile adhesives.* International Journal of Adhesion and Adhesives, 2018. **85**: p. 37-43.

[18] Rice, J.R., *A path independent integral and the approximate analysis of strain concentration by notches and cracks.* Journal of Applied Mechanics, 1968. **35**(2): p. 379-386.

[19] Rybicki, E.F. and M.F. Kanninen, *A finite element calculation of stress intensity factors by a modified crack closure integral.* Engineering Fracture Mechanics, 1977. **9**(4): p. 931-938.

[20] Leguillon, D., *Strength or toughness? A criterion for crack onset at a notch.* European Journal of Mechanics-A/Solids, 2002. **21**(1): p. 61-72.

[21] Williams, M.L., *The stresses around a fault or crack in dissimilar media.* Bulletin of the Seismological Society of America, 1959. **49**(2): p. 199-204.

[22] Bogy, D.B., *Edge-bonded dissimilar orthogonal elastic wedges under normal and shear loading.* Journal of Applied Mechanics, 1968. **35**(3): p. 460-466.

[23] Noda, N., R. Li, T. Miyazaki, R. Takaki and Y. Sano, *Convenient adhesive strength evaluation method in terms of the intensity of singular stress field.* International Journal of Computational Methods, 2019. **16**(01): p. 1850085.

[24] Goglio, L. and M. Rossetto, *Stress intensity factor in bonded joints: influence of the geometry.* International Journal of Adhesion and Adhesives, 2010. **30**(5): p. 313-321.

[25] Askarinejad, S., M.D. Thouless and N.A. Fleck, *Failure of a pre-cracked epoxy sandwich layer in shear.* European Journal of Mechanics-A/Solids, 2021. **85**: p. 104134.

[26] Akhavan-Safar, A., M.R. Ayatollahi, S. Rastegar and L.F.M. da Silva, *Impact of geometry on the critical values of the stress intensity factor of adhesively bonded joints.* Journal of Adhesion Science and Technology, 2017. **31**(18): p. 2071-2087.

[27] Liu, G.-R. and Y.-T. Gu, *An introduction to meshfree methods and their programming*. 2005, Dordrecht, The Netherlands: Springer Science & Business Media.

[28] Wang, J. and G. Liu, *A point interpolation meshless method based on radial basis functions.* International Journal for Numerical Methods in Engineering, 2002. **54**(11): p. 1623-1648.

[29] Dinis, L., R.N. Jorge and J. Belinha, *Analysis of 3D solids using the natural neighbour radial point interpolation method.* Computer Methods in Applied Mechanics and Engineering, 2007. **196**(13-16): p. 2009-2028.

[30] Belinha, J., *Meshless methods in biomechanics: Bone tissue remodelling analysis*. Vol. 16. 2014, Switzerland: Springer.

[31] Farahani, B.V., P.J. Tavares, P.M.G.P. Moreira and J. Belinha, *Stress intensity factor calculation through thermoelastic stress analysis, finite element and RPIM meshless method.* Engineering Fracture Mechanics, 2017. **183**: p. 66-78.

[32] Ramalho, L., I. Sánchez-Arce, R. Campilho, J. Belinha and F. Silva, *Strength prediction and stress analysis of adhesively bonded composite joints using meshless methods.* Procedia Manufacturing, 2020. **51**: p. 904-911.

[33] Sánchez-Arce, I., L. Ramalho, R. Campilho and J. Belinha, *Analyzing single-lap joints bonded with a brittle adhesive by an elastic meshless method.* Procedia Structural Integrity, 2020. **28**: p. 1084-1093.

[34] Wen, P.H., Y.D. Tang, J. Sladek and V. Sladek, *BEM analysis for curved cracks.* Engineering Analysis with Boundary Elements, 2021. **127**: p. 91-101.

[35] Useche, J. and C. Medina, *Boundary element analysis of laminated composite shear deformable shallow shells.* Composite Structures, 2018. **199**: p. 24-37.

[36] Shiah, Y.C. and M.R. Hematiyan, *Interlaminar Stresses Analysis of Three-Dimensional Composite Laminates by the Boundary Element Method.* Journal of Mechanics, 2018. **34**(6): p. 829-837.

[37] Jia, P.H., L. Lei, J. Hu, Y. Chen, K. Han, W.F. Huang, Z. Nie and Q.H. Liu, *Twofold domain decomposition method for the analysis of multiscale composite structures.* IEEE Transactions on Antennas and Propagation, 2019. **67**(9): p. 6090-6103.

[38] Campilho, R.D.S.G., M.D. Banea, A.M.G. Pinto, L.F.M. da Silva and A.M.P. De Jesus, *Strength prediction of single-and double-lap joints by standard and extended finite element modelling.* International Journal of Adhesion and Adhesives, 2011. **31**(5): p. 363-372.

[39] Campilho, R.D.S.G., A.M.G. Pinto, M.D. Banea, R.F. Silva and L.F.M. da Silva, *Strength improvement of adhesively-bonded joints using a reverse-bent geometry.* Journal of Adhesion Science and Technology, 2011. **25**(18): p. 2351-2368.

[40] Bathe, K.J., *Finite element procedures*. 2006: Klaus-Jurgen Bathe.

[41] Liu, G.R., *A point assembly method for stress analysis for two-dimensional solids.* International Journal of Solids and Structures, 2002. **39**(1): p. 261-276.

[42] Wang, J.G. and G.R. Liu, *On the optimal shape parameters of radial basis functions used for 2-D meshless methods.* Computer Methods in Applied Mechanics and Engineering, 2002. **191**(23-24): p. 2611-2630.

[43] Qian, Z. and A. Akisanya, *Wedge corner stress behaviour of bonded dissimilar materials.* Theoretical and Applied Fracture Mechanics, 1999. **32**(3): p. 209-222.

[44] Dundurs, J., *Discussion:"Edge-bonded dissimilar orthogonal elastic wedges under normal and shear loading".* Journal of Applied Mechanics, 1969. **35**: p. 460-466.

[45] Liu, G.R., *Meshfree Methods*. 2010, Boca Raton: CRC Press.

[46] Cordes, L.W. and B. Moran, *Treatment of material discontinuity in the element-free Galerkin method.* Computer Methods in Applied Mechanics and Engineering, 1996. **139**(1-4): p. 75-89.

[47] Ramalho, L.D.C., R.D.S.G. Campilho and J. Belinha, *Single lap joint strength prediction using the radial point interpolation method and the critical longitudinal strain criterion.* Engineering Analysis with Boundary Elements, 2020. **113 (January)**: p. 268-276.

[48] Gleich, D.M., M.J.L. Van Tooren and A. Beukers, *Analysis and evaluation of bondline thickness effects on failure load in adhesively bonded structures.* Journal of Adhesion Science and Technology, 2001. **15**(9): p. 1091-1101.

[49] Adams, R. and N. Peppiatt, *Stress analysis of adhesive-bonded lap joints.* Journal of strain analysis, 1974. **9**(3): p. 185-196.

[50] Ji, G., Z. Ouyang, G. Li, S. Ibekwe and S.S. Pang, *Effects of adhesive thickness on global and local Mode-I interfacial fracture of bonded joints.* International Journal of Solids and Structures, 2010. **47**(18-19): p. 2445-2458.

[51] Campilho, R.D.S.G., M.F.S.F. De Moura and J.J.M.S. Domingues, *Modeling single and double-lap repairs on composite materials.* Composites Science and Technology, 2005. **65**(13): p. 1948-1958.

[52] Nunes, S.L.S., R.D.S.G. Campilho, F.J.G. Da Silva, C.C.R.G. De Sousa, T.A.B. Fernandes, M.D. Banea and L.F.M. Da Silva, *Comparative failure assessment of single and double lap joints with varying adhesive systems.* The Journal of Adhesion, 2016. **92**(7-9): p. 610-634.

[53] Aydin, M.D., A. Özel and Ş. Temiz, *The effect of adherend thickness on the failure of adhesively-bonded single-lap joints.* Journal of Adhesion Science and Technology, 2005. **19**(8): p. 705-718.

[54] Fernandes, T.A.B., R.D.S.G. Campilho, M.D. Banea and L.F.M. da Silva, *Adhesive selection for single lap bonded joints: experimentation and advanced techniques for strength prediction.* The Journal of Adhesion, 2015. **91**(10-11): p. 841-862.

[55] Galvez, P., N.-A. Noda, R. Takaki, Y. Sano, T. Miyazaki, J. Abenojar and M.A. Martínez, *Intensity of singular stress field (ISSF) variation as a function of the Young's modulus in single lap adhesive joints.* International Journal of Adhesion and Adhesives, 2019. **95**: p. 102418.

PAPER 3

FRACTURE MECHANICS APPROACH TO STRESS SINGULARITY IN COMPOSITE ADHESIVE JOINTS

J.M.M. DIONÍSIO, L.D.C. RAMALHO, I.J. SÁNCHEZ-ARCE, R.D.S.G. CAMPILHO, J. BELINHA

3.3 Paper 3

3.3.1 Introduction

Since scientists started to explore ways to reach space, they understood that weight would be a crucial problem to solve in order to escape Earth's gravity. This dilemma initiated the investigation of different approaches to reduce the mass of structures. When thinking about a spacecraft, the characteristic that stands out in terms of its weight is its material(s). If the material is light, then the structure is also light. However, if the material does not provide stiffness and strength to withstand the stresses of Earth's gravity escape, the weight of the spacecraft becomes irrelevant. That's why it is so difficult to find the perfect material for these structures. Several materials were implemented in space vehicles through the years, such as wood, steel, and aluminium. They are still used today in some specific functions, but composite materials have widely replaced them. Composite materials emerged in aeroplanes during World War II (around 1940) due to their strength-to-weight properties but also because they proved to be transparent to radio frequencies. Since then, these materials have been highly studied [1, 2] and compose most of the structures in this sector. The developments achieved by the aeronautical industry spread out, and nowadays, these materials can be found in the most diverse sectors, such as the automotive, civil or medical [3].

A structure like an aeroplane comprises millions of components that need to be joined. Different joining techniques were used throughout engineering history, such as riveting and bolting, but more recently, adhesive bonding has gained much attention [3]. The main advantage of this approach is the low weight of the connection while improving stresses around the bonding areas [4]. Once again, aeronautical engineers first saw the possibilities brought by this technique and applied them to aeroplanes and spacecrafts. Nonetheless, the adhesive bonding process also has some disadvantages, such as the impossibility of disassembling the joint and the required curing time [5].

When engineers started to investigate adhesive bonding, the means at their disposal were scarce. Thus, the majority of the design process was performed through trial and error. However, this process was costly, so simple analytical analysis started to arise. In 1938, Volkersen [6] stood out as a pioneer in these analyses and published the first model to evaluate the stress distributions at mid-thickness, considering Single-Lap Joints (SLJ). Even so, Volkersen's approach did not consider the bending effect caused by the non-collinearity of the load path in SLJs. This effect leads to a bending moment that causes the joint's rotation, originating large deflections of the adherends. The investigators who followed tried to tackle these issues, emphasising Goland and Reissner [7] and Hart-Smith [8]. Nevertheless, all the models developed throughout the years presented problems, either because they were straightforward but posed many simplifications or because their formulation was too complex to solve analytically [9].

Despite their limitations, these models are still a reference today to understand elementary concepts regarding adhesive bonding [10].

The limits in joint design collapsed with the invention of the computer during World War II by Alan Turing. This discovery allowed engineers to analyse more intricate joint shapes and to perform more complex models. The computer initiated the numerical analysis era. In the early 1960s, Clough [11] conceived the concept of the Finite Element Method (FEM), a numerical approach that revolutionized structural engineering. Until today, FEM is the most widespread tool to perform numerical analysis [12]. With FEM, failure criteria to evaluate joint behaviour started to be introduced [13]. Continuum mechanics, fracture mechanics, Cohesive Zone Modeling (CZM), damage mechanics and the eXtended Finite Element Method (XFEM) are the most common approaches [13]. CZM stands out as the most applied technique and provides accurate strength predictions provided that the cohesive law shape and correspondent parameters were correctly defined. Neto et al. [14] investigated failure in composite adhesive joints (unidirectional carbon-epoxy pre-preg) bonded with two adhesives with different characteristics (one brittle and one ductile). They also evaluated several overlap lengths (L_O) in experimental tests. Then, CZM was applied to predict the results obtained in the experimental data. The numerical analysis considered geometrical non-linear effects and the orthotropic properties of the composite. The shape law used to perform the analysis was triangular. The results obtained from the numerical simulations with CZM were considered satisfactory for the brittle adhesive, while the same accuracy was not obtained for the ductile one. The authors concluded that the triangular law was not the best choice for the ductile adhesive since its behaviour resembles a trapezium shape. Even so, failure initiation and propagation were simulated by the model. More recently, Teimouri et al. [15] evaluated a trilinear cohesive law to simulate mode I fatigue delamination in composites undergoing large-scale fibre bridging. This model was constructed by overlapping two bilinear CZMs. The authors developed Abaqus subroutines and conducted FEM analysis to 3D Double Cantilever Beams (DCB) under high-cycle fatigue loading to implement these models. They found that this approach presents more accuracy than the bilinear models.

Another approach widely studied is fracture mechanics since it allows to assess discontinuities in materials, such as re-entrant corners at adhesive-adherend interface or defects [13]. The models based on this approach present typically on Stress Intensity Factors (SIF) or energetic concepts, such as the J-integral [16] or the Virtual Crack Closure Technique [17]. A SIF analysis permits to analyse the discontinuity via stresses and strains, while an energetic analysis relies on the amount of energy necessary to overcome material resistance [18]. In 2002, Leguillon [19] introduced the Finite Fracture Mechanics (FFM) technique that combines SIF with energetic principles. This method does not require an initial crack. In simple terms, a certain amount of energy is necessary to open the crack and sufficient stress to damage the material. In 2021, Fernandes et al. [20] investigated the fracture onset and crack deflection in multi-material adhesive

joints with thick bond lines (≈10 mm) under global mode I loading. They tested single-material (steel-steel and Glass Fibre Reinforced Polymer (GRFP)-GFRP) and multi-material (GFRP-GFRP) DCB joints bonded with a structural epoxy adhesive. The authors modelled the joints analytically, resorting to Kanninen model [21] considering an elastic-plastic beam and relied on FEM. They found an empirical relation defining the transition between non-cohesive and cohesive fracture onset. They also observed that the magnitude of the stress singularity at the pre-crack tip is superior to the one nearby the bi-material corners when the pre-crack length exceeds a specific value. Nonetheless, the crack propagation suddenly changes direction out of the adhesive mid-thickness, explained by the positive *T*-stresses along the crack tip.

Most adhesive joints have interface corners between the adhesive and the adherends that originate stress singularities. These stress singularities are often the initial point of failure in adhesive joints, so it is important to study and characterize them. To that end, the Intensity of Singular Stress Fields (ISSF), also known as General Stress Intensity Factor (GSIF), can be used. The ISSF is applicable to a variety of corner configurations with multiple materials, but depending on the material types, it can be formulated differently. The simplest scenario is when all the materials in the corner are isotropic, and the earliest works on the ISSF were focused on this case [22, 23]. Later, some authors also began to show interest in analysing the ISSF in corners made of only anisotropic materials, and one of the earliest examples of this approach is the work of Delale [24], with posterior examples found in references [25, 26], whose ISSF analysis is based on the Stroh formalism [27]. Yao et al. [28] presented an alternative way to perform this analysis based on the elastic governing equations and the asymptotic expansions of displacement and stress near the notch tip. Corners with both types of materials, isotropic and anisotropic, present the most challenging ISSF analysis. Ting and Chyanbin [29] proposed an adaptation of the Stroh formalism that could solve this problem, paving the way for the works of Barroso et al. [30, 31] and the current work that is based on this adaptation.

This work aims to evaluate the ISSF criterion on orthotropic materials. Single-Lap Joints (SLJ) made from Carbon Fibre Reinforced Polymer (CFRP) bonded with a brittle adhesive (Araldite AV-138) were used. To assess the influence of L_O on the experimental results, eight L_O were applied, starting at 10 mm and incrementing it 10 mm each time. Firstly, the experimental data, namely the maximum loads sustained by the joints, are analysed. Then, the modelling conditions and ISSF formulation are presented. Next, to strength predict the joints, the ISSF criterion is applied using FEM. Finally, the experimental data are compared to the numerical strength predictions to evaluate the accuracy of the criterion tested.

3.3.2 Experimental details

3.3.2.1 SLJ geometry and dimensions

The SLJ tested in this work for validation purposes are composed of CFRP adherends and the brittle adhesive Araldite® AV138. The base SLJ geometry and respective dimensional parameters are depicted in Figure 3.3.1. The relevant parameters, which fully define the SLJ geometry, are (in mm): $10<L_O<80$ (in intervals of 10), unsupported length (between testing grips) L_T=200, adherend thickness t_P=2.4, adhesive thickness t_A=0.2 and width B=15 (not shown in the figure). The boundary conditions presented in Figure 3.3.1 aim to emulate the gripping conditions in the testing machine and consists of fixing the left edge and pulling the right edge while restraining it transversely.

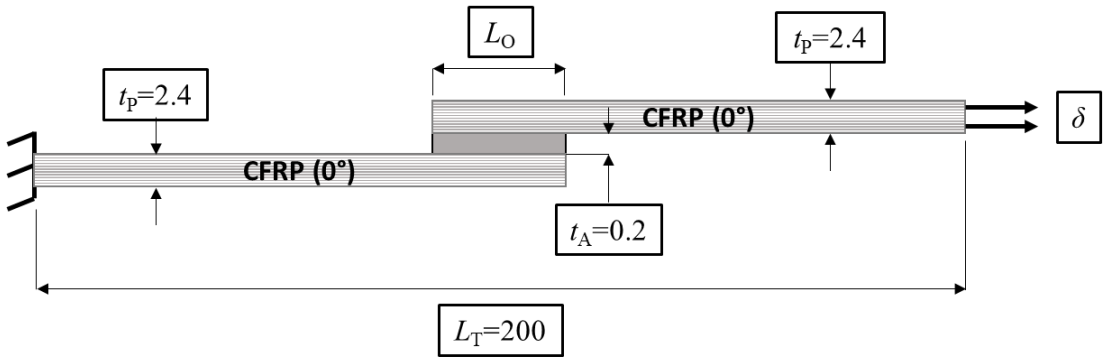

Figure 3.3.1 - SLJ geometry and respective dimensional parameters (in mm)

3.3.2.2 CFRP adherends and adhesive

The SLJs are made of CFRP adherends, using unidirectional pre-preg from SEAL® (Texipreg HS 160 RM; Legnano, Italy) to produce unidirectional laminates with a ply unit thickness of 0.15 mm. These adherends were cut from large plates with 300×300 mm^2 into small specimens. The bulk plates were produced by manual stacking and consolidation, considering a total of 20 plies, followed by one-hour curing in a hot-plates press with a temperature of 130 ºC and holding pressure of 2 bar. According to the manufacturer, for these working conditions (ply thickness, temperature and pressure), the fibre volume fraction is approximately 64%, and nearly null porosity content is guaranteed. Table 3.3.1 presents the elastic properties of a unidirectional lamina, modelled as elastic orthotropic in the FEM analysis [32].

Table 3.3.1 - Elastic constants of a unit ply with fibres along the x axis (y and z are the transverse and thickness directions, respectively) [32]

E_x=1.09E+05 MPa	ν_{xy}=0.342	G_{xy}=4315 MPa
E_y=8819 MPa	ν_{xz}=0.342	G_{xz}=4315 MPa
E_z=8819 MPa	ν_{yz}=0.380	G_{yz}=3200 MPa

Validation of the ISSF technique was accomplished in composite joints bonded using the two-part structural epoxy adhesive Araldite® AV138, which is one of the strongest from

this family of Araldite® adhesives although it is brittle. Actually, its tensile strength is nearly 40 MPa, but the tensile stress-tensile strain (σ-ε) behaviour up to failure is linear. This feature, associated with its high stiffness, leads to limitations regarding its application to bonded joints, which most often experience large stress concentrations (for example, at the overlap edges for SLJ [33]), resulting in premature failure at those sites. However, for short L_O, these adhesives typically behave better and can compete with more ductile adhesives due to the more uniform stress distributions in the elastic regime, which enables an efficient load transfer [34]. This adhesive was duly tested in former works [35], leading to the acquired average±deviation data presented in Table 3.3.2.

Table 3.3.2 - Mechanical properties of the adhesive [35]

Properties	AV 138
E (GPa)	4.89±0.81
v	0.35[1]
σ_y (MPa)	36.49±2.47
σ_f (MPa)	39.45±3.18
ε_f (%)	1.21±0.10
G (GPa)	1.56±0.01
τ_y (MPa)	25.1±0.33
τ_f (MPa)	30.2±0.40
γ_f (%)	7.8±0.7

[1] Data from the manufacturer.

On the one hand, tensile tests of adhesive bulk specimens (dogbone shape) allowed to estimate the relevant tensile data: Young's modulus (E), tensile yield stress (σ_y), tensile strength (σ_f) and tensile failure strain (ε_f). These specimens were fabricated as per the NF T 76-142 French standard, i.e., by mould injection, to produce high-quality and void-free specimens. A sample tensile stress-tensile strain (σ-ε) curve for this adhesive is presented in the mentioned work [35]. On the other hand, the shear properties of the adhesive, such as the shear modulus (G), shear yield stress (τ_y), shear strength (τ_f) and shear failure strain (γ_f), were taken from Thick Adherend Shear Tests (TAST) performed to thin adhesive layers. The specimens' fabrication and testing followed the recommendations of the ISO 11003-2:1999 standard. To comply with this standard, an alignment jig was fabricated to guarantee both longitudinal and transversal alignment and ensure the required bond length of 5 mm. The adherends were made of DIN C45E steel to promote the necessary stiffness, and thus to prevent adherend deformations to affect the stiffness measurements. All collected data is presented in Table 3.3.2.

3.3.2.3 *Joint production and testing*

The use of robust experimental procedures is essential for the accuracy of the obtained results and the robustness of the numerical validation processes. Fabrication of the CFRP SLJ was initiated by fabricating composite plates with a dimension of 300×300 mm^2, followed by cutting the adherends in a diamond disc table to their final dimensions. The plates were fabricated by hand lay-up up to reaching the $[0]_{16}$ configuration, followed by curing with temperature (130ºC) and pressure (2 bar) in a hot-plates press. Before the bonding process, the relevant surfaces were abraded with 320 grit sandpaper to remove the outer layer, improve the roughness and activate the surfaces, followed by cleaning with acetone to remove any contaminants and abraded particles [36]. SLJ assembly took place in a specific steel jig, composed of two plates: the lower one for the specimens' alignment and the upper one for pressure application. By using a set of spacers, it was possible to assure the correct t_A. Parallel to adherend bonding, end tabs were also bonded in place to enable centred gripping in the testing machine. After the adherends/spacers were set in place, the upper mould's plate squeezed the entire set, and the joints were left to cure for one week at room temperature and humidity. Finally, the specimens were demoulded and the resulting adhesive excess at the overlap boundaries removed by milling. The SLJs were tested under identical environmental conditions in a Shimadzu AG-X 100 electro-mechanical tester with a 1 mm/min velocity. The P-δ data was taken from a 100 kN load cell to measure P and from the grips' displacement for δ. Each joint configuration, defined by the respective L_O, was tested five times to produce representative results.

3.3.3 Numerical analysis

3.3.3.1 *Composite ISSF formulation*

The ISSF criterion is a fracture mechanics-based approach to evaluate discontinuities in single and multi-materials corners. In the case studied in this work, bi-material interface corners can be found in SLJ, such as those from Figure 3.3.2.

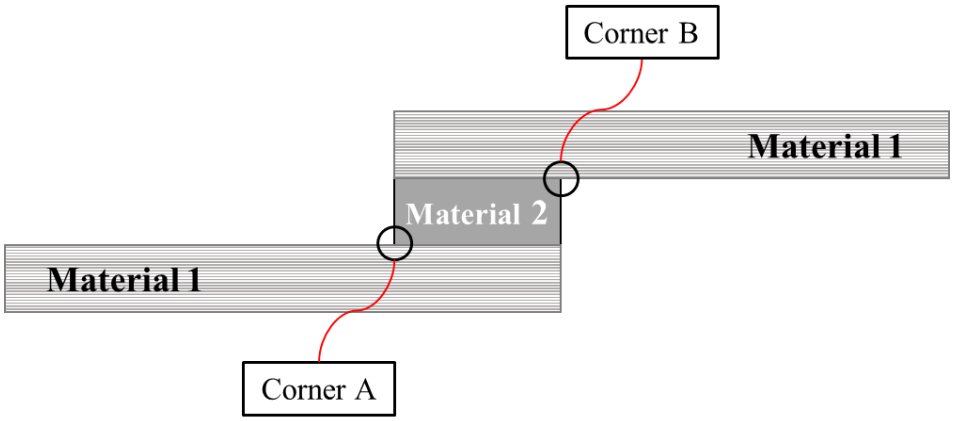

Figure 3.3.2 - Bi-material interface corners found in a SLJ

Since composite materials are considered in this investigation, a different formulation is required for the ISSF criterion. Thus, the following formulation considers the peculiarities of these materials and it is based on the references [30, 37]. In a three-dimensional Cartesian coordinate system, the constitutive law of a material can be defined as $\boldsymbol{\sigma} = \boldsymbol{C}\boldsymbol{\varepsilon}$, where $\boldsymbol{C}$ is the material constitutive matrix defined as follows:

$$\boldsymbol{C}^{-1} = \begin{bmatrix} \frac{1}{E_1} & -\frac{\nu_{12}}{E_1} & -\frac{\nu_{13}}{E_1} & 0 & 0 & 0 \\ -\frac{\nu_{21}}{E_2} & \frac{1}{E_2} & -\frac{\nu_{23}}{E_2} & 0 & 0 & 0 \\ -\frac{\nu_{31}}{E_3} & -\frac{\nu_{32}}{E_3} & \frac{1}{E_3} & 0 & 0 & 0 \\ 0 & 0 & 0 & \frac{1}{G_{23}} & 0 & 0 \\ 0 & 0 & 0 & 0 & \frac{1}{G_{13}} & 0 \\ 0 & 0 & 0 & 0 & 0 & \frac{1}{G_{12}} \end{bmatrix}, \tag{1}$$

and $\boldsymbol{\sigma}$ and $\boldsymbol{\varepsilon}$ are the stress and strain vectors, respectively, in Voigt notation. Here E is Young's modulus, ν is the Poisson's ratio and G is the shear modulus. As $\boldsymbol{C}$ is symmetric, the following conditions must be verified: $\nu_{12}/E_1 = \nu_{21}/E_2$, $\nu_{23}/E_2 = \nu_{32}/E_3$ and $\nu_{13}/E_1 = \nu_{31}/E_3$. The Stroh formalism [38] is defined by the following eigensystem:

$$\boldsymbol{N}\boldsymbol{\xi}_\alpha = p_\alpha \boldsymbol{\xi}_\alpha, \tag{2}$$

where p_α are the eigenvalues and $\boldsymbol{\xi}_\alpha$ are the eigenvectors of the system. In total, this system has 6 eigenvectors and eigenvalues since $\boldsymbol{N}$ is a 6×6 matrix, defined as:

$$N = \begin{bmatrix} \boldsymbol{N}_1 & \boldsymbol{N}_2 \\ \boldsymbol{N}_3 & \boldsymbol{N}_1^T \end{bmatrix}, \tag{3}$$

where $\boldsymbol{N}_1 = -\boldsymbol{T}^{-1}\boldsymbol{R}^T$, $\boldsymbol{N}_2 = -\boldsymbol{T}^{-1}$ and $\boldsymbol{N}_3 = \boldsymbol{R}\boldsymbol{T}^{-1}\boldsymbol{R}^T - \boldsymbol{Q}$, and:

$$\boldsymbol{Q} = \begin{bmatrix} C_{11} & C_{16} & C_{15} \\ C_{16} & C_{66} & C_{56} \\ C_{15} & C_{56} & C_{55} \end{bmatrix}; \quad \boldsymbol{R} = \begin{bmatrix} C_{16} & C_{12} & C_{14} \\ C_{66} & C_{26} & C_{46} \\ C_{56} & C_{25} & C_{45} \end{bmatrix}; \quad \boldsymbol{T} = \begin{bmatrix} C_{66} & C_{26} & C_{46} \\ C_{26} & C_{22} & C_{24} \\ C_{46} & C_{24} & C_{44} \end{bmatrix}. \tag{4}$$

The results of this eigensystem are complex. Thus, for a p_α and $\boldsymbol{\xi}_\alpha$ pair that satisfies equation (2), its complex conjugate $\bar{p}_\alpha$ and $\bar{\boldsymbol{\xi}}_\alpha$ will satisfy it too. Each eigenvector can be separated into two parts, $\boldsymbol{\xi}_\alpha^T = [\boldsymbol{a}_\alpha^T \quad \boldsymbol{b}_\alpha^T]$, being $\boldsymbol{a}_\alpha$ proportional to the displacement vector and $\boldsymbol{b}_\alpha$ proportional to the traction vector. Depending on the material properties, the number of eigenvalues and eigenvectors changes. For transversely isotropic materials, like unidirectional fibre-reinforced polymers, there are three different

eigenvalues and eigenvectors. However, for isotropic materials, as adhesives generally are, there is only one eigenvalue $p = i$, and its complex conjugate $\bar{p} = -i$, and two linearly independent eigenvectors. Therefore, in the latter case, a modification to the Stroh formalism is required, so equation (2) is changed to:

$$\boldsymbol{N}\boldsymbol{\xi}_1 = p\boldsymbol{\xi}_1 \;;\; \boldsymbol{N}\boldsymbol{\xi}_2 = p\boldsymbol{\xi}_2 + \boldsymbol{\xi}_1 \;;\; \boldsymbol{N}\boldsymbol{\xi}_3 = p\boldsymbol{\xi}_3, \tag{5}$$

which means that $\boldsymbol{\xi}_1$ and $\boldsymbol{\xi}_3$ can be determined solving the original eigensystem, but $\boldsymbol{\xi}_2^T = [\boldsymbol{a}_2^T \quad \boldsymbol{b}_2^T]$ is determined as follows:

$$-\left[\boldsymbol{Q} + \left(\boldsymbol{R} + \boldsymbol{R}^T\right)p + \boldsymbol{T}p^2\right]\boldsymbol{a}_2 = \left(2p\boldsymbol{T} + \boldsymbol{R} + \boldsymbol{R}^T\right)\boldsymbol{a}_1 \tag{6}$$

$$\boldsymbol{b}_2 = T\boldsymbol{a}_1 + \left(\boldsymbol{R}^T + p\boldsymbol{T}\right)\boldsymbol{a}_2 . \tag{7}$$

A vector $\boldsymbol{w}(r,\theta)^T = [\boldsymbol{u}(r,\theta)^T \quad \boldsymbol{\varphi}(r,\theta)^T]$, where $\boldsymbol{u}$ is the displacement vector and $\boldsymbol{\varphi}$ is the stress function vector, can be defined as:

$$w(r,\theta) = r^{\lambda} XZv , \tag{8}$$

where $\boldsymbol{v}$ is a constant vector, $\mathbf{X} = [\boldsymbol{\xi}_1 \quad \boldsymbol{\xi}_2 \quad \boldsymbol{\xi}_3 \quad \bar{\boldsymbol{\xi}}_1 \quad \bar{\boldsymbol{\xi}}_2 \quad \bar{\boldsymbol{\xi}}_3]$ and $\boldsymbol{Z}$ is determined in different ways depending on the number of linearly independent eigenvectors and eigenvalues. Thus, for three linearly independent eigenvectors and three eigenvalues:

$$Z(\theta) = \begin{bmatrix} \left\langle \zeta_{\alpha}^{\lambda}(\theta) \right\rangle & 0_{3\times3} \\ 0_{3\times3} & \left\langle \bar{\zeta}_{\alpha}^{\lambda}(\theta) \right\rangle \end{bmatrix}, \tag{9}$$

where angle brackets represent diagonal matrices. For two linearly independent eigenvectors and one eigenvalue, $\mathbf{Z}$ is also dependent on λ and it is defined as:

$$Z(\theta,\lambda) = \begin{bmatrix} \boldsymbol{\Psi}(\theta,\lambda) & 0_{3\times3} \\ 0_{3\times3} & \bar{\boldsymbol{\Psi}}(\theta,\lambda) \end{bmatrix}, \tag{10}$$

with:

$$\boldsymbol{\Psi}^{\lambda}(\theta) = \begin{bmatrix} \zeta^{\lambda}(\theta) & K(\theta,\lambda)\zeta^{\lambda}(\theta) & 0 \\ 0 & \zeta^{\lambda}(\theta) & 0 \\ 0 & 0 & \zeta^{\lambda}(\theta) \end{bmatrix}, \tag{11}$$

being $K(\theta,\lambda) = \lambda \sin(\theta)/\zeta(\theta)$ and $\zeta_{\alpha}^{\lambda}(\theta) = [\cos(\theta) + p_{\alpha}\sin(\theta)]^{\lambda}$.

Considering a material *m* in a bi-material wedge, defined by an initial angle θ_{m-1} and an end angle θ_m, the following relation can be established:

$$w(r,\theta_m) = E(\lambda,\theta_m,\theta_{m-1})\,w(r,\theta_{m-1}), \tag{12}$$

being:

$$E\left(\lambda,\theta_m,\theta_{m-1}\right)=X\boldsymbol{Z}^{\lambda}\left(\theta_m\right)\left[\boldsymbol{Z}^{\lambda}\left(\theta_{m-1}\right)\right]^{-1}\boldsymbol{X}^{-1}, \tag{13}$$

where $\boldsymbol{Z}^{\lambda}(\theta_m)\left[\boldsymbol{Z}^{\lambda}(\theta_{m-1})\right]^{-1}$ can be simplified to $\boldsymbol{Z}^{\lambda}(\theta_m,\theta_{m-1})$, which is also dependent on the number of linearly independent eigenvectors and eigenvalues. As a result, for three linearly independent eigenvectors and three eigenvalues, it can be written:

$$\boldsymbol{Z}^{\lambda}\left(\theta_m,\theta_{m-1}\right)=\begin{bmatrix}\left\langle\zeta_{\alpha}^{\lambda}\left(\theta_m,\theta_{m-1}\right)\right\rangle & 0_{3\times3}\\ 0_{3\times3} & \left\langle\bar{\zeta}_{\alpha}^{\lambda}\left(\theta_m,\theta_{m-1}\right)\right\rangle\end{bmatrix}, \tag{14}$$

while for two linearly independent eigenvectors and one eigenvalue, $\boldsymbol{Z}$ is also dependent on λ and it is defined as:

$$\boldsymbol{Z}^{\lambda}\left(\theta_m,\theta_{m-1},\lambda\right)=\begin{bmatrix}\boldsymbol{\Psi}\left(\theta_m,\theta_{m-1},\lambda\right) & 0_{3\times3}\\ 0_{3\times3} & \bar{\boldsymbol{\Psi}}\left(\theta_m,\theta_{m-1},\lambda\right)\end{bmatrix}, \tag{15}$$

with:

$$\Psi\left(\theta_m,\theta_{m-1},\lambda\right)=\begin{bmatrix}\zeta^{\lambda}\left(\theta_m,\theta_{m-1}\right) & K\left(\theta_m,\theta_{m-1},\lambda\right)\zeta^{\lambda}\left(\theta_m,\theta_{m-1}\right) & 0\\ 0 & \zeta^{\lambda}\left(\theta_m,\theta_{m-1}\right) & 0\\ 0 & 0 & \zeta^{\lambda}\left(\theta_m,\theta_{m-1}\right)\end{bmatrix}, \tag{16}$$

being $\zeta_{\alpha}(\theta_m,\theta_{m-1})=\zeta_{\alpha}(\theta_m)/\zeta_{\alpha}(\theta_{m-1})$ and:

$$K\left(\theta_m,\theta_{m-1},\lambda\right)=\frac{\lambda\sin\left(\theta_m-\theta_{m-1}\right)}{\zeta\left(\theta_m\right)\zeta\left(\theta_{m-1}\right)}. \tag{17}$$

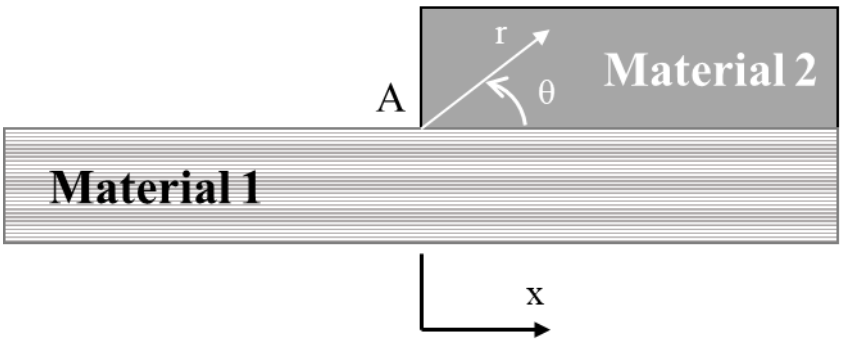

Figure 3.3.3 - Wedge corner in a bi-material interface

In a wedge made of two perfectly bonded materials, as shown in Figure 3.3.3, it is possible to relate $\boldsymbol{w}(r,\theta_0)$ with $\boldsymbol{w}(r,\theta_2)$. If $\boldsymbol{w}(r,\theta_1)=\boldsymbol{E}(\lambda,\theta_1,\theta_0)\boldsymbol{w}(r,\theta_0)$ and $\boldsymbol{w}(r,\theta_2)=\boldsymbol{E}(\lambda,\theta_2,\theta_1)\boldsymbol{w}(r,\theta_1)$, then:

$$w\left(r,\theta_2\right)=\boldsymbol{K}_W\left(\lambda\right)w\left(r,\theta_0\right), \tag{18}$$

being $\boldsymbol{K}_W(\lambda) = \boldsymbol{E}(\lambda, \theta_2, \theta_1)\boldsymbol{E}(\lambda, \theta_1, \theta_0)$ called the transfer matrix. Afterwards, it is necessary to impose boundary conditions to $\boldsymbol{K}_W$. In adhesive joints, the outer faces of the interface wedge are free.

Now it is necessary to impose the boundary conditions. In adhesive joints, both outer faces of the interface wedge are free. Thus, $\boldsymbol{\varphi}(r, \theta_0) = \boldsymbol{\varphi}(r, \theta_2) = 0$ must be imposed, and the following boundary condition matrices are used:

$$\boldsymbol{D}_0 = \boldsymbol{D}_2 = \begin{bmatrix} 0_{3\times3} & \mathbf{I}_{3\times3} \\ \mathbf{I}_{3\times3} & 0_{3\times3} \end{bmatrix}. \tag{19}$$

These boundary condition matrices are used to modify the transfer matrix:

$$\boldsymbol{K}_{WBC}(\lambda) = \boldsymbol{D}_2 \boldsymbol{K}_W \boldsymbol{D}_0^T . \tag{20}$$

Considering the boundary conditions, the system of equations is rewritten as:

$$\begin{bmatrix} 0_{3\times1} \\ \boldsymbol{u}(r, \theta_2) \end{bmatrix} = \begin{bmatrix} \boldsymbol{K}_{WBC}^{(1)}(\lambda) & \boldsymbol{K}_{WBC}^{(2)}(\lambda) \\ \boldsymbol{K}_{WBC}^{(3)}(\lambda) & \boldsymbol{K}_{WBC}^{(4)}(\lambda) \end{bmatrix} \begin{bmatrix} 0_{3\times1} \\ \boldsymbol{u}(r, \theta_0) \end{bmatrix}. \tag{21}$$

From equation (21), the following is verified $\mathbf{0}_{3\times1} = \boldsymbol{K}_{WBC}^{(2)}(\lambda)\boldsymbol{u}(r, \theta_0)$. Therefore, a non-trivial solution is found if and only if:

$$\left|\boldsymbol{K}_{WBC}^{(2)}(\lambda)\right| = 0 . \tag{22}$$

The solutions to equation (22) are the characteristic exponents of the bi-material corner (λ). There is an infinite number of solutions to equation (22) but, near the corner, the singularities λ<1 overwhelm the other λ since they are the solutions that produce the singularity. Thus, only λ<1 are considered in the current study. With λ determined, the next step is the calculation of the stress and displacement around the interface corner. So, for a given angle (θ) inside a material (m), the polar stress components can be defined as:

$$\begin{gathered} f_{rr} = -\boldsymbol{s}_r^T(\theta)\boldsymbol{\varphi}_{,\theta}(r, \theta)/r;\ f_{\theta\theta} = \boldsymbol{n}^T(\theta)\boldsymbol{\varphi}_{,r}(r, \theta); \\ f_{r\theta} = -\boldsymbol{n}^T(\theta)\boldsymbol{\varphi}_{,\theta}(r, \theta)/r = \boldsymbol{s}_r^T(\theta)\boldsymbol{\varphi}_{,r}(r, \theta) \end{gathered}, \tag{23}$$

while the displacements are defined as:

$$g_r = -\boldsymbol{s}_r^T(\theta)\boldsymbol{u}(r, \theta)/r;\quad g_\theta = \boldsymbol{n}^T(\theta)u(r, \theta), \tag{24}$$

where $\boldsymbol{s}_r^T = [\cos(\theta) \quad \sin(\theta) \quad 0]$ and $\boldsymbol{n}^T = [\sin(\theta) \quad -\cos(\theta) \quad 0]$. To determine the components in equations (23) and (24), it is first necessary to determine $\boldsymbol{w}(r, \theta_0)$ and $\boldsymbol{w}(r, \theta_1)$ for each λ. Due to the boundary conditions, $\boldsymbol{\varphi}(r, \theta_0) = \mathbf{0}_{3\times1}$ and $\boldsymbol{u}(r, \theta_0)$ is determined by solving $\mathbf{0}_{3\times1} = \boldsymbol{K}_{WBC}^{(2)}(\lambda)\boldsymbol{u}(r, \theta_0)$, as it can be inferred from equation (21). Therefore, $\boldsymbol{w}(r, \theta_0)^T = [\boldsymbol{u}(r, \theta_0)^T \quad \boldsymbol{\varphi}(r, \theta_0)^T]$. Having determined $\boldsymbol{w}(r, \theta_0)$,

$\boldsymbol{w}(r,\theta_1)$ is determined by simply using equation (12). Then, equation (12) can be used to determine $\boldsymbol{w}(r,\theta)$ and its derivatives, needed for equations (23) and (24), for each λ in a material *m*, by substituting θ_m by θ. It is important to note that the components of equations (23) and (24) have to be standardized since if $\boldsymbol{w}(r,\theta_0)$ is a solution so is $c\boldsymbol{w}(r,\theta_0)$, where c is any constant, i.e. there are infinite solutions to this problem. In the current work, this standardization was performed by analysing f_{ij} and g_i around the whole interface corner, finding the maximum value of any component, and then dividing f_{ij} and g_i by that maximum value. Ensuring that f_{ij} and g_i are at most equal to 1.

Knowing the singularity exponents (λ) and the stress (*f*) and displacement (*g*) functions, it is possible to define the stress and displacement near the singularity as:

$$\sigma_{ij} = \sum_{k=1}^{n} H_k r^{\lambda_k - 1} f_{ij}\left(\lambda_k, \theta\right), \tag{25}$$

$$u_j = \sum_{k=1}^{n} H_k r^{\lambda_k} g_j\left(\lambda_k, \theta\right), \tag{26}$$

being *n* the number of singularity exponents (λ), which is dependent on the geometry and materials of the interface corner. H_k is the ISSF, or GSIF, which is a scalar value related to the singularity component *k*.

There are different alternatives to determine the ISSF. For example, Qian and Akisanya [39] used a line integral encircling the interface corner to determine the ISSF. However, in the current work, another method was used to determine the ISSF. The method used is based on the extrapolation of the ISSF from values near the corner to the corner. A similar method was used by Klusák et al. [40]. A *n* number of points at different angles (θ) and at a fixed radius (*r*) are needed to perform this extrapolation, e.g., if there are two singularity components λ_1 and λ_2, then two different angles are needed. So, for a radius *r,* ***H*** can be determined with the following equation:

$$\begin{bmatrix} r^{\lambda_1-1} f_{\theta\theta}\left(\lambda_1, \theta_{n+1}\right) & \cdots & r^{\lambda_n-1} f_{\theta\theta}\left(\lambda_n, \theta_{n+1}\right) \\ \vdots & \ddots & \vdots \\ r^{\lambda_1-1} f_{\theta\theta}\left(\lambda_1, \theta_{n+n}\right) & \cdots & r^{\lambda_n-1} f_{\theta\theta}\left(\lambda_n, \theta_{n+n}\right) \end{bmatrix} \begin{bmatrix} H_1 \\ \vdots \\ H_n \end{bmatrix} = \begin{bmatrix} \sigma_{\theta\theta}\left(r, \theta_{n+1}\right) \\ \vdots \\ \sigma_{\theta\theta}\left(r, \theta_{n+n}\right) \end{bmatrix}. \tag{27}$$

This equation is solved for several different *r*, which allows the extrapolation to *r*=0 mm from an *r* interval where ***H*** is stable. This will be the actual ***H*** at the interface corner.

3.3.3.2 Model preparation and processing

Eight meshes were created for each different L_O to perform the FE Analysis (FEA). However, in the vicinity of the interface corners, the meshes were all equal (Figure 3.3.4 (a)). The dimensions and boundary conditions presented in Figure 3.3.4 (b) were used to create the meshes. The left boundary was considered fixed (U_x=U_y=U_z=0), while δ was imposed in the right boundary. The FEA was performed using a custom MATLAB program developed by the authors and every element is a quadrilateral element with

four nodes. From the results obtained with the FEA, a MATLAB script was developed to apply the process described in Section 3.3.3.1 and perform the ISSF analysis, allowing the prediction of P_m values based on the ISSF at the interface corner. All simulations were made under small strains and plane strain conditions.

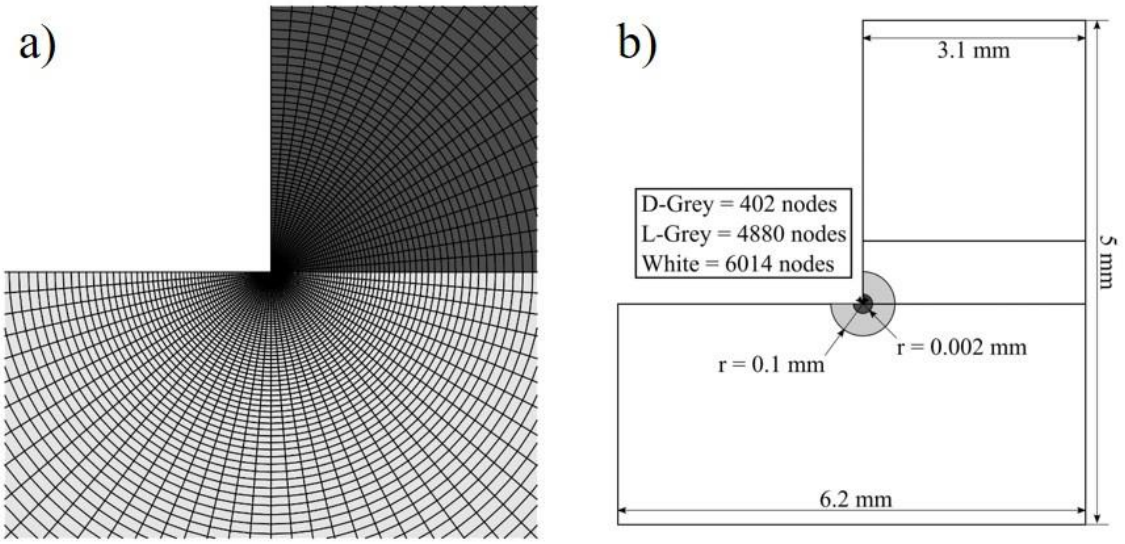

Figure 3.3.4 - Mesh applied around the interface corner: elements disposal (a) and mesh information (b)

3.3.4 Results

3.3.4.1 Test results and discussion

The experimental data and respective discussion are presented for further comparison with the ISSF predictions for validation purposes. In the SLJ experiments with the chosen adhesive, all failures were cohesive in the adhesive layer, i.e., with a visible adhesive layer on both failed surfaces throughout the entire L_O. Usually, interfacial failures are associated with poor specimen fabrication and surface preparation, and these were successfully prevented by the process described in section 3.3.2.3.

Figure 3.3.5 plots the obtained experimental data from the tests, namely the average P_m and respective minimum and maximum value as a function of L_O. It is clear that L_O influences P_m by a monotonic increase of P_m with this parameter, which is the expected behaviour given the corresponding increase of the shear-resistant bonded area of adhesive and agrees with previously published works for different adhesives, including brittle ones [35]. Nevertheless, brittle adhesives usually behave better for small L_O while failing to compete with ductile adhesives for large L_O, even if the latter present lower uniaxial strength, and the P_m-L_O tendency is only nearly proportional for the smaller L_O, up to approximately 20 mm. Actually, the relative P_m improvement between L_O=10 and 20 mm is 0.78%, compared to the theoretical 100% suggested by the duplication of area. This proportionality is quickly cancelled for higher L_O, and between L_O=10 and 80 mm, the relative improvement is only 94.13%. In absolute terms, P_m increases by 13.1 kN

between the limit L_O. The reported behaviour is associated with this adhesive's marked brittleness, as shown in the mechanical characterization of section 3.3.2.2. Owing to the clear lack of capacity to undergo plasticity, added to the known marked stress concentrations in SLJ, which increase with L_O [33], the joint performance deteriorates with higher L_O, and the strength averaged to the bonded area diminishes as well. Actually, the SLJ stresses in the adhesive layer are overstudied [41], and it usually results, under the scope of 2D modelling, in peel and shear stresses measured over a rectangular coordinate system. Due to the SLJ asymmetry, peel stresses are highly concentrated at the overlap edges while reaching small compressive portions at the inner overlap. Shear stresses present a smoother gradient but also peaking at the overlap ends. In both cases, peak stresses highly increase with L_O due to increased joint rotation (peel stresses) and shear-lag effects (shear stresses), leading to the aforementioned behaviour, i.e., clear lack of proportionally by increasing L_O.

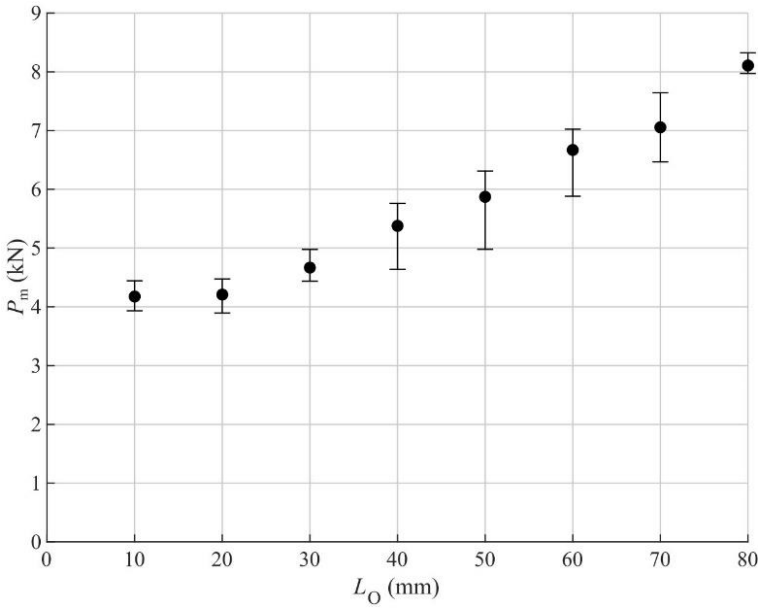

Figure 3.3.5 - Experimental P_m vs L_O data

3.3.4.2 ISSF and polar stress evaluation

The experimental data gathered allowed the start of the ISSF criterion analysis. Initially, the bi-material interface corner found in the SLJ considered was inspected. Figure 3.3.6 schematically represents the bi-material interface corner considered in the present work.

Figure 3.3.6 also shows the anti-symmetry axis considered since only one interface corner was evaluated, in this case, the lower interface corner. As shown in Figure 3.3.3, point A represents the corner tip and it is considered the centre of the polar coordinate system, from which coordinate r starts. For coordinate θ, the imaginary horizontal line intercepting the corner tip represents the baseline in which θ=0°. Considering counter clockwise rotation as positive, every positive angle is part of the adhesive while negative

angles say respect to the adherend. Thus, for discretising the corner geometry, the angles comprised by the adhesive and by the adherend were considered. For the adherend, the angles covered are in the interval-π<θ<0 rad, thus θ_0=-π rad. On the other hand, for the adhesive, the angle interval is 0<θ<π/2 rad, originating θ_2=π/2 rad. An additional angle was considered, representing the adhesive-adherend separation interface, which, in this case, is collinear to the imaginary horizontal line that intercepts point A, thus θ_1=0 rad. At this stage, the CFRP and adhesive properties were also introduced in matrix ***C*** from equation (1), as described in section 3.3.2.2.

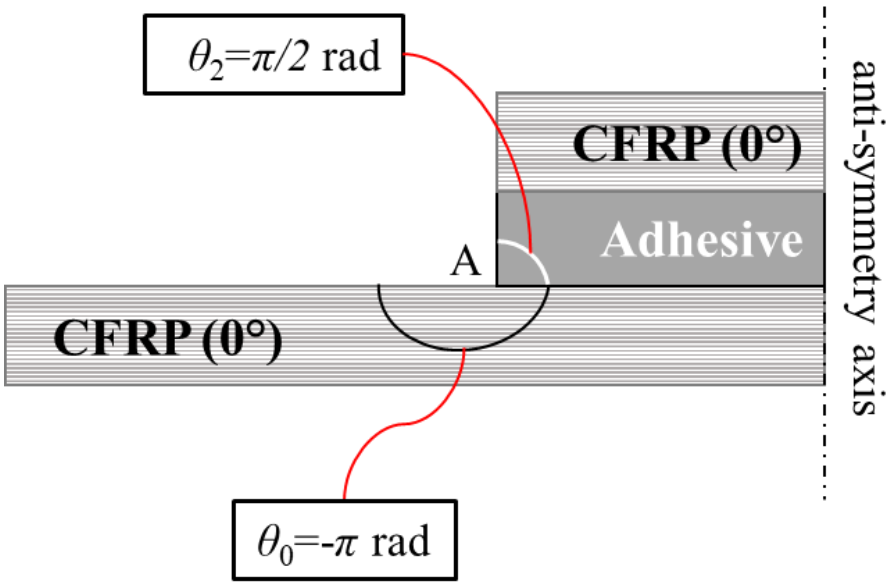

Figure 3.3.6 - Schematic representation of the bi-material interface corner considered in this work

The previous steps made the stress singularity exponents λ determination possible by solving equation (22). As described in section 3.3.3.1, the resolution of equation (22) originates an infinite number of solutions since it is a periodic function. However, only the solutions in the interval 0<λ<1 were considered for this study since they represent singular solutions. Nonetheless, the rigid body rotation solution (λ=1) and the non-singular solutions (λ>1) can also be considered, but their influence is not significant. In the studied interval, three solutions were found, with the following values: λ_1=0.6055, λ_2=0.7347 and λ_3=0.9866. Notwithstanding, the formulation presented in section 3.3.3.1 considers a three-dimensional coordinate system, contrary to the planar analysis (plane strain) imposed in this work. Therefore, λ_2 was excluded from the analysis since it represents an anti-plane solution.

The final step of the ISSF criterion was the determination of the stress singularity components *H*, resorting to equation (27). The objective was to find the components *H* at the corner tip. However, point A is defined by *r*=0 mm, thus not being possible to obtain *H* from equation (27) directly. So, the components *H* were obtained for different radius from the interface corner, in the interval 0<*r*<0.1, and then extrapolated to point A. Analysing equation (27), the $f_{\theta\theta}$ functions from the left side matrix of this equation

were attained through equation (23). This determination demanded two new angles (θ_4=π/4 rad and θ_5=-3π/4 rad) to perform the extrapolations. These angles correspond to nodes integrated within the FEM mesh modelled and were chosen based on the $\sigma_{\theta\theta}$ curves that will be presented later in this section. In that manner, one angle (θ_5) is in the ascending part of these curves and the other (θ_4) on the descending one. Additionally, one angle (θ_4) corresponds to nodes in the adhesive layer and the other (θ_5) in the adherend layer. Analysing now the right side of equation (27), the $\sigma_{\theta\theta}$ values correspond to the numerically obtained stresses from the FEM simulations in the same nodes as those used to determine $f_{\theta\theta}$. Thus, the H components are attained for the different radius. The extrapolations were performed at an interval that showed linear stability in the H-r curves obtained through the procedure described. Figure 3.3.7 presents the H_1-r curve obtained for the L_O=60 mm case. This paper only presents the H_1 component since it is the most significant to the final result. However, the procedure is the same for the H_2 component. The extrapolation for this case was performed from the interval between 0.01 and 0.02 mm. Since the nodes in this interval are extremely close to the corner tip, it was assumed that they predominantly belong to the zone of validity of this interface corner singular stress field. Figure 3.3.7 also presents H_1 extrapolations for the L_O studied in this work. These components were determined by imposing H_1 as the H_1 obtained for the L_O=60 mm case at failure displacement. Thus, the inverse procedure was performed.

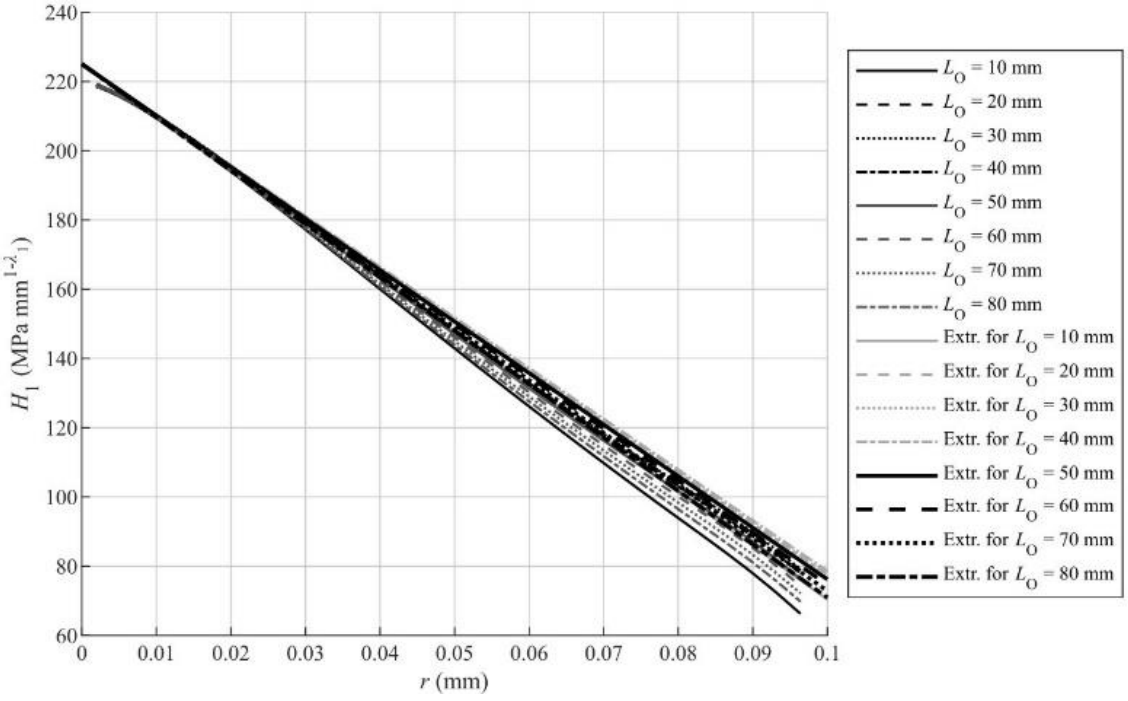

Figure 3.3.7 - H_1-r curves and extrapolations obtained for the L_O=60 mm case

In order to assess the validity of the H_1 determination procedure and understand the influence of which singularity component in the results, a comparison between the analytical and the numerical stresses was performed. The analytical stresses were

obtained from equation (25), while the numerical stresses were extracted from the FEM simulations. For an accurate analysis, the stresses were compared at a fixed radius (r=0.0022 mm) and throughout the all corner-angle interval ($-\pi<\theta<\pi/2$). Also, to compare the different L_O, the stresses were evaluated when H_1 was the same for all the L_O. Figure 3.3.8 shows the three polar stress components plots.

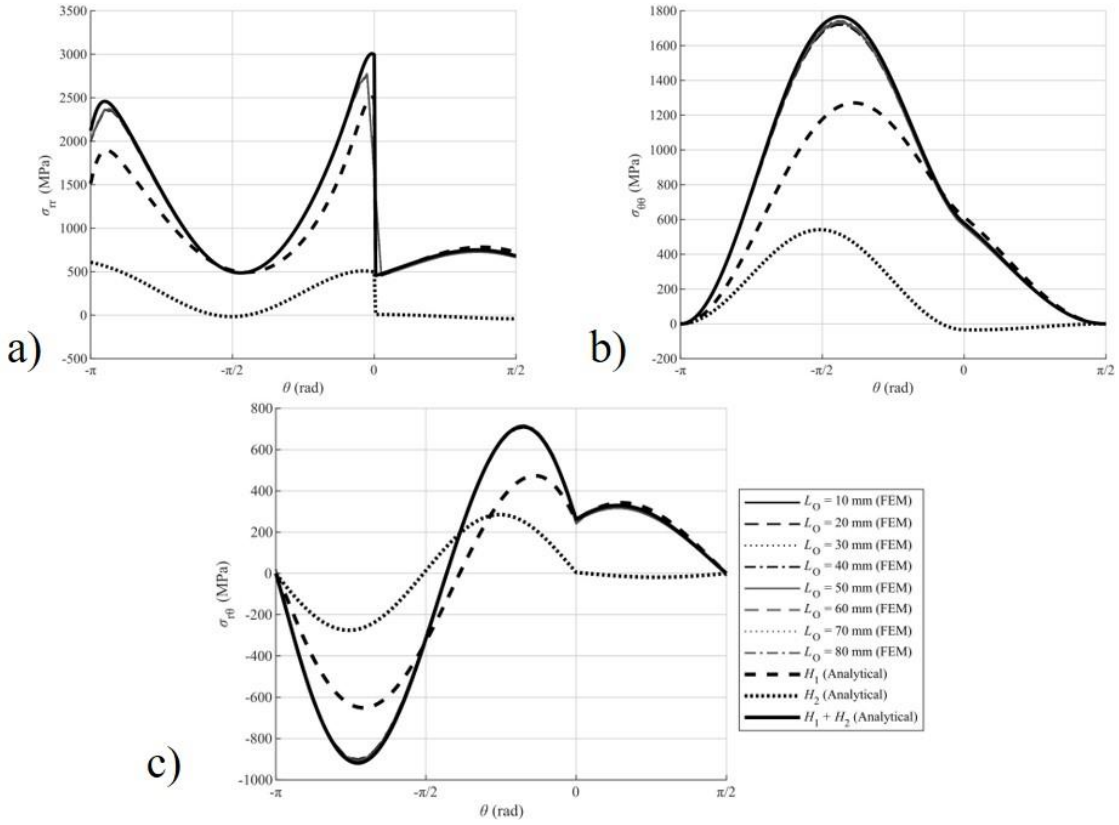

Figure 3.3.8 - Analytical and numerical polar stress components comparison: a) σ_{rr}, b) $\sigma_{\theta\theta}$ and c) $\sigma_{r\theta}$

Analysing the numerical and analytical plots for the different L_O, it is perceptible that they are very similar in the majority of the angle interval. Only minor differences are found when the curve's peak. These deviations are explained by the non-consideration of the finite stresses (or non-singular) terms in the analytical plots. However, this proves that the singular components can accurately describe the joint behaviour near the corner and validates the implemented procedure. The graphs also present the plots of the analytical stresses resultant from each singularity component separately. These curves show the more significant influence of the first singularity component H_1 in the results, justifying why only this component was analysed in this work.

3.3.4.3 ISSF-based strength analysis

As in any other mechanical criterion, the final phase of an ISSF-based analysis was the evaluation of the joint behaviour to understand if failure was achieved or not. In this case, the parameter defining failure is P_m. This parameter was already established experimentally but not numerically. For that, it was necessary to determine the critical

stress singularity components H_c. Over the years, different approaches to solve this problem were investigated and documented, such as the work of Galvez et al. [42]. This work, among others, resorted to integrals that surround all the corner area to determine H_c. But these approaches reveal extreme complexity in the implementation and require considerable computational resources. With that in mind, a more straightforward technique of determining H_c was used in this work that combines experimental and numerical data. The procedure is the same as described in section 3.3.4.2. The only difference from a regular ISSF analysis is that the imposed load of the FEM numerical simulation was the P_m experimentally determined for each L_O. This detail leads to the determination of H values that, in this case, were used as the H_c values for each L_O. Actually, Figure 3.3.7 plot was attained considering this condition for the L_O=60 mm case. Thus, the value found when the extrapolation intercepted the y-axis (r=0 mm) was used as H_{1c} for this L_O. This procedure was repeated for all L_O, resulting in the values presented in Table 3.3.3.

Table 3.3.3 - H_{1c} values determined for each L_O

L_O used to determine H_{1c} (mm)	H_{1c} (MPa.mm$^{1-\lambda}$)
10	185.59
20	181.48
30	189.48
40	205.46
50	210.96
60	225.05
70	223.27
80	240.29

Then, as explained in the previous section, each one of these H_{1c} was imposed for the other L_O, and the stresses and, consequently, the predicted P_m values were attained from the extrapolations. This process permitted to obtain strength predictions for each L_O based on each H_{1c}, which was considerably easier to implement. Figure 3.3.9 displays the strength predictions accomplished.

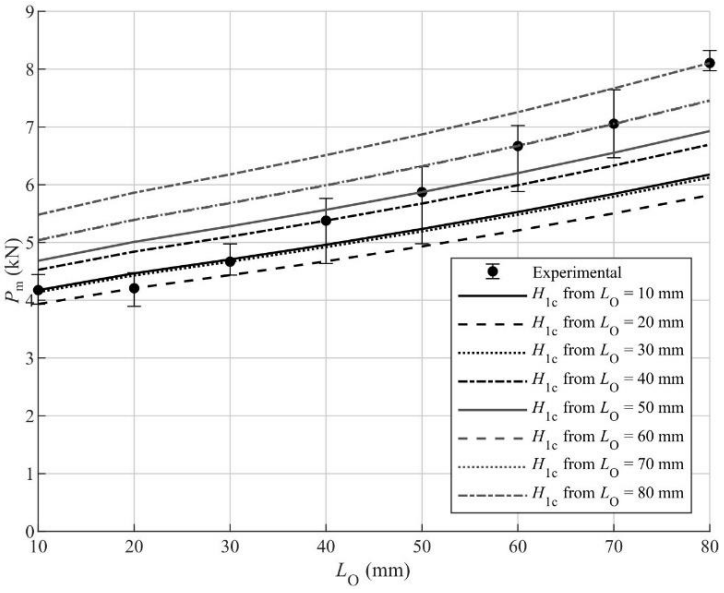

Figure 3.3.9 - Strength predictions for each L_O using each H_{1c}

A detailed analysis of this graph reveals that the strength increases between L_O resultant from each H_{1c} prediction are, generally, smaller than those verified through the experimental values. This behaviour is not verified only between two L_O (10 and 20 mm), where the experimental strength increase observed is 32.47 N while the predicted ones round between 288.25 and 381.55 N. This is clearly an anomaly related to the experimental P_m value for L_O=10 mm, which does not follow the proportional tendency of the rest of the P_m values. Therefore, the strength predictions performed with this L_O can be considered flawed, even leading to predictions superior to those observed for L_O=20 mm and L_O=30 mm. Nonetheless, the remaining strength predictions confirm that if this value were correct, it would follow the same trend.

Regarding the accuracy of the strength predictions, it is possible to state that the greater the difference between the L_O of the prediction and the one used to determine H_{1c}, the greater the difference between the prediction and the experimental P_m. This observation is proved, for example, when L_O=20 mm was used for the prediction of the joint with L_O=80 mm, where a 2287.22 N difference was found, which corresponds to an error of 28.22%. Yet, if using L_O=30 mm to predict the same joint, the error reduces to 24.45%, equivalent to a 3.76% error reduction. On the other hand, if an L_O closer to the L_O used to determine H_{1c} is used, i.e., if the predicted joint L_O has an absolute deviation of 40 mm (±20 mm) from the L_O used to perform the prediction, the percentual deviation diminishes considerably. Considering the same case presented before, and now using L_O=70 mm to predict the L_O=80 mm joint, the difference found was 646.96 N, resulting in a percentual deviation of 7.98% relative to the experimental value. Obviously, these behaviours were not found for strength predictions resorting to L_O=10 mm, due to the already discussed anomaly.

Finally, it is also discernible that when predicting the strength of an L_O larger than the one used to determine H_{1c}, the result is always an underprediction, while the inverse behaviour is also verifiable, i.e. when predicting the strength of an L_O smaller than the one used to determine H_{1c}, an over-prediction is always attained. Besides the L_O=10 mm case, this situation does not occur only in another case: between L_O=60 mm and L_O=70 mm. Here, the strength predictions found were so similar that a peculiarity arose. Namely, the strength predictions obtained with L_O=60 mm showed to be higher than those found for L_O=70 mm, which can be explained by the geometrical properties of these joints and the stresses found when solving the ISSF criterion and numerical simulations.

3.3.5 Conclusions

The work presented in this paper intended to propose and evaluate a new method for the determination of critical stress singularities, necessary to the ISSF criterion applied to composite adhesive joints. With that purpose, initially, experimental tests were performed to SLJ made from CFRP bonded with a brittle adhesive and with eight different L_O. The experimental data collected from the tests was treated and the average maximum loads (P_m) sustained by each joint were extracted. The implementation of the ISSF criterion started with the definition of the materials and bi-material corner geometry considered. This geometry and material combination revealed the existence of three singularity exponents λ characterising the analysed corner. However, since a plane-strain analysis was carried out, one of those exponents λ was not considered in the criterion for representing an anti-plane solution. Therefore, only two exponents were used, leading to two stress singularity components (H_1 and H_2). The method proposed to determine the critical stress singularities (H_c) consisted of using the experimentally determined P_m as the imposed load in numerical FEM simulation for each L_O. The resultant stress singularities were then used as H_c for each L_O. The strength predictions obtained revealed an anomaly in the experimental P_m value for L_O=10 mm, flawing the results attained with this L_O. From the results, it can be concluded that, for the prediction, it is better to resort to L_O closer (±20 mm) to the one intended to predict since smaller percentual deviations to the experimental value were found (usually under 10%). It was also detectable that predicting the strength of an L_O larger than the one used to determine H_{1c} resulted in an underprediction, whereas the inverse behaviour is also verifiable. The only exception was found between L_O=60 mm and L_O=70 mm, which showed similar strength predictions with slightly higher ones for L_O=60 mm. So, based on the results found, it would be advisable to only predict the strength of joints with L_O larger than the L_O used to determine H_{1c}. This warning is due to safety reasons for the mechanical projects. Regarding the proposed methodology, the results found can be considered promising, considering the simplicity of the same compared to the until now widespread approaches. That way, this method deserves further research, namely with different joint geometries or geometrical features (other than L_O). Concluding, the proposed method was successfully applied to composite adhesive joints and a bi-material interface corner.

3.3.6 References

[1] Avila, A.F. and P. Bueno, *An experimental and numerical study on adhesive joints for composites.* Composite Structures, 2004. **64**(3-4): p. 531-537.

[2] Li, X., D. Ma, H. Liu, W. Tan, X. Gong, C. Zhang and Y. Li, *Assessment of failure criteria and damage evolution methods for composite laminates under low-velocity impact.* Composite Structures, 2019. **207**: p. 727-739.

[3] Da Silva, L.F., A. Öchsner and R.D. Adams, *Handbook of adhesion technology*. 2011, Berlin, Germany: Springer Science & Business Media.

[4] Petrie, E.M., *Handbook of adhesives and sealants*. 2000, U.S: McGraw-Hill.

[5] Du, J., F.T. Salmon and A.V. Pocius, *Modeling of cohesive failure processes in structural adhesive bonded joints.* Journal of Adhesion Science and Technology, 2004. **18**(3): p. 287-299.

[6] Volkersen, O., *Die Nietkraftverteilung in zugbeanspruchten Nietverbindungen mit konstanten Laschenquerschnitten.* Jahrbuch der Deutschen Luftfahrtforschung, 1938. **15**: p. 41-47.

[7] Goland, M. and E. Reissner, *The stresses in cemented joints.* Journal of Applied Mechanics, 1944. **66**: p. A17-A27.

[8] Hart-Smith, L.J., *Adhesive-bonded single-lap joints*, in *NASA Contract Report, NASA CR-112236*. 1973.

[9] da Silva, L.F., P.J. das Neves, R. Adams and J. Spelt, *Analytical models of adhesively bonded joints—Part I: Literature survey.* International Journal of Adhesion and Adhesives, 2009. **29**(3): p. 319-330.

[10] Rodríguez, R.Q., W.P. De Paiva, P. Sollero, M.R.B. Rodrigues and É.L. De Albuquerque, *Failure criteria for adhesively bonded joints.* International Journal of Adhesion and Adhesives, 2012. **37**: p. 26-36.

[11] Clough, R.W. *The finite element method in plane stress analysis*. in *Proceedings of 2nd ASCE Conference on Electronic Computation*. 1960. Pittsburgh Pa.

[12] Campilho, R.D., *Strength prediction of adhesively-bonded joints*. 2017, Boca Raton, U.S.: CRC Press.

[13] Ramalho, L.D.C., R.D.S.G. Campilho, J. Belinha and L.F.M. da Silva, *Static strength prediction of adhesive joints: A review.* International Journal of Adhesion and Adhesives, 2020. **96**: p. 102451.

[14] Neto, J.A.B.P., R.D.S.G. Campilho and L.F.M. Da Silva, *Parametric study of adhesive joints with composites.* International Journal of Adhesion and Adhesives, 2012. **37**: p. 96-101.

[15] Teimouri, F., M. Heidari-Rarani and F.H. Aboutalebi, *Finite element modeling of mode I fatigue delamination growth in composites under large-scale fiber bridging.* Composite Structures, 2021. **263**: p. 113716.

[16] Rice, J.R., *A path independent integral and the approximate analysis of strain concentration by notches and cracks.* Journal of Applied Mechanics, 1968. **35**(2): p. 379-386.

[17] Rybicki, E.F. and M.F. Kanninen, *A finite element calculation of stress intensity factors by a modified crack closure integral.* Engineering Fracture Mechanics, 1977. **9**(4): p. 931-938.

[18] Anderson, T.L., *Fracture mechanics: fundamentals and applications*. 2017, Boca Raton, U.S.: CRC press.

[19] Leguillon, D., *Strength or toughness? A criterion for crack onset at a notch.* European Journal of Mechanics-A/Solids, 2002. **21**(1): p. 61-72.

[20] Fernandes, R.L., M.K. Budzik, R. Benedictus and S.T. de Freitas, *Multi-material adhesive joints with thick bond-lines: Crack onset and crack deflection.* Composite Structures, 2021. **266**: p. 113687.

[21] Kanninen, M.F., *An augmented double cantilever beam model for studying crack propagation and arrest.* International Journal of Fracture, 1973. **9**: p. 83–92.

[22] Williams, M.L., *The stresses around a fault or crack in dissimilar media.* Bulletin of the Seismological Society of America, 1959. **49**(2): p. 199-204.

[23] Bogy, D.B., *Two edge-bonded elastic wedges of different materials and wedge angles under surface tractions.* Journal of Applied Mechanics, 1971. **38**(2): p. 377-386.

[24] Delale, F., *Stress singularities in bonded anisotropic materials.* International Journal of Solids and Structures, 1984. **20**(1): p. 31-40.

[25] Pageau, S.S. and S.B. Biggers Jr, *A finite element approach to three-dimensional singular stress states in anisotropic multi-material wedges and junctions.* International Journal of Solids and Structures, 1996. **33**(1): p. 33-47.

[26] Chen, H., *Stress singularities in anisotropic multi-material wedges and junctions.* International Journal of Solids and Structures, 1998. **35**(11): p. 1057-1073.

[27] Stroh, A.N., *Steady state problems in anisotropic elasticity*. Journal of Mathematics and Physics, 1962. **41**(1-4): p. 77-103.

[28] Yao, S., M. Zappalorto, W. Pan, C. Cheng and Z. Niu, *Two dimensional displacement and stress fields for tri-material V-notches and sharp inclusions in anisotropic plates.* European Journal of Mechanics-A/Solids, 2020. **80**: p. 103927.

[29] Ting, T.C.T. and H. Chyanbin, *Sextic formalism in anisotropic elasticity for almost non-semisimple matrix N.* International Journal of Solids and Structures, 1988. **24**(1): p. 65-76.

[30] Barroso, A., V. Mantič and F. París, *Singularity analysis of anisotropic multimaterial corners.* International Journal of Fracture, 2003. **119**(1): p. 1-23.

[31] Barroso, A., J.C. Marín, V. Mantič and F. París, *Premature failures in standard test specimens with composite materials induced by stress singularities in adhesive joints.* International Journal of Adhesion and Adhesives, 2020. **97**: p. 102478.

[32] Campilho, R.D.S.G., M.F.S.F. De Moura and J.J.M.S. Domingues, *Modelling single and double-lap repairs on composite materials.* Composites Science and Technology, 2005. **65**(13): p. 1948-1958.

[33] Nunes, S.L.S., R.D.S.G. Campilho, F.J.G. da Silva, C.C.R.G. de Sousa, T.A.B. Fernandes, M.D. Banea and L.F.M. da Silva, *Comparative failure assessment of single and double-lap joints with varying adhesive systems.* The Journal of Adhesion, 2016. **92**: p. 610-634.

[34] Campilho, R.D.S.G., M.D. Banea, A.M.G. Pinto, L.F.M. da Silva and A.M.P. de Jesus, *Strength prediction of single- and double-lap joints by standard and extended finite element modelling.* International Journal of Adhesion and Adhesives, 2011. **31**(5): p. 363-372.

[35] De Sousa, C.C.R.G., R.D.S.G. Campilho, E.A.S. Marques, M. Costa and L.F.M. da Silva, *Overview of different strength prediction techniques for single-lap bonded joints.* Proceedings of the Institution of Mechanical Engineers, Part L: Journal of Materials: Design Applications, 2017. **231**: p. 210-223.

[36] Wang, S., W. Liang, L. Duan, G. Li and J. Cui, *Effects of loading rates on mechanical property and failure behavior of single-lap adhesive joints with carbon fiber reinforced plastics and aluminum alloys.* The International Journal of Advanced Manufacturing Technology, 2020. **106**(5): p. 2569-2581.

[37] Mantič, V., A. Barroso and F. París, *Singular Elastic Solutions in Anisotropic Multimaterial Corners: Applications to Composites*, in *Mathematical Methods and Models in Composites*. 2013, World Scientific. p. 425-495.

[38] Stroh, A.N., *Steady State Problems in Anisotropic Elasticity.* 1962. **41**(1-4): p. 77-103.

[39] Qian, Z.Q. and A.R. Akisanya, *Wedge corner stress behaviour of bonded dissimilar materials.* Theoretical and Applied Fracture Mechanics, 1999. **32**(3): p. 209-222.

[40] Klusák, J., T. Profant and M. Kotoul, *Various methods of numerical estimation of generalized stress intensity factors of bi-material notches.* Applied and Computational Mechanics, 2009. **3**(2).

[41] Fernandes, T.A.B., R.D.S.G. Campilho, M.D. Banea and L.F.M. da Silva, *Adhesive selection for single lap bonded joints: Experimentation and advanced techniques for strength prediction.* The Journal of Adhesion, 2015. **91**(10-11): p. 841-862.

[42] Galvez, P., N.-A. Noda, R. Takaki, Y. Sano, T. Miyazaki, J. Abenojar and M.A. Martínez, *Intensity of singular stress field (ISSF) variation as a function of the Young's modulus in single lap adhesive joints.* International Journal of Adhesion and Adhesives, 2019. **95**: p. 102418.

PAPER 4

MESHLESS ANALYSIS OF THE STRESS SINGULARITY IN COMPOSITE ADHESIVE JOINTS

L.D.C. RAMALHO, J.M.M. DIONÍSIO, I.J. SÁNCHEZ-ARCE, R.D.S.G. CAMPILHO, J. BELINHA

3.4 Paper 4

3.4.1 Introduction

Within the range of techniques used to connect materials, adhesive bonding has had much attention from engineers in the past couple of centuries. However, traces of this technique can be found throughout humankind history. Recent archaeological discoveries made in Italy showed that Neanderthals, living in Europe about 55000 to 40000 years ago, would leave their caves to collect resin from pine trees. They then used it to glue stone tools to handles made of bones or wood [1]. Nonetheless, only during the 20th-century engineers started to explore the possibilities offered by adhesive bonding in structural applications. The aeronautical engineers were the first to investigate and benefit from the advantages of this process. By incorporating adhesive bonding in aeroplanes, they achieved a considerable reduction of the structure's weight without compromising its strength. The technique also allows connecting different materials and more uniform stress distribution along the bonded area's width when compared to conventional bonding approaches [2]. Nowadays, it can be found in the most diverse engineering areas, such as automotive, civil and electrical.

A similar history can be associated with composite materials. This material category is the target of intense investigation by the engineers at the moment. Despite that, composite materials can be dated to the Mesopotamians and Egyptians (1500 B.C.). The first record of these materials is inscribed in the *Old Testament*, where it is described that clay bricks were reinforced with straw fibres. Identically, the aeronautical industry first took advantage of these materials in the past century. World War II also contributed to the increase in the use of composite materials in aeroplanes. Since their applications result in structural weight reductions, aeroplanes could fly longer distances, which was a significant advantage during the battle for the skies. The main characteristic that distinguishes composite materials from conventional construction materials is their excellent specific mechanical properties. Similarly to adhesive bonding, these materials are widespread thought the engineering industry. A recent design that combines composite materials and adhesive bonding are sandwich structures. These structures are composed of two face sheets typically designated by laminates adhesively bonded to a core [3]. The core is usually light and can have different shapes, such as foams or honeycombs. This structure has been vastly studied and implemented in the industry. Li and Wang [4] investigated the bending behaviour of sandwich structures with three-dimensional (3D) printed cores. These authors studied three core designs (truss, conventional honeycomb and re-entrant honeycomb) and the laminates used were from two types of Carbon Fibre Reinforced Polymer (CFRP). Three-point bending tests were performed and the flexural stiffness, flexural strength and energy absorption were evaluated. Due to the relatively homogeneous stress distribution, the re-entrant honeycomb sandwich structures presented an interesting failure mode and the best

capacity to absorb energy, contrary to the other two cores that showed earlier catastrophic failure. On the other hand, the truss sandwich structure revealed the highest flexural stiffness and strength. Elamin et al. [5] and He et al. [6] also recently studied these structures.

In the year before World War II, Volkersen [7] published what is considered the pioneer study regarding adhesive joints. In his work, he presented the first strength prediction model to evaluate adhesive joint behaviour. These models are essential to engineers since they allow the design of structures before being produced, thus saving resources and money. From this work until today, these models evolved in ways that Volkersen could have never imagined. The most significant influencer of this development was the computer. Before its invention, the strength prediction approaches were performed analytically, like Volkersen's work. However, the formulations usually were very simple and presented many simplifications [8]. Computers granted the appearance of numerical methods, which enabled the creation of far more complex formulations and intricate designs. Therefore, nowadays, nearly all scientific community resorts to numerical methods. Analytical models are still used as an initial indicator of joint behaviour. In 2009, da Silva et al. [9] performed a comparative study between different analytical approaches to predict the strength of adhesive joints, such as Volkersen [7], Goland and Reissner [10] or Hart-Smith [11].

The introduction of numerical methods enabled engineers to evaluate the failure of adhesively-bonded joints from a different perspective. In 2020, Ramalho et al. [12] summed up the most commonly applied approaches to joint failure. The authors highlighted five categories: continuum mechanics, fracture mechanics, damage mechanics, Cohesive Zone Modelling (CZM) and the eXtended Finite Element Method (XFEM). It was concluded that the majority of the works published with these approaches resort to the Finite Element Method (FEM) and that CZM is the most commonly applied technique to evaluate adhesive joint failure. Campilho et al. [13] investigated the influence of three different CZM law shapes (triangular, exponential and trapezoidal) in the strength prediction of SLJ with a thin adhesive layer. The objective was to evaluate if the law shape severely influences the strength predictions or if a CZM shape that may not be the most suited for a particular adhesive and present fewer convergence problems can be applied for attaining a faster solution. The adherends used were from unidirectional CFRP pre-preg and two adhesives were tested (a ductile and a fragile). Various L_O were also studied, and the simulations were performed through FEM. The results distinguished two different trends. In the case of the ductile adhesive, a significant influence of the CZM shape was observed in the results, being the trapezoidal shape the most suited. It was also found that for smaller $L_{O,}$ the shape influence is more prominent. In the opposite direction, for the brittle adhesive, it was concluded that the CZM shape could be neglected without compromising the strength predictions.

One other procedure to evaluate joint failure that is also widely explored is fracture mechanics. Its purpose is to approach joint failure based on the discontinuities of a structure, like re-entrant corners or defects. Two paths can be followed: the Stress Intensity Factors (SIF) or the energetic approach. The last one is based on the energy necessary to overcome the material resistance and allow crack growth [14]. The most widespread methods that rely on energetic concepts are the J-integral [15] and the Virtual Crack Closure Technique (VCCT) [16]. In 2020, Jones et al. [17] implemented a verification process to compare VCCT and FEM strength predictions of a bonded joint analysis tool designated HyperSizer (developed by NASA). The results showed excellent accuracy from the tool, with an average difference of 5.2 % to the FEM results. The authors also validated these results by comparison to experimental tests with errors between 1 and 30%. Finally, they implemented the process into HyperSizer for the analysis of bonded joints. On the other hand, the SIF relies on combinations of stresses and strains to evaluate joint failure [14]. Recently, the ISSF emerged as an up-and-coming technique based on the SIF. The ISSF, also known as General Stress Intensity Factor (GSIF), is a tool that can provide important information to aid in the design of adhesive joints. The ISSF is closely related to the SIF proposed by Irwin [18], but it can be applied to any corner and even in multi-material corners, not just single-material sharp cracks. The ISSF has been successfully applied to multi-material corners where both materials are isotropic [19-21]. When studying corners with just anisotropic materials, the ISSF analysis requires a different formulation. One of the earliest examples of a solution for this problem was proposed by Delale [22], with later applications from references [23, 24], among others. The solutions presented previously were based on the Stroh formalism [25], but an alternative approach, based on the elastic governing equations and the asymptotic expansions of displacement and stress near the notch tip, can also be found in reference [26]. However, composite adhesive joints have both types of materials since adhesives are generally isotropic and the composite substrates are anisotropic. This requires an adaption of the Stroh formalism, as proposed by Ting and Chyanbin [27]. This modification was used in several subsequent works to analyse bi-material corners of composite adhesive joints [28, 29]. In 2002, Leguillon [30] proposed a new method that combines stress and energy concepts to define joint failure.

Over the years, the approaches described before have been all implemented resorting to FEM. However, more recently, a new group of numerical techniques has aroused the curiosity of engineers, named meshless methods. The obstacle of FEM is the dependency on the discretization of the object studied, which can be problematic, for example, when problems with large deformations are treated [31]. Therefore, meshless methods try to overcome this handicap and do not rely on a mesh to discretize the studied object. Currently, two meshless approaches stand out: the RPIM and the Natural Neighbours Radial Point Interpolation Method (NNRPIM). Wang et al. [32] relied on the RPIM to impose periodic boundary conditions to representative volume element (REV) models of 3D braided composites on either periodic or non-periodic meshes. This type

of composite presents advantages in the out-of-plane properties over unidirectional fibre composites and laminates. Due to the necessity of imposing periodic boundary conditions, creating a periodic mesh reveals considerable adversities. For this reason, the RPIM was implemented by the authors. The study disclosed accurate predictions of the elastic constants for the non-periodic mesh RVE model using RPIM-based periodic boundary conditions when compared with those found for the periodic mesh. Moreover, the relative errors of the predicted modulus in *z* tension are about 3-4 % for both meshes. Regarding the NNRPIM, a recent investigation performed by Ramalho et al. [33] applied this technique to SLJ with composite adherends and three different adhesives scaled in terms of brittleness (one fragile and two ductile). A new continuum mechanics based criterion was applied for the strength predictions, named Critical Longitudinal Strain (CLS). The stress distributions were compared to previously obtained FEM stress distributions to assess the NNRPIM's suitability, leading to similar results. The authors concluded that one of the main goals of this work was fulfilled: the simulation of an adhesively-bonded composite SLJ through a meshless method. However, the second objective was not accomplished since the two ductile adhesives did not allow to estimate the critical parameters of the CLS criterion. Thence, they concluded that this criterion presents several limitations when analysing ductile adhesives. Nevertheless, for the brittle adhesive, the results were alluring, with errors bellow 10 %.

The present work aims to validate the ISSF criterion through a meshless method, the RPIM, applied to SLJ with CFRP adherends and a brittle adhesive. Several L_O were tested (between 10 and 80 mm) to evaluate this parameter's influence on the strength predictions. The joints were experimentally tested and then evaluated through the ISSF criterion. For the strength predictions, an extrapolation based method is implemented to determine H_c. Finally, the experimental data are compared with the predicted strengths to assess the suitability of the method.

3.4.2 Materials and methods

3.4.2.1 Joint geometry

The base adhesive joint geometry to validate the ISSF technique for orthotropic adherends is the SLJ, using CFRP adherends and a strong but brittle adhesive from Araldite®, the AV138. Figure 3.4.1 depicts the SLJ layout and dimensions. The main variables and respective nomenclature are as follows (all dimensions are given in mm): L_O between 10 and 80 (intervals of 10), the joint length between gripping points L_T=200, adherend thickness t_P=2.4, adhesive thickness t_A=0.2 and width B=15 (B is not present in Figure 3.4.1). The applied boundary conditions are schematically drawn in Figure 3.4.1 and comprise clamping one joint edge (left in the figure) and tensile pulling while preventing transverse motion at the other edge (right in the figure).

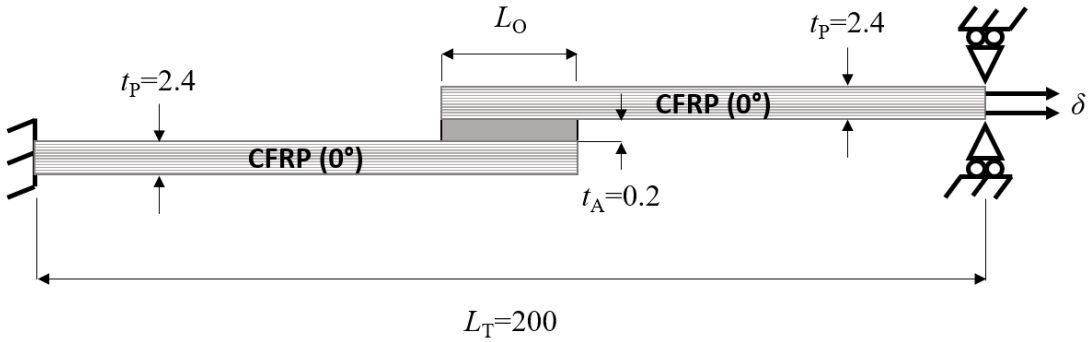

Figure 3.4.1 - SLJ joint dimensions (in mm) and boundary conditions

3.4.2.2 Joint materials

The materials that compose the SLJ are CFRP (adherends) and Araldite® AV138 (adhesive). The adherends were fabricated from unidirectional pre-preg SEAL® (SEAL® Texipreg HS 160 RM; SEAL® from Legnano, Italy), aiming to fabricate CFRP plates with thickness of 3 mm and $[0]_{20}$ lay-up. Thus, a unidirectional lay-up was used, with a ply unit thickness of 0.15 mm. Initially, these plates were produced by manual stacking plies with an area of 300×300 mm^2 and curing the bulk set using a hot press for one hour at 130ºC and 2 bar pressure. These are the recommended curing conditions by the manufacturer, leading to a theoretical fibre volume fraction of almost 64%, with reduced porosity content and overall best characteristics. After this process, the plates were cut to the adherends' final dimensions. Table 3.4.1 provides the elastic orthotropic constants of a single unidirectional ply (or unidirectional plate) [34].

Table 3.4.1 - Elastic orthotropic constants of a single unidirectional ply with the fibres oriented the *x* axis (*y* and *z* are the transverse and thickness directions, respectively) [35]

E_x=1.09E+05 MPa	ν_{xy}=0.342	G_{xy}=4315 MPa
E_y=8819 MPa	ν_{xz}=0.342	G_{xz}=4315 MPa
E_z=8819 MPa	ν_{yz}=0.380	G_{yz}=3200 MPa

The Araldite® AV138 has a tensile strength of nearly 40 MPa, although being brittle, thus exhibiting a linear behaviour until failure in the tensile stress-tensile strain (σ-ε) curve. Jointly with its stiffness, the performance in bonded joints is often limited, especially for large L_O, due to premature failure onset at the overlap edges [36]. Characterization of this adhesive was previously accomplished [37], resulting in the information provided in Table 3.4.2, in which ν is the Poisson ratio. The tensile properties were acquired with bulk (dogbone) tests, leading to the following data: Young's modulus (E), tensile yield stress (σ_y), tensile strength (σ_f) and tensile failure strain (ε_f). Specimen fabrication and testing followed the French standard NF T 76-142. The shear properties were obtained from Thick Adherend Shear Tests (TAST), giving the shear modulus (G), shear yield stress (τ_y), shear strength (τ_f) and shear failure strain (γ_f). In this case, the TAST testing procedure is described in the standard ISO 11003-2:1999. The procedure involves an

alignment jig to cure the adhesive and promote L_O=5 mm. DIN C45E steel adherends were used to minimize adherend deformations and provide accurate *G* measurements.

Table 3.4.2 - Collected properties of the Araldite® AV138 [37]

E (GPa)	4.89±0.81	G (GPa)	1.56±0.01
ν	0.35[1]	τ_y (MPa)	25.1±0.33
σ_y (MPa)	36.49±2.47	τ_f (MPa)	30.2±0.40
σ_f (MPa)	39.45±3.18	γ_f (%)	7.8±0.7
ε_f (%)	1.21±0.10		

[1] Data from the manufacturer.

3.4.2.3 Fabrication and tensile testing

The SLJ fabrication process, considering the adherends' manufacturing and preparation as specified in the previous section of this paper, began by preparing the bonding surfaces. This process involved manual abrasion with fine mesh sandpaper (grit 320), which enabled the removal of the resin-rich layer resulting from the consolidation process, increasing the surface roughness and activating the surfaces, thus ensuring a strong bond. Next, the surfaces were duly cleaned with acetone in order to eliminate dirt and particles [38]. The joints were then assembled by placing the adherends in a jig constituted by two parts: lower plate for the specimens' alignment and upper plate to apply pressure and assure t_A. Calibrated spacers between the adherends were used to achieve the correct t_A. At this stage, alignment tabs were also glued at the joint ends to centre the specimens between grips of the testing equipment. Adhesive curing took place for one week at typical conditions (room temperature and humidity). After demoulding the specimens from the jig, these were trimmed, i.e., the excess adhesive was removed by milling in proper equipment. Tensile testing was done using an electro-mechanical machine (Shimadzu AG-X 100; load cell of 100 kN) at a prescribed speed of 1 mm/min. The necessary data for further processing and analysis was the load (P; measured from the load cell) and displacement (δ; measured by approximation from the moving crosshead to which the upper grip is attached). For each joint configuration (completely defined by the respective L_O), five specimens were tested, resulting in at least four valid results.

3.4.3 Numerical analysis

3.4.3.1 RPIM description

Most of the RPIM implementation is similar to the FEM, with the difference that the latter uses a mesh, while the former does not, but it uses a grid similar to a FEM mesh

to create the integration point. In the RPIM, a domain Ω is discretized into a nodal set $\mathbf{N}=\{n_1, n_2, \ldots, n_N\}$ with coordinates $\mathbf{X}=\{x_1, x_2, \ldots, x_N\} \in \Omega$. Then, integration points are created with the aid of a background integration grid, which is only used for this step. Having the integration points, it is necessary to determine their influence domains, whose FEM counterpart are the elements. It is recommended that the number of nodes in each influence domain does not significantly vary. In the present work, the influence domain of each integration point is composed of the 16 nodes closest to it, which is a value within the range suggested in previous works [39, 40]. Any given node in the domain will thus belong to several influence domains. This occurrence is called domain overlapping and imposes nodal connectivity [39], just as elements sharing nodes do in the FEM. An example of the concepts described previously is shown in Figure 3.4.2 for two integration points.

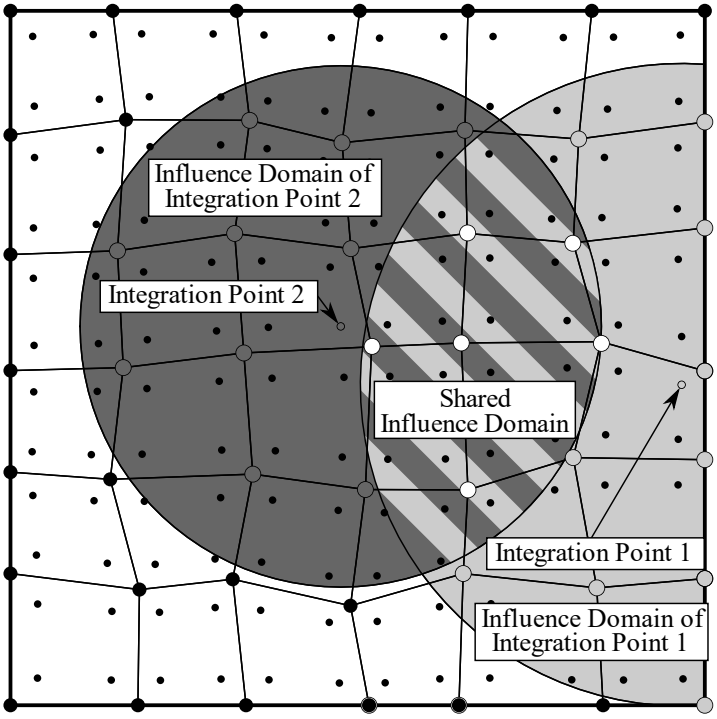

Figure 3.4.2 - Example of two RPIM influence domains and their overlap

In addition to the dichotomy between influence domains and elements, the RPIM and the FEM also have different shape functions, which are described in section 3.4.3.1.1 for the RPIM. Besides those two differences, the RPIM and the FEM have similar implementations. Namely, a global stiffness matrix is assembled from all the local stiffness matrices obtained using the shape functions and material properties, the boundary conditions are imposed, and the global system of equations is solved. It is important to note that the boundary conditions in the RPIM can be imposed just as they are in FEM because the RPIM possesses the Kronecker delta property [39].

3.4.3.1.1 RPIM shape functions

For an integration point $\boldsymbol{x}_I \subset \mathbb{R}^d$, in the domain Ω, presented in section 3.4.3.1, the Radial Point Interpolation (RPI) function of $\boldsymbol{x}_I$ is defined as [39]:

$$u^h(\boldsymbol{x}_I) = \boldsymbol{r}(\boldsymbol{x}_I)^T \boldsymbol{a}(\boldsymbol{x}_I) + \boldsymbol{p}(\boldsymbol{x}_I)^T \boldsymbol{b}(\boldsymbol{x}_I), \quad (1)$$

being $\boldsymbol{a}(\boldsymbol{x}_I)$ and $\boldsymbol{b}(\boldsymbol{x}_I)$ the non-constant coefficients of $\boldsymbol{r}(\boldsymbol{x}_I)$ and $\boldsymbol{p}(\boldsymbol{x}_I)$, respectively. While $\boldsymbol{a}(\boldsymbol{x}_I)$ and $\boldsymbol{r}(\boldsymbol{x}_I)$ will have a size equal to n, $\boldsymbol{b}(\boldsymbol{x}_I)$ and $\boldsymbol{p}(\boldsymbol{x}_I)$ will have a size equal to m (n is the total number of nodes in the influence domain of $\boldsymbol{x}_I$ and m is the number of monomials of the complete polynomial basis, defined according to Pascal's triangle). A linear polynomial basis was used in this work since using a higher basis increases the computational times while not changing the results in any observable manner. Among other alternatives for the Radial Basis Function (RBF), such as the Gaussian RBF or the thin plate spline RBF, the multi-quadrics RBF (MQ-RBF) was chosen to be used in this work. This RBF is defined as $r_i(x_I) = \left(d_{iI}^2 + (\gamma d_a)^2\right)^p$ [39], where γ and p are function shape parameters, d_a is the integration weight of the integration point $\boldsymbol{x}_I$, and d_{iI} is the Euclidean norm between node i and the integration point I. The influence of the shape parameters was previously studied by Wang and Liu [41], who suggested that they should be γ=1.03 and p=1.42, which are the values used in this work. Imposing $u^h(\boldsymbol{x}_I)$ to pass through all the nodal values n of the influence domain of $\boldsymbol{x}_I$ leads to the following system of equations [39]:

$$\boldsymbol{R}\boldsymbol{a}(\boldsymbol{x}_I) + \boldsymbol{P}\boldsymbol{b}(\boldsymbol{x}_I) = \boldsymbol{u}_s, \quad (2)$$

where $\boldsymbol{u}_s^T = \{u_1 \quad u_2 \quad \dots \quad u_n\}$ is a vector with the field function values at each node inside the influence domain of $\boldsymbol{x}_I$, which (depending on the problem under analysis) can be the displacement, velocity, temperature, or other variables. The MQ-RBF moment matrix ($\boldsymbol{R}$) will have a size equal to $n \times n$, while the polynomial moment matrix ($\boldsymbol{P}$) will have a size equal to $m \times n$. To obtain a unique solution, it is necessary to add another set of equations [39]:

$$\boldsymbol{P}^T \boldsymbol{a}(\boldsymbol{x}_I) = 0. \quad (3)$$

The combination of Equations (2) and (3) leads to the final set of equations [39]:

$$\begin{bmatrix} \boldsymbol{R} & \boldsymbol{P} \\ \boldsymbol{P}^T & \boldsymbol{Z} \end{bmatrix} \begin{Bmatrix} \boldsymbol{a}(\boldsymbol{x}_I) \\ \boldsymbol{b}(\boldsymbol{x}_I) \end{Bmatrix} = \boldsymbol{M}_T \begin{Bmatrix} \boldsymbol{a}(\boldsymbol{x}_I) \\ \boldsymbol{b}(\boldsymbol{x}_I) \end{Bmatrix} = \begin{Bmatrix} \boldsymbol{u}_s \\ \boldsymbol{z} \end{Bmatrix}, \quad (4)$$

being Z_{ij}=0 and z_i=0 for i,j = 1, 2, ..., m [39]. Then, $\boldsymbol{a}(\boldsymbol{x}_I)$ and $\boldsymbol{b}(\boldsymbol{x}_I)$ can be obtained:

$$\begin{Bmatrix} \boldsymbol{a}(\boldsymbol{x}_I) \\ \boldsymbol{b}(\boldsymbol{x}_I) \end{Bmatrix} = \boldsymbol{M}_T^{-1} \begin{Bmatrix} \boldsymbol{u}_s \\ \boldsymbol{z} \end{Bmatrix}. \quad (5)$$

By substituting $\boldsymbol{M}_T^{-1}\{\boldsymbol{u}_s \quad \boldsymbol{z}\}^T$ into Equation (1), the following is obtained:

$$u^h(\boldsymbol{x}_I) = \left\{\boldsymbol{r}(\boldsymbol{x}_I)^T \quad \boldsymbol{p}(\boldsymbol{x}_I)^T\right\} \boldsymbol{M}_T^{-1} \begin{Bmatrix} \boldsymbol{u}_s \\ \boldsymbol{z} \end{Bmatrix}. \quad (6)$$

The field function value for an interest point $\boldsymbol{x}_I$ is interpolated using the shape function values at the nodes inside the influence domain of $\boldsymbol{x}_I$, which can be identified in Equation (6) [39]:

$$u^h(\boldsymbol{x}_I) = \left\{ \boldsymbol{\Phi}(\boldsymbol{x}_I)^T \quad \boldsymbol{\Psi}(\boldsymbol{x}_I)^T \right\} \boldsymbol{M}_T^{-1} \begin{Bmatrix} \boldsymbol{u}_s \\ \boldsymbol{z} \end{Bmatrix}, \tag{7}$$

being $\boldsymbol{\Psi}(\boldsymbol{x}_I) = \{\psi_1(\boldsymbol{x}_I) \quad \psi_2(\boldsymbol{x}_I) \quad \dots \quad \psi_n(\boldsymbol{x}_I)\}^T$ and $\boldsymbol{\Phi}(\boldsymbol{x}_I) = \{\varphi_1(\boldsymbol{x}_I) \quad \varphi_2(\boldsymbol{x}_I) \quad \dots \quad \varphi_n(\boldsymbol{x}_I)\}^T$ a by-product vector with no relevant meaning and the interpolation shape function, respectively. A more complete formulation of the RPIM, including the derivatives of the shape functions needed to solve the $\boldsymbol{Ku} = \boldsymbol{f}$ system of equations, can be found in the literature [39].

3.4.3.2 ISSF formulation for composites

Considering a three-dimensional Cartesian coordinate system, the constitutive law of a material can be defined as $\boldsymbol{\sigma} = \boldsymbol{C\varepsilon}$, where $\boldsymbol{C}$ is a symmetric matrix defined as follows:

$$\boldsymbol{C} = \begin{bmatrix} \frac{1}{E_1} & -\frac{\nu_{12}}{E_1} & -\frac{\nu_{13}}{E_1} & 0 & 0 & 0 \\ -\frac{\nu_{21}}{E_2} & \frac{1}{E_2} & -\frac{\nu_{23}}{E_2} & 0 & 0 & 0 \\ -\frac{\nu_{31}}{E_3} & -\frac{\nu_{32}}{E_3} & \frac{1}{E_3} & 0 & 0 & 0 \\ 0 & 0 & 0 & \frac{1}{G_{23}} & 0 & 0 \\ 0 & 0 & 0 & 0 & \frac{1}{G_{13}} & 0 \\ 0 & 0 & 0 & 0 & 0 & \frac{1}{G_{12}} \end{bmatrix}, \tag{8}$$

where $\boldsymbol{\sigma}$ and $\boldsymbol{\varepsilon}$ are the stress and strain vectors, respectively, in Voigt notation. Since $\boldsymbol{C}$ is symmetric, the following must be true: $\nu_{12}/E_1 = \nu_{21}/E_2$, $\nu_{23}/E_2 = \nu_{32}/E_3$ and $\nu_{13}/E_1 = \nu_{31}/E_3$. The Stroh formalism [42] is defined by the following eigensystem:

$$\boldsymbol{N}\boldsymbol{\xi}_\alpha = p_\alpha \boldsymbol{\xi}_\alpha, \tag{9}$$

being p_α and $\boldsymbol{\xi}_\alpha$ the eigenvalues and the eigenvectors of this system, respectively. This system has 6 eigenvectors and eigenvalues, and $\boldsymbol{N}$ is defined as:

$$N = \begin{bmatrix} \boldsymbol{N}_1 & \boldsymbol{N}_2 \\ \boldsymbol{N}_3 & \boldsymbol{N}_1^T \end{bmatrix}, \tag{10}$$

where $\boldsymbol{N}_1 = -\boldsymbol{T}^{-1}\boldsymbol{R}^T$, $\boldsymbol{N}_2 = -\boldsymbol{T}^{-1}$ and $\boldsymbol{N}_3 = \boldsymbol{R}\boldsymbol{T}^{-1}\boldsymbol{R}^T - \boldsymbol{Q}$, and:

$$\boldsymbol{Q}=\begin{bmatrix} C_{11} & C_{16} & C_{15} \\ C_{16} & C_{66} & C_{56} \\ C_{15} & C_{56} & C_{55} \end{bmatrix};\quad \boldsymbol{R}=\begin{bmatrix} C_{16} & C_{12} & C_{14} \\ C_{66} & C_{26} & C_{46} \\ C_{56} & C_{25} & C_{45} \end{bmatrix};\quad \boldsymbol{T}=\begin{bmatrix} C_{66} & C_{26} & C_{46} \\ C_{26} & C_{22} & C_{24} \\ C_{46} & C_{24} & C_{44} \end{bmatrix}. \tag{11}$$

The eigenvalues and eigenvectors of this system are complex. Therefore, if p_α and $\boldsymbol{\xi}_\alpha$ are valid for Equation (9), $\bar{p}_\alpha$ and $\bar{\boldsymbol{\xi}}_\alpha$ are valid too, where the overbar is the complex conjugate. The eigenvectors can be divided into two parts, $\boldsymbol{\xi}_\alpha^T=[\boldsymbol{a}_\alpha^T \quad \boldsymbol{b}_\alpha^T]$, where $\boldsymbol{a}_\alpha$ is proportional to the displacement vector and $\boldsymbol{b}_\alpha$ is proportional to the traction vector. Transverse isotropic materials, as are unidirectional fibre-reinforced composites, have three different eigenvalues and three linearly independent eigenvectors and their corresponding conjugates. However, isotropic materials, as adhesives generally are, have a single eigenvalue $p=i$ and two linearly independent eigenvectors. Therefore, a modification to the Stroh formalism, presented in Equation (9), is needed [43]:

$$\boldsymbol{N}\boldsymbol{\xi}_1=p\boldsymbol{\xi}_1\ ;\ \boldsymbol{N}\boldsymbol{\xi}_2=p\boldsymbol{\xi}_2+\boldsymbol{\xi}_1\ ;\ \boldsymbol{N}\boldsymbol{\xi}_3=p\boldsymbol{\xi}_3, \tag{12}$$

which means that $\boldsymbol{\xi}_1$ and $\boldsymbol{\xi}_3$ can be determined using Equation (9), but $\boldsymbol{\xi}_2^T=[\boldsymbol{a}_2^T \quad \boldsymbol{b}_2^T]$ is determined as follows [43]:

$$-\left[\boldsymbol{Q}+\left(\boldsymbol{R}+\boldsymbol{R}^T\right)p+\boldsymbol{T}p^2\right]\boldsymbol{a}_2=\left(2p\boldsymbol{T}+\boldsymbol{R}+\boldsymbol{R}^T\right)\boldsymbol{a}_1, \tag{13}$$

$$\boldsymbol{b}_2=T\boldsymbol{a}_1+\left(\boldsymbol{R}^T+p\boldsymbol{T}\right)\boldsymbol{a}_2. \tag{14}$$

A vector $\boldsymbol{w}(r,\theta)^T=[\boldsymbol{u}(r,\theta)^T \quad \boldsymbol{\varphi}(r,\theta)^T]$, where $\boldsymbol{u}$ is the displacement vector and $\boldsymbol{\varphi}$ is the stress function vector, can be defined as [43]:

$$w(r,\theta)=r^\lambda XZv, \tag{15}$$

where $\boldsymbol{q}$ is a constant vector, $\mathbf{X}=[\boldsymbol{\xi}_1 \quad \boldsymbol{\xi}_2 \quad \boldsymbol{\xi}_3 \quad \bar{\boldsymbol{\xi}}_1 \quad \bar{\boldsymbol{\xi}}_2 \quad \bar{\boldsymbol{\xi}}_3]$ and, for materials with three linearly independent eigenvectors and three eigenvalues [43], $\mathbf{Z}(\theta)$ is given by:

$$Z(\theta)=\begin{bmatrix} \left\langle \zeta_\alpha^\lambda(\theta)\right\rangle & 0_{3\times3} \\ 0_{3\times3} & \left\langle \bar{\zeta}_\alpha^\lambda(\theta)\right\rangle \end{bmatrix}, \tag{16}$$

where angle brackets represent diagonal matrices. For materials with just two linearly independent eigenvectors and one eigenvalue, $\mathbf{Z}(\theta)$ is also dependent on λ and it is defined as [43]:

$$Z(\theta,\lambda)=\begin{bmatrix} \boldsymbol{\Psi}(\theta,\lambda) & 0_{3\times3} \\ 0_{3\times3} & \bar{\boldsymbol{\Psi}}(\theta,\lambda) \end{bmatrix}, \tag{17}$$

with:

$$\boldsymbol{\Psi}^\lambda(\theta)=\begin{bmatrix} \zeta^\lambda(\theta) & K(\theta,\lambda)\zeta^\lambda(\theta) & 0 \\ 0 & \zeta^\lambda(\theta) & 0 \\ 0 & 0 & \zeta^\lambda(\theta) \end{bmatrix}, \tag{18}$$

being $K(\theta,\lambda)=\lambda\sin(\theta)/\zeta(\theta)$ and $\zeta_\alpha^\lambda(\theta)=[\cos(\theta)+p_\alpha\sin(\theta)]^\lambda$.

Considering a material *m* in a bi-material wedge, defined by an initial angle θ_{m-1} and an end angle θ_m, the following relation can be established [43]:

$$w(r,\theta_m) = E(\lambda,\theta_m,\theta_{m-1})\,w(r,\theta_{m-1}), \tag{19}$$

being:

$$E(\lambda,\theta_m,\theta_{m-1}) = X\boldsymbol{Z}^{\lambda}(\theta_m)\left[\boldsymbol{Z}^{\lambda}(\theta_{m-1})\right]^{-1}\boldsymbol{X}^{-1}, \tag{20}$$

where $\boldsymbol{Z}^{\lambda}(\theta_m)\left[\boldsymbol{Z}^{\lambda}(\theta_{m-1})\right]^{-1}$ can be simplified to $\boldsymbol{Z}^{\lambda}(\theta_m,\theta_{m-1})$, which for materials with three linearly independent eigenvectors and three eigenvalues gives [43]:

$$\boldsymbol{Z}^{\lambda}(\theta_m,\theta_{m-1}) = \begin{bmatrix} \left\langle \zeta_{\alpha}^{\lambda}(\theta_m,\theta_{m-1})\right\rangle & 0_{3\times3} \\ 0_{3\times3} & \left\langle \bar{\zeta}_{\alpha}^{\lambda}(\theta_m,\theta_{m-1})\right\rangle \end{bmatrix}, \tag{21}$$

while for materials with just two linearly independent eigenvectors and one eigenvalue it is also dependent on λ and is defined as [43]:

$$\boldsymbol{Z}^{\lambda}(\theta_m,\theta_{m-1},\lambda) = \begin{bmatrix} \boldsymbol{\Psi}(\theta_m,\theta_{m-1},\lambda) & 0_{3\times3} \\ 0_{3\times3} & \bar{\boldsymbol{\Psi}}(\theta_m,\theta_{m-1},\lambda) \end{bmatrix}, \tag{22}$$

with:

$$\Psi(\theta_m,\theta_{m-1},\lambda) = \begin{bmatrix} \zeta^{\lambda}(\theta_m,\theta_{m-1}) & K(\theta_m,\theta_{m-1},\lambda)\zeta^{\lambda}(\theta_m,\theta_{m-1}) & 0 \\ 0 & \zeta^{\lambda}(\theta_m,\theta_{m-1}) & 0 \\ 0 & 0 & \zeta^{\lambda}(\theta_m,\theta_{m-1}) \end{bmatrix}, \tag{23}$$

where $\zeta_{\alpha}(\theta_m,\theta_{m-1}) = \zeta_{\alpha}(\theta_m)/\zeta_{\alpha}(\theta_{m-1})$ and:

$$K(\theta_m,\theta_{m-1},\lambda) = \frac{\lambda\sin(\theta_m-\theta_{m-1})}{\zeta(\theta_m)\zeta(\theta_{m-1})}. \tag{24}$$

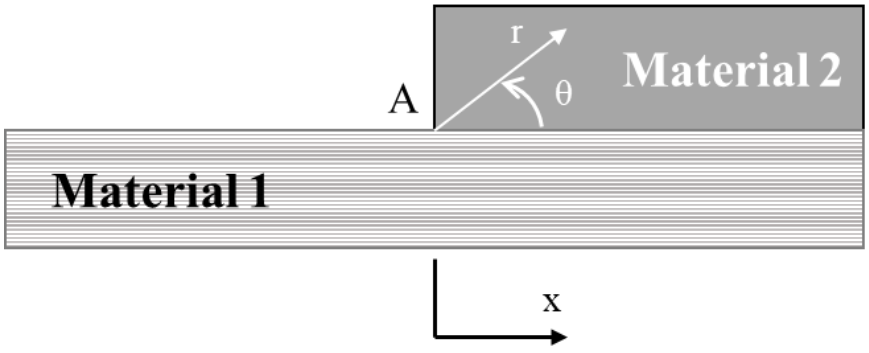

Figure 3.4.3 - Wedge corner in a bi-material interface

In a wedge made of two perfectly bonded materials, as in Figure 3.4.3, it is possible to relate $\boldsymbol{w}(r,\theta_0)$ with $\boldsymbol{w}(r,\theta_2)$. If $\boldsymbol{w}(r,\theta_1) = \boldsymbol{E}(\lambda,\theta_1,\theta_0)\boldsymbol{w}(r,\theta_0)$ and $\boldsymbol{w}(r,\theta_2) = \boldsymbol{E}(\lambda,\theta_2,\theta_1)\boldsymbol{w}(r,\theta_1)$:

$$w(r,\theta_2) = \boldsymbol{K}_W(\lambda)\,w(r,\theta_0), \tag{25}$$

being $\boldsymbol{K}_W(\lambda) = \boldsymbol{E}(\lambda, \theta_2, \theta_1)\boldsymbol{E}(\lambda, \theta_1, \theta_0)$ called the transfer matrix. Now it is necessary to impose the boundary conditions. In adhesive joints, both outer faces of the interface wedge are free, thus $\boldsymbol{\varphi}(r, \theta_0) = \boldsymbol{\varphi}(r, \theta_2) = \mathbf{0}$ must be imposed. Thus, the following boundary condition matrices are used [28]:

$$\boldsymbol{D}_0 = \boldsymbol{D}_2 = \begin{bmatrix} 0_{3\times3} & \mathbf{I}_{3\times3} \\ \mathbf{I}_{3\times3} & 0_{3\times3} \end{bmatrix}. \tag{26}$$

These boundary condition matrices are used to modify the transfer matrix [28]:

$$\boldsymbol{K}_{WBC}(\lambda) = \boldsymbol{D}_2 \boldsymbol{K}_W \boldsymbol{D}_0^T. \tag{27}$$

Considering the boundary conditions, the system of equations is rewritten as [28]:

$$\begin{bmatrix} 0_{3\times1} \\ \boldsymbol{u}(r, \theta_2) \end{bmatrix} = \begin{bmatrix} \boldsymbol{K}_{WBC}^{(1)}(\lambda) & \boldsymbol{K}_{WBC}^{(2)}(\lambda) \\ \boldsymbol{K}_{WBC}^{(3)}(\lambda) & \boldsymbol{K}_{WBC}^{(4)}(\lambda) \end{bmatrix} \begin{bmatrix} 0_{3\times1} \\ \boldsymbol{u}(r, \theta_0) \end{bmatrix}. \tag{28}$$

From Equation (28), the following is verified: $\mathbf{0}_{3\times1} = \boldsymbol{K}_{WBC}^{(2)}(\lambda)\boldsymbol{u}(r, \theta_0)$. Therefore, a non-trivial solution is found if and only if:

$$\left|\boldsymbol{K}_{WBC}^{(2)}(\lambda)\right| = 0. \tag{29}$$

This is how the characteristic exponents of the bi-material corner are obtained. There is an infinite number of λ that can be obtained, but to study the singularity, only λ<1 are essential since these are the ones characterizing the singularity. Having determined λ, it is now possible to determine the stress and displacement around the interface corner. For a given angle (θ) inside a material (m), the polar stress components can be defined as [43]:

$$\begin{gathered} f_{rr} = -\boldsymbol{s}_r^T(\theta)\boldsymbol{\varphi}_{,\theta}(r, \theta)/r;\ f_{\theta\theta} = \boldsymbol{n}^T(\theta)\boldsymbol{\varphi}_{,r}(r, \theta); \\ f_{r\theta} = -\boldsymbol{n}^T(\theta)\boldsymbol{\varphi}_{,\theta}(r, \theta)/r = \boldsymbol{s}_r^T(\theta)\boldsymbol{\varphi}_{,r}(r, \theta) \end{gathered}, \tag{30}$$

while the displacements are defined as [43]:

$$g_r = -\boldsymbol{s}_r^T(\theta)\boldsymbol{u}(r, \theta)/r;\quad g_\theta = \boldsymbol{n}^T(\theta)u(r, \theta), \tag{31}$$

where $\boldsymbol{s}_r^T = [\cos(\theta) \quad \sin(\theta) \quad 0]$ and $\boldsymbol{n}^T = [\sin(\theta) \quad -\cos(\theta) \quad 0]$. To determine the components in Equations (30) and (31), it is first necessary to determine $\boldsymbol{w}(r, \theta_0)$ and $\boldsymbol{w}(r, \theta_1)$ for each λ. First, it is known that $\boldsymbol{\varphi}(r, \theta_0) = \mathbf{0}_{3\times1}$, due to the boundary conditions, and $\boldsymbol{u}_0$ is determined by solving $\mathbf{0}_{3\times1} = \boldsymbol{K}_{WBC}^{(2)}(\lambda)\boldsymbol{u}(r, \theta_0)$. So, $\boldsymbol{w}(r, \theta_0)$ can be assembled as $\boldsymbol{w}(r, \theta_0)^T = [\boldsymbol{u}(r, \theta_0)^T \quad \boldsymbol{\varphi}(r, \theta_0)^T]$. Knowing $\boldsymbol{w}(r, \theta_0)$, $\boldsymbol{w}(r, \theta_1)$ is determined by simply using Equation (19). Then, the components of Equations (30) and (31) for each λ, and its derivatives in order to r and θ, in a material (m) and at a given angle (θ), inside m, can be determined using Equation (19), being the angle θ_m substituted by θ. The components of Equations (23) and (24) have to be standardized, because if $\boldsymbol{w}(r, \theta_0)$ is a solution so is $c\boldsymbol{w}(r, \theta_0)$, where c is any constant. In this work, this standardization was performed by finding the maximum value of the components in the angle range encompassing the whole corner and dividing all the components by

that value. Having the singularity components (λ) and the stress (f) and displacement (g) functions near the singularity, the stress and displacement can be described as:

$$\sigma_{ij} = \sum_{k=1}^{n} H_k r^{\lambda_k - 1} f_{ij}\left(\lambda_k, \theta\right), \tag{32}$$

$$u_j = \sum_{k=1}^{n} H_k r^{\lambda_k} g_j\left(\lambda_k, \theta\right), \tag{33}$$

being n the number of singularity exponents (λ), which depends on the interface corner's geometry and materials. H_k is the ISSF or GSIF, which is a scalar value related to the singularity component k. The ISSF can be determined in different ways. For example, Qian and Akisanya [44] used a line integral encircling the interface corner to determine the ISSF. In the current work, the ISSF was determined by extrapolating it to the corner from values near the corner, similarly to the method used by Klusák et al. [45]. This method requires a n number of points at different angles (θ) and at a fixed radius (r) to determine a n number of ISSF, e.g., if there are two singularity components λ_1 and λ_2, two different angles are needed. Therefore, $\boldsymbol{H}$ can be determined at r using the following equation:

$$\begin{bmatrix} r^{\lambda_1 - 1} f_{\theta\theta}\left(\lambda_1, \theta_{n+1}\right) & \cdots & r^{\lambda_n - 1} f_{\theta\theta}\left(\lambda_n, \theta_{n+1}\right) \\ \vdots & \ddots & \vdots \\ r^{\lambda_1 - 1} f_{\theta\theta}\left(\lambda_1, \theta_{n+n}\right) & \cdots & r^{\lambda_n - 1} f_{\theta\theta}\left(\lambda_n, \theta_{n+n}\right) \end{bmatrix} \begin{bmatrix} H_1 \\ \vdots \\ H_n \end{bmatrix} = \begin{bmatrix} \sigma_{\theta\theta}\left(r, \theta_{n+1}\right) \\ \vdots \\ \sigma_{\theta\theta}\left(r, \theta_{n+n}\right) \end{bmatrix}, \tag{34}$$

where $\sigma_{\theta\theta}$ is extracted from the RPIM simulations. The solution of Equation (34) is obtained for several different r, and it is then extrapolated to r=0 mm, from an r interval where it is stable, to obtain $\boldsymbol{H}$ at the interface corner.

3.4.3.3 Numerical modelling

To perform the numerical analysis, eight different discretisations were created, one for each different L_O, but the discretisation near the interface corners was the same regardless of L_O. The dimensions of the region that is discretized in the same manner are displayed in Figure 3.4.4 a) along with the number of nodes in that region, also the radial part of that region is shown in Figure 3.4.4 b). The overall dimensions of the joint are the same as the experimental joints, shown in Figure 3.4.1. The left boundary was considered fixed (U_x=U_y=U_z=0), while δ was imposed at the right boundary. The RPIM analysis was then performed using the authors' own MATLAB program. Additionally, a script to apply the equations of section 3.4.3.2 was developed to perform the ISSF analysis from the RPIM results. This script also allows to predict the maximum load (P_m) values based on the ISSF at the interface corner. All RPIM simulations assumed small strains and plane strain conditions, with 16 nodes per influence domain, and the shape function parameters γ=1.03 and p=1.42. It is also important to note that the influence domains near the interface have to be treated differently and a solution similar to the solution of reference [46] was adopted.

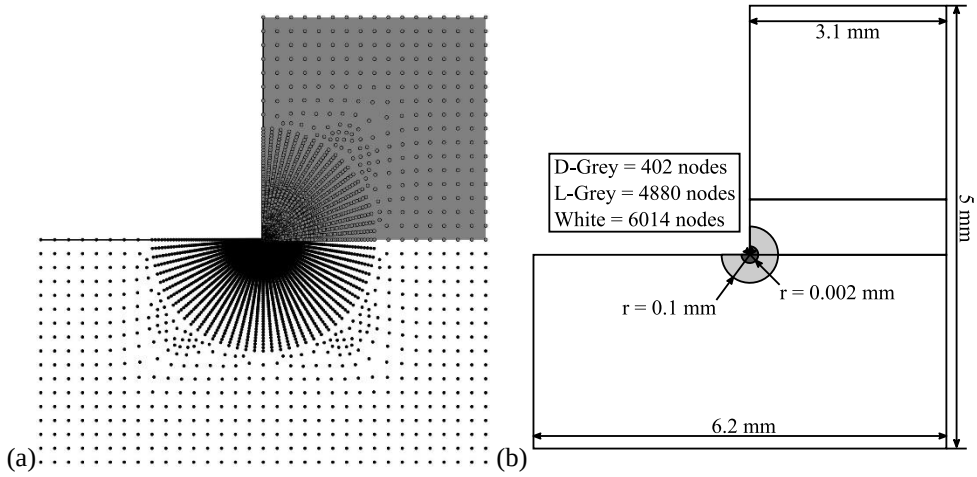

Figure 3.4.4 - (a) Discretization in an area of 1×1 mm² around the interface corner (b) Details of the discretization in the area around the interface corner

3.4.4 Results and discussion

3.4.4.1 Experimental results

Initially, the experimental data from the tensile tests is presented and analysed to serve as the basis for validating the ISSF technique that constitutes the primary purpose of this work. It should be initially mentioned that all failures were cohesive in the adhesive layer, which obliges to identify, after failure, a visible and homogeneous layer of adhesive on both adherends. Thus, no signs of interfacial (adhesive) or interlaminar failures were detected. In the particular case of interfacial failures, these are typically linked to poor fabrication, which would render the results not valid for the purpose of this work.

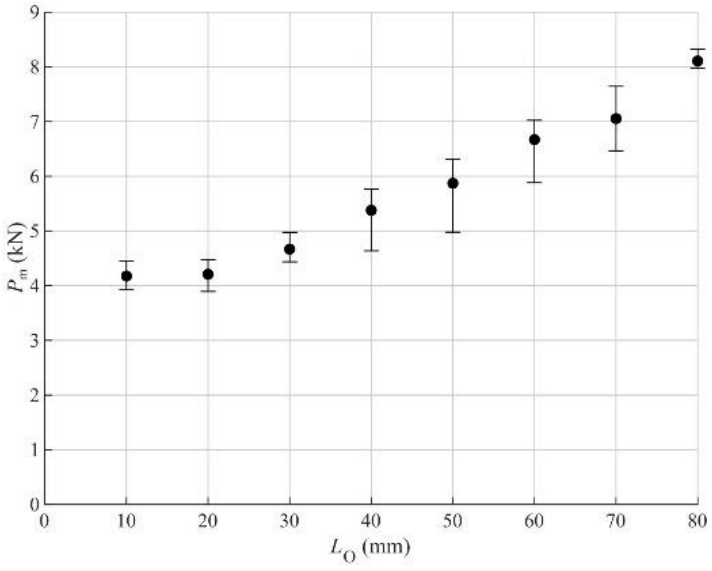

Figure 3.4.5 - P_m-L_O plot resultant from the experimental data

The analysed experimental data is collected in Figure 3.4.5 in the form of a P_m-L_O plot, including each L_O data point's minimum and maximum value. There is a marked L_O effect on P_m, translated by a regular increase of P_m with L_O. This tendency is documented in the literature notwithstanding the adhesive type, and it is closely related to the higher shear bonding area joining the two adherends [37]. Between adhesive types, brittle adhesives like the Araldite® AV138 perform well for short L_O but worse for high L_O due to the marked stress concentrations at the overlap edges [47]. In this case, the SLJ show a non-proportional improvement of P_m with L_O. For instance, the relative (%) P_m improvement between L_O=10 and 40 mm is only 28.79%, while reaching 94.13% between L_O=10 and 80 mm (limit L_O tested). The absolute P_m difference between the limit L_O was 13.1 kN. This behaviour is precisely related to the inability of this brittle adhesive to deal with the increasing peak stresses developing in the joint. These adhesive characteristics were reported in section 3.4.2.2, leading to a major performance depreciation for large L_O, quantified by the reduced P_m over the bonded area given by $L_O \times B$. The aforementioned stresses are not presented here due to being over addressed in the literature [48] and report on both peel (through-thickness normal) and shear stresses highly increasing at the overlap edges as L_O increases, while the central region is not transferring loads between the adherends. In particular, peel stresses are especially harmful to the adhesive at the overlap edges while quickly vanishing for the inner overlap. On the other hand, the shear stress gradient is less evident, but shear peak stresses are also found at the overlap edges, compared to a lighter loaded inner overlap [48]. In subsequent sections, these experimental results will be used for ISSF validation by direct P_m comparison.

3.4.4.2 ISSF analysis

After the numerical simulations have been completed, the ISSF analysis could be initialized. Firstly, the corner geometry was discretized. **Erro! A origem da referência não foi encontrada.** presents a scheme of the joint example studied in this work, in this case, a SLJ.

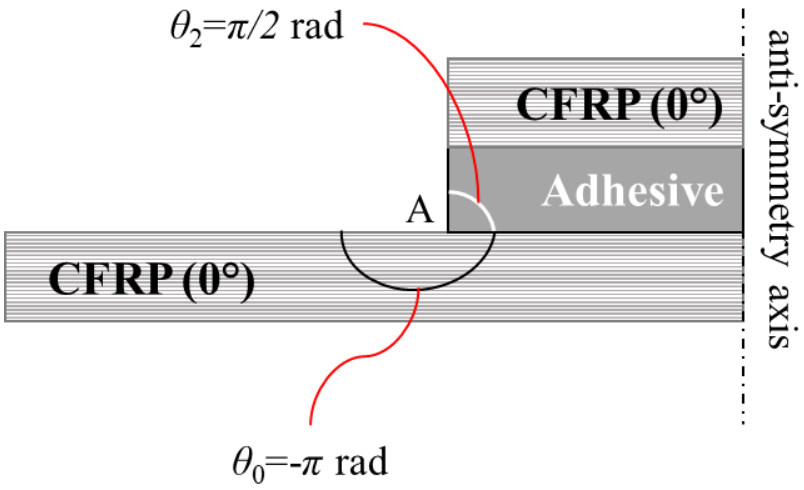

Figure 3.4.6 - SLJ corner geometry

The corner geometry necessary for this criterion consists of the angles formed between the materials where the corner is located. The starting points are the corner tip (point A) and the horizontal line where the adhesive and the CFRP are in contact, intercepting the corner tip (point A). This geometry is then defined by three angles, considering counter clockwise as positive. The first angle corresponds to the CFRP (θ_0=-π rad), while the third angle represents the adhesive (θ_2=π/2 rad), as shown in **Erro! A origem da referência não foi encontrada.**. The angle θ_1 is related to the horizontal line described before, being equal to 0 rad. This analysis is similar to other multi-material corners. At this stage, the CFRP and adhesive properties are also essential to compose matrix ***C*** from Equation (8). Next, the stress singularity exponents λ can be obtained, resorting to Equation (29). Since this equation presents the terms *cos* and *sin*, it can be considered periodic, originating an infinite number of solutions. However, only the solutions comprised in the interval 0<λ<1 are treated in the present study since they represent singular solutions. Therefore, three exponents λ were found: λ_1=0.6055, λ_2=0.7347 and λ_3=0.9866. In the present study, a plane-strain analysis was carried out. Thus, the exponent λ_2 was not considered since it corresponds to an anti-plane solution. The first phase of the criterion was finished by finding two new angles necessary to perform the procedure of the next phase. The angles chosen were θ_4=π/4 rad and θ_5=-3π/4 rad. These were not randomly chosen and intended to allow a stress singularity determination based on the nodes. One angle (θ_4) is in the descending part of the $\sigma_{\theta\theta}$ curve and the other (θ_5) in the ascending part of the same curve.

Advancing in the ISSF criterion, the next stage was the determination of the stress singularity components, i.e., the ISSF values designated H_1 and H_2. Since a planar analysis was considered, only two singular exponents λ were found. Thus only two stress singularities are considered (H_1 and H_2). In order to exemplify the H determination process, the case L_O=50 mm is considered. This process consists of solving the system from Equation (34). The matrix on the left side of the equation was completed by determining the $f_{\theta\theta}$ functions from Equation (30), while the right side corresponds to the

tangential numerical stresses obtained from the RPIM simulation described in section 3.4.3.3. The unknowns of the expression are H_1 and H_2. Nonetheless, these parameters cannot be directly determined for the corner tip since r=0 mm. Therefore, they were firstly obtained for several r in the interval 0<r<0.1 mm. Then, H_n (n=1 or n=2) were extrapolated from the values between 0.01 and 0.02 mm to the corner tip (r=0 mm). The extrapolation interval was chosen for its linear stability in the H-r curves and its proximity to the corner tip. Figure 3.4.7 shows the H_1-r curves and extrapolations for the case considered (L_O=50 mm). Only the H_1 component is presented since it is the most significant.

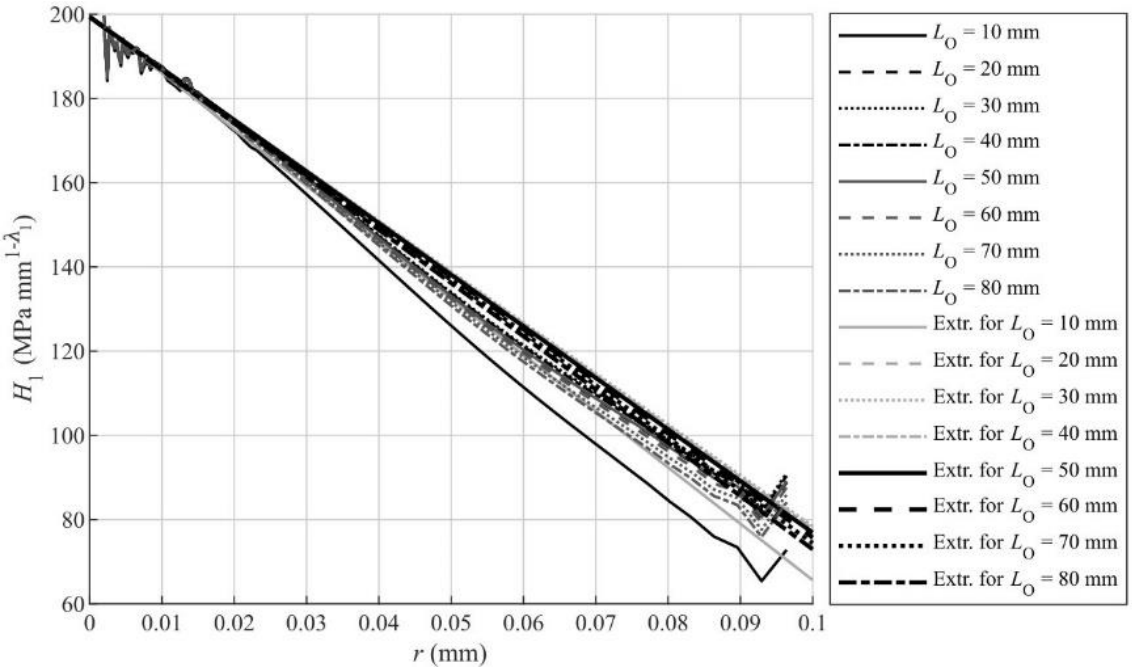

Figure 3.4.7 - H_1-r curves and extrapolations for the L_O=50 mm case

The graph also presents the H_1-r curves and extrapolations for other L_O. These were determined by imposing H_1 at r=0 mm as the H_1 determined for the L_O=50 mm case. The procedure described for this case was performed for each L_O. From the analysis of the H_1-r curves, an oscillation in the values between 0<r<0.01 mm is perceptible. This behaviour is due to the numerical approach (RPIM) used. Since the nodes in this interval are closer to the corner tip, the stresses are influenced by the higher concentration of influence domains and their overlapping, thus influencing the H_1 determination.

A comparison between the numerical and the analytical stresses was carried out to validate the presented H estimations. The numerical stresses were obtained from the RPIM simulations, while the analytical ones result from Equation (32). A specific r was chosen (r=0.0022 mm), where H_1 would be the same for all L_O, to evaluate the similarity between the stresses. Then, these were determined for all the angles comprised by the geometry of the SLJ considered. The obtained results are presented in Figure 3.4.8. The two components from Equation (32) were also plotted separately to demonstrate the

more significant influence of the first singularity component in the corner evaluation. Once again, some fluctuations are observed in the numerical stresses due to the RPIM approach and its dependence on the influence domains.

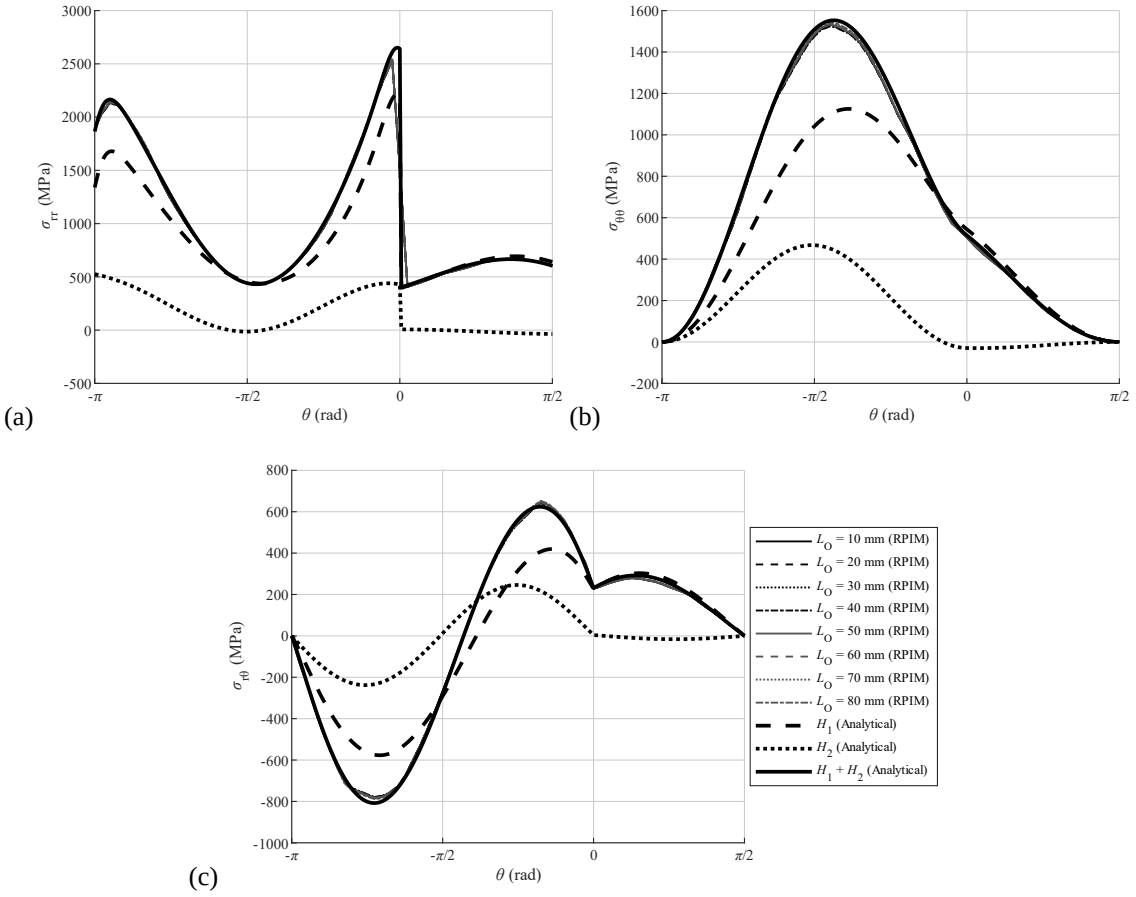

Figure 3.4.8 - Comparison between numerical and analytical stresses and between stress singularity components

3.4.4.3 Joint strength predictions

The final step of this work consisted of predicting P_m and respective comparison with the results extracted from the experimental data. In that regard, it was necessary to determine H_c. Currently, there are no standardized experimental methods to determine H_c. With that in mind, a formulation relying on a combination of experimental and numerical data was implemented in this work. The proposed method consists of performing numerical simulations with the experimental P_m by each joint of different L_O as the imposed natural boundary conditions. Then, by the process described in section 3.4.4.2, the H_n values were determined and used as the H_{nc} values (n=1 or n=2) for each L_O. The procedure and results presented in section 3.4.4.2 exemplify this method for the L_O=50 mm case. Initially, H_1 was determined, resorting to an RPIM simulation where the experimentally determined P_m for the L_O=50 mm joint was used as the imposed load.

The attained result was 199.37 MPa mm$^{1-\lambda}$, as perceptible in Figure 3.4.7, and it was used as the H_{1c} for this L_O. The H_{1c} were determined for all the L_O this way, resulting in the values presented in Table 3.4.3. The H_{2c} values can be determined during the same procedure.

Table 3.4.3 - H_{1c} values for each L_O

L_O used to determine H_{1c} (mm)	H_{1c} (MPa.mm$^{1-\lambda}$)
10	180.62
20	172.34
30	179.91
40	194.73
50	199.37
60	211.95
70	209.44
80	224.45

Finally, these H_{1c} were used to extrapolate the strength predictions for the other L_O. The same strategy was implemented for all L_O, originating the P_m predictions presented in Figure 3.4.9, where each curve contains the strength prediction for that L_O and the extrapolations for the other L_O.

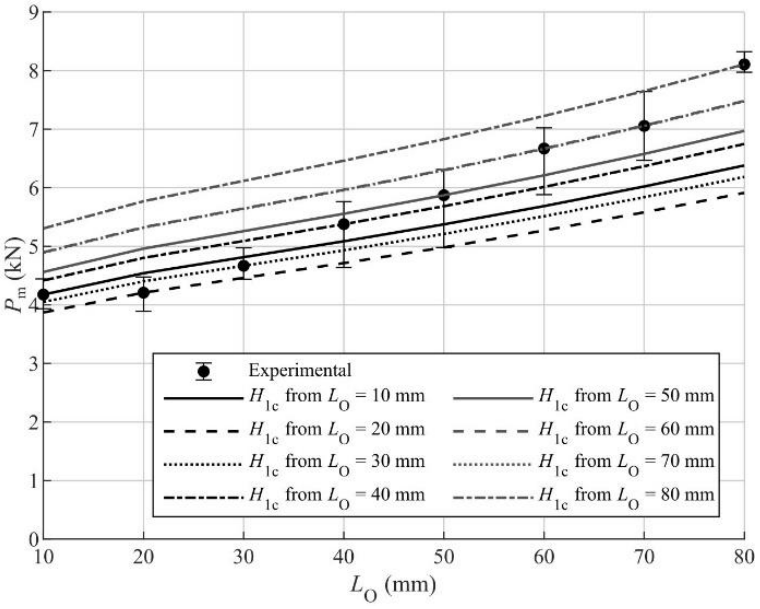

Figure 3.4.9 - P_m prediction graph for all the L_O

In general, P_m increases are smaller than those demonstrated in the experimental results. The only exception to this rule is the P_m increase between L_O=10 and 20 mm. In fact, the experimental P_m increase is considerably smaller than those predicted with the different H_{1c}. Nonetheless, this deviation to the behaviour detected between the other L_O can be ignored since the experimental P_m for L_O=10 mm is anomalous concerning the

proportionality of the experimental P_m-L_O curve. The most accentuated differences are verified between L_O=70 and 80 mm, where the experimental P_m increase was 1051.24 N and the predictions varied between 332.25 and 455.52 N. On the other hand, between L_O=60 and 70 mm, the discrepancies are much smaller, with a few prediction cases that even surpass the experimental P_m increase.

Another particularity from the obtained results is that, when predicting P_m for an L_O larger than the L_O used to determine H_{1c}, the result is generally an underprediction. However, two special cases break this law. The first is related to the same problem observed for the P_m prediction increases, i.e., when predicting the strength of the L_O=20 mm and the L_O=30 mm joints using L_O=10 mm to obtain H_{1c}, the outcome is an overprediction. Once again, this is due to the incongruous L_O=10 mm experimental P_m value. The second case is when L_O=60 mm was used to predict P_m of the L_O=70 mm joint, which resulted in a slight overprediction, with an error of 0.1%. As a matter of fact, all the P_m predictions attained using L_O=60 mm present marginally higher results than the P_m predictions reached when using L_O=70 mm. The contrary behaviour is also true, i.e., predicting P_m of an L_O smaller than the L_O used to determine H_{1c} originates over predictions, with the same two exceptions described.

Regarding the fluctuations between experimental and predicted P_m, it is safe to affirm that the higher the difference between the L_O used to obtain H_{1c} and the predicted joint L_O, the higher the percentual deviation in the results. The highest percentual deviation found was when L_O=80 mm was utilised to predict P_m for L_O=20 mm (37.10%), confirming the previous statement. However, if an L_O is used to predict P_m of a joint with an L_O that does not differ in more than 20 mm (±20 mm) from that L_O, the deviations decrease considerably. In this situation, the case where L_O=40 mm was used to predict P_m for L_O=20 mm revealed the higher discrepancy (14.11%). Considering the same situation, the majority of the other cases presents percentual deviations inferior to 10%. As mentioned before, all P_m predictions attained with L_O=60 mm and L_O=70 mm present incredibly similar results, with fluctuations below 1%.

3.4.5 Conclusions

The present study aimed to validate the use of the ISSF criterion in meshless methods. Firstly, SLJ composed of CFRP and bonded with a brittle adhesive were experimentally tested to collect the average P_m. Also, to evaluate the influence of L_O in the final results, eight different L_O were tested, between 10 and 80 mm. Then, the ISSF criterion was implemented. This implementation allowed concluding that, for the geometry and material combination applied in this work, three singularity exponents λ characterize the bi-material interface corner. However, one of those λ corresponded to an anti-plane solution, reason for excluding it from the analysis since a plane strain condition was implemented. Regarding H_{1c}, necessary for the P_m prediction, an alternative to the usually complex methods that have already been investigated is implemented. It consists of numerically simulating the joints, considering the experimentally determined P_m as the imposed loads. For this, the RPIM was used, intending to fulfil the primary objective of this work. These simulations were then used to determine the H_1 values that were considered the H_{1c} for each L_O. The proposed method showed some variance depending on which L_O is used, except when comparing the H_{1c} obtained with L_O=60 and 70 mm, which were very similar. The results showed P_m increases between L_O generally smaller than those verified experimentally. Also, when predicting P_m of an L_O larger than the L_O used to determine H_{1c}, the result was an underprediction. The only exceptions to these patterns were the L_O=10 mm case, which revealed unsatisfactory results due to an anomaly in the experimental data, and the L_O=60 and 70 mm cases, where the P_m predictions attained with L_O=60 mm were slightly higher than those of L_O=70 mm, but incredibly similar (percentual deviations below 1%). With this in mind, when applying this methodology, it is recommended to only predict P_m of joints with a L_O larger than the L_O used to determine H_{1c}. However, given the simplicity of the applied method, the results are auspicious. In that sense, it can be concluded that the ISSF criterion can be applied to meshless methods, to composite materials and to different corner geometries.

3.4.6 References

[1] Degano, I., S. Soriano, P. Villa, L. Pollarolo, J.J. Lucejko, Z. Jacobs, K. Douka, S. Vitagliano and C. Tozzi, *Hafting of Middle Paleolithic tools in Latium (central Italy): new data from Fossellone and Sant'Agostino caves.* PLoS One, 2019. **14**(6): p. e0213473.

[2] Petrie, E.M., *Handbook of adhesives and sealants*. 2000, U.S: McGraw-Hill.

[3] Borsellino, C., L. Calabrese and A. Valenza, *Experimental and numerical evaluation of sandwich composite structures.* Composites Science and Technology, 2004. **64**(10-11): p. 1709-1715.

[4] Li, T. and L. Wang, *Bending behavior of sandwich composite structures with tunable 3D-printed core materials.* Composite Structures, 2017. **175**: p. 46-57.

[5] Elamin, M., B. Li and K.T. Tan, *Impact damage of composite sandwich structures in arctic condition.* Composite Structures, 2018. **192**: p. 422-433.

[6] He, W., J. Liu, S. Wang and D. Xie, *Low-velocity impact response and post-impact flexural behaviour of composite sandwich structures with corrugated cores.* Composite Structures, 2018. **189**: p. 37-53.

[7] Volkersen, O., *Die Nietkraftverteilung in zugbeanspruchten Nietverbindungen mit konstanten Laschenquerschnitten.* Jahrbuch der Deutschen Luftfahrtforschung, 1938. **15**: p. 41-47.

[8] Campilho, R.D., *Strength prediction of adhesively-bonded joints*. 2017, Boca Raton, U.S.: CRC Press.

[9] da Silva, L.F., P.J. das Neves, R. Adams, A. Wang and J. Spelt, *Analytical models of adhesively bonded joints—Part II: Comparative study.* International Journal of Adhesion and Adhesives, 2009. **29**(3): p. 331-341.

[10] Goland, M. and E. Reissner, *The stresses in cemented joints.* Journal of Applied Mechanics, 1944. **66**: p. A17-A27.

[11] Hart-Smith, L.J., *Adhesive-bonded single-lap joints*, in *NASA Contract Report, NASA CR-112236*. 1973.

[12] Ramalho, L.D.C., R.D.S.G. Campilho, J. Belinha and L.F.M. da Silva, *Static strength prediction of adhesive joints: A review.* International Journal of Adhesion and Adhesives, 2020. **96**: p. 102451.

[13] Campilho, R.D.S.G., M.D. Banea, J.A.B.P. Neto and L.F.M. da Silva, *Modelling adhesive joints with cohesive zone models: effect of the cohesive law shape of the adhesive layer.* International Journal of Adhesion and Adhesives, 2013. **44**: p. 48-56.

[14] Anderson, T.L., *Fracture mechanics: fundamentals and applications*. 2017, Boca Raton, U.S.: CRC press.

[15] Rice, J.R., *A path independent integral and the approximate analysis of strain concentration by notches and cracks.* Journal of Applied Mechanics, 1968. **35**(2): p. 379-386.

[16] Rybicki, E.F. and M.F. Kanninen, *A finite element calculation of stress intensity factors by a modified crack closure integral.* Engineering Fracture Mechanics, 1977. **9**(4): p. 931-938.

[17] Jones, S., B. Stier, B.A. Bednarcyk, E.J. Pineda and U.R. Palliyaguru. *Verification, Validation, and Limits of Applicability of a Rapid Bonded Joint Analysis Tool*. in *AIAA Scitech 2020 Forum*. 2020.

[18] Irwin, G.R., *Analysis of Stresses and Strains Near the End of a Crack Traversing a Plate.* Journal of Applied Mechanics, 1957. **24**(3): p. 361-364.

[19] Qian, Z.Q. and A.R. Akisanya, *Wedge corner stress behaviour of bonded dissimilar materials.* Theoretical and Applied Fracture Mechanics, 1999. **32**(3): p. 209-222.

[20] Wu, Z., S. Tian, Y. Hua and X. Gu, *On the interfacial strength of bonded scarf joints.* Engineering Fracture Mechanics, 2014. **131**: p. 142-149.

[21] Galvez, P., N.-A. Noda, R. Takaki, Y. Sano, T. Miyazaki, J. Abenojar and M.A. Martínez, *Intensity of singular stress field (ISSF) variation as a function of the Young's modulus in single lap adhesive joints.* International Journal of Adhesion and Adhesives, 2019. **95**: p. 102418.

[22] Delale, F., *Stress singularities in bonded anisotropic materials.* International Journal of Solids and Structures, 1984. **20**(1): p. 31-40.

[23] Chen, H.-P., *Stress singularities in anisotropic multi-material wedges and junctions.* International Journal of Solids and Structures, 1998. **35**(11): p. 1057-1073.

[24] Pageau, S.S. and S.B. Biggers, *A finite element approach to three-dimensional singular stress states in anisotropic multi-material wedges and junctions.* International Journal of Solids and Structures, 1996. **33**(1): p. 33-47.

[25] Stroh, A.N., *Steady State Problems in Anisotropic Elasticity.* 1962. **41**(1-4): p. 77-103.

[26] Yao, S., M. Zappalorto, W. Pan, C. Cheng and Z. Niu, *Two dimensional displacement and stress fields for tri-material V-notches and sharp inclusions in anisotropic plates.* European Journal of Mechanics - A/Solids, 2020. **80**: p. 103927.

[27] Ting, T.C.T. and H. Chyanbin, *Sextic formalism in anisotropic elasticity for almost non-semisimple matrix N.* International Journal of Solids and Structures, 1988. **24**(1): p. 65-76.

[28] Barroso, A., V. Mantič and F. París, *Singularity analysis of anisotropic multimaterial corners.* International Journal of Fracture, 2003. **119**(1): p. 1-23.

[29] Barroso, A., J.C. Marín, V. Mantič and F. París, *Premature failures in standard test specimens with composite materials induced by stress singularities in adhesive joints.* International Journal of Adhesion and Adhesives, 2020. **97**: p. 102478.

[30] Leguillon, D., *Strength or toughness? A criterion for crack onset at a notch.* European Journal of Mechanics-A/Solids, 2002. **21**(1): p. 61-72.

[31] Liu, G.-R. and Y.-T. Gu, *An introduction to meshfree methods and their programming*. 2005, Dordrecht, The Netherlands: Springer Science & Business Media.

[32] Wang, R., L. Zhang, D. Hu, C. Liu, X. Shen, C. Cho and B. Li, *A novel approach to impose periodic boundary condition on braided composite RVE model based on RPIM.* Composite Structures, 2017. **163**: p. 77-88.

[33] Ramalho, L.D.C., I.J. Sánchez-Arce, R.D.S.G. Campilho and J. Belinha, *Strength prediction of composite single lap joints using the radial point interpolation method.* Composite Structures, 2021. **259**: p. 113228.

[34] Campilho, R.D.S.G., M.F.S.F. De Moura and J.J.M.S. Domingues, *Modelling single and double-lap repairs on composite materials.* Composites Science and Technology, 2005. **65**(13): p. 1948-1958.

[35] Oliveira, J.J.G., R.D.S.G. Campilho, F.J.G. Silva, E.A.S. Marques, J.J.M. Machado and L.F.M. da Silva, *Adhesive thickness effects on the mixed-mode fracture toughness of bonded joints.* The Journal of Adhesion, 2020. **96**(1-4): p. 300-320.

[36] Campilho, R.D.S.G., M.F.S.F. de Moura and J.J.M.S. Domingues, *Stress and failure analyses of scarf repaired CFRP laminates using a cohesive damage model.* Journal of Adhesion Science and Technology, 2007. **21**(9): p. 855-870.

[37] De Sousa, C.C.R.G., R.D.S.G. Campilho, E.A.S. Marques, M. Costa and L.F.M. da Silva, *Overview of different strength prediction techniques for single-lap bonded joints.* Proceedings of the Institution of Mechanical Engineers, Part L: Journal of Materials: Design Applications, 2017. **231**: p. 210-223.

[38] Wang, S., W. Liang, L. Duan, G. Li and J. Cui, *Effects of loading rates on mechanical property and failure behavior of single-lap adhesive joints with carbon fiber reinforced plastics and aluminum alloys.* The International Journal of Advanced Manufacturing Technology, 2020. **106**(5): p. 2569-2581.

[39] Belinha, J., *Meshless methods in biomechanics: Bone tissue remodelling analysis*. Vol. 16. 2014, Switzerland: Springer.

[40] Liu, G.R., *A point assembly method for stress analysis for two-dimensional solids.* International Journal of Solids and Structures, 2002. **39**(1): p. 261-276.

[41] Wang, J.G. and G.R. Liu, *On the optimal shape parameters of radial basis functions used for 2-D meshless methods.* Computer Methods in Applied Mechanics and Engineering, 2002. **191**(23-24): p. 2611-2630.

[42] Stroh, A.N., *Steady state problems in anisotropic elasticity.* Journal of Mathematics and Physics, 1962. **41**(1-4): p. 77-103.

[43] Mantič, V., A. Barroso and F. París, *Singular Elastic Solutions in Anisotropic Multimaterial Corners: Applications to Composites*, in *Mathematical Methods and Models in Composites*. 2013, World Scientific. p. 425-495.

[44] Qian, Z. and A. Akisanya, *Wedge corner stress behaviour of bonded dissimilar materials.* Theoretical and Applied Fracture Mechanics, 1999. **32**(3): p. 209-222.

[45] Klusák, J., T. Profant and M. Kotoul, *Various methods of numerical estimation of generalized stress intensity factors of bi-material notches.* Applied and Computational Mechanics, 2009. **3**(2).

[46] Ramalho, L.D.C., I.J. Sánchez-Arce, R.D.S.G. Campilho and J. Belinha, *Strength prediction of composite single lap joints using the critical longitudinal strain criterion and a meshless method.* International Journal of Adhesion and Adhesives, 2021. **108**: p. 102884.

[47] Nunes, S.L.S., R.D.S.G. Campilho, F.J.G. da Silva, C.C.R.G. de Sousa, T.A.B. Fernandes, M.D. Banea and L.F.M. da Silva, *Comparative failure assessment of single and double-lap joints with varying adhesive systems.* The Journal of Adhesion, 2016. **92**: p. 610-634.

[48] Barbosa, N.G.C., R.D.S.G. Campilho, F.J.G. Silva and R.D.F. Moreira, *Comparison of different adhesively-bonded joint types for mechanical structures.* Applied Adhesion Science, 2018. **6**(1): p. 15.

CONCLUSIONS

4 CONCLUSIONS

The present work aimed to propose and evaluate a different approach to the stress singularities in bonded joints studied by fracture mechanics techniques. This goal was accomplished by experimentally testing SLJs bonded with two different materials (aluminium and CFRP) and a brittle adhesive, and then compare the obtained data to the numerical models created resorting to the FEM and RPIM. Different L_O were also tested to assess this parameter influence in the final results. The validation of the proposed method was also achieved by analysing the polar stresses around the interface adhesive/adherend corner tip. All the developed work was presented in the scientific paper form with the intention of publishing it in specialised journals, divided into four papers.

The first step in each of the four papers was the experimental data analysis, in which the average maximum loads (P_m) sustained by the SLJs was collected. Regarding the aluminium SLJs (Papers 1 and 2), four L_O were tested (starting at 12.5 mm and incrementing it by 12.5 mm each time), while eight L_O (starting at 10 mm and incrementing it by 10 mm each time) were evaluated in the composite SLJs (Papers 3 and 4). The treated data allowed understanding that the P_m-L_O curve is linear, presenting a monotonic increase. The only exception to this behaviour was found in the L_O=10 mm composite SLJs, where P_m did not follow the tendency. However, this was treated as an experimental anomaly, not questioning the observed behaviour. For higher L_O, it was perceptible that the linear tendency of the P_m-L_O curves was not verified, marked by smaller strength increases between L_O. Nonetheless, this observation is normal in adhesives such as those used due to their brittleness, not allowing the joint to accommodate the increasing peak stresses.

The ISSF criterion was applied resorting to two different formulations. The formulation presented in Papers 1 and 2 is exclusively appropriate to isotropic materials such as aluminium or the adhesive, while the formulation of Papers 3 and 4 is also appropriate to orthotropic materials. Notwithstanding, the only difference between the formulations is the determination of the eigenvalues. In Papers 1 and 2, it was verified that two components characterise the stress singularity (H_1 and H_2). Yet, for the orthotropic formulation (Papers 3 and 4), three components arose. However, one of them corresponded to an anti-plane solution, and it was not considered.

The method proposed to determine the critical stress singularities (H_c) consisted of using the experimentally determined P_m as the imposed load in numerical FEM (Papers 1 and 3) and RPIM (Papers 2 and 4) simulations for each L_O. The resultant stress singularities were then used as H_c for each L_O. Relatively to the FEM, the RPIM results presented

some oscillations that can be explained by the overlapping of influence domains, although not influencing the final predictions. In general, predicted strengths were lower than the experimental strength when the H_{1c} determined with a smaller L_O was used to predict the strength of a larger L_O. The strength predictions attained with L_O=10 mm for the composite SLJs (Papers 3 and 4) were the only case where this rule was not verified, but since it was established that an anomaly was found in the experimental data, this confirms the veracity of the statement. For engineering purposes, since it is better to have conservative strength predictions, due to safety reasons, it would be advisable to only predict the strength of joints with L_O larger than the L_O used to determine H_c.

Taking into account the obtained results, it can be concluded that this technique is very promising. Moreover, the fact that it also contributes significantly to reducing the computational resources for numerical simulations is extremely important. Its validity was proved to both isotropic and orthotropic materials, which is significant nowadays, considering the widespread of multi-material structures. The ISSF criterion was also validated for finite element-based analysis and meshless methods.

However, like in any other subject in engineering and investigation, this work can be further improved with:

- new experimental testing to the composite adhesive joints to confirm the anomaly detected in the L_O=10 mm case;
- analysis of different adhesive joint configurations, such as double-lap joints or scarf joints;
- analysis of the influence of other geometrical properties such as the adhesive thickness or the adherend thickness;
- analysis of different corner geometries, such as corners with other angles;
- analysis of different material combinations;
- non-planar or plane-stress analysis that could sharpen the method's capacity.

ANNEXES

JOINT MANUFACTURING PROCESS AND SPECIMEN TESTING

The manufacturing process started with the cut of the composite plies.

A 1 – Composite plies cut

Then, the stacking was performed, assuring that all the layers were aligned at 0°. The plies were slightly heated for better adhesion. Afterwards, a Teflon coating film was applied to the composite plate to avoid the resin's escape during the curing process in the hot plates press, as well as two calibrated bars orientated in the direction of the fibres.

A 2 - Hot plates press and detail of the hot plates

The cure consisted of a thermic cycle at a pressure of 4 bar. After that time, the cooling process starts by setting a 20°C temperature in the press. When the plate reached 60°C, it was removed from the press and left to cool at room temperature.

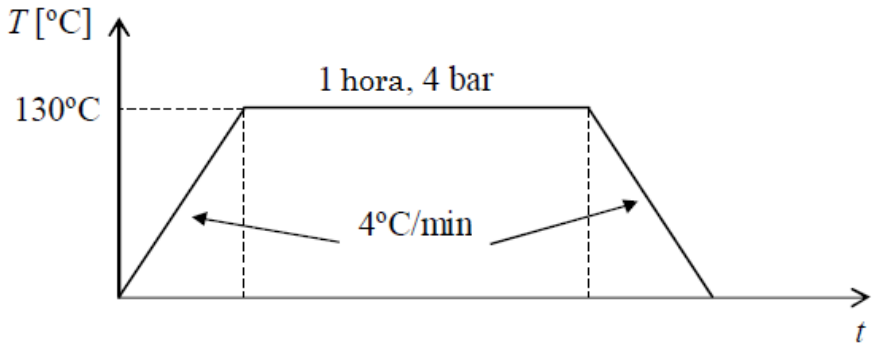

A 3 - Cure thermic cycle

From this phase on, the manufacturing process was common to both types of joints. Therefore, the adherends were cut, and the surface was prepared for the application of the adhesive.

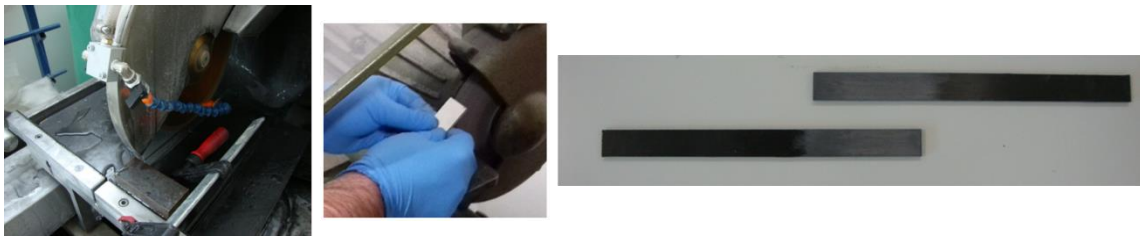

A 4 - Adherend cut and surface preparation

The joints were placed in a jig, assuring a perfect alignment. Readily, the adhesive was applied as well as small calibrated wires that ensure the correct adhesive thickness.

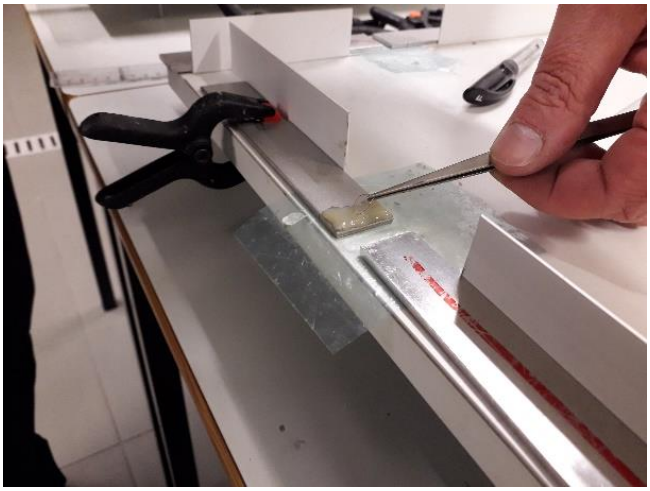

A 5 - Adhesive application

Finally, the adhesive had time to cure, and in the end, the excess of this material was removed.

A 6 - Adhesive cure and post-cure finishes

The joints were tested using a SHIMADZU electro-mechanical testing machine. This device has a 100 kN load cell, and the tests were performed at room temperature. These tests were executed with a 1 mm/min velocity. Twenty specimens with aluminium adherends (five for each L_O) and forty specimens with composite adherends (also five for each L_O) were evaluated.

A 7 - SHIMADZU electro mechanical testing machine and specimen testing

PAPER 1

FRACTURE MECHANICS APPROACH TO STRESS SINGULARITY IN ADHESIVE JOINTS

INTERNATIONAL JOURNAL OF FRACTURE

Int J Fract
https://doi.org/10.1007/s10704-021-00594-z

ORIGINAL PAPER

Fracture mechanics approach to stress singularity in adhesive joints

J. M. M. Dionísio · L. D. C. Ramalho · I. J. Sánchez-Arce · R. D. S. G. Campilho · J. Belinha

Received: 20 April 2021 / Accepted: 20 September 2021

Abstract Adhesives offer significant advantages when joining materials since they do not create discontinuities in the material, unlike bolting or riveting. Another interest of adhesive joints is the possibility of joining different materials and the lower weight. The analysis of the stress singularity in adhesive joints can provide a better understanding of joint behaviour, and it is mesh independent. The ISSF is based on a fracture mechanics concept, the Stress Intensity Factor (SIF). However, generally, the SIF is only applicable to cracks in a single material, while the ISSF is applicable to multi-material corners and does not require a crack. This work aims to study the stress singularity of aluminium adhesive joints bonded with a brittle adhesive with four different overlap lengths (L_O) by determining the singularity's exponents and its intensity. A method for joint strength prediction using the ISSF is also proposed. Additionally, the interface corner's stress is studied, with the different singularity components presented separately to assess their influence on the overall stress. These predictions are also compared with the experimental strength to verify this strength prediction criterion's accuracy when applied to brittle adhesives. In conclusion, the ISSF criterion provides accurate results and can be utilised for further studies in this area.

Keywords ISSF criterion · Adhesive joints · Finite Element Method · Single-lap joints

J. M. M. Dionísio · R. D. S. G. Campilho (✉) · J. Belinha
Departamento de Engenharia Mecânica, Instituto Superior de Engenharia do Porto, Instituto Politécnico do Porto, Rua Dr. António Bernardino de Almeida, 431, 4200-072 Porto, Portugal
e-mail: raulcampilho@gmail.com

L. D. C. Ramalho · I. J. Sánchez-Arce · R. D. S. G. Campilho
INEGI – Pólo FEUP, Rua Dr. Roberto Frias, s/n, 4200-465 Porto, Portugal

1 Introduction

Optimal structural design is intrinsically associated with multi-component structures since it is possible to optimise the specific strength and stiffness by combining different materials, each one tailored for its function within the structure (Jairaja and Naik 2019), and also to expedite fabrication and reduce the associated costs in structures with complex shapes, which can benefit from division in simpler shapes joined together (Jeevi et al. 2019). Depending on the application and design restrictions, varying joining techniques can be applied. A significant body of knowledge exists in the literature, including a comparison between joining technologies for selected purposes (Garrido et al. 2018). The most relevant joining methods for industrial applications are riveting, bolting, welding, brazing, and adhesive bonding. Although adhesive joints are used historically, their

Published online: 26 October 2021

structural use was only widely developed in the first half of the twentieth century by the aeronautical field. With the advancements in the adhesives' formulations, resulting in ever-increasing adhesive and joint performance, and design tools, consisting of simulation packages and suitable criteria for strength prediction, adhesive bonding is now essential in structural applications including aerospace, aeronautical, automotive, sports, civil engineering structures and electronics (Gui et al. 2018). This option became possible due to a set of characteristics (over conventional techniques) such as the unnecessity of drilling or damaging the parent materials to be joined, saving weight, improving stresses across the bonding regions, and ease of joining different materials. Possible limitations are the typical impossibility to disassemble after joining, required curing time, lack of confidence in the design, especially for fatigue and long-term analyses, and large scatter in experimental testing (Du et al. 2004).

Since the use of adhesive joints has been increasing in several industries in recent times (Konstantakopoulou et al. 2016), it is important to use design tools that accurately model and predict the behaviour of adhesive joints to reduce the amount of experimental tests needed, which are, usually, costlier and take more time than numerical simulations. In the early stages of adhesive joint analysis, analytical methods were used to determine the stress distributions at the adhesive layer, namely the Volkersen (1938) model, the Goland and Reissner (1944) model or the Hart-Smith (1973) model. However, these models have severe limitations since, for some, the formulation is difficult, while for others, the formulation is simple, but many assumptions are made, rendering the resulting stress distribution less accurate. These limitations mean that in recent years most literature focuses on numerical methods to analyse adhesive joints, although examples of analytical models developed in recent times can still be found, like the work by Carbas et al. (2014) for graded adhesive joints. A literature review by Ramalho et al. (2020) found that the most commonly used method to predict the strength of adhesive joints is Cohesive Zone Models (CZM), used together with the Finite Element Method (FEM) (Blackman et al. 2003). CZM generally provide accurate strength predictions, as long as the cohesive law shape/formulation and the respective parameters are appropriate. A simple triangular law can be used for brittle adhesives, but ductile adhesives generally require more complex laws, such as the trapezoidal law or an exponential law (Carvalho and Campilho 2017). Campilho et al. (2013) evaluated the CZM accuracy of adhesive layers modelled with different law shapes in predicting the strength of composite single-lap joints (SLJ) under different geometries. The obtained results showed that triangular CZM models are most suitable for brittle adhesives, while ductile adhesives can be accurately dealt with trapezoidal CZM laws that capture the high-stress levels after damage onset. Despite this fact, the relative errors of these two law shapes were always under 10%, reinforcing that CZM, which is based on an area concept for crack propagation, i.e., mainly depending on the fracture energies, which gives satisfactory results even with less adequate models. Even though the strength predictions with CZM are accurate, these models have a significant drawback in that they require extensive experimental testing because the cohesive law parameters change with the adhesive thickness (t_A) and other geometric parameters affecting the damage zone in the adhesive in the advent of crack propagation. The t_A effect in CZM modelling with a triangular law was addressed by Xu and Wei (2013) by simulating SLJ with different t_A, particularly showing that smaller t_A increases the joint strength. Additionally, the proposed CZM yielded accurate strength predictions for the brittle adhesive, although the ductile adhesive joint performance with the smallest t_A is underestimated. Demiral and Kadioglu (2018) also showed the t_A influence on strength by CZM, namely SLJ strength reduction by increasing t_A, although this effect was much smaller than that of the overlap length (L_O), whose increase highly benefited the joint strength. Therefore, authors have also experimented with other methods to predict joint strength, such as the eXtended FEM (XFEM) (Stein et al. 2017), sometimes also combined with CZM (Stuparu et al. 2016), or even the common FEM using failure criteria based on continuum mechanics (Sánchez-Arce et al. 2021), fracture mechanics (Jiang et al. 2021) or damage mechanics (Sugiman and Ahmad 2017). Some authors have also used the previous criteria with meshless methods (Ramalho et al. 2019) or meshless methods combined with CZM (Tsai et al. 2014) to predict joint strength.

Fracture mechanics, in particular, can assess stress or strain singularities due to material discontinuities

(Da Silva and Campilho 2012), which in bonded joints are usually related to the sharp corners at the overlap edges at the interface between an adherend and the adhesive layer. Conventionally, fracture mechanics can rely on stress intensity factors (Parks 1974; Matos et al. 1989) or energetic approaches (Lazzarin and Zambardi 2001), depending on the materials' fracture toughness. In the last option, the most widespread techniques are the J-integral (Rice 1968) and the Virtual Crack Closure Technique (VCCT) (Rybicki and Kanninen 1977). More recently, Finite Fracture Mechanics (FFM) was proposed by Leguillon (2002), consisting of a coupled stress-energy criterion for crack initiation and accounting for published work on adhesive joints (Hell et al. 2014). FFM does not require an initial crack and, for crack initiation, both a stress and an energetic criterion should be fulfilled. However, it is essentially applicable to brittle adhesives. In adhesive joints, as previously discussed, there exists a stress singularity at the adhesive/adherend interface corners, whose magnitude is usually called Intensity of Singular Stress Fields (ISSF) or Generalised Stress Intensity Factor (GSIF). The first published works trying to characterise this singularity date back to the mid-twentieth century (Williams 1959; Bogy 1968).

This singularity analysis has been performed in many different types of adhesive joints, including scarf joints (Wu et al. 2014), butt joints (Afendi et al. 2013), Double Lap Joints (DLJ) (Mintzas and Nowell 2012) and SLJ (Rastegar et al. 2018). Zhang et al. (2015) proposed a new method to calculate the ISSF in bonded butt joints under tension and bending, due to the known difficulties in using the FEM because of the existing singularity. The new method only considers stresses of the first elements at the end of the interface between the adhesive and adherend materials. Different combinations of materials and values of tA were analysed and positively validated against experiments from previous works. It was also found that the ISSF was dependent on the joint materials and that the ISSF increased with tA until tA reached the joint width. Interactions between the singular stress fields at the two adhesive/adherend interfaces were also found, although this issue was remitted to future works. In the work of Li et al. (2018), SLJ and DLJ bonded joints were used to investigate the adhesive strength by evaluating and minimising the ISSF at the interface end. It was shown that the ISSF diminishes by increasing the adherends' thickness (t_P) and that the minimum ISSF is achieved for a sufficiently high adherend thickness. Due to the DLJ having twice the bonding area and suppressing peel stresses and transverse deflection, the equivalent strength condition between identical material SLJ and DLJ was evaluated by the ISSF, leading to an equal strength between a SLJ with an adherend thickness of 7 mm and a DLJ with 1.5 mm. Galvez et al. (2019) applied the ISSF concept to analyse mixed adhesive joints, i.e., with two adhesives in the bond line (with different stiffness and mechanical properties), to achieve strength optimisation. Four adhesive combinations were tested, including the two with single use of each of the adhesives. The proposed approach was based on the reciprocal work contour integral method (RWCIM), and it involved estimating the ISSF for the reference models (joints with the single adhesive), which were then applied for the unknown solution (mixed-adhesive joints). A clear improvement was found for one of the mixed-adhesive joint configurations, with a 36% reduction in the ISSF, when compared to the single-adhesive solutions.

The present work aims at studying the singularity in SLJ, with different L_O, bonded with a brittle adhesive and proposing a method to determine joint strength using the ISSF. The ISSF analysis and the strength predictions are performed using the FEM. This analysis is done to a material combination that was never previously studied using the ISSF. The stress around the interface corner is also studied, with the different singularity components presented separately to assess their influence on the overall stress. Additionally, a comparison between the stress obtained with the ISSF formula and the stress extracted from the FEM for the different L_O is compared to validate the formulation used to obtain the ISSF. The mesh independence of this approach is also assessed by studying two different mesh refinement levels. Finally, these predictions are also compared with the experimental strength to verify this strength prediction criterion's accuracy when applied to brittle adhesives.

2 Experimental work

2.1 Joint geometry

In this work, SLJ made of aluminium adherends bonded with the adhesive Araldite® AV138 were studied. The geometry and boundary conditions of the numerical model are shown in Fig. 1. The SLJ was fixed at the left boundary, and a displacement (δ) was imposed at the right boundary. Four different L_O were tested, from 12.5 to 50 mm in increments of 12.5 mm. The other relevant geometrical properties are the adherend thickness t_P = 3 mm, the adhesive thickness t_A = 0.2 mm, the total joint length L_T = 180 mm and the joint width B = 25 mm.

2.2 Materials

The SLJ were fabricated from Al6082-T651 aluminium alloy adherends. The adherend material is commonly used for structural appliances since it has good strength and ductility. Full characterisation of this aluminium is presented in previous works (Campilho et al. 2011a,b), consisting of tensile bulk testing and subsequent data analysis of the load–displacement (P–δ) curves. The collected data is presented in Table 1 (E is Young's modulus, v the Poisson coefficient, σ_y the tensile yield stress, σ_f the tensile strength and ε_f the tensile failure strain).

Application of the ISSF to bonded joints was assessed by SLJ bonded with the Araldite® AV138, a strong but brittle epoxy adhesive. This adhesive has a tensile strength of approximately 40 MPa, which is significant for modern adhesives, but its brittleness highly limits the associated bonded joints' performance, especially for high L_O. For short L_O, in which stresses in the bond line tend to be more uniform due to smaller shear-lag and rotation effects, this adhesive still manages to compete with ductile adhesives, but it quickly fails to work for high L_O, in which stress gradients become significant. These findings were reported in reference (Campilho et al. 2011a). This adhesive was evaluated by different testing architectures to acquire the required data to input into the models. The tensile mechanical properties (E, σ_y, σ_f and ε_f) were acquired from tensile tests to bulk specimens, considering the French standard NF T 76–142 indications for the geometry and fabrication process. The mechanical shear properties (shear modulus—G, shear yield stress—τ_y, shear strength—τ_f and shear failure strain—γ_f) were obtained from Thick Adherend Shear Tests (TAST). For this test, the 11003-2:1999 ISO standard was followed regarding the fabrication and testing procedures. Thus, all specimens were cured in a rigid mould to ensure the proper adherends' longitudinal alignment, and DIN C45E steel adherends were used to minimise adherend-induced deformations affecting the obtained results. Table 2 collects all data for the adhesive. It should be mentioned that Hooke's law relationship for isotropic materials (between E and G), and also the expected s_y/t_y relationship by Tresca or von Mises criteria, are not met in the obtained data due to different restraint conditions (unrestrained adhesive in the bulk tests vs. restrained adhesive in the TAST tests).

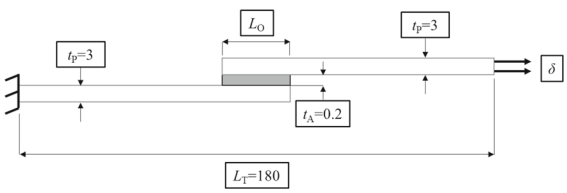

Fig. 1 Geometry and boundary conditions of the SLJ (dimensions in mm)

Table 1 Mechanical properties of the aluminium adherends (Campilho et al. 2011a,b)

Property	Value
E (GPa)	70.1 ± 0.83
ν	0.30
σ_y (MPa)	261.67 ± 7.65
σ_f (MPa)	324.00 ± 0.16
e_f (%)	21.70 ± 4.24

Table 2 Mechanical properties of the adhesive (De Sousa et al. 2017)

Property	AV138
E (GPa)	4.89 ± 0.81
ν	0.35[a]
σ_y (MPa)	36.49 ± 2.47
σ_f (MPa)	39.45 ± 3.18
e_f (%)	1.21 ± 0.10
G (GPa)	1.56 ± 0.01
τ_y (MPa)	25.1 ± 0.33
τ_f (MPa)	30.2 ± 0.40
γ_f (%)	7.8 ± 0.7

[a]Data from the manufacturer

2.3 Fabrication and testing

For the joint fabrication, it was initially necessary to prepare the bonding surfaces. This process consisted of the adherends sandblasting with corundum sand followed by cleaning the surface with acetone until no traces of contaminants exist that can prevent a good bond. After the surface preparation, it was necessary to prepare the joints for bonding. With this purpose, the adherends should be aligned in a bonding jig and, to assure the designated t_A for the joints, calibrated nylon wires with 0.2 mm diameter were attached to the adherends at the overlap ends to stop the adherends' from entering contact when pressed and acquire t_A = 0.2 mm. The adherends were then bonded together by applying adhesive to one of the elements and subsequent position the other adherend correctly. Then, pressure was applied with grips to reach the required thickness and cast out the excess adhesive, which was later removed after its cure. Due to the low pressure applied to the joints (minimum to expel the excess adhesive and promote the adherend/wire/adherend contact), it was assumed that the associated wires' deformation was negligible, and that t_A would be accurately achieved by this process. Moreover, the t_A accuracy was checked after adhesive curing by direct measurements. The removal of the excess adhesive is done after its cure to achieve the joint's theoretical layout without adhesive flaws at the joint boundaries. For testing, the joints were placed between the Universal Testing Machine (UTM) clamps using L_T = 180 mm for all L_O. All the joints were experimentally tested using a UTM Shimadzu AG-X 100 with a 100 kN load cell. The tests were performed with a constant speed of 1 mm/min. The average failure load from each set was considered as the experimental maximum load (P_m).

3 Numerical work

3.1 ISSF technique

The SIF is mainly used to characterise the stress fields of sharp cracks. However, the ISSF also allows the evaluation of multi-material corners with the most diverse geometries. Figure 2 presents an example of these corners for the geometry used in this work, i.e., SLJ. The stress near the interface corner can be

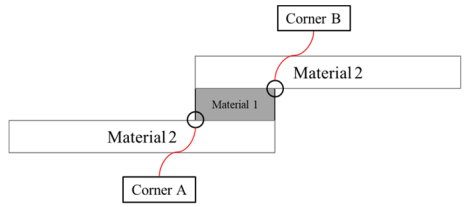

Fig. 2 Example of multi-material corners in SLJ that the ISSF can evaluate

described, in polar coordinates (r,θ), such as those presented in Fig. 3, using the interface singularity as:

$$\sigma_{ij} = \sum_{n=1}^{\infty} H_n r^{\lambda_n - 1} f_{ij}(\lambda_n, \theta). \quad (1)$$

Additionally, the displacement in the same region, using the same coordinate system, can be described as:

$$u_j = \sum_{n=1}^{\infty} H_n r^{\lambda_n} g_j(\lambda_n, \theta), \quad (2)$$

where n is the number of exponents (λ), which varies with the geometry of the interface corner, and H_n is a scalar value representing the ISSF. The exponents are determined by finding the solution for the following equation (Qian and Akisanya 1999):

$$0 = e^2 + b^2 - (\lambda c)^2 - (\lambda d)^2, \quad (3)$$

where the equations to determine the parameters e, b, c and d can be found in Appendix 1. In these equations, θ_1 and θ_2 are the angles of the material interface corner, and α and β are the Dundurs parameters (Dundurs 1969), defined as follows:

$$\alpha = \frac{G_1(\kappa_2 + 1) - G_2(\kappa_1 + 1)}{G_1(\kappa_2 + 1) + G_2(\kappa_1 + 1)} \quad (4)$$

$$\beta = \frac{G_1(\kappa_2 - 1) - G_2(\kappa_1 - 1)}{G_1(\kappa_2 + 1) + G_2(\kappa_1 + 1)} \quad (5)$$

where $\kappa_m = 3 - 4\nu_m$ in plane strain cases and G_m is the shear modulus of material m. The subscripts 1 and 2 in κ and μ represent the two materials. Having

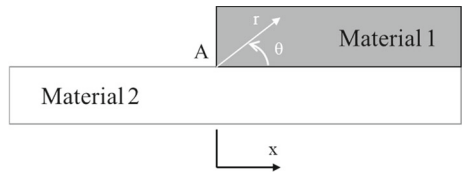

Fig. 3 Polar coordinates system

determined λ using Eq. (3), it is then possible to calculate the $f_{ij}(\lambda_n, \theta)$ and $g_j(\lambda_n, \theta)$ by solving the following system of equations:

$$\{ g^m_{rr} \quad g^m_{\theta} \quad f^m_{rr} \quad f^m_{\theta\theta} \quad f^m_{\theta} \}^T = \boldsymbol{N_m X_m Y}, \tag{6}$$

where m indicates the material and the matrices $\boldsymbol{N}_m$ and $\boldsymbol{X}_m$, and vector $\boldsymbol{Y}$, are defined as (Qian and Akisanya 1999):

$$\boldsymbol{N}_m = \begin{bmatrix} \frac{(\kappa_m - \lambda)\cos([\lambda-1]\theta)}{2G_m} & \frac{(-\kappa_m + \lambda)\sin([\lambda-1]\theta)}{2G_m} & -\frac{\cos([\lambda+1]\theta)}{2G_m} & \frac{\sin([\lambda+1]\theta)}{2G_m} \\ \frac{(\kappa_m + \lambda)\sin([\lambda-1]\theta)}{2G_m} & \frac{(\kappa_m + \lambda)\cos([\lambda-1]\theta)}{2G_m} & \frac{\sin([\lambda+1]\theta)}{2G_m} & \frac{\cos([\lambda+1]\theta)}{2G_m} \\ -(\lambda^2 - 3\lambda)\cos([\lambda-1]\theta) & (\lambda^2 - 3\lambda)\sin([\lambda-1]\theta) & -\lambda\cos([\lambda+1]\theta) & \lambda\sin([\lambda+1]\theta) \\ (\lambda^2 + \lambda)\cos([\lambda-1]\theta) & -(\lambda^2 + \lambda)\sin([\lambda-1]\theta) & \lambda\cos([\lambda+1]\theta) & -\lambda\sin([\lambda+1]\theta) \\ (\lambda^2 - \lambda)\sin([\lambda-1]\theta) & (\lambda^2 - \lambda)\cos([\lambda-1]\theta) & \lambda\sin([\lambda+1]\theta) & \lambda\cos([\lambda+1]\theta) \end{bmatrix} \tag{7}$$

$$\boldsymbol{X}_1 = \begin{bmatrix} 1 & 0 \\ 0 & 1 \\ \chi_{31} & \chi_{32} \\ \chi_{41} & \chi_{42} \end{bmatrix}; \boldsymbol{X}_2 = \begin{bmatrix} \chi_{51} & \chi_{52} \\ \chi_{61} & \chi_{62} \\ \chi_{71} & \chi_{72} \\ \chi_{81} & \chi_{82} \end{bmatrix}; \boldsymbol{Y} = \begin{Bmatrix} y_1 \\ y_2 \end{Bmatrix}, \tag{8}$$

being the components of $\boldsymbol{X}_m$ and $\boldsymbol{Y}$ given by the equations in Appendix 2 (Qian and Akisanya 1999). There are several ways to determine the H_n using numerical methods. A popular method is performing an integration over a line, or area, encircling the interface corner as Qian and Akisanya (1999) did. Alternately, the H_n values can also be determined by extrapolating to the corner the H_n from values near the corner (Klusák et al. 2009). This was the method used in this work. For a n number of λ, a n number of points at different angles (θ) is needed to determine the H_n values at a fixed radius (r), by solving the following system of equations for the $\boldsymbol{H}$ vector:

$$\begin{bmatrix} r^{\lambda_1 - 1} f_{\theta\theta}(\lambda_1, \theta_{n+1}) & \cdots & r^{\lambda_n - 1} f_{\theta\theta}(\lambda_n, \theta_{n+1}) \\ \vdots & \ddots & \vdots \\ r^{\lambda_1 - 1} f_{\theta\theta}(\lambda_1, \theta_{n+n}) & \cdots & r^{\lambda_n - 1} f_{\theta\theta}(\lambda_n, \theta_{n+n}) \end{bmatrix} \begin{Bmatrix} H_1 \\ \vdots \\ H_n \end{Bmatrix} = \begin{Bmatrix} \sigma_{\theta\theta}(r, \theta_{n+1}) \\ \vdots \\ \sigma_{\theta\theta}(r, \theta_{n+n}) \end{Bmatrix}. \tag{9}$$

The solution of Eq. 9 is obtained for several different r, and it is then extrapolated to $r = 0$ mm, from an r interval where it is stable, to obtain $\boldsymbol{H}$ at the interface corner.

3.2 Modelling conditions

A FEM analysis was performed to validate the ISSF criterion. For that, a MATLAB based tool was used, where the finite element discretisation was created, and the natural and essential boundary conditions were imposed. A script was added to this tool with the previously described ISSF formulation. The SLJ was modelled accordingly to Fig. 1. The left boundary was considered fixed ($U_x = U_y = U_z = 0$), while δ was imposed in the right boundary. The simulations were executed considering plane strain, linear elastic material behaviour and small deformations. For these simulations, four-node quadrilateral elements were chosen to describe the whole model. Two different refinements near the interface corner were applied to discretise the interface corner in order to evaluate the mesh's influence on the results of the ISSF analysis.

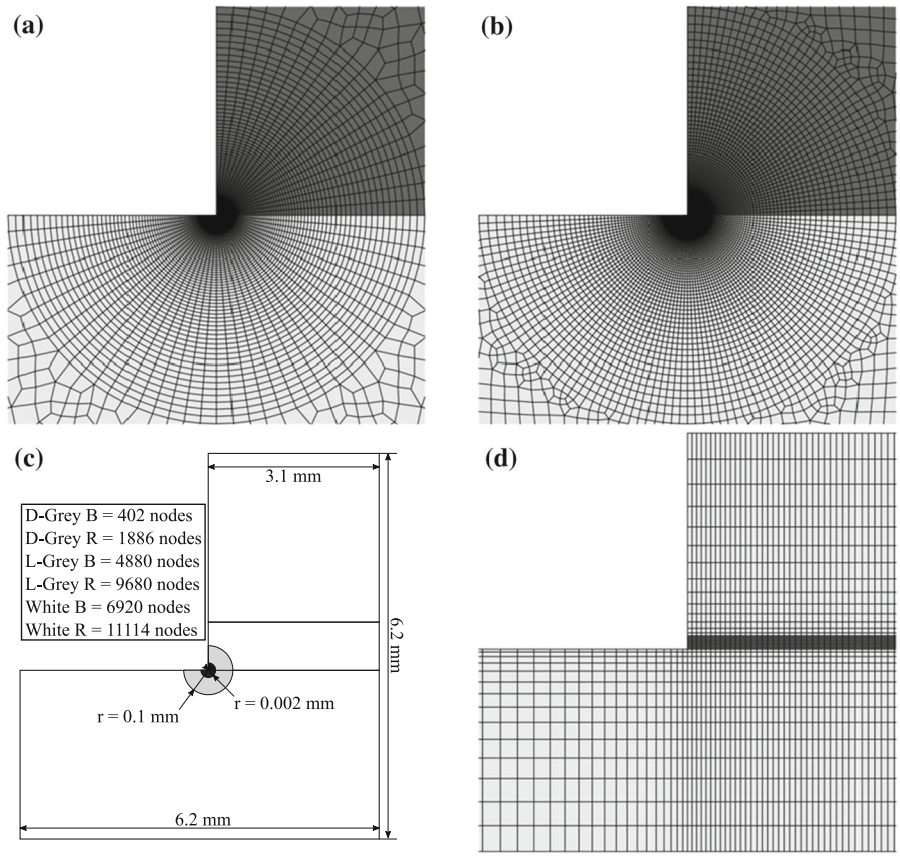

Fig. 4 Baseline (**a**) and refined (**b**) discretisation near the interface corner, dimensions and the number of nodes in the region near the corner (**c**) and discretization for the stress analysis (**d**)

These discretizations near the corner were the same for all the studied L_O. The more refined mesh had approximately double the number of nodes when compared with the baseline mesh in this region. The radial region of the two discretizations used in the ISSF analysis is presented in Fig. 4a and b, with Fig. 4c showing the dimensions and the number of nodes in the region near the corner that was discretized in the same manner for all L_O. After these simulations were solved, the P_m values were determined through the ISSF criterion and then compared to the experimental data. An analysis of the stress in the mid-thickness line of the adhesive was also performed. To do this, a new set of discretizations for each L_O was needed. An example of this discretization at the left end of the overlap for the joint with L_O = 25 mm is shown in Fig. 4d. For the other L_O, the discretizations are similar. This discretization has 14 elements along the adherend thickness and six elements along the adhesive thickness. These simulations were performed under the same assumptions as the ISSF simulations, namely plane strain, linear elastic material behaviour and small deformations.

4 Results

4.1 Experimental data and analysis

Every single one of the SLJ tested presented cohesive failure in the adhesive layer. On top of that, none of the adherends displayed plastic deformation, as it can be proved by the load–displacement curves from Fig. 5, considering the sample cases of L_O = 12.5 (a) and 50 mm (b). All curves show a small loss of linearity between 3 and 4 kN, but this issue was experimentally identified as a minor gripping problem in the testing machine. In all cases, failure takes place without visible plasticization. This, allied to the experimental data's low variation, proves that the specimens were correctly prepared. Figure 6 presents the average P_m sustained by the joints for each L_O tested. From the observation of this graph, it is perceptible that the joint

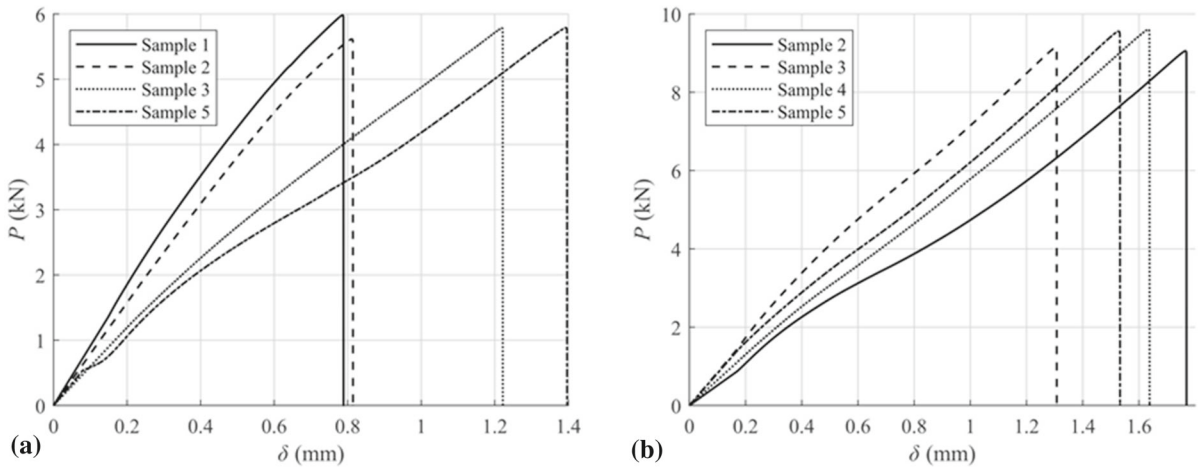

Fig. 5 Load–displacement curves for the SLJ bonded with the Araldite® AV138: L_O = 12.5 (**a**) and 50 mm (**b**)

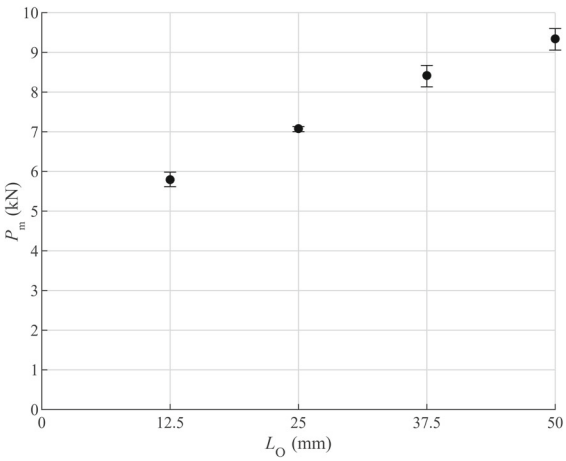

Fig. 6 Average P_m sustained by the joints for each L_O tested

strength increases with each increment of L_O. This fact is in line with previous works where different adhesive types were tested, including the one used in this analysis (De Sousa et al. 2017). However, although the curve is nearly linear, P_m is not proportional to L_O, in the sense that the P_m/L_O ratio markedly diminishes for higher L_O, thus emphasizing the joints' performance reduction. This behaviour is due to the adhesive's brittleness, which does not accommodate the increasing peak stresses with L_O and fails prematurely, and contrasts with that of ductile adhesives, which usually manage to produce proportional P_m–L_O curves up to some extent (Nunes et al. 2016).

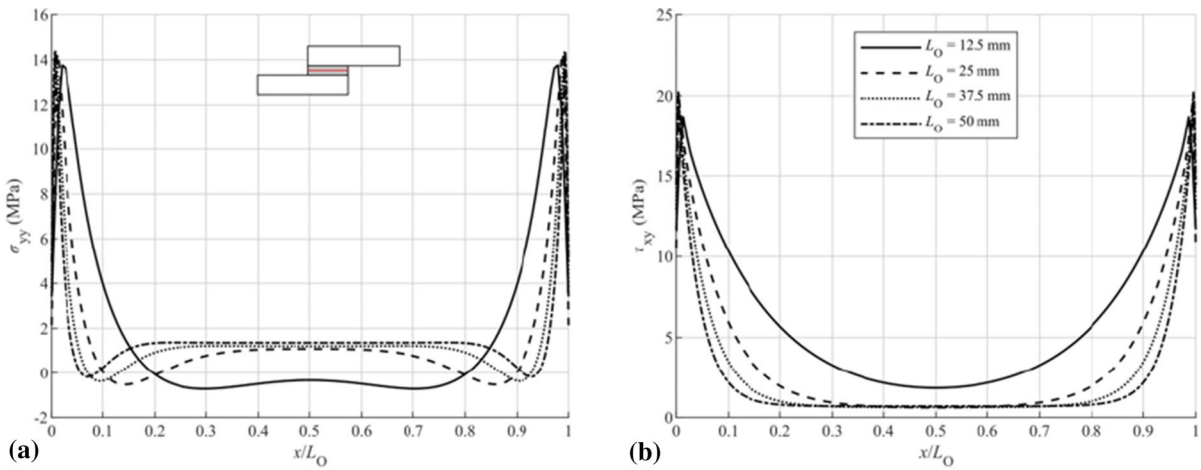

Fig. 7 σ_{yy} (**a**) and τ_{xy} (**b**) stresses along the adhesive layer

4.2 Stress analysis in the adhesive layer mid-thickness

The stress distributions along the adhesive layer are also crucial in this analysis. Figure 7 shows the peel (σ_{yy}) (a) and shear (τ_{xy}) (b) stresses along the adhesive layer mid-thickness, marked in red in the diagram of Fig. 7a. The adhesive length was normalised by L_O to allow an easier comparison. The mesh used to obtain these stresses had to be different from the radial mesh because this mesh cannot provide a steady set of nodes along the mid-thickness of the adhesive. Thus, a structured mesh was considered for this analysis only (Fig. 4d), while the other conditions remain equal. In this work, significant σ_{yy} stresses were observed at the overlap ends, mainly due to the joint rotation during the experimental tests. In fact, this is a common problem found in SLJ, and it arises since the overall joint deformation is ruled by the stiffer adherends, while the compliant adhesive is forced to follow the adherends separation at the overlap edges due to their opposed curvature. Owing to the same effect, compressive stresses are found towards the centre of the overlap (Fernandes et al. 2015). The singularity effect should also be considered, but it was numerically found that this effect was negligible since stresses were taken at the adhesive mid-thickness. Analysing the stress variation with L_O, it was concluded that incrementing this parameter led to higher σ_{yy} peak stresses. As a result, P_m averaged to the bonded area reduces by increasing L_O. τ_{xy} stresses are also present in this joint type. The characteristic distribution consists of a small load towards the centre of the overlap, while in the ends, τ_{xy} stresses increase. This distribution is related to each adherend's varying longitudinal strains along the overlap (Jiang and Qiao 2015). Similarly to σ_{yy} stresses, τ_{xy} peak stresses increase with L_O. This fact is again related to the higher longitudinal strains of the adherends for bigger L_O (Campilho et al. 2011a). Based on this analysis, higher L_O should affect the joint strength, especially for this type of adhesive.

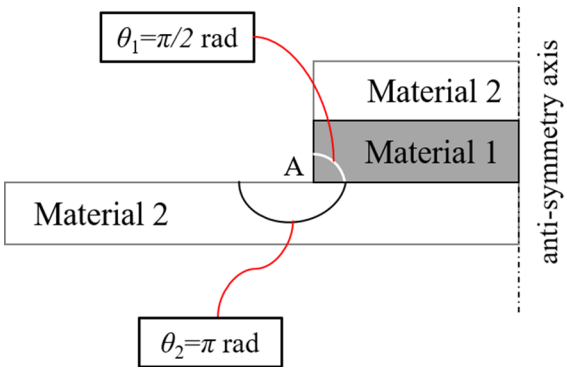

Fig. 8 Anti-symmetry of the SLJ and corner geometry

4.3 ISSF calculation

The SLJ geometry presents anti-symmetry, shown in Fig. 8, allowing the ISSF calculation for only one interface corner. The ISSF calculation was performed using the extrapolation method described in Sect. 3.1. The procedure started with the determination of the eigenvalues (λ_n) following Eq. (3). Considering the combination of materials and geometry of the joints tested, as presented in Fig. 8, with $\theta_1 = \pi/2$ rad and $\theta_2 = \pi$ rad, two different exponents were found: $\lambda_1 = 0.6539$ and $\lambda_2 = 0.9984$. Therefore, according to Eq. (9), two different angles are needed to perform the extrapolation, equal to the number of exponents. The angles chosen were: $\theta_3 = \pi/4$ rad and $\theta_4 = -3\pi/4$ rad, because this way the determination of H_1 and H_2 is based on nodes in the two materials, being one in the ascending part of the $\sigma_{\theta\theta}$ curve (θ_4) and the other in the descending part of the $\sigma_{\theta\theta}$ curve (θ_3).

Considering $L_O = 37.5$ mm as an example, the values of H_1 and H_2 were extrapolated to $r = 0$ mm from the values in the interval $0.01 < r < 0.02$ mm, which are close enough to the corner tip to be influenced by other singularities. This extrapolation was performed when the reaction forces equalled the experimental failure at the joint end where δ was imposed. The process is the same for the other L_O. Figure 9 presents the H_1 extrapolations with the baseline discretization (a) and the refined discretization (b) for the $L_O = 37.5$ mm case. This figure only presents the first singularity (H_1) component since it is the most important. However, the same extrapolation can be used to obtain the second singularity (H_2) component. The comparison between the discretisations in Fig. 9 reveals that this calculation is discretisation independent. The graphs also show the H_1 extrapolations for the other L_O. These were performed at an imposed δ where H_1 would be the same as the H_1 of $L_O = 37.5$ mm at failure displacement. The comparison between the different L_O shows a more pronounced slope in the extrapolation for larger L_O.

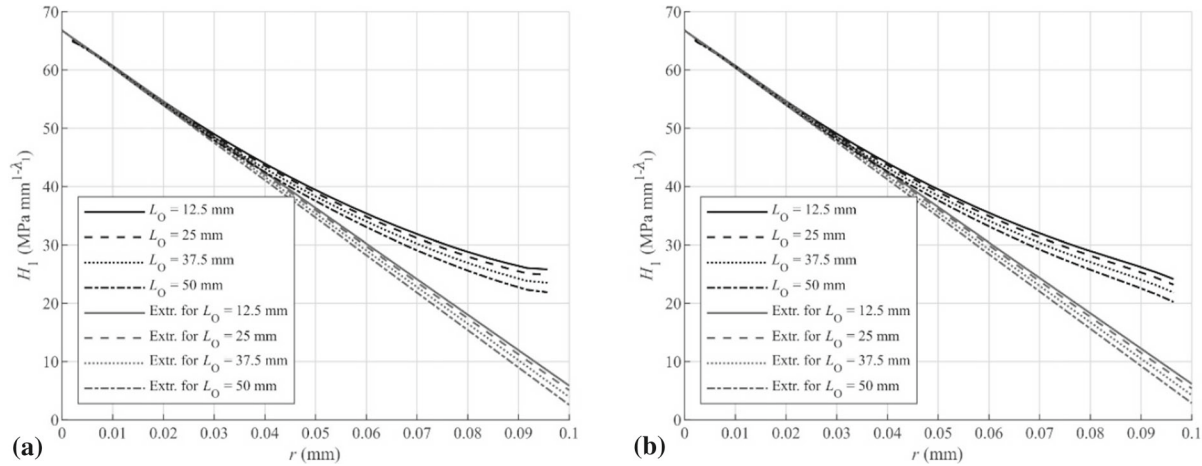

Fig. 9 H_1 extrapolation for the $L_O = 37.5$ mm SLJ using the FEM with the baseline discretisation (**a**) and the refined discretisation (**b**)

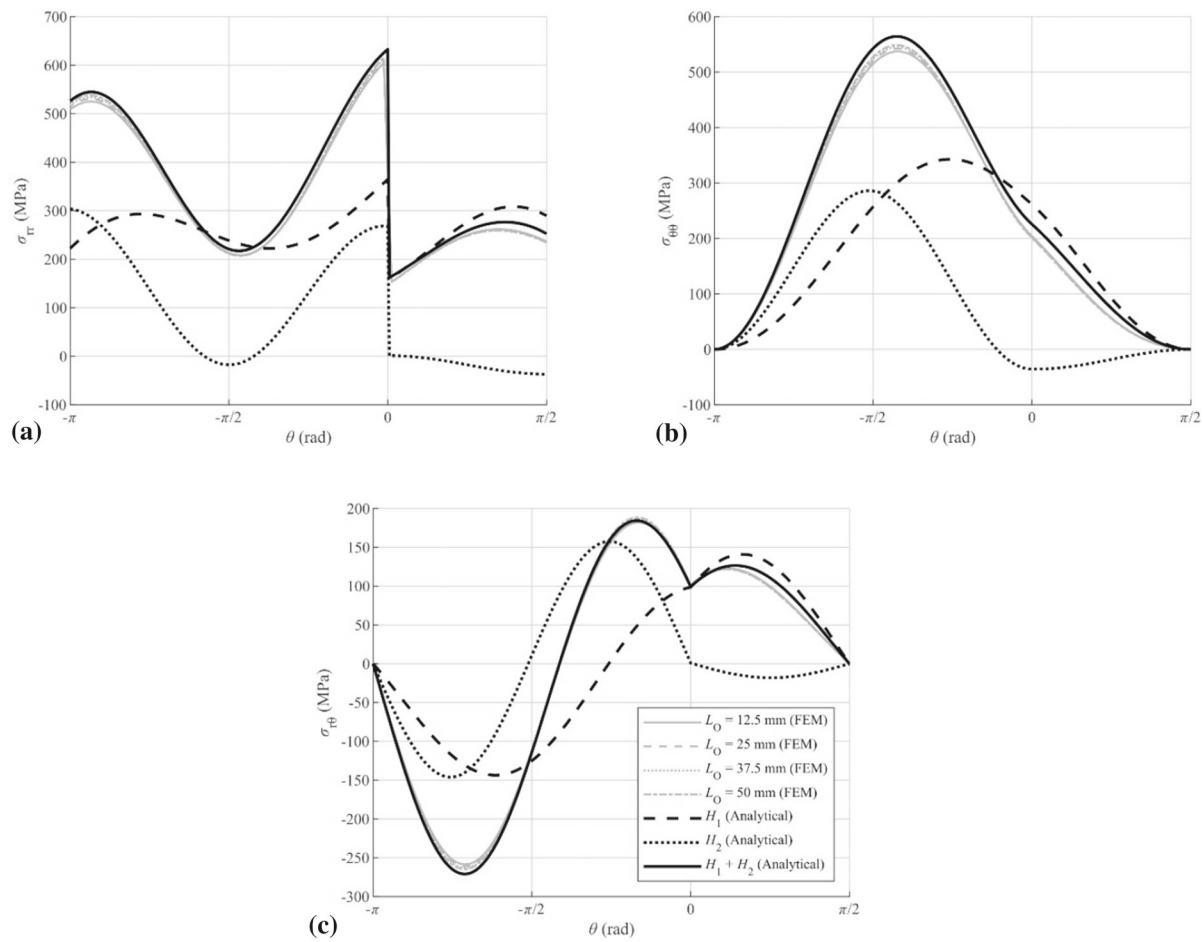

Fig. 10 Stress components using the FEM with the refined discretisation compared to the analytical stress

Figure 10 compares the stresses obtained from the numerical simulations and the ones predicted by the analytical formula. The numerical stresses were obtained at $r = 0.02$ mm from the interface corner and when H_1 was the same for all L_O. In Fig. 10, it can be observed that the analytical stress is very similar to the numerical stress, thus proving that the analytical functions obtained with Eq. (6) fit well the numerical stresses for the three different components and showing that the stress singularity dominates this region. The comparison of the numerical results shows that the stress components are almost the same for all L_O, which would be expected in a case where H_1 was the same for all L_O.

4.4 Strength prediction

In order to predict the joint strength, it is necessary to determine the critical ISSF (H_c). However, there is no standardized purely experimental test that allows this determination. The widespread methods to obtain this parameter are usually based on integrals and their implementation is often considerably intricate. Therefore, a combination of numerical simulations and experimental data was used. This type of hybrid experimental/numerical approach to determine failure criteria has been used previously for other criteria, such as the CLS criterion (Ramalho et al. 2021), but also to determine H_c (Akhavan-Safar et al. 2017). The method proposed here consists of experimentally testing a SLJ of a given L_O and determining its P_m. Afterwards, a numerical simulation of the same joint is

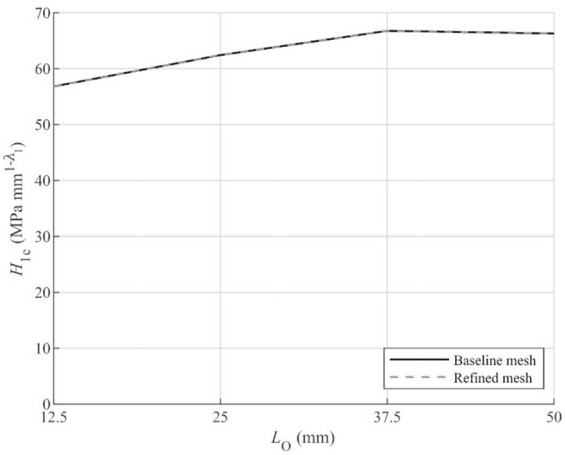

Fig. 11 Comparison of the predicted H_{1c} values for the different L_O and discretisations

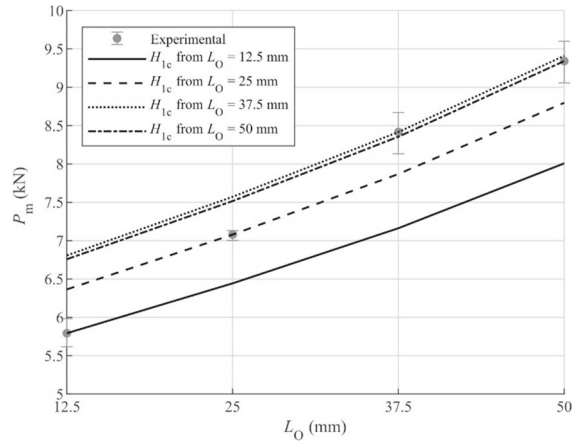

Fig. 12 Strength predictions using the FEM with the refined discretisation

to be performed using the previously determined P_m as the imposed load. Then, the extracted singularity (H_n) components ($n = 1$ or $n = 2$) were used as the critical ISSF for both singularities (H_{nc}), which make possible the P_m prediction for different L_O. Since H_1 component is the most significant one, this method was used to obtain the H_{1c} estimates for each experimentally tested L_O.

Figure 11 shows that the H_{1c} values predicted using the two different discretisations present differences below 1%. It also shows that the H_{1c} estimated using $L_O = 37.5$ mm and $L_O = 50$ mm are similar, but for smaller L_O, the H_{1c} estimates are lower. This occurs because even an adhesive as brittle as this has a small amount of plasticity in longer L_O, which means that some energy would have to be spent in plasticizing the adhesive before a crack would form. Furthermore, in longer L_O, the crack can propagate stably for a few moments, but for shorter L_O, the joints fail as soon as there is a crack. Finally, P_m was predicted using each one of those H_{1c}. For example, using the H_{1c} obtained with the experiments and numerical simulations of $L_O = 12.5$ mm, P_m was numerically predicted for the other L_O (25, 37.5 and 50 mm). The same procedure was done for the H_{1c} obtained with the other L_O. Figure 12 presents the strength predictions only for the refined mesh since the results are similar to those obtained with the baseline mesh. On the other hand, it is observable that, as L_O increases, the curve slopes also increase. This fact is contrary to the experimental results where, for larger L_O, increasing L_O diminishes the returns in strength. However, this slope increase is

minimal, and it is not a significant issue in the L_O range tested. For the largest L_O, the predicted strength increase is in line with what was verified experimentally, i.e., approximately a 1 kN strength increase between L_O = 37.5 mm and L_O = 50 mm. For the two shortest L_O, the predicted strength increases when L_O increases are smaller than those found experimentally, i.e., the strength prediction increase between L_O = 12.5 mm and L_O = 25 mm is smaller than 1 kN, while the experimental strength increase was over 1 kN.

By analysing the strength predictions for the L_O = 12.5 mm, it is perceptible that the nearest prediction (beyond its own H_{1c} curve) is the curve of H_{1c} determined with L_O = 25 mm. However, the joint strength is overpredicted, and the percentual deviation between this prediction and the experimental data is 9.75%, which can be considered high. The other two predictions are also higher than the experimental value, being the L_O = 37.5 mm case the furthest away with a percentual deviation of 17.33%. For L_O = 25 mm, similar behaviour is observed for the two highest L_O. Nonetheless, for the L_O = 12.5 mm prediction case, the joint strength is underpredicted with a percentual deviation of 8.92%. For the largest L_O, it is clear that the predictions are identical, with a percentual deviation of 0.84% when a L_O = 50 mm was used to predict the strength of the L_O = 37.5 mm joint and the same percentual deviation on the contrary case. For both these cases, the worst-case scenario is predicting the strength with a L_O = 12.5 mm, where percentual deviations over 16% were found.

5 Conclusions

The present work focused on the ISSF criterion, comparing the numerical analysis performed through FEM with experimental data. This work's geometry and material combination lead to the existence of two components that characterise the stress singularity at the adhesive/adherend interface corner, being the first singularity the most significant one. The extrapolation method used to determine H_1 showed independence from the discretisation. This is a major advantage when compared to the stress, which is affected by the stress singularity in the corner, meaning that finer discretisations lead to higher stress levels in this region. The method proposed to determine H_{1c} showed some variance depending on which L_O is used, except when comparing the H_{1c} obtained with L_O = 37.5 mm with the one obtained with L_O = 50 mm, which were similar. The strength predictions were lower than the experiments when the H_{1c} determined with a smaller L_O was used to predict a larger L_O's joint strength. However, joint strength was over predicted when an L_O smaller than the L_O with which H_{1c} was determined was used. The only exceptions to this rule are the two largest L_O, because the H_{1c} predicted with those two L_O are similar, meaning that the strength predictions for L_O = 37.5 mm using the H_{1c} determined with L_O = 50 mm, and vice-versa, are identical to the experimental P_m. Since it is better to have conservative P_m predictions due to safety reasons, it would be advisable to only predict P_m of joints with L_O larger than the L_O used to determine H_{1c}. The results found in this work revealed to be very promising, with very accurate results achieved, considering the simplicity of the method applied to determine H_{1c}. Although the method's validity was only checked for a specific adhesive system, this technique can be further studied in the field of adhesive joints and applied to different systems/joint types, provided that further validation is accomplished.

Author contributions JD: development and implementation of the FEM routines, data analyses, original draft; LR: development and implementation of the FEM routines, data analyses, original draft; IS: conceptualisation, experimental analysis, development, supervision, review & editing; RC: final review, project administration, funding acquisition, supervision; JB: final review, project administration, funding acquisition, supervision.

Funding This work has been funded by the Ministério da Ciência, Tecnologia e Ensino Superior through the Fundação para a Ciência e a Tecnologia (from Portugal), under project fundings 'MIT-EXPL/ISF/0084/2017', 'POCI-01-0145-FEDER-028351', and 'SFRH/BD/147628/2019'. Additionally, the authors acknowledge the funding provided by the Associated Laboratory for Energy, Transports and Aeronautics (LAETA), under project 'UIDB/50022/2020'.

Data availability Not applicable.

Code availability Not applicable.

Declarations

Conflict of interest Not applicable.

Appendix 1

$$e = (\alpha-\beta)(\cos[2\lambda\theta_1] - \cos[2\lambda\theta_1 - 2\lambda\theta_2] + \lambda^2[\cos(2\theta_1) - \cos(2\theta_1 + 2\theta_2) - 1 + \cos(2\theta_2)]) + (1+\alpha)(1-\cos[2\lambda\theta_1]) - (1-\beta)(1-\cos[2\lambda\theta_2]) \tag{10}$$

$$b = (\alpha-\beta)(\sin[2\lambda\theta_1] - \sin[2\lambda\theta_1 - 2\lambda\theta_2] - \lambda^2[\sin(2\theta_1) - \sin(2\theta_1 + 2\theta_2) + \sin(2\theta_2)]) - (1+\alpha)\sin(2\lambda\theta_1) - (1-\beta)\sin(2\lambda\theta_2) \tag{11}$$

$$c = (\alpha-\beta)(\cos[2\lambda\theta_1] - \cos[2\lambda\theta_1 + 2\theta_2] + \cos[2\lambda\theta_2] - \cos(2\lambda\theta_2 - 2\theta_1) - 1 + \cos(2\theta_1)) + (1+\alpha)(1-\cos[2\theta_1]) - (1-\beta)(1-\cos[2\theta_2]) \tag{12}$$

$$d = (\alpha-\beta)(\sin[2\theta_1] + \sin[2\lambda\theta_2 - 2\theta_1] - \sin[2\lambda\theta_1] + \sin(2\lambda\theta_1 + 2\theta_2) - \sin(2\theta_2)) - (1+\alpha)\sin(2\theta_1) - (1-\beta)\sin(2\theta_2) \tag{13}$$

Appendix 2

$$\chi_{31} = -\cos(2\lambda\theta_1) - \lambda\cos(2\theta_1) \tag{14}$$

$$\chi_{32} = \sin(2\lambda\theta_1) - \lambda\sin(2\theta_1) \tag{15}$$

$$\chi_{41} = \sin(2\lambda\theta_1) + \lambda\sin(2\theta_1) \tag{16}$$

$$\chi_{42} = \cos(2\lambda\theta_1) - \lambda\cos(2\theta_1) \tag{17}$$

$$\chi_{51} = \frac{1-\beta+(\alpha-\beta)(\lambda-\cos(2\lambda\theta_1)-\lambda\cos(2\theta_1))}{1+\alpha} \tag{18}$$

$$\chi_{52} = \frac{(\alpha-\beta)(\sin(2\lambda\theta_1)-\lambda\sin(2\theta_1))}{1+\alpha} \tag{19}$$

$$\chi_{61} = -\frac{(\alpha-\beta)(\sin(2\lambda\theta_1)+\lambda\sin(2\theta_1))}{1+\alpha} \tag{20}$$

$$\chi_{62} = \frac{1-\beta-(\alpha-\beta)(\lambda+\cos(2\lambda\theta_1)-\lambda\cos(2\theta_1))}{1+\alpha} \tag{21}$$

$$\chi_{71} = \frac{(\alpha-\beta)(\sin[2\lambda\theta_1]+\lambda\sin[2\theta_1])(\sin[2\lambda\theta_2]-\lambda\sin[2\theta_2])}{1+\alpha} - \frac{(1-\beta+[\alpha-\beta][\lambda-\cos(2\lambda\theta_1)-\lambda\cos(2\theta_1)])(\cos[2\lambda\theta_2]+\lambda\cos[2\theta_2])}{1+\alpha} \tag{22}$$

$$\chi_{72} = -\frac{(\alpha-\beta)(\sin[2\lambda\theta_1]-\lambda\sin[2\theta_1])(\cos[2\lambda\theta_2]+\lambda\cos[2\theta_2])}{1+\alpha} - \frac{(1-\beta-[\alpha-\beta][\lambda+\cos(2\lambda\theta_1)-\lambda\cos(2\theta_1)])(\sin[2\lambda\theta_2]-\lambda\sin[2\theta_2])}{1+\alpha} \tag{23}$$

$$\chi_{81} = -\frac{(\alpha-\beta)(\sin[2\lambda\theta_1]+\lambda\sin[2\theta_1])(\cos[2\lambda\theta_2]-\lambda\cos[2\theta_2])}{1+\alpha} - \frac{(1-\beta+[\alpha-\beta][\lambda-\cos(2\lambda\theta_1)-\lambda\cos(2\theta_1)])(\sin[2\lambda\theta_2]+\lambda\sin[2\theta_2])}{1+\alpha} \tag{24}$$

$$\chi_{82} = -\frac{(\alpha-\beta)(\sin[2\lambda\theta_1]-\lambda\sin[2\theta_1])(\sin[2\lambda\theta_2]+\lambda\sin[2\theta_2])}{1+\alpha} - \frac{(1-\beta-[\alpha-\beta][\lambda+\cos(2\lambda\theta_1)-\lambda\cos(2\theta_1)])(\cos[2\lambda\theta_2]-\lambda\cos[2\theta_2])}{1+\alpha} \tag{25}$$

$$y_1 = \frac{c-e}{\lambda([\lambda+1-\cos(2\lambda\theta_1)-\lambda\cos(2\theta_1)][c-e]+b+d)} \tag{26}$$

$$y_2 = \frac{b+d}{\lambda([\lambda+1-\cos(2\lambda\theta_1)-\lambda\cos(2\theta_1)][c-e]+b+d)} \tag{27}$$

References

Afendi M, Majid MA, Daud R, Rahman AA, Teramoto T (2013) Strength prediction and reliability of brittle epoxy adhesively bonded dissimilar joint. Int J Adhes Adhes 45:21–31. https://doi.org/10.1016/j.ijadhadh.2013.03.008

Akhavan-Safar A, Ayatollahi MR, Rastegar S, da Silva LFM (2017) Impact of geometry on the critical values of the stress intensity factor of adhesively bonded joints. J Adhes Sci Technol 31:2071–2087

Blackman BRK, Hadavinia H, Kinloch AJ, Williams JG (2003) The use of a cohesive zone model to study the fracture of fibre composites and adhesively-bonded joints. Int J Fract 119:25–46. https://doi.org/10.1023/A:1023998013255

Bogy DB (1968) Edge-bonded dissimilar orthogonal elastic wedges under normal and shear loading. J Appl Mech 35:460–466. https://doi.org/10.1115/1.3601236

Campilho RDSG, Banea MD, Pinto AMG, da Silva LFM, De Jesus AMP (2011a) Strength prediction of single-and double-lap joints by standard and extended finite element

modelling. Int J Adhes Adhes 31:363–372. https://doi.org/10.1016/j.ijadhadh.2010.09.008

Campilho RDSG, Pinto AMG, Banea MD, Silva RF, da Silva LFM (2011b) Strength improvement of adhesively-bonded joints using a reverse-bent geometry. J Adhes Sci Technol 25:2351–2368. https://doi.org/10.1163/016942411X580081

Campilho RDSG, Banea MD, Neto JABP, da Silva LFM (2013) Modelling adhesive joints with cohesive zone models: effect of the cohesive law shape of the adhesive layer. Int J Adhes Adhes 44:48–56. https://doi.org/10.1016/j.ijadhadh.2013.02.006

Carbas RJC, Da Silva LFM, Critchlow GW (2014) Adhesively bonded functionally graded joints by induction heating. Int J Adhes Adhes 48:110–118. https://doi.org/10.1016/j.ijadhadh.2013.09.045

Carvalho UTF, Campilho RDSG (2017) Validation of pure tensile and shear cohesive laws obtained by the direct method with single-lap joints. Int J Adhes Adhes 77:41–50. https://doi.org/10.1016/j.ijadhadh.2017.04.002

Da Silva LFM, Campilho RDSG (2012) Advances in numerical modelling of adhesive joints. Springer, Heidelberg. https://doi.org/10.1007/978-3-642-23608-2_1

De Sousa CCRG, Campilho RDSG, Marques EAS, Costa M, da Silva LFM (2017) Overview of different strength prediction techniques for single-lap bonded joints. Proc Inst Mech Eng L 231:210–223. https://doi.org/10.1177/1464420716675746

Demiral M, Kadioglu F (2018) Failure behaviour of the adhesive layer and angle ply composite adherends in single lap joints: a numerical study. Int J Adhes Adhes 87:181–190. https://doi.org/10.1016/j.ijadhadh.2018.10.010

Du J, Salmon FT, Pocius AV (2004) Modeling of cohesive failure processes in structural adhesive bonded joints. J Adhes Sci Technol 18:287–299. https://doi.org/10.1163/156856104773635436

Dundurs J (1969) Discussion:"edge-bonded dissimilar orthogonal elastic wedges under normal and shear loading." J Appl Mech 35:460–466. https://doi.org/10.1115/1.3564739

Fernandes TAB, Campilho RDSG, Banea MD, da Silva LFM (2015) Adhesive selection for single lap bonded joints: experimentation and advanced techniques for strength prediction. J Adhes 91:841–862. https://doi.org/10.1080/00218464.2014.994703

Galvez P, Noda N-A, Takaki R, Sano Y, Miyazaki T, Abenojar J, Martínez MA (2019) Intensity of singular stress field (ISSF) variation as a function of the Young's modulus in single lap adhesive joints. Int J Adhes Adhes 95:102418. https://doi.org/10.1016/j.ijadhadh.2019.102418

Garrido M, António D, Lopes JG, Correia JR (2018) Performance of different joining techniques used in the repair of bituminous waterproofing membranes. Constr Build Mater 158:346–358. https://doi.org/10.1016/j.conbuildmat.2017.09.180

Goland M, Reissner E (1944) The stresses in cemented joints. J Appl Mech 66:A17–A27. https://doi.org/10.1115/1.4009336

Gui C, Bai J, Zuo W (2018) Simplified crashworthiness method of automotive frame for conceptual design. Thin Wall Struct 131:324–335. https://doi.org/10.1016/j.tws.2018.07.005

Hart-Smith LJ (1973) Adhesive-bonded single-lap joints. NASA Contract Report, NASA CR-112236

Hell S, Weißgraeber P, Felger J, Becker W (2014) A coupled stress and energy criterion for the assessment of crack initiation in single lap joints: a numerical approach. Eng Fract Mech 117:112–126. https://doi.org/10.1016/j.engfracmech.2014.01.012

Jairaja R, Naik GN (2019) Single and dual adhesive bond strength analysis of single lap joint between dissimilar adherends. Int J Adhes Adhes 92:142–153. https://doi.org/10.1016/j.ijadhadh.2019.04.016

Jeevi G, Nayak SK, Abdul Kader M (2019) Review on adhesive joints and their application in hybrid composite structures. J Adhes Sci Technol 33:1497–1520. https://doi.org/10.1080/01694243.2018.1543528

Jiang W, Qiao P (2015) An improved four-parameter model with consideration of Poisson's effect on stress analysis of adhesive joints. Eng Struct 88:203–215. https://doi.org/10.1016/j.engstruct.2015.01.027

Jiang Z, Fang Z, Yan L, Wan S, Fang Y (2021) Mixed-mode I/II fracture criteria for adhesively-bonded pultruded GFRP/steel joint. Compos Struct 255:113012. https://doi.org/10.1016/j.compstruct.2020.113012

Klusák J, Profant T, Kotoul M (2009) Various methods of numerical estimation of generalized stress intensity factors of bi-material notches. J Appl Comput Mech 3:297–304

Konstantakopoulou M, Deligianni A, Kotsikos G (2016) Failure of dissimilar material bonded joints. Phys Sci Rev. https://doi.org/10.1515/9783110339727-007

Lazzarin P, Zambardi R (2001) A finite-volume-energy based approach to predict the static and fatigue behavior of components with sharp V-shaped notches. Int J Fract 112:275–298. https://doi.org/10.1023/A:1013595930617

Leguillon D (2002) Strength or toughness? A criterion for crack onset at a notch. Eur J Mech A 21:61–72. https://doi.org/10.1016/S0997-7538(01)01184-6

Li R, Noda N-A, Takaki R, Sano Y, Takase Y, Miyazaki T (2018) Most suitable evaluation method for adhesive strength to minimize bend effect in lap joints in terms of the intensity of singular stress field. Int J Adhes Adhes 86:45–58. https://doi.org/10.1016/j.ijadhadh.2018.08.006

Matos PPL, McMeeking RM, Charalambides PG, Drory MD (1989) A method for calculating stress intensities in bimaterial fracture. Int J Fract 40:235–254. https://doi.org/10.1007/BF00963659

Mintzas A, Nowell D (2012) Validation of an Hcr-based fracture initiation criterion for adhesively bonded joints. Eng Fract Mech 80:13–27. https://doi.org/10.1016/j.engfracmech.2011.09.020

Nunes SLS, Campilho RDSG, da Silva FJG, de Sousa CCRG, Fernandes TAB, Banea MD, da Silva LFM (2016) Comparative failure assessment of single and double-lap joints with varying adhesive systems. J Adhes 92:610–634. https://doi.org/10.1080/00218464.2015.1103227

Parks DM (1974) A stiffness derivative finite element technique for determination of crack tip stress intensity factors. Int J Fract 10:487–502. https://doi.org/10.1007/BF00155252

Qian Z, Akisanya A (1999) Wedge corner stress behaviour of bonded dissimilar materials. Theor Appl Fract Mech

32:209–222. https://doi.org/10.1016/S0167-8442(99)00041-5

Ramalho LDC, Campilho RDSG, Belinha J (2019) Predicting single-lap joint strength using the natural neighbour radial point interpolation method. J Braz Soc Mech Sci 41:362. https://doi.org/10.1007/s40430-019-1862-0

Ramalho LDC, Campilho RDSG, Belinha J, da Silva LFM (2020) Static strength prediction of adhesive joints: a review. Int J Adhes Adhes 96:102451. https://doi.org/10.1016/j.ijadhadh.2019.102451

Ramalho LDC, Sánchez-Arce IJ, Campilho RDSG, Belinha J (2021) Strength prediction of composite single lap joints using the critical longitudinal strain criterion and a meshless method. Int J Adhes Adhes 108:102884. https://doi.org/10.1016/j.ijadhadh.2021.102884

Rastegar S, Ayatollahi MR, Akhavan-Safar A, da Silva LFM (2018) Prediction of the critical stress intensity factor of single-lap adhesive joints using a coupled ratio method and an analytical model. Proc Inst Mech Eng L 233:1393–1403. https://doi.org/10.1177/1464420718755630

Rice JR (1968) A path independent integral and the approximate analysis of strain concentration by notches and cracks. J Appl Mech 35:379–386. https://doi.org/10.1115/1.3601206

Rybicki EF, Kanninen MF (1977) A finite element calculation of stress intensity factors by a modified crack closure integral. Eng Fract Mech 9:931–938. https://doi.org/10.1016/0013-7944(77)90013-3

Sánchez-Arce I, Ramalho L, Campilho R, Belinha J (2021) Material non-linearity in the numerical analysis of SLJ bonded with ductile adhesives: a meshless approach. Int J Adhes Adhes 104:102716. https://doi.org/10.1016/j.ijadhadh.2020.102716

Stein N, Dölling S, Chalkiadaki K, Becker W, Weißgraeber P (2017) Enhanced XFEM for crack deflection in multi-material joints. Int J Fract 207:193–210. https://doi.org/10.1007/s10704-017-0228-9

Stuparu F, Constantinescu DM, Apostol DA, Sandu M (2016) A combined cohesive elements—XFEM approach for analyzing crack propagation in bonded joints. J Adhes 92:535–552. https://doi.org/10.1080/00218464.2015.1115355

Sugiman S, Ahmad H (2017) Comparison of cohesive zone and continuum damage approach in predicting the static failure of adhesively bonded single lap joints. J Adhes Sci Technol 31:552–570. https://doi.org/10.1080/01694243.2016.1222048

Tsai C, Guan Y, Ohanehi D, Dillard J, Dillard D, Batra R (2014) Analysis of cohesive failure in adhesively bonded joints with the SSPH meshless method. Int J Adhes Adhes 51:67–80. https://doi.org/10.1016/j.ijadhadh.2014.02.009

Volkersen O (1938) Die Nietkraftverteilung in zugbeanspruchten Nietverbindungen mit konstanten Laschenquerschnitten. Jahrb Dtsch Luftfahrtforsch 15:41–47

Williams ML (1959) The stresses around a fault or crack in dissimilar media. Bull Seismol Soc Am 49:199–204

Wu Z, Tian S, Hua Y, Gu X (2014) On the interfacial strength of bonded scarf joints. Eng Fract Mech 131:142–149. https://doi.org/10.1016/j.engfracmech.2014.07.026

Xu W, Wei Y (2013) Influence of adhesive thickness on local interface fracture and overall strength of metallic adhesive bonding structures. Int J Adhes Adhes 40:158–167. https://doi.org/10.1016/j.ijadhadh.2012.07.012

Zhang Y, Wu P, Duan M (2015) A mesh-independent technique to evaluate stress singularities in adhesive joints. Int J Adhes Adhes 57:105–117. https://doi.org/10.1016/j.ijadhadh.2014.12.003

PAPER 2

ANALYSIS OF STRESS SINGULARITY IN ADHESIVE JOINTS USING MESHLESS METHODS

ENGINEERING ANALYSIS WITH BOUNDARY ELEMENTS

Engineering Analysis with Boundary Elements

Analysis of stress singularity in adhesive joints using meshless methods

--Manuscript Draft--

Manuscript Number:	EABE-D-21-00346R1
Article Type:	Full Length Article
Keywords:	ISSF criterion; RPIM; Adhesive Joints; Single Lap Joints; meshless methods
Corresponding Author:	L.D.C Ramalho INEGI: Instituto de Ciencia e Inovacao em Engenharia Mecanica e Engenharia Porto, PORTUGAL
First Author:	L.D.C Ramalho
Order of Authors:	L.D.C Ramalho
	J.M.M. Dionísio
	I.J. Sánchez-Arce
	R.D.S.G. Campilho
	J. Belinha
Abstract:	Recent years saw a rise in the application of bonding techniques in the engineering industry. This fact is due to the various advantages of this technique when compared to traditional joining methods, such as riveting or bolting. The growth of bonding methods demands faster and more powerful tools to analyse the behaviour of products. For that reason, adhesive joints have been the subject of intensive investigation over the past few years. Recently, a fracture mechanics based approach emerged with great potential to evaluate joint behaviour, called Intesity of Singular Stress Fields (ISSF), similar to the Stress Intensity Factor (SIF) concept. However, it allows the study of multi-material corners and does not require an initial crack. This approach was not yet tested with meshless methods. The present work intends to fill this gap, resorting to the Radial Point Interpolation Method (RPIM). With this purpose, adhesive joints with four different overlap lengths (L O) bonded with a brittle adhesive were studied. The interface corner's stresses were also evaluated. The predicted strengths were compared with the experimental data to assess the accuracy of the applied methods. In conclusion, the ISSF criterion proved to be applicable to meshless methods, namely the RPIM.
Suggested Reviewers:	
Opposed Reviewers:	
Response to Reviewers:	

PAPER 3

FRACTURE MECHANICS APPROACH TO STRESS SINGULARITY IN COMPOSITE ADHESIVE JOINTS

COMPOSITE STRUCTURES

Composite Structures 276 (2021) 114507

Contents lists available at ScienceDirect

Composite Structures

journal homepage: www.elsevier.com/locate/compstruct

Fracture mechanics approach to stress singularities in composite adhesive joints

J.M.M. Dionísio [a], L.D.C. Ramalho [b], I.J. Sánchez-Arce [b], R.D.S.G. Campilho [a,b,*], J. Belinha [a]

[a] Departamento de Engenharia Mecânica, Instituto Superior de Engenharia do Porto, Instituto Politécnico do Porto, Rua Dr. António Bernardino de Almeida, 431, 4200-072 Porto, Portugal
[b] INEGI – Pólo FEUP, Rua Dr. Roberto Frias, s/n, 4200-465 Porto, Portugal

ARTICLE INFO

Keywords:
ISSF criterion
Adhesive joints
Composite materials
Finite element method
Single-lap joints

ABSTRACT

Structural design has significantly changed over the years driven by a weight reduction goal. In that sense, composite materials established themselves as the material of excellence in most engineering areas, replacing wood, steel and aluminium. Connection processes also experienced a transformation, with adhesive bonding standing out. Those new materials and techniques require deep research until they could be applied to structures. These studies led to the appearance of different methods for evaluating material and bond performance. Fracture mechanics is an approach based on material discontinuities or defects. Recently, a new fracture mechanics based technique arose called Intensity of Singular Stress Fields (ISSF). It hinges on the Stress Intensity Factors (SIF) approach but does not require an initial crack. This investigation aims to evaluate the applicability of this technique to composite materials. For that, Single-Lap Joints (SLJ) made from Carbon Fibre Reinforced Polymer (CFRP) bonded with a brittle adhesive and eight different overlap lengths (L_O) are analysed. The numerical simulations and strength predictions are performed through the Finite Element Method (FEM) and MATLAB software. Finally, the numerical predictions are compared to the experimental data. It can be concluded that the ISSF is applicable to orthotropic materials.

1. Introduction

Since scientists started to explore ways to reach space, they understood that weight would be a crucial problem to solve in order to escape Earth's gravity. This dilemma initiated the investigation of different approaches to reduce the mass of structures. When thinking about a spacecraft, the characteristic that stands out in terms of its weight is its material(s). If the material is light, then the structure is also light. However, if the material does not provide stiffness and strength to withstand the stresses of Earth's gravity escape, the weight of the spacecraft becomes irrelevant. That is why it is so difficult to find the perfect material for these structures. Several materials were implemented in space vehicles through the years, such as wood, steel, and aluminium. They are still used today in some specific functions, but composite materials have widely replaced them. Composite materials emerged in aeroplanes during World War II (around 1940) due to their strength-to-weight properties but also because they proved to be transparent to radio frequencies. Since then, these materials have been highly studied [1,2] and compose most of the structures in this sector. The developments achieved by the aeronautical industry spread out, and nowadays, these materials can be found in the most diverse sectors, such as the automotive, civil or medical [3].

A structure like an aeroplane comprises millions of components that need to be joined. Different joining techniques were used throughout engineering history, such as riveting and bolting, but more recently, adhesive bonding has gained much attention [3]. The main advantage of this approach is the low weight of the connection while improving stresses around the bonding areas [4]. Once again, aeronautical engineers first saw the possibilities brought by this technique and applied them to aeroplanes and spacecrafts. Nonetheless, the adhesive bonding process also has some disadvantages, such as the impossibility of disassembling the joint and the required curing time [5].

When engineers started to investigate adhesive bonding, the means at their disposal were scarce. Thus, the majority of the design process was performed through trial and error. However, this process was costly, so simple analytical analysis started to arise. In 1938, Volkersen [6] stood out as a pioneer in these analyses and published the first model to evaluate the stress distributions at mid-thickness, considering

* Corresponding author at: Departamento de Engenharia Mecânica, Instituto Superior de Engenharia do Porto, Instituto Politécnico do Porto, Rua Dr. António Bernardino de Almeida, 431, 4200-072 Porto, Portugal.
E-mail address: raulcampilho@gmail.com (R.D.S.G. Campilho).

https://doi.org/10.1016/j.compstruct.2021.114507
Received 20 July 2021; Accepted 1 August 2021
Available online 6 August 2021

Single-Lap Joints (SLJ). Even so, Volkersen's approach did not consider the bending effect caused by the non-collinearity of the load path in SLJs. This effect leads to a bending moment that causes the joint's rotation, originating large deflections of the adherends. The investigators who followed tried to tackle these issues, emphasising Goland and Reissner [7] and Hart-Smith [8]. Nevertheless, all the models developed throughout the years presented problems, either because they were straightforward but posed many simplifications or because their formulation was too complex to solve analytically [9]. Despite their limitations, these models are still a reference today to understand elementary concepts regarding adhesive bonding [10].

The limits in joint design collapsed with the invention of the computer during World War II by Alan Turing. This discovery allowed engineers to analyse more intricate joint shapes and to perform more complex models. The computer initiated the numerical analysis era. In the early 1960s, Clough [11] conceived the concept of the Finite Element Method (FEM), a numerical approach that revolutionized structural engineering. Until today, FEM is the most widespread tool to perform numerical analysis [12]. With FEM, failure criteria to evaluate joint behaviour started to be introduced [13]. Continuum mechanics, fracture mechanics, Cohesive Zone Modeling (CZM), damage mechanics and the eXtended Finite Element Method (XFEM) are the most common approaches [13]. CZM stands out as the most applied technique and provides accurate strength predictions provided that the cohesive law shape and correspondent parameters were correctly defined. Neto et al. [14] investigated failure in composite adhesive joints (unidirectional carbon-epoxy pre-preg) bonded with two adhesives with different characteristics (one brittle and one ductile). They also evaluated several overlap lengths (L_O) in experimental tests. Then, CZM was applied to predict the results obtained in the experimental data. The numerical analysis considered geometrical nonlinear effects and the orthotropic properties of the composite. The shape law used to perform the analysis was triangular. The results obtained from the numerical simulations with CZM were considered satisfactory for the brittle adhesive, while the same accuracy was not obtained for the ductile one. The authors concluded that the triangular law was not the best choice for the ductile adhesive since its behaviour resembles a trapezium shape. Even so, failure initiation and propagation were simulated by the model. More recently, Teimouri et al. [15] evaluated a trilinear cohesive law to simulate mode I fatigue delamination in composites undergoing large-scale fibre bridging. This model was constructed by overlapping two bilinear CZMs. The authors developed Abaqus subroutines and conducted FEM analysis to 3D Double Cantilever Beams (DCB) under high-cycle fatigue loading to implement these models. They found that this approach presents more accuracy than the bilinear models.

Another approach widely studied is fracture mechanics since it allows to assess discontinuities in materials, such as re-entrant corners at the adhesive-adherend interface or defects [13]. The models based on this approach typically use the Stress Intensity Factor (SIF) or energetic concepts, such as the J-integral [16] or the Virtual Crack Closure Technique [17]. A SIF analysis permits to analyse the discontinuity via stresses and strains, while an energetic analysis relies on the amount of energy necessary to overcome material resistance [18]. In 2002, Leguillon [19] introduced the Finite Fracture Mechanics (FFM) technique that combines stress with energetic principles. This method does not require an initial crack. In simple terms, a certain amount of energy is necessary to open the crack and sufficient stress to damage the material. In 2021, Fernandes et al. [20] investigated the fracture onset and crack deflection in multi-material adhesive joints with thick bond lines ($\approx$10 mm) under global mode I loading. They tested single-material (steel-steel and Glass Fibre Reinforced Polymer (GRFP)-GFRP) and multi-material (GFRP-GFRP) DCB joints bonded with a structural epoxy adhesive. The authors modelled the joints analytically, resorting to Kanninen model [21] considering an elastic–plastic beam and relied on FEM. They found an empirical relation defining the transition between non-cohesive and cohesive fracture onset. They also observed that the magnitude of the stress singularity at the pre-crack tip is superior to the one nearby the bi-material corners when the pre-crack length exceeds a specific value. Nonetheless, the crack propagation suddenly changes direction out of the adhesive mid-thickness, explained by the positive T-stresses along the crack tip.

Most adhesive joints have sharp interface corners between the adhesive and the adherends that originate stress singularities. These stress singularities are often the initial point of failure in adhesive joints, so it is important to study and characterize them. To that end, the Intensity of Singular Stress Fields (ISSF), also known as General Stress Intensity Factor (GSIF), can be used. The ISSF is applicable to a variety of corner configurations with multiple materials, but depending on the material types, it can be formulated differently. The simplest scenario is when all the materials in the corner are isotropic, and the earliest works on the ISSF were focused on this case [22,23]. Later, some authors also began to show interest in analysing the ISSF in corners made of only anisotropic materials, and one of the earliest examples of this approach is the work of Delale [24], with posterior examples found in references [25,26], whose ISSF analysis is based on the Stroh formalism [27]. Yao et al. [28] presented an alternative way to perform this analysis based on the elastic governing equations and the asymptotic expansions of displacement and stress near the notch tip. Corners with both types of materials, isotropic and anisotropic, present the most challenging ISSF analysis. Ting and Chyanbin [29] proposed an adaptation of the Stroh formalism that could solve this problem, paving the way for the works of Barroso et al. [30,31] and the current work that is based on this adaptation.

This work aims to evaluate the ISSF criterion on orthotropic materials. Single-Lap Joints (SLJ) made from Carbon Fibre Reinforced Polymer (CFRP) bonded with a brittle adhesive (Araldite AV-138) were used. To assess the influence of L_O on the experimental results, eight L_O were applied, starting at 10 mm and incrementing it 10 mm each time. Firstly, the experimental data, namely the maximum loads sustained by the joints, are analysed. Then, the modelling conditions and ISSF formulation are presented. Next, to strength predict the joints, the ISSF criterion is applied using the FEM. Finally, the experimental data are compared to the numerical strength predictions to evaluate the accuracy of the criterion tested.

2. Experimental details

2.1. SLJ geometry and dimensions

The SLJ tested in this work for validation purposes are composed of CFRP adherends and the brittle adhesive Araldite® AV138. The base SLJ geometry and respective dimensional parameters are depicted in Fig. 1. The relevant parameters, which fully define the SLJ geometry, are (in mm): $10 < L_O < 80$ (in intervals of 10), unsupported length (between testing grips) $L_T = 200$, adherend thickness $t_P = 2.4$, adhesive thickness $t_A = 0.2$ and width $B = 15$ (not shown in the figure). The boundary conditions presented in Fig. 1 aim to emulate the gripping conditions in the testing machine and consist of fixing the left edge and pull the right edge while restraining it transversely.

2.2. CFRP adherends and adhesive

The SLJ are made of CFRP adherends, using unidirectional pre-preg from SEAL® (Texipreg HS 160 RM; Legnano, Italy) to produce unidirectional laminates with a ply unit thickness of 0.15 mm. These adherends were cut from large plates with 300 × 300 mm^2 into small specimens. The bulk plates were produced by manual stacking and consolidation, considering a total of 20 plies, followed by one-hour curing in a hot-plates press with a temperature of 130 °C and holding pressure of 2 bar. According to the manufacturer, for these working

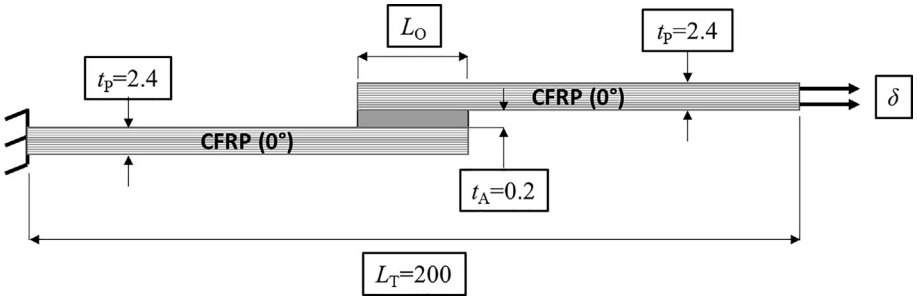

Fig. 1. SLJ geometry and respective dimensional parameters (in mm).

conditions (ply thickness, temperature and pressure), the fibre volume fraction is approximately 64%, and nearly null porosity content is guaranteed. Table 1 presents the elastic properties of a unidirectional lamina, modelled as elastic orthotropic in the FEM analysis [32].

Validation of the ISSF technique was accomplished in composite joints bonded using the two-part structural epoxy adhesive Araldite® AV138, which is one of the strongest from this family of Araldite® adhesives although it is brittle. Actually, its tensile strength is nearly 40 MPa, but the tensile stress-tensile strain (σ-ε) behaviour up to failure is linear. This feature, associated with its high stiffness, leads to limitations regarding its application to bonded joints, which most often experience large stress concentrations (for example, at the overlap edges for SLJ [33]), resulting in premature failure at those sites. However, for short L_O, these adhesives typically behave better and can compete with more ductile adhesives due to the more uniform stress distributions in the elastic regime, which enables an efficient load transfer [34]. This adhesive was duly tested in former works [35], leading to the acquired average ± deviation data presented in Table 2. On the one hand, tensile tests of adhesive bulk specimens (dogbone shape) allowed to estimate the relevant tensile data: Young's modulus (E), tensile yield stress (σ_y), tensile strength (σ_f) and tensile failure strain (ε_f). These specimens were fabricated as per the NF T 76–142 French standard, i.e., by mould injection, to produce high-quality and void-free specimens. A sample tensile stress-tensile strain (σ-ε) curve for this adhesive is presented in the mentioned work [35]. On the other hand, the shear properties of the adhesive, such as the shear modulus (G), shear yield stress (τ_y), shear strength (τ_f) and shear failure strain (γ_f), were taken from Thick Adherend Shear Tests (TAST) performed to thin adhesive layers. The specimens' fabrication and testing followed the recommendations of the ISO 11003–2:1999 standard. To comply with this standard, an alignment jig was fabricated to guarantee both longitudinal and transversal alignment and ensure the required bond length of 5 mm. The adherends were made of DIN C45E steel to promote the necessary stiffness, and thus to prevent adherend deformations to affect the stiffness measurements. All collected data is presented in Table 2.

2.3. Joint production and testing

The use of robust experimental procedures is essential for the accuracy of the obtained results and the robustness of the numerical validation processes. Fabrication of the CFRP SLJ was initiated by fabricating composite plates with a dimension of 300 × 300 mm^2, followed by cutting the adherends in a diamond disc table to their final dimensions. The plates were fabricated by hand lay-up up to reaching the $[0]_{16}$ configuration, followed by curing with temperature (130 °C) and pressure (2 bar) in a hot-plates press. Before the bonding process, the relevant surfaces were abraded with 320 grit sandpaper to remove the outer layer, improve the roughness and activate the surfaces, followed by cleaning with acetone to remove any contaminants and abraded particles [36]. SLJ assembly took place in a specific steel jig, composed of two plates: the lower one for the specimens' alignment and the upper one for pressure application. By using a set of spacers, it was possible to assure the correct t_A. Parallel to adherend bonding, end tabs were also bonded in place to enable centred gripping in the testing machine. After the adherends/spacers were set in place, the upper mould's plate squeezed the entire set, and the joints were left to cure for one week at room temperature and humidity. Finally, the specimens were demoulded and the resulting adhesive excess at the overlap boundaries removed by milling. The SLJs were tested under identical environmental conditions in a Shimadzu AG-X 100 electro-mechanical tester with a 1 mm/min velocity. The P-δ data was taken from a 100 kN load cell to measure P and from the grips' displacement for δ. Each joint configuration, defined by the respective L_O, was tested five times to produce representative results.

Table 1
Elastic constants of a unit ply with fibres along the x axis (y and z are the transverse and thickness directions, respectively) [32].

E_x = 1.09E + 05 MPa	ν_{xy} = 0.342	G_{xy} = 4315 MPa
E_y = 8819 MPa	ν_{xz} = 0.342	G_{xz} = 4315 MPa
E_z = 8819 MPa	ν_{yz} = 0.380	G_{yz} = 3200 MPa

Table 2
Mechanical properties of the adhesive [35].

Properties	AV 138
E (GPa)	4.89 ± 0.81
ν	0.35[1]
σ_y (MPa)	36.49 ± 2.47
σ_f (MPa)	39.45 ± 3.18
ε_f (%)	1.21 ± 0.10
G (GPa)	1.56 ± 0.01
τ_y (MPa)	25.1 ± 0.33
τ_f (MPa)	30.2 ± 0.40
γ_f (%)	7.8 ± 0.7

[1]Data from the manufacturer.

3. Numerical analysis

3.1. Composite ISSF formulation

The ISSF criterion is a fracture mechanics based approach to evaluate discontinuities in single and multi-materials corners. In the case studied in this work, bi-material interface corners can be found in SLJ, such as those from Fig. 2.

Since composite materials are considered in this investigation, a different formulation is required for the ISSF criterion. Thus, the following formulation considers the peculiarities of these materials and it is based on the references [30,37]. In a three-dimensional Cartesian

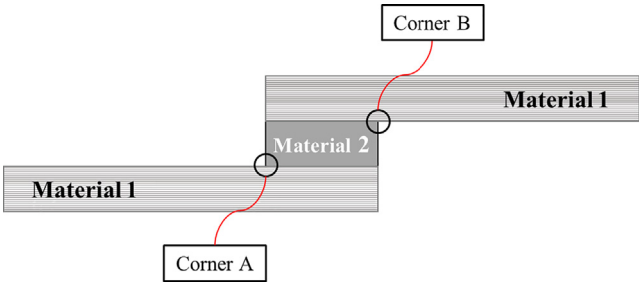

Fig. 2. Bi-material interface corners found in a SLJ.

coordinate system, the constitutive law of a material can be defined as $\boldsymbol{\sigma} = \boldsymbol{C\varepsilon}$, where $\boldsymbol{C}$ is the material constitutive matrix defined as follows:

$$\boldsymbol{C}^{-1} = \begin{bmatrix} \frac{1}{E_1} & -\frac{\nu_{12}}{E_1} & -\frac{\nu_{13}}{E_1} & 0 & 0 & 0 \\ -\frac{\nu_{21}}{E_2} & \frac{1}{E_2} & -\frac{\nu_{23}}{E_2} & 0 & 0 & 0 \\ -\frac{\nu_{31}}{E_3} & -\frac{\nu_{32}}{E_3} & \frac{1}{E_3} & 0 & 0 & 0 \\ 0 & 0 & 0 & \frac{1}{G_{23}} & 0 & 0 \\ 0 & 0 & 0 & 0 & \frac{1}{G_{13}} & 0 \\ 0 & 0 & 0 & 0 & 0 & \frac{1}{G_{12}} \end{bmatrix} \tag{1}$$

and $\boldsymbol{\sigma}$ and $\boldsymbol{\varepsilon}$ are the stress and strain vectors, respectively, in Voigt notation. Here E is Young's modulus, ν is the Poisson's ratio and G is the shear modulus. As $\boldsymbol{C}^{-1}$ is symmetric, the following conditions must be verified: $\nu_{12}/E_1 = \nu_{21}/E_2$, $\nu_{23}/E_2 = \nu_{32}/E_3$ and $\nu_{13}/E_1 = \nu_{31}/E_3$. The Stroh formalism [38] is defined by the following eigensystem:

$$\boldsymbol{N\xi}_\alpha = p_\alpha \boldsymbol{\xi}_\alpha \tag{2}$$

where p_α are the eigenvalues and $\boldsymbol{\xi}_\alpha$ are the eigenvectors of the system. In total, this system has 6 eigenvectors and eigenvalues since $\boldsymbol{N}$ is a 6×6 matrix, defined as:

$$\boldsymbol{N} = \begin{bmatrix} \boldsymbol{N}_1 & \boldsymbol{N}_2 \\ \boldsymbol{N}_3 & \boldsymbol{N}_1^T \end{bmatrix} \tag{3}$$

where $\boldsymbol{N}_1 = -\boldsymbol{T}^{-1}\boldsymbol{R}^T$, $\boldsymbol{N}_2 = -\boldsymbol{T}^{-1}$ and $\boldsymbol{N}_3 = \boldsymbol{RT}^{-1}\boldsymbol{R}^T - \boldsymbol{Q}$, and:

$$\boldsymbol{Q} = \begin{bmatrix} C_{11} & C_{16} & C_{15} \\ C_{16} & C_{66} & C_{56} \\ C_{15} & C_{56} & C_{55} \end{bmatrix}; \quad \boldsymbol{R} = \begin{bmatrix} C_{16} & C_{12} & C_{14} \\ C_{66} & C_{26} & C_{46} \\ C_{56} & C_{25} & C_{45} \end{bmatrix}; \quad \boldsymbol{tT} = \begin{bmatrix} C_{66} & C_{26} & C_{46} \\ C_{26} & C_{22} & C_{24} \\ C_{46} & C_{24} & C_{44} \end{bmatrix} \tag{4}$$

The results of this eigensystem are complex. Thus, for a p_α and $\boldsymbol{\xi}_\alpha$ pair that satisfies Eq. (2), its complex conjugate $\bar{p}_\alpha$ and $\bar{\boldsymbol{\xi}}_\alpha$ will satisfy it too. Each eigenvector can be separated into two parts, $\boldsymbol{\xi}_\alpha^T = \begin{bmatrix} \boldsymbol{a}_\alpha^T & \boldsymbol{b}_\alpha^T \end{bmatrix}$, being $\boldsymbol{a}_\alpha$ proportional to the displacement vector and $\boldsymbol{b}_\alpha$ proportional to the traction vector. Depending on the material properties, the number of eigenvalues and eigenvectors changes. For transversely isotropic materials, like unidirectional fibre-reinforced polymers, there are three different eigenvalues and eigenvectors. However, for isotropic materials, as adhesives generally are, there is only one eigenvalue $p = i$, and its complex conjugate $\bar{p} = -i$, and two linearly independent eigenvectors. Therefore, in the latter case, a modification to the Stroh formalism is required, so Eq. (2) is changed to:

$$\boldsymbol{N\xi}_1 = p\boldsymbol{\xi}_1 \;;\; \boldsymbol{N\xi}_2 = p\boldsymbol{\xi}_2 + \boldsymbol{\xi}_1 \;;\; \boldsymbol{N\xi}_3 = p\boldsymbol{\xi}_3 \tag{5}$$

which means that $\boldsymbol{\xi}_1$ and $\boldsymbol{\xi}_3$ can be determined solving the original eigensystem, but $\boldsymbol{\xi}_2^T = \begin{bmatrix} \boldsymbol{a}_2^T & \boldsymbol{b}_2^T \end{bmatrix}$ is determined as follows:

$$-\left[\boldsymbol{Q} + (\boldsymbol{R} + \boldsymbol{R}^T)p + \boldsymbol{T}p^2\right]\boldsymbol{a}_2 = (2p\boldsymbol{T} + \boldsymbol{R} + \boldsymbol{R}^T)\boldsymbol{a}_1 \tag{6}$$

$$\boldsymbol{b}_2 = \boldsymbol{T}\boldsymbol{a}_1 + (\boldsymbol{R}^T + p\boldsymbol{T})\boldsymbol{a}_2 \tag{7}$$

A vector $\boldsymbol{w}(r,\theta)^T = \begin{bmatrix} \boldsymbol{u}(r,\theta)^T & \boldsymbol{\varphi}(r,\theta)^T \end{bmatrix}$, where $\boldsymbol{u}$ is the displacement vector and $\boldsymbol{\varphi}$ is the stress function vector, can be defined as:

$$\boldsymbol{w}(r,\theta) = r^\lambda \boldsymbol{XZq} \tag{8}$$

where $\boldsymbol{q}$ is a constant vector, $\mathbf{X} = \begin{bmatrix} \boldsymbol{\xi}_1 & \boldsymbol{\xi}_2 & \boldsymbol{\xi}_3 & \bar{\boldsymbol{\xi}}_1 & \bar{\boldsymbol{\xi}}_2 & \bar{\boldsymbol{\xi}}_3 \end{bmatrix}$ and $\boldsymbol{Z}$ is determined in different ways depending on the number of linearly independent eigenvectors and eigenvalues. Thus, for three linearly independent eigenvectors and three eigenvalues:

$$\boldsymbol{Z}(\theta) = \begin{bmatrix} \left\langle \zeta_\alpha^\lambda(\theta) \right\rangle & \mathbf{0}_{3\times3} \\ \mathbf{0}_{3\times3} & \left\langle \bar{\zeta}_\alpha^\lambda(\theta) \right\rangle \end{bmatrix} \tag{9}$$

where angle brackets represent diagonal matrices. For two linearly independent eigenvectors and one eigenvalue, $\mathbf{Z}$ is also dependent on λ and it is defined as:

$$\boldsymbol{Z}(\theta,\lambda) = \begin{bmatrix} \boldsymbol{\Psi}(\theta,\lambda) & \mathbf{0}_{3\times3} \\ \mathbf{0}_{3\times3} & \bar{\boldsymbol{\Psi}}(\theta,\lambda) \end{bmatrix} \tag{10}$$

with:

$$\boldsymbol{\Psi}^\lambda(\theta) = \begin{bmatrix} \zeta^\lambda(\theta) & K(\theta,\lambda)\zeta^\lambda(\theta) & 0 \\ 0 & \zeta^\lambda(\theta) & 0 \\ 0 & 0 & \zeta^\lambda(\theta) \end{bmatrix} \tag{11}$$

being $K(\theta,\lambda) = \lambda \sin(\theta)/\zeta(\theta)$ and $\zeta_\alpha^\lambda(\theta) = [\cos(\theta) + p_\alpha \sin(\theta)]^\lambda$.

Considering a material m in a bi-material wedge, defined by an initial angle θ_{m-1} and an end angle θ_m, the following relation can be established:

$$\boldsymbol{w}(r,\theta_m) = \boldsymbol{E}(\lambda,\theta_m,\theta_{m-1})\boldsymbol{w}(r,\theta_{m-1}), \tag{12}$$

being:

$$\boldsymbol{E}(\lambda,\theta_m,\theta_{m-1}) = \boldsymbol{XZ}^\lambda(\theta_m)\left[\boldsymbol{Z}^\lambda(\theta_{m-1})\right]^{-1}\boldsymbol{X}^{-1} \tag{13}$$

where $\boldsymbol{Z}^\lambda(\theta_m)\left[\boldsymbol{Z}^\lambda(\theta_{m-1})\right]^{-1}$ can be simplified to $\boldsymbol{Z}^\lambda(\theta_m,\theta_{m-1})$,which is also dependent on the number of linearly independent eigenvectors and eigenvalues. As a result, for three linearly independent eigenvectors and three eigenvalues, it can be written:

$$\boldsymbol{Z}^\lambda(\theta_m,\theta_{m-1}) = \begin{bmatrix} \left\langle \zeta_\alpha^\lambda(\theta_m,\theta_{m-1}) \right\rangle & \mathbf{0}_{3\times3} \\ \mathbf{0}_{3\times3} & \left\langle \bar{\zeta}_\alpha^\lambda(\theta_m,\theta_{m-1}) \right\rangle \end{bmatrix} \tag{14}$$

while for two linearly independent eigenvectors and one eigenvalue, $\boldsymbol{Z}$ is also dependent on λ and it is defined as:

$$\boldsymbol{Z}^\lambda(\theta_m,\theta_{m-1},\lambda) = \begin{bmatrix} \boldsymbol{\Psi}(\theta_m,\theta_{m-1},\lambda) & \mathbf{0}_{3\times3} \\ \mathbf{0}_{3\times3} & \bar{\boldsymbol{\Psi}}(\theta_m,\theta_{m-1},\lambda) \end{bmatrix} \tag{15}$$

with:

$$\boldsymbol{\Psi}(\theta_m,\theta_{m-1},\lambda) = \begin{bmatrix} \zeta^\lambda(\theta_m,\theta_{m-1}) & K(\theta_m,\theta_{m-1},\lambda)\zeta^\lambda(\theta_m,\theta_{m-1}) & 0 \\ 0 & \zeta^\lambda(\theta_m,\theta_{m-1}) & 0 \\ 0 & 0 & \zeta^\lambda(\theta_m,\theta_{m-1}) \end{bmatrix} \tag{16}$$

being $\zeta_\alpha(\theta_m,\theta_{m-1}) = \zeta_\alpha(\theta_m)/\zeta_\alpha(\theta_{m-1})$ and:

$$K(\theta_m,\theta_{m-1},\lambda) = \frac{\lambda \sin(\theta_m - \theta_{m-1})}{\zeta(\theta_m)\zeta(\theta_{m-1})} \tag{17}$$

In a wedge made of two perfectly bonded materials, as shown in Fig. 3, it is possible to relate $\boldsymbol{w}(r,\theta_0)$ with $\boldsymbol{w}(r,\theta_2)$. If $\boldsymbol{w}(r,\theta_1) = \boldsymbol{E}(\lambda,\theta_1,\theta_0)\boldsymbol{w}(r,\theta_0)$ and $\boldsymbol{w}(r,\theta_2) = \boldsymbol{E}(\lambda,\theta_2,\theta_1)\boldsymbol{w}(r,\theta_1)$, then:

$$\boldsymbol{w}(r,\theta_2) = \boldsymbol{K}_W(\lambda)\boldsymbol{w}(r,\theta_0) \tag{18}$$

being $\boldsymbol{K}_W(\lambda) = \boldsymbol{E}(\lambda,\theta_2,\theta_1)\boldsymbol{E}(\lambda,\theta_1,\theta_0)$ called the transfer matrix. Afterwards, it is necessary to impose boundary conditions to $\boldsymbol{K}_W$. In adhesive joints, the outer faces of the interface wedge are free.

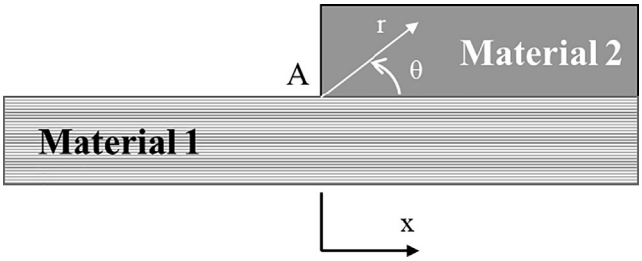

Fig. 3. Wedge corner in a bi-material interface.

Now it is necessary to impose the boundary conditions. In adhesive joints, both outer faces of the interface wedge are free. Thus, $\boldsymbol{\varphi}(r,\theta_0)=\boldsymbol{\varphi}(r,\theta_2)=0$ must be imposed, and the following boundary condition matrices are used:

$$\boldsymbol{D}_0=\boldsymbol{D}_2=\begin{bmatrix}\boldsymbol{0}_{3\times3} & \boldsymbol{I}_{3\times3}\\ \boldsymbol{I}_{3\times3} & \boldsymbol{0}_{3\times3}\end{bmatrix} \tag{19}$$

These boundary condition matrices are used to modify the transfer matrix:

$$\boldsymbol{K}_{WBC}(\lambda)=\boldsymbol{D}_2\boldsymbol{K}_W\boldsymbol{D}_0^T \tag{20}$$

Considering the boundary conditions, the system of equations is rewritten as:

$$\begin{bmatrix}\boldsymbol{0}_{3\times1}\\ \boldsymbol{u}(r,\theta_2)\end{bmatrix}=\begin{bmatrix}\boldsymbol{K}_{WBC}^{(1)}(\lambda) & \boldsymbol{K}_{WBC}^{(2)}(\lambda)\\ \boldsymbol{K}_{WBC}^{(3)}(\lambda) & \boldsymbol{K}_{WBC}^{(4)}(\lambda)\end{bmatrix}\begin{bmatrix}\boldsymbol{0}_{3\times1}\\ \boldsymbol{u}(r,\theta_0)\end{bmatrix} \tag{21}$$

From Eq. (21), the following is verified $0_{3\times1}=\boldsymbol{K}_{WBC}^{(2)}(\lambda)\boldsymbol{u}(r,\theta_0)$. Therefore, a non-trivial solution is found if and only if:

$$\left|\boldsymbol{K}_{WBC}^{(2)}(\lambda)\right|=0 \tag{22}$$

The solutions to Eq. (22) are the characteristic exponents of the bi-material corner (λ). There is an infinite number of solutions to Eq. (22) but, near the corner, the singularities $\lambda<1$ overwhelm the other λ since they are the solutions that produce the singularity. Thus, only $\lambda<1$ are considered in the current study. With λ determined, the next step is the calculation of the stress and displacement around the interface corner. So, for a given angle (θ) inside a material (m), the polar stress components can be defined as:

$$\begin{aligned} f_{rr}&=-\boldsymbol{s}_r^T(\theta)\boldsymbol{\varphi}_{,\theta}(r,\theta)/r;\quad f_{\theta\theta}=\boldsymbol{n}^T(\theta)\boldsymbol{\varphi}_{,r}(r,\theta);\\ f_{r\theta}&=-\boldsymbol{n}^T(\theta)\boldsymbol{\varphi}_{,\theta}(r,\theta)/r=\boldsymbol{s}_r^T(\theta)\boldsymbol{\varphi}_{,r}(r,\theta)\end{aligned} \tag{23}$$

while the displacements are defined as:

$$g_r=-\boldsymbol{s}_r^T(\theta)\boldsymbol{u}(r,\theta)/r;\quad g_\theta=\boldsymbol{n}^T(\theta)u(r,\theta) \tag{24}$$

where $\boldsymbol{s}_r^T=[\cos(\theta)\quad \sin(\theta)\quad 0]$ and $\boldsymbol{n}^T=[\sin(\theta)\quad -\cos(\theta)\quad 0]$. To determine the components in Eqs. (23) and (24), it is first necessary to determine $\boldsymbol{w}(r,\theta_0)$ and $\boldsymbol{w}(r,\theta_1)$ for each λ. Due to the boundary conditions, $\boldsymbol{\varphi}(r,\theta_0)=0_{3\times1}$ and $\boldsymbol{u}(r,\theta_0)$ is determined by solving $0_{3\times1}=\boldsymbol{K}_{WBC}^{(2)}(\lambda)\boldsymbol{u}(r,\theta_0)$, as it can be inferred from Eq. (21). Therefore, $\boldsymbol{w}(r,\theta_0)^T=[\boldsymbol{u}(r,\theta_0)^T\quad \boldsymbol{\varphi}(r,\theta_0)^T]$. Having determined $\boldsymbol{w}(r,\theta_0)$, $\boldsymbol{w}(r,\theta_1)$ is determined by simply using Eq. (12). Then, Eq. (12) can be used to determine $\boldsymbol{w}(r,\theta)$ and its derivatives, needed for Eqs. (23) and (24), for each λ in a material m, by substituting θ_m by θ. It is important to note that the components of Eqs. (23) and (24) have to be standardized since if $\boldsymbol{w}(r,\theta_0)$ is a solution so is $c\boldsymbol{w}(r,\theta_0)$, where c is any constant, i.e. there are infinite solutions to this problem. In the current work, this standardization was performed by analysing f_{ij} and g_i around the whole interface corner, finding the maximum value of any component, and then dividing f_{ij} and g_i by that maximum value. Ensuring that f_{ij} and g_i are at most equal to 1.

Knowing the singularity exponents (λ) and the stress (f) and displacement (g) functions, it is possible to define the stress and displacement near the singularity as:

$$\sigma_{ij}=\sum_{k=1}^{n}H_k r^{\lambda_k-1}f_{ij}(\lambda_k,\theta) \tag{25}$$

$$u_j=\sum_{k=1}^{n}H_k r^{\lambda_k}g_j(\lambda_k,\theta) \tag{26}$$

being n the number of singularity exponents (λ), which is dependent on the geometry and materials of the interface corner. H_k is the ISSF, or GSIF, which is a scalar value related to the singularity component k.

There are different alternatives to determine the ISSF. For example, Qian and Akisanya [39] used a line integral encircling the interface corner to determine the ISSF. However, in the current work, another method was used to determine the ISSF. The method used is based on the extrapolation of the ISSF from values near the corner to the corner. A similar method was used by Klusák et al. [40]. A n number of points at different angles (θ) and at a fixed radius (r) are needed to perform this extrapolation, e.g., if there are two singularity components λ_1 and λ_2, then two different angles are needed. So, for a radius r, $\boldsymbol{H}$ can be determined with the following equation:

$$\begin{bmatrix} r^{\lambda_1-1}f_{\theta\theta}(\lambda_1,\theta_{n+1}) & \cdots & r^{\lambda_n-1}f_{\theta\theta}(\lambda_n,\theta_{n+1})\\ \vdots & \ddots & \vdots\\ r^{\lambda_1-1}f_{\theta\theta}(\lambda_1,\theta_{n+n}) & \cdots & r^{\lambda_n-1}f_{\theta\theta}(\lambda_n,\theta_{n+n})\end{bmatrix}\begin{bmatrix}H_1\\ \vdots\\ H_n\end{bmatrix}=\begin{bmatrix}\sigma_{\theta\theta}(r,\theta_{n+1})\\ \vdots\\ \sigma_{\theta\theta}(r,\theta_{n+n})\end{bmatrix} \tag{27}$$

This equation is solved for several different r, which allows the extrapolation to $r=0$ mm from an r interval where $\boldsymbol{H}$ is stable. This will be the actual $\boldsymbol{H}$ at the interface corner.

3.2. Model preparation and processing

Eight meshes were created for each different L_O to perform the FE Analysis (FEA). However, in the vicinity of the interface corners, the meshes were all equal (Fig. 4 (a)). The dimensions and boundary conditions presented in Fig. 4 (b) were used to create the meshes in that region. The left boundary was considered fixed ($U_x=U_y=U_z=0$), while δ was imposed in the right boundary. The FEA was performed using a custom MATLAB program developed by the authors and every element is a quadrilateral element with four nodes. From the results obtained with the FEA, a MATLAB script was developed to apply the process described in Section 3.1 and perform the ISSF analysis, allowing the prediction of P_m values based on the ISSF at the interface corner. All simulations were made under small strains and plane strain conditions.

4. Results

4.1. Test results and discussion

The experimental data and respective discussion are presented for further comparison with the ISSF predictions for validation purposes. In the SLJ experiments with the chosen adhesive, all failures were cohesive in the adhesive layer, i.e., with a visible adhesive layer on both failed surfaces throughout the entire L_O. Usually, interfacial failures are associated with poor specimen fabrication and surface preparation, and these were successfully prevented by the process described in section 2.3.

Fig. 5 plots the obtained experimental data from the tests, namely the average P_m and respective minimum and maximum value as a function of L_O. It is clear that L_O influences P_m by a monotonic increase of P_m with this parameter, which is the expected behaviour given the corresponding increase of the shear-resistant bonded area of adhesive

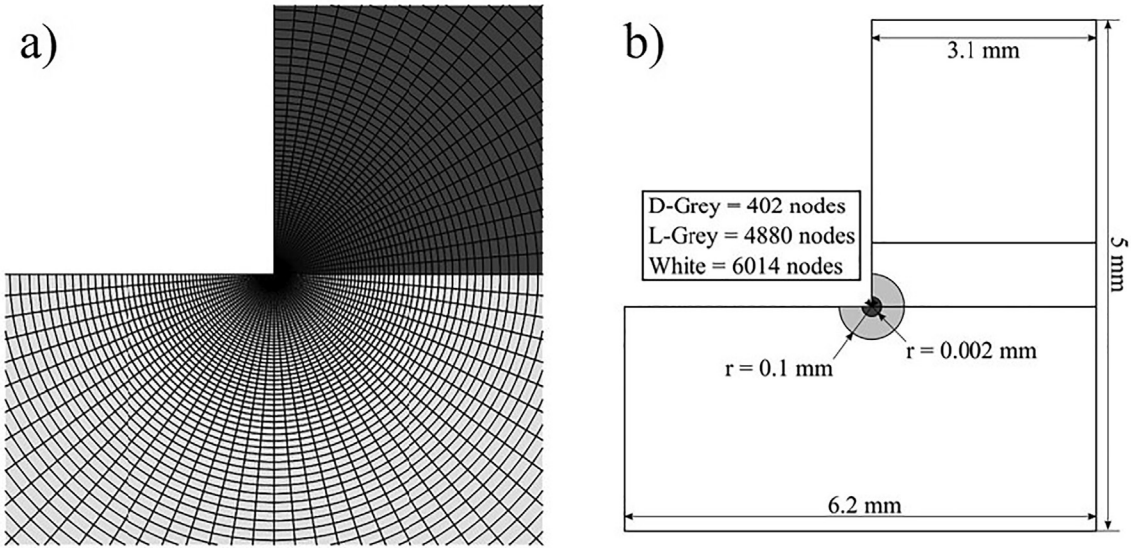

Fig. 4. Mesh applied around the interface corner: elements disposal (a) and mesh information (b).

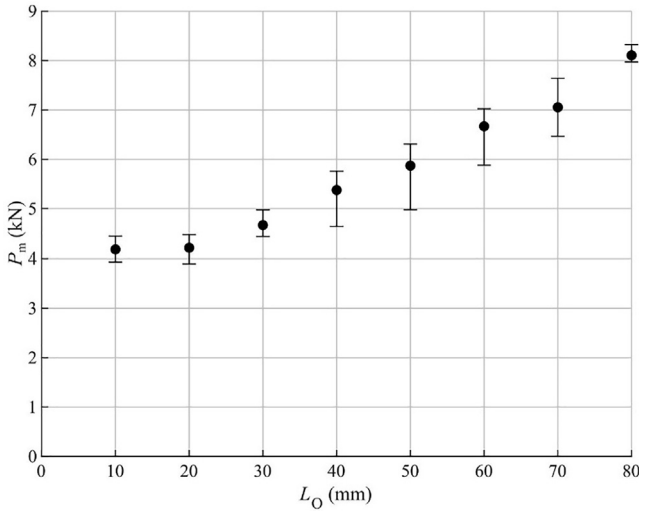

Fig. 5. Experimental P_m vs L_O data.

and agrees with previously published works for different adhesives, including brittle ones [35]. Nevertheless, brittle adhesives usually behave better for small L_O while failing to compete with ductile adhesives for large L_O, even if the latter present lower uniaxial strength, and the P_m-L_O tendency is only nearly proportional for the smaller L_O, up to approximately 20 mm. Actually, the relative P_m improvement between L_O = 10 and 20 mm is 0.78%, compared to the theoretical 100% suggested by the duplication of area. This proportionality is quickly cancelled for higher L_O, and between L_O = 10 and 80 mm, the relative improvement is only 94.13%. In absolute terms, P_m increases by 13.1 kN between the limit L_O. The reported behaviour is associated with this adhesive's marked brittleness, as shown in the mechanical characterization of section 2.2. Owing to the clear lack of capacity to undergo plasticity, added to the known marked stress concentrations in SLJ, which increase with L_O [33], the joint performance deteriorates with higher L_O, and the strength averaged to the bonded area diminishes as well. Actually, the SLJ stresses in the adhesive layer are overstudied [41], and it usually results, under the scope of 2D modelling, in peel and shear stresses measured over a rectangular coordinate system. Due to the SLJ asymmetry, peel stresses are highly concentrated at the overlap edges while reaching small compressive portions at the inner overlap. Shear stresses present a smoother gradient but also peaking at the overlap ends. In both cases, peak stresses highly increase with L_O due to increased joint rotation (peel stresses) and shear-lag effects (shear stresses), leading to the aforementioned behaviour, i.e., clear lack of proportionally by increasing L_O.

4.2. ISSF and polar stress evaluation

The experimental data gathered allowed the start of the ISSF criterion analysis. Initially, the bi-material interface corner found in the SLJ considered was inspected. Fig. 6 schematically represents the bi-material interface corner considered in the present work.

Fig. 6 also shows the anti-symmetry axis considered since only one interface corner was evaluated, in this case, the lower interface corner. As shown in Fig. 3, point A represents the corner tip and it is considered the centre of the polar coordinate system, from which coordinate r starts. For coordinate θ, the imaginary horizontal line intercepting the corner tip represents the baseline in which θ = 0°. Considering counterclockwise rotation as positive, every positive angle is part of the adhesive while negative angles belong to the adherend. Thus, for discretizing the corner geometry, the angles comprised by the adhesive and by the adherend were considered. For the adherend, the angles

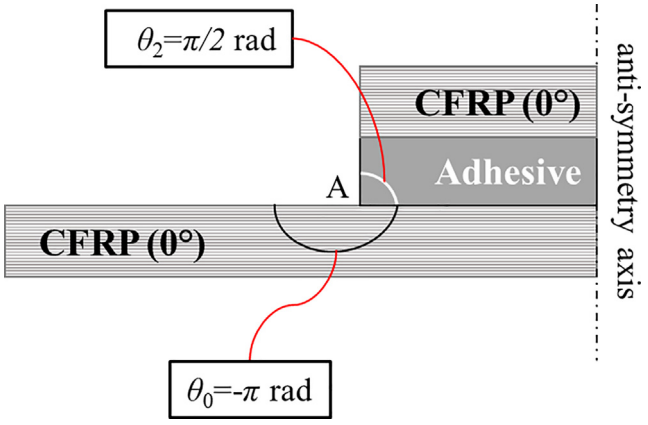

Fig. 6. Schematic representation of the bi-material interface corner considered in this work.

covered are in the interval $-\pi \leq \theta < 0$ rad, thus $\theta_0 = -\pi$ rad. On the other hand, for the adhesive, the angle interval is $0 < \theta \leq \pi/2$ rad, originating $\theta_2 = \pi/2$ rad. An additional angle was considered, representing the adhesive-adherend separation interface, which, in this case, is collinear to the imaginary horizontal line that intercepts point A, thus $\theta_1 = 0$ rad. At this stage, the CFRP and adhesive properties were also introduced in matrix $\boldsymbol{C}$ from Eq. (1), as described in section 2.2.

The previous steps made the stress singularity exponents λ determination possible by solving Eq. (22). As described in section 3.1, the resolution of Eq. (22) originates an infinite number of solutions since it is a periodic function. However, only the solutions in the interval $0 < \lambda < 1$ were considered for this study since they represent singular solutions. Nonetheless, the rigid body rotation solution ($\lambda = 1$) and the non-singular solutions ($\lambda > 1$) can also be considered, but their influence is not significant. In the studied interval, three solutions were found, with the following values: $\lambda_1 = 0.6055$, $\lambda_2 = 0.7347$ and $\lambda_3 = 0.9866$. Notwithstanding, the formulation presented in section 3.1 considers a three-dimensional coordinate system, contrary to the planar analysis (plane strain) imposed in this work. Therefore, λ_2 was excluded from the analysis since it represents an anti-plane solution.

The final step of the ISSF criterion was the determination of the stress singularity components H, resorting to Eq. (27). The objective was to find the components H at the corner tip. However, point A is defined by $r = 0$ mm, thus not being possible to obtain H from Eq. (27) directly. So, the components H were obtained for different radii from the interface corner, in the interval $0 < r < 0.1$ mm, and then extrapolated to point A. Analysing Eq. (27), the $f_{\theta\theta}$ functions from the left side matrix of this equation were attained through Eq. (23). This determination demanded two new angles ($\theta_4 = \pi/4$ rad and $\theta_5 = -3\pi/4$ rad) to perform the extrapolations. These angles correspond to nodes integrated within the FEM mesh modelled and were chosen based on the $\sigma_{\theta\theta}$ curves that will be presented later in this section. In that manner, one angle (θ_5) is in the ascending part of these curves and the other (θ_4) on the descending one. Additionally, one angle (θ_4) corresponds to nodes in the adhesive layer and the other (θ_5) in the adherend layer. Analysing now the right side of Eq. (27), the $\sigma_{\theta\theta}$ values correspond to the numerically obtained stresses from the FEM simulations in the same nodes as those used to determine $f_{\theta\theta}$. Thus, the H components are attained for the different radius. The extrapolations were performed at an interval that showed linear stability in the H-r curves obtained through the procedure described. Fig. 7 presents the H_1-r curve obtained for the $L_O = 60$ mm case. This paper only presents the H_1 component since it is the most significant to the final result. However, the procedure is the same for the H_2 component. The extrapolation for this case was performed from the interval between 0.01 and 0.02 mm. Since the nodes in this interval are extremely close to the corner tip, it was assumed that they predominantly belong to the zone of validity of this interface corner singular stress field. Fig. 7 also presents H_1 extrapolations for the L_O studied in this work. These components were determined by imposing H_1 as the H_1 obtained for the $L_O = 60$ mm case at failure displacement. Thus, the inverse procedure was performed.

In order to assess the validity of the H_1 determination procedure and understand the influence of this singularity component in the results, a comparison between the analytical and the numerical stresses was performed. The analytical stresses were obtained from Eq. (25), while the numerical stresses were extracted from the FEM simulations. For an accurate analysis, the stresses were compared at a fixed radius ($r = 0.0022$ mm) and throughout the all corner angle interval ($-\pi < \theta < \pi/2$). Also, to compare the different L_O, the stresses were evaluated when H_1 was the same for all the L_O. Fig. 8 shows the three polar stress components plots.

Analysing the numerical and analytical plots for the different L_O, it is perceptible that they are very similar in the majority of the angle interval. Only minor differences are found when the curve's peak. These deviations are explained by the non-consideration of the finite stresses (or non-singular) terms in the analytical plots. However, this proves that the singular components can accurately describe the joint behaviour near the corner and validates the implemented procedure. The graphs also present the plots of the analytical stresses resultant from each singularity component separately. These curves show the more significant influence of the first singularity component H_1 in the results, justifying why only this component was analysed in this work.

4.3. ISSF-based strength analysis

As in any other mechanical criterion, the final phase of an ISSF-based analysis was the evaluation of the joint behaviour to understand if failure was achieved or not. In this case, the parameter defining failure is P_m. This parameter was already established experimentally but not numerically. For that, it was necessary to determine the critical stress singularity components H_c. Over the years, different approaches to solve this problem were investigated and documented, such as the

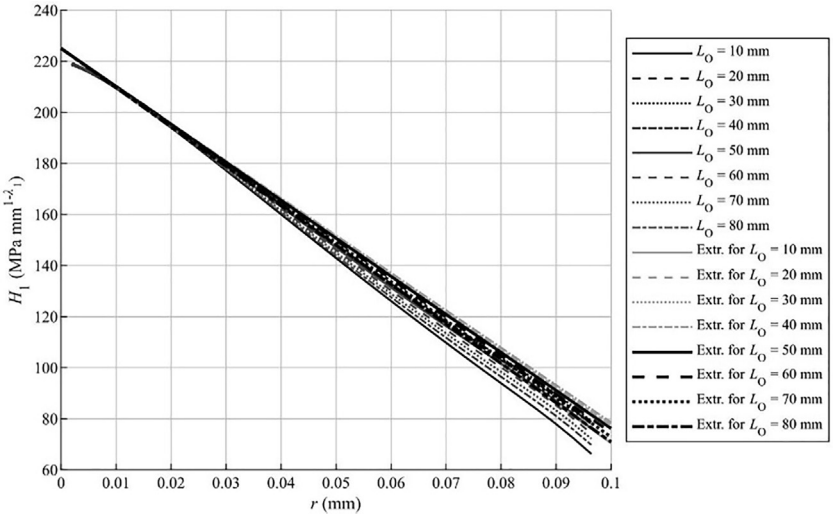

Fig. 7. H_1-r curves and extrapolations obtained for the $L_O = 60$ mm case.

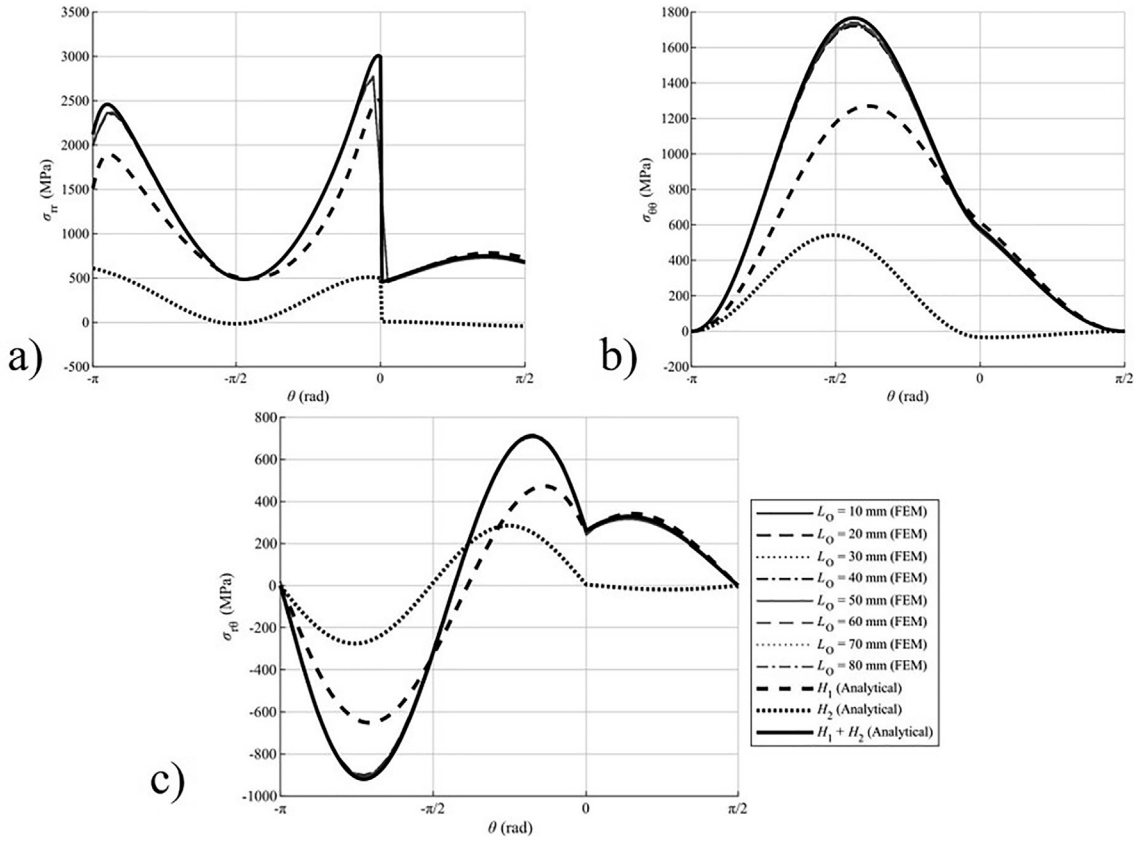

Fig. 8. Analytical and numerical polar stress components comparison: a) σ_{rr}, b) $\sigma_{\theta\theta}$ and c) $\sigma_{r\theta}$.

work of Galvez et al. [42]. This work, among others, resorted to integrals that surround all the corner area to determine H_c. But these approaches reveal extreme complexity in the implementation and require considerable computational resources. With that in mind, a more straightforward technique of determining H_c was used in this work that combines experimental and numerical data. The procedure is the same as described in section 4.2. The only difference from a regular ISSF analysis is that the imposed load of the FEM numerical simulation was the P_m experimentally determined for each L_O. This detail leads to the determination of H values that, in this case, were used as the H_c values for each L_O. Actually, Fig. 7 plot was attained considering this condition for the $L_O = 60$ mm case. Thus, the value found when the extrapolation intercepted the y-axis ($r = 0$ mm) was used as H_{1c} for this L_O. This procedure was repeated for all L_O, resulting in the values presented in Table 3.

Then, as explained in the previous section, each one of these H_{1c} was imposed for the other L_O, and the stresses and, consequently, the predicted P_m values were attained from the extrapolations. This process permitted to obtain strength predictions for each L_O based on each H_{1c}, which was considerably easier to implement. Fig. 9 displays the strength predictions accomplished.

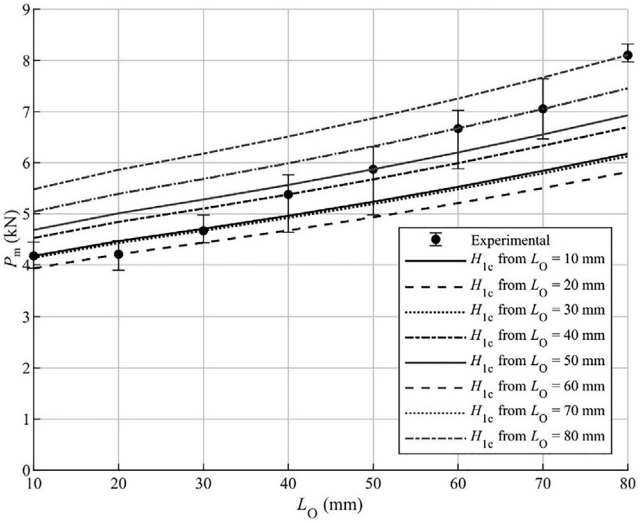

Fig. 9. Strength predictions for each L_O using each H_{1c}.

Table 3
H_{1c} values determined for each L_O.

Lo used to determine H_{1c} (mm)	H_{1c} (MPa.mm$^{1-\lambda_1}$)
10	185.59
20	181.48
30	189.48
40	205.46
50	210.96
60	225.05
70	223.27
80	240.29

A detailed analysis of this graph reveals that the strength increases between L_O resultant from each H_{1c} prediction are, generally, smaller than those verified through the experimental values. This behaviour is not verified only between two L_O (10 and 20 mm), where the experimental strength increase observed is 32.47 N while the predicted ones round between 288.25 and 381.55 N. This is clearly an anomaly related to the experimental P_m value for $L_O = 10$ mm, which does not follow the proportional tendency of the rest of the P_m values.

Therefore, the strength predictions performed with this L_O can be considered flawed, even leading to predictions superior to those observed for $L_O = 20$ mm and $L_O = 30$ mm. Nonetheless, the remaining strength predictions confirm that if this value were correct, it would follow the same trend.

Regarding the accuracy of the strength predictions, it is possible to state that the greater the difference between the L_O of the prediction and the one used to determine H_{1c}, the greater the difference between the prediction and the experimental P_m. This observation is proved, for example, when $L_O = 20$ mm was used for the prediction of the joint with $L_O = 80$ mm, where a 2287.22 N difference was found, which corresponds to an error of 28.22%. Yet, if using $L_O = 30$ mm to predict the same joint, the error reduces to 24.45%, equivalent to a 3.76% error reduction. On the other hand, if an L_O closer to the L_O used to determine H_{1c} is used, i.e., if the predicted joint L_O has an absolute deviation of 40 mm (± 20 mm) from the L_O used to perform the prediction, the percentual deviation diminishes considerably. Considering the same case presented before, and now using $L_O = 70$ mm to predict the $L_O = 80$ mm joint, the difference found was 646.96 N, resulting in a percentual deviation of 7.98% relative to the experimental value. Obviously, these behaviours were not found for strength predictions resorting to $L_O = 10$ mm, due to the already discussed anomaly.

Finally, it is also discernible that when predicting the strength of an L_O larger than the one used to determine H_{1c}, the result is always an underprediction, while the inverse behaviour is also verifiable, i.e. when predicting the strength of an L_O smaller than the one used to determine H_{1c}, an over-prediction is always attained. Besides the $L_O = 10$ mm case, this situation does not occur only in another case: between $L_O = 60$ mm and $L_O = 70$ mm. Here, the strength predictions found were so similar that a peculiarity arose. Namely, the strength predictions obtained with $L_O = 60$ mm showed to be higher than those found for $L_O = 70$ mm, which can be explained by the geometrical properties of these joints and the stresses found when solving the ISSF criterion and numerical simulations.

5. Conclusions

The work presented in this paper intended to propose and evaluate a new method for the determination of critical stress singularities, necessary to the ISSF criterion applied to composite adhesive joints. With that purpose, initially, experimental tests were performed to SLJ made from CFRP bonded with a brittle adhesive and with eight different L_O. The experimental data collected from the tests was treated and the average maximum loads (P_m) sustained by each joint were extracted. The implementation of the ISSF criterion started with the definition of the materials and bi-material corner geometry considered. This geometry and material combination revealed the existence of three singularity exponents λ characterising the analysed corner. However, since a plane-strain analysis was carried out, one of those exponents λ was not considered in the criterion for representing an anti-plane solution. Therefore, only two exponents were used, leading to two stress singularity components (H_1 and H_2). The method proposed to determine the critical stress singularities (H_c) consisted of using the experimentally determined P_m as the imposed load in numerical FEM simulation for each L_O. The resultant stress singularities were then used as H_c for each L_O. The strength predictions obtained revealed an anomaly in the experimental P_m value for $L_O = 10$ mm, flawing the results attained with this L_O. From the results, it can be concluded that, for the prediction, it is better to resort to L_O closer (± 20 mm) to the one intended to predict since smaller percentual deviations to the experimental value were found (usually under 10%). It was also detectable that predicting the strength of an L_O larger than the one used to determine H_{1c} resulted in an underprediction, whereas the inverse behaviour is also verifiable. The only exception was found between $L_O = 60$ mm and $L_O = 70$ mm, which showed similar strength predictions with slightly higher ones for $L_O = 60$ mm. So, based on the results found, it would be advisable to only predict the strength of joints with L_O larger than the L_O used to determine H_{1c}. This warning is due to safety reasons for the mechanical projects. Regarding the proposed methodology, the results found can be considered promising, considering the simplicity of the same compared to the until now widespread approaches. That way, this method deserves further research, namely with different joint geometries or geometrical features (other than L_O). Concluding, the proposed method was successfully applied to composite adhesive joints and a bi-material interface corner.

6. Declarations

Funding

This work has been funded by the Ministério da Ciência, Tecnologia e Ensino Superior through the Fundação para a Ciência e a Tecnologia (from Portugal), under project fundings 'MIT-EXPL/ISF/0084/2017′, 'POCI-01-0145-FEDER-028351′, and 'SFRH/BD/147628/2019′. Additionally, the authors acknowledge the funding provided by the Associated Laboratory for Energy, Transports and Aeronautics (LAETA), under project 'UIDB/50022/2020′.

Data availability statement

The raw data required to reproduce these findings cannot be shared at this time as the data also forms part of an ongoing study. The processed data required to reproduce these findings cannot be shared at this time as the data also forms part of an ongoing study.

Authors' contribution

Luís Ramalho: development and implementation of the FEM routines, data analyses, original draft.

João Dionísio: development and implementation of the FEM routines, data analyses, original draft.

Isidro Sánchez: conceptualisation, experimental analysis, development, supervision, review & editing.

Raúl Campilho: final review, project administration, funding acquisition, supervision.

Jorge Belinha: final review, project administration, funding acquisition, supervision.

Declaration of Competing Interest

The authors declare that they have no known competing financial interests or personal relationships that could have appeared to influence the work reported in this paper.

References

[1] Ávila AF, Bueno PdO. An experimental and numerical study on adhesive joints for composites. Compos Struct 2004;64(3-4):531–7.
[2] Li Xi, Ma D, Liu H, Tan W, Gong X, Zhang C, et al. Assessment of failure criteria and damage evolution methods for composite laminates under low-velocity impact. Compos Struct 2019;207:727–39.
[3] Da Silva LF, Öchsner A, Adams RD. Handbook of adhesion technology. Berlin, Germany: Springer Science & Business Media; 2011.
[4] Petrie EM. Handbook of adhesives and sealants. U.S: McGraw-Hill; 2000.
[5] Du J, Salmon FT, Pocius AV. Modeling of cohesive failure processes in structural adhesive bonded joints. J Adhes Sci Technol 2004;18(3):287–99.
[6] Volkersen O. Die Nietkraftverteilung in zugbeanspruchten Nietverbindungen mit konstanten Laschenquerschnitten. Jahrb Dtsch Luftfahrtforsch 1938;15:41–7.
[7] Goland M, Reissner E. The stresses in cemented joints. J Appl Mech 1944;66:A17–27.
[8] Hart-Smith LJ. Adhesive-bonded single-lap joints. NASA Contract Report, NASA CR-112236, 1973.
[9] da Silva LFM, das Neves PJC, Adams RD, Spelt JK. Analytical models of adhesively bonded joints—Part I: Literature survey. Int J Adhes Adhes 2009;29(3):319–30.
[10] Quispe Rodríguez R, de Paiva WP, Sollero P, Bertoni Rodrigues MR, de Albuquerque ÉL. Failure criteria for adhesively bonded joints. Int J Adhes Adhes 2012;37:26–36.
[11] Clough RW. The finite element method in plane stress analysis. in Proceedings of 2nd ASCE Conference on Electronic Computation, Pittsburgh Pa; 1960.

[12] Campilho RD. Strength prediction of adhesively-bonded joints. Boca Raton, U. S.: CRC Press; 2017.
[13] Ramalho LDC, Campilho RDSG, Belinha J, da Silva LFM. Static strength prediction of adhesive joints: A review. Int J Adhes Adhes 2020;96:102451.
[14] Neto JABP, Campilho RDSG, da Silva LFM. Parametric study of adhesive joints with composites. Int J Adhes Adhes 2012;37:96–101.
[15] Teimouri F, Heidari-Rarani M, Aboutalebi FH. Finite element modeling of mode I fatigue delamination growth in composites under large-scale fiber bridging. Compos Struct 2021;263:113716.
[16] Rice JR. A path independent integral and the approximate analysis of strain concentration by notches and cracks. J Appl Mech 1968;35(2):379–86.
[17] Rybicki EF, Kanninen MF. A finite element calculation of stress intensity factors by a modified crack closure integral. Eng Fract Mech 1977;9(4):931–8.
[18] Anderson TL. Fracture mechanics: fundamentals and applications. U.S.: CRC Boca Raton, U.S.; 2017.
[19] Leguillon D. Strength or toughness? A criterion for crack onset at a notch. Eur J Mech A/Solids 2002;21(1):61–72.
[20] Fernandes RL, Budzik MK, Benedictus R, de Freitas ST. Multi-material adhesive joints with thick bond-lines: Crack onset and crack deflection. Compos Struct 2021;266:113687.
[21] Kanninen MF. An augmented double cantilever beam model for studying crack propagation and arrest. Int J Fract 1973;9:83–92.
[22] Williams ML. The stresses around a fault or crack in dissimilar media. Bull Seismol Soc Am 1959;49(2):199–204.
[23] Bogy DB. Two edge-bonded elastic wedges of different materials and wedge angles under surface tractions. J Appl Mech 1971;38(2):377–86.
[24] Delale F. Stress singularities in bonded anisotropic materials. Int J Solids Struct 1984;20(1):31–40.
[25] Pageau SS, Biggers SB. A finite element approach to three-dimensional singular stress states in anisotropic multi-material wedges and junctions. Int J Solids Struct 1996;33(1):33–47.
[26] Chen H. Stress singularities in anisotropic multi-material wedges and junctions. Int J Solids Struct 1998;35(11):1057–73.
[27] Stroh AN. Steady state problems in anisotropic elasticity. J Math Phys 1962;41 (1–4):77–103.
[28] Yao S, Zappalorto M, Pan W, Cheng C, Niu Z. Two dimensional displacement and stress fields for tri-material V-notches and sharp inclusions in anisotropic plates. Eur J Mech A/Solids 2020;80:103927.
[29] Ting TCT, Chyanbin H. Sextic formalism in anisotropic elasticity for almost non-semisimple matrix N. Int J Solids Struct 1988;24(1):65–76.
[30] Barroso A, Mantič V, París F. Singularity analysis of anisotropic multimaterial corners. Int J Fract 2003;119(1):1–23.
[31] Barroso A, Marín JC, Mantič V, París F. Premature failures in standard test specimens with composite materials induced by stress singularities in adhesive joints. Int J Adhes Adhes 2020;97:102478.
[32] Campilho RDSG, de Moura MFSF, Domingues JJMS. Modelling single and double-lap repairs on composite materials. Compos Sci Technol 2005;65(13):1948–58.
[33] Nunes SLS, Campilho RDSG, da Silva FJG, de Sousa CCRG, Fernandes TAB, Banea MD, et al. Comparative failure assessment of single and double-lap joints with varying adhesive systems. J Adhes 2016;92(7-9):610–34.
[34] Campilho RDSG, Banea MD, Pinto AMG, da Silva LFM, de Jesus AMP. Strength prediction of single- and double-lap joints by standard and extended finite element modelling. Int J Adhes Adhes 2011;31(5):363–72.
[35] De Sousa CCRG, Campilho RDSG, Marques EAS, Costa M, da Silva LFM. Overview of different strength prediction techniques for single-lap bonded joints. Proc Inst Mech Eng, Part L: J Mater: Des Appl 2017;231:210–23.
[36] Wang S, Liang W, Duan L, Li G, Cui J. Effects of loading rates on mechanical property and failure behavior of single-lap adhesive joints with carbon fiber reinforced plastics and aluminum alloys. Int J Adv Manuf Technol 2020;106(5-6):2569–81.
[37] Mantič V, Barroso A, París F. Singular Elastic Solutions in Anisotropic Multimaterial Corners: Applications to Composites. In: Mathematical Methods and Models in Composites. World Scientific; 2013. p. 425–95.
[38] Stroh AN. Steady State Problems in Anisotropic Elasticity. 1962. 41(1-4): p. 77–103.
[39] Qian ZQ, Akisanya AR. Wedge corner stress behaviour of bonded dissimilar materials. Theor Appl Fract Mech 1999;32(3):209–22.
[40] Klusák J, Profant T, Kotoul M. Various methods of numerical estimation of generalized stress intensity factors of bi-material notches. Appl Comput Mech 2009;3(2).
[41] Fernandes TAB, Campilho RDSG, Banea MD, da Silva LFM. Adhesive selection for single lap bonded joints: Experimentation and advanced techniques for strength prediction. J Adhes 2015;91(10-11):841–62.
[42] Galvez P, Noda N-A, Takaki R, Sano Y, Miyazaki T, Abenojar J, et al. Intensity of singular stress field (ISSF) variation as a function of the Young's modulus in single lap adhesive joints. Int J Adhes Adhes 2019;95:102418.

PAPER 4

MESHLESS ANALYSIS OF THE STRESS SINGULARITY IN COMPOSITE ADHESIVE JOINTS

COMPOSITE STRUCTURES

Composite Structures 280 (2022) 114910

Contents lists available at ScienceDirect

Composite Structures

journal homepage: www.elsevier.com/locate/compstruct

Meshless analysis of the stress singularity in composite adhesive joints

L.D.C. Ramalho [b,*], J.M.M. Dionísio [a], I.J. Sánchez-Arce [a], R.D.S.G. Campilho [a,b], J. Belinha [a]

[a] Departamento de Engenharia Mecânica, Instituto Superior de Engenharia do Porto, Instituto Politécnico do Porto, Rua Dr. António Bernardino de Almeida, 431, 4200-072 Porto, Portugal

[b] INEGI – Pólo FEUP, Rua Dr. Roberto Frias, s/n, 4200-465 Porto, Portugal

ARTICLE INFO

Keywords:
Composite materials
ISSF criterion
RPIM
Adhesive joints
Meshless methods

ABSTRACT

Adhesives are an exceptionally well-suited method for joining composites. Unlike other methods, such as bolting or riveting, adhesives do not introduce holes in their joining material. This is a significant advantage in the case of composites because the holes required by bolting or riveting induce stress concentrations and can also lead to tears, burrs or delamination. A point of concern in adhesive joints is the adhesive/adherend interface corner where a stress singularity occurs, and failure usually initiates. Thus, it is crucial to study this stress singularity to better understand adhesive joints' mechanical behaviour.

The goal of this work is to validate the application of the Intensity of Singular Stress Fields (ISSF) criterion to meshless methods, in this case, the Radial Point Interpolation Method (RPIM). With this purpose, eight overlap lengths (L_O) in single-lap joints (SLJ) composed of Carbon Fibre Reinforced Polymer (CFRP) and bonded with a brittle adhesive were experimentally and numerically tested. Furthermore, an extrapolation based method is implemented to determine the critical stress singularity components (H_c) necessary for the strength predictions. In the end, the experimental and numerical results are compared to assess the suitability of the method. It was found that the ISSF criterion can be accurately applied to meshless methods and composite materials successfully, given the simplicity of the method applied.

1. Introduction

Within the range of techniques used to connect materials, adhesive bonding has had much attention from engineers in the past couple of centuries. However, traces of this technique can be found throughout humankind history. Recent archaeological discoveries made in Italy showed that Neanderthals, living in Europe about 55,000 to 40000 years ago, would leave their caves to collect resin from pine trees. They then used it to glue stone tools to handles made of bones or wood [1]. Nonetheless, only during the 20th-century engineers started to explore the possibilities offered by adhesive bonding in structural applications. The aeronautical engineers were the first to investigate and benefit from the advantages of this process. By incorporating adhesive bonding in aeroplanes, they achieved a considerable reduction of the structure's weight without compromising its strength. The technique also allows connecting different materials and more uniform stress distribution along the bonded area's width when compared to conventional bonding approaches [2]. Nowadays, it can be found in the most diverse engineering areas, such as automotive, civil and electrical.

A similar history can be associated with composite materials. This material category is the target of intense investigation by the engineers at the moment. Despite that, composite materials can be dated to the Mesopotamians and Egyptians (1500BCE). The first record of these materials is inscribed in the *Old Testament*, where it is described that clay bricks were reinforced with straw fibres. Identically, the aeronautical industry first took advantage of these materials in the past century. World War II also contributed to the increase in the use of composite materials in aeroplanes. Since their applications result in structural weight reductions, aeroplanes could fly longer distances, which was a significant advantage during the battle for the skies. The main characteristic that distinguishes composite materials from conventional construction materials is their excellent specific mechanical properties. Similarly to adhesive bonding, these materials are widespread thought the engineering industry. A recent design that combines composite materials and adhesive bonding are sandwich structures. These structures are composed of two face sheets typically designated by laminates adhesively bonded to a core [3]. The core is usually light and can have different shapes, such as foams or honeycombs. This structure has been vastly studied and implemented in the industry. Li and Wang [4] investigated the bending behaviour of sandwich structures with three-

* Corresponding author.
E-mail address: lramalho@inegi.up.pt (L.D.C. Ramalho).

https://doi.org/10.1016/j.compstruct.2021.114910
Received 29 June 2021; Accepted 26 October 2021
Available online 3 November 2021

dimensional (3D) printed cores. These authors studied three core designs (truss, conventional honeycomb and re-entrant honeycomb) and the laminates used were from two types of CFRP. Three-point bending tests were performed and the flexural stiffness, flexural strength and energy absorption were evaluated. Due to the relatively homogeneous stress distribution, the re-entrant honeycomb sandwich structures presented an interesting failure mode and the best capacity to absorb energy, contrary to the other two cores that showed earlier catastrophic failure. On the other hand, the truss sandwich structure revealed the highest flexural stiffness and strength. Elamin et al. [5] and He et al. [6] also recently studied these structures.

In the year before World War II, Volkersen [7] published what is considered the pioneer study regarding adhesive joints. In his work, he presented the first strength prediction model to evaluate adhesive joint behaviour. These models are essential to engineers since they allow the design of structures before being produced, thus saving resources and money. From this work until today, these models evolved in ways that Volkersen could have never imagined. The most significant influencer of this development was the computer. Before its invention, the strength prediction approaches were performed analytically, like Volkersen's work. However, the formulations usually were very simple and presented many simplifications [8]. Computers granted the appearance of numerical methods, which enabled the creation of far more complex formulations and intricate designs. Therefore, nowadays, nearly all scientific community resorts to numerical methods. Analytical models are still used as an initial indicator of joint behaviour. In 2009, da Silva et al. [9] performed a comparative study between different analytical approaches to predict the strength of adhesive joints, such as Volkersen [7], Goland and Reissner [10] or Hart-Smith [11].

The introduction of numerical methods enabled engineers to evaluate the failure of adhesively-bonded joints from a different perspective. In 2020, Ramalho et al. [12] summed up the most commonly applied approaches to joint failure. The authors highlighted five categories: continuum mechanics, fracture mechanics, damage mechanics, Cohesive Zone Modelling (CZM) and the eXtended Finite Element Method (XFEM). It was concluded that the majority of the works published with these approaches resorts to the Finite Element Method (FEM) and that CZM is the most commonly applied technique to evaluate adhesive joint failure. Campilho et al. [13] investigated the influence of three different CZM law shapes (triangular, exponential and trapezoidal) in the strength prediction of SLJ with a thin adhesive layer. The objective was to evaluate if the law shape severely influences the strength predictions or if a CZM shape that may not be the most suited for a particular adhesive and present fewer convergence problems can be applied for attaining a faster solution. The adherends used were from unidirectional CFRP pre-preg and two adhesives were tested (a ductile and a fragile). Various L_O were also studied, and the simulations were performed through FEM. The results distinguished two different trends. In the case of the ductile adhesive, a significant influence of the CZM shape was observed in the results, being the trapezoidal shape the most suited. It was also found that for smaller L_O, the shape influence is more prominent. In the opposite direction, for the brittle adhesive, it was concluded that the CZM shape could be neglected without compromising the strength predictions.

One other procedure to evaluate joint failure that is also widely explored is fracture mechanics. Its purpose is to approach joint failure based on the discontinuities of a structure, like re-entrant corners or defects. Two paths can be followed: the Stress Intensity Factors (SIF) or the energetic approach. The last one is based on the energy necessary to overcome the material resistance and allow crack growth [14]. The most widespread methods that rely on energetic concepts are the J-integral [15] and the Virtual Crack Closure Technique (VCCT) [16]. In 2020, Jones et al. [17] implemented a verification process to compare VCCT and FEM strength predictions of a bonded joint analysis tool designated HyperSizer (developed by NASA). The results showed excellent accuracy from the tool, with an average difference of 5.2 % to the FEM results. The authors also validated these results by comparison to experimental tests with errors between 1 and 30%. Finally, they implemented the process into HyperSizer for the analysis of bonded joints. On the other hand, the SIF relies on combinations of stresses and strains to evaluate joint failure [14]. Recently, the ISSF emerged as an up-and-coming technique based on the SIF. The ISSF, also known as General Stress Intensity Factor (GSIF), is a tool that can provide important information to aid in the design of adhesive joints. The ISSF is closely related to the SIF proposed by Irwin [18], but it can be applied to any corner and even in multi-material corners, not just single-material sharp cracks. The ISSF has been successfully applied to multi-material corners where both materials are isotropic [19-21]. When studying corners with just anisotropic materials, the ISSF analysis requires a different formulation. One of the earliest examples of a solution for this problem was proposed by Delale [22], with later applications from references [23,24], among others. The solutions presented previously were based on the Stroh formalism [25], but an alternative approach, based on the elastic governing equations and the asymptotic expansions of displacement and stress near the notch tip, can also be found in reference [26]. However, composite adhesive joints have both types of materials since adhesives are generally isotropic and the composite substrates are anisotropic. This requires an adaption of the Stroh formalism, as proposed by Ting and Chyanbin [27]. This modification was used in several subsequent works to analyse bi-material corners of composite adhesive joints [28,29]. In 2002, Leguillon [30] proposed a new method that combines stress and energy concepts to define joint failure.

Over the years, the approaches described before have been all implemented resorting to FEM. However, more recently, a new group of numerical techniques has aroused the curiosity of engineers, named meshless methods. The obstacle of FEM is the dependency on the discretization of the object studied, which can be problematic, for example, when problems with large deformations are treated [31]. Therefore, meshless methods try to overcome this handicap and do not rely on a mesh to discretize the studied object. Currently, two meshless approaches stand out: the RPIM and the Natural Neighbours Radial Point Interpolation Method (NNRPIM). Wang et al. [32] relied on the RPIM to impose periodic boundary conditions to representative volume element (REV) models of 3D braided composites on either periodic or non-periodic meshes. This type of composites presents advantages in the out-of-plane properties over unidirectional fibre composites and laminates. Due to the necessity of imposing periodic boundary conditions, creating a periodic mesh reveals considerable adversities. For this reason, the RPIM was implemented by the authors. The study disclosed accurate predictions of the elastic constants for the non-periodic mesh RVE model using RPIM-based periodic boundary conditions when compared with those found for the periodic mesh. Moreover, the relative errors of the predicted modulus in z tension are about 3–4% for both meshes. Regarding the NNRPIM, a recent investigation performed by Ramalho et al. [33] applied this technique to SLJ with composite adherends and three different adhesives scaled in terms of brittleness (one fragile and two ductile). A new continuum mechanics based criterion was applied for the strength predictions, named Critical Longitudinal Strain (CLS). The stress distributions were compared to previously obtained FEM stress distributions to assess the NNRPIM's suitability, leading to similar results. The authors concluded that one of the main goals of this work was fulfilled: the simulation of an adhesively-bonded composite SLJ through a meshless method. However, the second objective was not accomplished since the two ductile adhesives did not allow to estimate the critical parameters of the CLS criterion. Thence, they concluded that this criterion presents several limitations when analysing ductile adhesives. Nevertheless, for the brittle adhesive, the results were alluring, with errors bellow 10 %.

The present work aims to validate the ISSF criterion through a meshless method, the RPIM, applied to SLJ with CFRP adherends and a brittle adhesive. Several L_O were tested (between 10 and 80 mm) to evaluate this parameter's influence on the strength predictions. The

joints were experimentally tested and then evaluated through the ISSF criterion. For the strength predictions, an extrapolation based method is implemented to determine H_c. Finally, the experimental data are compared with the predicted strengths to assess the suitability of the method.

2. Materials and methods

2.1. Joint geometry

The base adhesive joint geometry to validate the ISSF technique for orthotropic adherends is the SLJ, using CFRP adherends and a strong but brittle adhesive from Araldite®, the AV138. Fig. 1 depicts the SLJ layout and dimensions. The main variables and respective nomenclature are as follows (all dimensions are given in mm): L_O between 10 and 80 (intervals of 10), the joint length between gripping points $L_T = 200$, adherend thickness $t_P = 2.4$, adhesive thickness $t_A = 0.2$ and width $B = 15$ (B is not present in Fig. 1. The applied boundary conditions are schematically drawn in Fig. 1 and comprise clamping one joint edge (left in the figure) and tensile pulling while preventing transverse motion at the other edge (right in the figure).

2.2. Joint materials

The materials that compose the SLJ are CFRP (adherends) and Araldite® AV138 (adhesive). The adherends were fabricated from unidirectional pre-preg SEAL® (SEAL® Texipreg HS 160 RM; SEAL® from Legnano, Italy), aiming to fabricate CFRP plates with thickness of 3 mm and $[0]_{20}$ lay-up. Thus, a unidirectional lay-up was used, with a ply unit thickness of 0.15 mm. Initially, these plates were produced by manual stacking plies with an area of 300 × 300 mm^2 and curing the bulk set using a hot press for one hour at 130 °C and 2 bar pressure. These are the recommended curing conditions by the manufacturer, leading to a theoretical fibre volume fraction of almost 64%, with reduced porosity content and overall best characteristics. After this process, the plates were cut to the adherends' final dimensions. Table 1 provides the elastic orthotropic constants of a single unidirectional ply (or unidirectional plate) [34].

The Araldite® AV138 has a tensile strength of nearly 40 MPa, although being brittle, thus exhibiting a linear behaviour until failure in the tensile stress-tensile strain (σ-ε) curve. Jointly with its stiffness, the performance in bonded joints is often limited, especially for large L_O, due to premature failure onset at the overlap edges [36]. Characterization of this adhesive was previously accomplished [37], resulting in the information provided in Table 2, in which ν is the Poisson ratio. The tensile properties were acquired with bulk (dogbone) tests, leading to the following data: Young's modulus (E), tensile yield stress (σ_y), tensile strength (σ_f) and tensile failure strain (ε_f). Specimen fabrication and testing followed the French standard NF T 76-142. The shear properties were obtained from Thick Adherend Shear Tests (TAST), giving the shear modulus (G), shear yield stress (τ_y), shear strength (τ_f) and shear failure strain (γ_f). In this case, the TAST testing procedure is described in the standard ISO 11003–2:1999. The procedure involves an alignment jig to cure the adhesive and promote $L_O = 5$ mm. DIN C45E steel adherends were used to minimize adherend deformations and provide accurate G measurements.

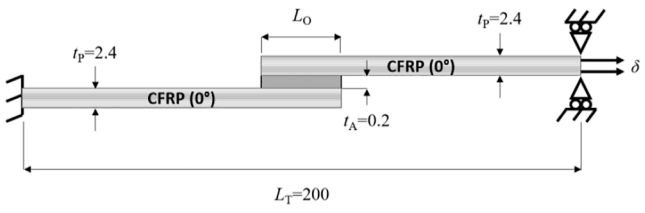

Fig. 1. SLJ joint dimensions (in mm) and boundary conditions.

Table 1
Elastic orthotropic constants of a single unidirectional ply with the fibres oriented the x axis (y and z are the transverse and thickness directions, respectively) [35].

$E_x = 1.09E + 05$ MPa	$\nu_{xy} = 0.342$	$G_{xy} = 4315$ MPa
$E_y = 8819$ MPa	$\nu_{xz} = 0.342$	$G_{xz} = 4315$ MPa
$E_z = 8819$ MPa	$\nu_{yz} = 0.380$	$G_{yz} = 3200$ MPa

Table 2
Collected properties of the Araldite® AV138 [37].

E (GPa)	4.89 ± 0.81	G (GPa)	1.56 ± 0.01
ν	0.35[1]	τ_y (MPa)	25.1 ± 0.33
σ_y (MPa)	36.49 ± 2.47	τ_f (MPa)	30.2 ± 0.40
σ_f (MPa)	39.45 ± 3.18	γ_f (%)	7.8 ± 0.7
ε_f (%)	1.21 ± 0.10		

[1] Data from the manufacturer.

2.3. Fabrication and tensile testing

The SLJ fabrication process, considering the adherends' manufacturing and preparation as specified in the previous section of this paper, began by preparing the bonding surfaces. This process involved manual abrasion with fine mesh sandpaper (grit 320), which enabled the removal of the resin-rich layer resulting from the consolidation process, increasing the surface roughness and activating the surfaces, thus ensuring a strong bond. Next, the surfaces were duly cleaned with acetone in order to eliminate dirt and particles [38]. The joints were then assembled by placing the adherends in a jig constituted by two parts: lower plate for the specimens' alignment and upper plate to apply pressure and assure t_A. Calibrated spacers between the adherends were used to achieve the correct t_A. At this stage, alignment tabs were also glued at the joint ends to centre the specimens between grips of the testing equipment. Adhesive curing took place for one week at typical conditions (room temperature and humidity). After demoulding the specimens from the jig, these were trimmed, i.e., the excess adhesive was removed by milling in proper equipment. Tensile testing was done using an electro-mechanical machine (Shimadzu AG-X 100; load cell of 100 kN) at a prescribed speed of 1 mm/min. The necessary data for further processing and analysis was the load (P; measured from the load cell) and displacement (δ; measured by approximation from the moving crosshead to which the upper grip is attached). For each joint configuration (completely defined by the respective L_O), five specimens were tested, resulting in at least four valid results.

3. Numerical analysis

3.1. RPIM description

Most of the RPIM implementation is similar to the FEM, with the difference that the latter uses a mesh, while the former does not, but it uses a grid similar to a FEM mesh to create the integration point. In the RPIM, a domain Ω is discretized into a nodal set $N = \{n_1, n_2, \ldots, n_N\}$ with coordinates $\mathbf{X} = \{x_1, x_2, \ldots, x_N\} \in \Omega$. Then, integration points are created with the aid of a background integration grid, which is only used for this step. Having the integration points, it is necessary to determine their influence domains, whose FEM counterpart are the elements. It is recommended that the number of nodes in each influence domain does not significantly vary. In the present work, the influence domain of each integration point is composed of the 16 nodes closest to it, which is a value within the range suggested in previous works [39,40]. Any given node in the domain will thus belong to several influence domains. This occurrence is called domain overlapping and imposes nodal connectivity

[39], just as elements sharing nodes do in the FEM. An example of the concepts described previously is shown in Fig. 2 for two integration points.

In addition to the dichotomy between influence domains and elements, the RPIM and the FEM also have different shape functions, which are described in section 3.1.1 for the RPIM. Besides those two differences, the RPIM and the FEM have similar implementations. Namely, a global stiffness matrix is assembled from all the local stiffness matrices obtained using the shape functions and material properties, the boundary conditions are imposed, and the global system of equation is solved. It is important to note that the boundary conditions in the RPIM can be imposed just as they are in FEM because the RPIM possesses the Kronecker delta property [39].

4. RPIM shape functions

For an integration point $\boldsymbol{x}_I \subset \mathbb{R}^d$, in the domain Ω, presented in section 3.1, the Radial Point Interpolation (RPI) function of $\boldsymbol{x}_I$ is defined as [39]:

$$u^h(\boldsymbol{x}_I) = \boldsymbol{r}(\boldsymbol{x}_I)^T \boldsymbol{a}(\boldsymbol{x}_I) + \boldsymbol{p}(\boldsymbol{x}_I)^T \boldsymbol{b}(\boldsymbol{x}_I) \tag{1}$$

being $\boldsymbol{a}(\boldsymbol{x}_I)$ and $\boldsymbol{b}(\boldsymbol{x}_I)$ the non-constant coefficients of $\boldsymbol{r}(\boldsymbol{x}_I)$ and $\boldsymbol{p}(\boldsymbol{x}_I)$, respectively. While $\boldsymbol{a}(\boldsymbol{x}_I)$ and $\boldsymbol{r}(\boldsymbol{x}_I)$ will have a size equal to n, $\boldsymbol{b}(\boldsymbol{x}_I)$ and $\boldsymbol{p}(\boldsymbol{x}_I)$ will have a size equal to m (n is the total number of nodes in the influence domain of $\boldsymbol{x}_I$ and m is the number of monomials of the complete polynomial basis, defined according to Pascal's triangle). A linear polynomial basis was used in this work since using a higher basis increases the computational times while not changing the results in any observable manner. Among other alternatives for the Radial Basis Function (RBF), such as the Gaussian RBF or the thin plate spline RBF, the multi-quadrics RBF (MQ-RBF) was chosen to be used in this work. This RBF is defined as $r_i(x_I) = \left(d_{iI}^2 + (\gamma d_a)^2\right)^p$ [39], where γ and p are function shape parameters, d_a is the integration weight of the integration point $\boldsymbol{x}_I$, and d_{iI} the Euclidean norm between node i and the integration point I. The influence of the shape parameters was previously studied by Wang and Liu [41], who suggested that they should be $\gamma = 1.03$ and $p = 1.42$, which are the values used in this work. Imposing $u^h(\boldsymbol{x}_I)$ to pass through all the nodal values n of the influence domain of $\boldsymbol{x}_I$ leads to the following system of equations [39]:

$$\boldsymbol{R}\boldsymbol{a}(\boldsymbol{x}_I) + \boldsymbol{P}\boldsymbol{b}(\boldsymbol{x}_I) = \boldsymbol{u}_s \tag{2}$$

where $\boldsymbol{u}_s^T = \{ u_1 \quad u_2 \quad \dots \quad u_n \}$ is a vector with the field function values at each node inside the influence domain of $\boldsymbol{x}_I$, which (depending on the problem under analysis) can be the displacement, velocity, temperature, or other variables. The MQ-RBF moment matrix ($\boldsymbol{R}$) will have a size equal to $n \times n$, while the polynomial moment matrix ($\boldsymbol{P}$) will have a size equal to $m \times n$. To obtain a unique solution, it is necessary to add another set of equations [39]:

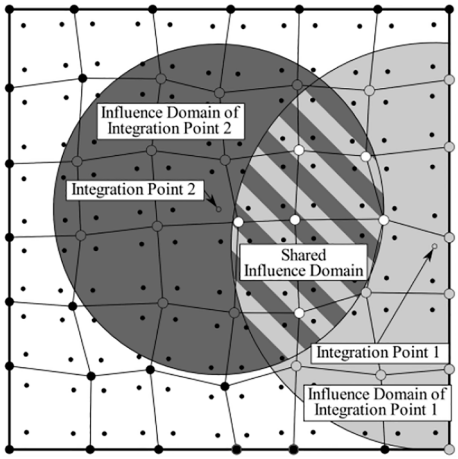

Fig. 2. Example of two RPIM influence domains and their overlap.

$$\boldsymbol{P}^T \boldsymbol{a}(\boldsymbol{x}_I) = 0 \tag{3}$$

The combination of Equations and leads to the final set of equations [39]:

$$\begin{bmatrix} \boldsymbol{R} & \boldsymbol{P} \\ \boldsymbol{P}^T & \boldsymbol{Z} \end{bmatrix} \begin{Bmatrix} \boldsymbol{a}(\boldsymbol{x}_I) \\ \boldsymbol{b}(\boldsymbol{x}_I) \end{Bmatrix} = \boldsymbol{M}_T \begin{Bmatrix} \boldsymbol{a}(\boldsymbol{x}_I) \\ \boldsymbol{b}(\boldsymbol{x}_I) \end{Bmatrix} = \begin{Bmatrix} \boldsymbol{u}_s \\ \boldsymbol{z} \end{Bmatrix} \tag{4}$$

being $Z_{ij} = 0$ and $z_i = 0$ for $i,j = 1, 2, \dots, m$ [39]. Then, $\boldsymbol{a}(\boldsymbol{x}_I)$ and $\boldsymbol{b}(\boldsymbol{x}_I)$ can be obtained:

$$\begin{Bmatrix} \boldsymbol{a}(\boldsymbol{x}_I) \\ \boldsymbol{b}(\boldsymbol{x}_I) \end{Bmatrix} = \boldsymbol{M}_T^{-1} \begin{Bmatrix} \boldsymbol{u}_s \\ \boldsymbol{z} \end{Bmatrix} \tag{5}$$

By substituting $\boldsymbol{M}_T^{-1} \{ \boldsymbol{u}_s \quad \boldsymbol{z} \}^T$ into Eq. (1), the following is obtained:

$$u^h(\boldsymbol{x}_I) = \{ \boldsymbol{r}(\boldsymbol{x}_I)^T \quad \boldsymbol{p}(\boldsymbol{x}_I)^T \} \boldsymbol{M}_T^{-1} \begin{Bmatrix} \boldsymbol{u}_s \\ \boldsymbol{z} \end{Bmatrix} \tag{6}$$

The field function value for an interest point $\boldsymbol{x}_I$ is interpolated using the shape function values at the nodes inside the influence domain of $\boldsymbol{x}_I$, which can be identified in Eq. (6) [39]:

$$u^h(\boldsymbol{x}_I) = \{ \boldsymbol{\Phi}(\boldsymbol{x}_I)^T \quad \boldsymbol{\Psi}(\boldsymbol{x}_I)^T \} \boldsymbol{M}_T^{-1} \begin{Bmatrix} \boldsymbol{u}_s \\ \boldsymbol{z} \end{Bmatrix} \tag{7}$$

being $\Psi(\boldsymbol{x}_I) = \{ \psi_1(\boldsymbol{x}_I) \quad \psi_2(\boldsymbol{x}_I) \quad \cdots \quad \psi_n(\boldsymbol{x}_I) \}^T$ and $\Phi(\boldsymbol{x}_I) = \{ \varphi_1(\boldsymbol{x}_I) \quad \varphi_2(\boldsymbol{x}_I) \quad \cdots \quad \varphi_n(\boldsymbol{x}_I) \}^T$ a by-product vector with no relevant meaning and the interpolation shape function, respectively. A more complete formulation of the RPIM, including the derivatives of the shape functions needed to solve the $\boldsymbol{K}\boldsymbol{u} = \boldsymbol{f}$ system of equations, can be found in the literature [39].

4.1. ISSF formulation for composites

Considering a three-dimensional Cartesian coordinate system, the constitutive law of a material can be defined as $\boldsymbol{\sigma} = \boldsymbol{C}\boldsymbol{\varepsilon}$, where $\boldsymbol{C}$ is a symmetric matrix defined as follows:

$$\boldsymbol{C} = \begin{bmatrix} \frac{1}{E_1} & -\frac{\nu_{12}}{E_1} & -\frac{\nu_{13}}{E_1} & 0 & 0 & 0 \\ -\frac{\nu_{21}}{E_2} & \frac{1}{E_2} & -\frac{\nu_{23}}{E_2} & 0 & 0 & 0 \\ -\frac{\nu_{31}}{E_3} & -\frac{\nu_{32}}{E_3} & \frac{1}{E_3} & 0 & 0 & 0 \\ 0 & 0 & 0 & \frac{1}{G_{23}} & 0 & 0 \\ 0 & 0 & 0 & 0 & \frac{1}{G_{13}} & 0 \\ 0 & 0 & 0 & 0 & 0 & \frac{1}{G_{12}} \end{bmatrix} \tag{8}$$

where $\boldsymbol{\sigma}$ and $\boldsymbol{\varepsilon}$ are the stress and strain vectors, respectively, in Voigt notation. Since $\boldsymbol{C}$ is symmetric, the following must be true: $\nu_{12}/E_1 = \nu_{21}/E_2$, $\nu_{23}/E_2 = \nu_{32}/E_3$ and $\nu_{13}/E_1 = \nu_{31}/E_3$. The Stroh formalism [42] is defined by the following eigensystem:

$$\boldsymbol{N}\boldsymbol{\xi}_\alpha = p_\alpha \boldsymbol{\xi}_\alpha \tag{9}$$

being p_α and $\boldsymbol{\xi}_\alpha$ the eigenvalues and the eigenvectors of this system, respectively. This system has 6 eigenvectors and eigenvalues, and $\boldsymbol{N}$ is defined as:

$$\boldsymbol{N} = \begin{bmatrix} \boldsymbol{N}_1 & \boldsymbol{N}_2 \\ \boldsymbol{N}_3 & \boldsymbol{N}_1^T \end{bmatrix} \tag{10}$$

where $\boldsymbol{N}_1 = -\boldsymbol{T}^{-1}\boldsymbol{R}^T$, $\boldsymbol{N}_2 = -\boldsymbol{T}^{-1}$ and $\boldsymbol{N}_3 = \boldsymbol{R}\boldsymbol{T}^{-1}\boldsymbol{R}^T - \boldsymbol{Q}$, and:

$$\boldsymbol{Q} = \begin{bmatrix} C_{11} & C_{16} & C_{15} \\ C_{16} & C_{66} & C_{56} \\ C_{15} & C_{56} & C_{55} \end{bmatrix}; \quad \boldsymbol{R} = \begin{bmatrix} C_{16} & C_{12} & C_{14} \\ C_{66} & C_{26} & C_{46} \\ C_{56} & C_{25} & C_{45} \end{bmatrix}; \quad \boldsymbol{T} = \begin{bmatrix} C_{66} & C_{26} & C_{46} \\ C_{26} & C_{22} & C_{24} \\ C_{46} & C_{24} & C_{44} \end{bmatrix} \tag{11}$$

The eigenvalues and eigenvectors of this system are complex. Therefore, if p_α and $\boldsymbol{\xi}_\alpha$ are valid for equation (9), $\overline{p}_\alpha$ and $\overline{\boldsymbol{\xi}}_\alpha$ are valid too, where the overbar is the complex conjugate. The eigenvectors can be divided into two parts, $\boldsymbol{\xi}_\alpha^T = \begin{bmatrix} \boldsymbol{a}_\alpha^T & \boldsymbol{b}_\alpha^T \end{bmatrix}$, where $\boldsymbol{a}_\alpha$ is proportional to the displacement vector and $\boldsymbol{b}_\alpha$ is proportional to the traction vector. Transverse isotropic materials, as are unidirectional fibre-reinforced composites, have three different eigenvalues and three linearly independent eigenvectors and their corresponding conjugates. However, isotropic materials, as adhesives generally are, have a single eigenvalue $p = i$ and two linearly independent eigenvectors. Therefore, a modification to the Stroh formalism, presented in Eq. (9), is needed [43]:

$$\boldsymbol{N}\boldsymbol{\xi}_1 = p\boldsymbol{\xi}_1 \;\; ; \;\; \boldsymbol{N}\boldsymbol{\xi}_2 = p\boldsymbol{\xi}_2 + \boldsymbol{\xi}_1 \;\; ; \;\; \boldsymbol{N}\boldsymbol{\xi}_3 = p\boldsymbol{\xi}_3 \tag{12}$$

which means that $\boldsymbol{\xi}_1$ and $\boldsymbol{\xi}_3$ can be determined using equation, but $\boldsymbol{\xi}_2^T = \begin{bmatrix} \boldsymbol{a}_2^T & \boldsymbol{b}_2^T \end{bmatrix}$ is determined as follows [43]:

$$-\left[\boldsymbol{Q} + \left(\boldsymbol{R} + \boldsymbol{R}^T\right)p + \boldsymbol{T}p^2\right]\boldsymbol{a}_2 = \left(2p\boldsymbol{T} + \boldsymbol{R} + \boldsymbol{R}^T\right)\boldsymbol{a}_1 \tag{13}$$

$$\boldsymbol{b}_2 = T\boldsymbol{a}_1 + \left(\boldsymbol{R}^T + p\boldsymbol{T}\right)\boldsymbol{a}_2 \tag{14}$$

A vector $\boldsymbol{w}(r,\theta)^T = \begin{bmatrix} \boldsymbol{u}(r,\theta)^T & \boldsymbol{\varphi}(r,\theta)^T \end{bmatrix}$, where $\boldsymbol{u}$ is the displacement vector and $\boldsymbol{\varphi}$ is the stress function vector, can be defined as [43]:

$$\boldsymbol{w}(r,\theta) = r^\lambda \boldsymbol{X}\boldsymbol{Z}\boldsymbol{q} \tag{15}$$

where $\boldsymbol{q}$ is a constant vector, $\mathbf{X} = \begin{bmatrix} \boldsymbol{\xi}_1 & \boldsymbol{\xi}_2 & \boldsymbol{\xi}_3 & \overline{\boldsymbol{\xi}}_1 & \overline{\boldsymbol{\xi}}_2 & \overline{\boldsymbol{\xi}}_3 \end{bmatrix}$ and, for materials with three linearly independent eigenvectors and three eigenvalues [43], $\mathbf{Z}(\theta)$ is given by:

$$\boldsymbol{Z}(\theta) = \begin{bmatrix} \langle \zeta_\alpha^\lambda(\theta) \rangle & \mathbf{0}_{3\times3} \\ \mathbf{0}_{3\times3} & \langle \overline{\zeta}_\alpha^\lambda(\theta) \rangle \end{bmatrix} \tag{16}$$

where angle brackets represent diagonal matrices. For materials with just two linearly independent eigenvectors and one eigenvalue, $\mathbf{Z}(\theta)$ is also dependent on λ and it is defined as [43]:

$$\boldsymbol{Z}(\theta,\lambda) = \begin{bmatrix} \boldsymbol{\Psi}(\theta,\lambda) & \mathbf{0}_{3\times3} \\ \mathbf{0}_{3\times3} & \overline{\boldsymbol{\Psi}}(\theta,\lambda) \end{bmatrix} \tag{17}$$

with:

$$\boldsymbol{\Psi}^\lambda(\theta) = \begin{bmatrix} \zeta^\lambda(\theta) & K(\theta,\lambda)\zeta^\lambda(\theta) & 0 \\ 0 & \zeta^\lambda(\theta) & 0 \\ 0 & 0 & \zeta^\lambda(\theta) \end{bmatrix} \tag{18}$$

being $K(\theta,\lambda) = \lambda\sin(\theta)/\zeta(\theta)$ and $\zeta_\alpha^\lambda(\theta) = [\cos(\theta) + p_\alpha \sin(\theta)]^\lambda$.

Considering a material m in a bi-material wedge, defined by an initial angle θ_{m-1} and an end angle θ_m, the following relation can be established [43]:

$$\boldsymbol{w}(r,\theta_m) = \boldsymbol{E}(\lambda,\theta_m,\theta_{m-1})\boldsymbol{w}(r,\theta_{m-1}), \tag{19}$$

being:

$$\boldsymbol{E}(\lambda,\theta_m,\theta_{m-1}) = \boldsymbol{X}\boldsymbol{Z}^\lambda(\theta_m)\left[\boldsymbol{Z}^\lambda(\theta_{m-1})\right]^{-1}\boldsymbol{X}^{-1} \tag{20}$$

where $\boldsymbol{Z}^\lambda(\theta_m)\left[\boldsymbol{Z}^\lambda(\theta_{m-1})\right]^{-1}$ can be simplified to $\boldsymbol{Z}^\lambda(\theta_m,\theta_{m-1})$, which for materials with three linearly independent eigenvectors and three eigenvalues gives [43]:

$$\boldsymbol{Z}^\lambda(\theta_m,\theta_{m-1}) = \begin{bmatrix} \langle \zeta_\alpha^\lambda(\theta_m,\theta_{m-1}) \rangle & \mathbf{0}_{3\times3} \\ \mathbf{0}_{3\times3} & \left\langle \overline{\zeta}_\alpha^\lambda(\theta_m,\theta_{m-1}) \right\rangle \end{bmatrix} \tag{21}$$

while for materials with just two linearly independent eigenvectors and one eigenvalue it is also dependent on λ and is defined as [43]:

$$\boldsymbol{Z}^\lambda(\theta_m,\theta_{m-1},\lambda) = \begin{bmatrix} \boldsymbol{\Psi}(\theta_m,\theta_{m-1},\lambda) & \mathbf{0}_{3\times3} \\ \mathbf{0}_{3\times3} & \overline{\boldsymbol{\Psi}}(\theta_m,\theta_{m-1},\lambda) \end{bmatrix} \tag{22}$$

with:

$$\boldsymbol{\Psi}(\theta_m,\theta_{m-1},\lambda) = \begin{bmatrix} \zeta^\lambda(\theta_m,\theta_{m-1}) & K(\theta_m,\theta_{m-1},\lambda)\zeta^\lambda(\theta_m,\theta_{m-1}) & 0 \\ 0 & \zeta^\lambda(\theta_m,\theta_{m-1}) & 0 \\ 0 & 0 & \zeta^\lambda(\theta_m,\theta_{m-1}) \end{bmatrix} \tag{23}$$

where $\zeta_\alpha(\theta_m,\theta_{m-1}) = \zeta_\alpha(\theta_m)/\zeta_\alpha(\theta_{m-1})$ and:

$$K(\theta_m,\theta_{m-1},\lambda) = \frac{\lambda sin(\theta_m - \theta_{m-1})}{\zeta(\theta_m)\zeta(\theta_{m-1})} \tag{24}$$

In a wedge made of two perfectly bonded materials, as in Fig. 3, it is possible to relate $\boldsymbol{w}(r,\theta_0)$ with $\boldsymbol{w}(r,\theta_2)$. If $\boldsymbol{w}(r,\theta_1) = \boldsymbol{E}(\lambda,\theta_1,\theta_0)\boldsymbol{w}(r,\theta_0)$ and $\boldsymbol{w}(r,\theta_2) = \boldsymbol{E}(\lambda,\theta_2,\theta_1)\boldsymbol{w}(r,\theta_1)$:

$$\boldsymbol{w}(r,\theta_2) = \boldsymbol{K}_W(\lambda)\boldsymbol{w}(r,\theta_0) \tag{25}$$

being $\boldsymbol{K}_W(\lambda) = \boldsymbol{E}(\lambda,\theta_2,\theta_1)\boldsymbol{E}(\lambda,\theta_1,\theta_0)$ called the transfer matrix. Now it is necessary to impose the boundary conditions. In adhesive joints, both outer faces of the interface wedge are free, thus $\boldsymbol{\varphi}(r,\theta_0) = \boldsymbol{\varphi}(r,\theta_2) = 0$ must be imposed. Thus, the following boundary condition matrices are used [28]:

$$\boldsymbol{D}_0 = \boldsymbol{D}_2 = \begin{bmatrix} \mathbf{0}_{3\times3} & \boldsymbol{I}_{3\times3} \\ \boldsymbol{I}_{3\times3} & \mathbf{0}_{3\times3} \end{bmatrix} \tag{26}$$

These boundary condition matrices are used to modify the transfer matrix [28]:

$$\boldsymbol{K}_{WBC}(\lambda) = \boldsymbol{D}_2\boldsymbol{K}_W\boldsymbol{D}_0^T \tag{27}$$

Considering the boundary conditions, the system of equations is rewritten as [28]:

$$\begin{bmatrix} \mathbf{0}_{3\times1} \\ \boldsymbol{u}(r,\theta_2) \end{bmatrix} = \begin{bmatrix} \boldsymbol{K}_{WBC}^{(1)}(\lambda) & \boldsymbol{K}_{WBC}^{(2)}(\lambda) \\ \boldsymbol{K}_{WBC}^{(3)}(\lambda) & \boldsymbol{K}_{WBC}^{(4)}(\lambda) \end{bmatrix} \begin{bmatrix} \mathbf{0}_{3\times1} \\ \boldsymbol{u}(r,\theta_0) \end{bmatrix} \tag{28}$$

From Eq. (28), the following is verified: $0_{3\times1} = \boldsymbol{K}_{WBC}^{(2)}(\lambda)\boldsymbol{u}(r,\theta_0)$. Therefore, a non-trivial solution is found if and only if:

$$\left|\boldsymbol{K}_{WBC}^{(2)}(\lambda)\right| = 0 \tag{29}$$

This is how the characteristic exponents of the bi-material corner are obtained. There is an infinite number of λ that can be obtained, but to study the singularity, only $\lambda < 1$ are essential since these are the ones characterizing the singularity. Having determined λ, it is now possible to

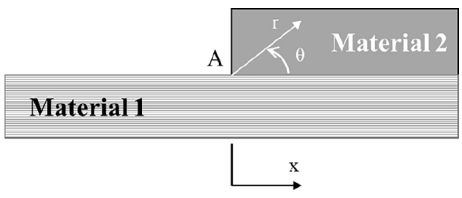

Fig. 3. Wedge corner in a bi-material interface.

determine the stress and displacement around the interface corner. For a given angle (θ) inside a material (m), the polar stress components can be defined as [43]:

$$f_{rr} = -\boldsymbol{s}_r^T(\theta)\boldsymbol{\varphi}_{,\theta}(r,\theta)/r; \quad f_{\theta\theta} = \boldsymbol{n}^T(\theta)\boldsymbol{\varphi}_{,r}(r,\theta); \\ f_{r\theta} = -\boldsymbol{n}^T(\theta)\boldsymbol{\varphi}_{,\theta}(r,\theta)/r = \boldsymbol{s}_r^T(\theta)\boldsymbol{\varphi}_{,r}(r,\theta) \tag{30}$$

while the displacements are defined as [43]:

$$g_r = -\boldsymbol{s}_r^T(\theta)\boldsymbol{u}(r,\theta)/r; \quad g_\theta = \boldsymbol{n}^T(\theta)u(r,\theta) \tag{31}$$

where $\boldsymbol{s}_r^T = [\cos(\theta) \quad \sin(\theta) \quad 0]$ and $\boldsymbol{n}^T = [\sin(\theta) \quad -\cos(\theta) \quad 0]$. To determine the components in equations and, it is first necessary to determine $\boldsymbol{w}(r,\theta_0)$ and $\boldsymbol{w}(r,\theta_1)$ for each λ. First, it is known that $\boldsymbol{\varphi}(r,\theta_0) = 0_{3\times1}$, due to the boundary conditions, and $\boldsymbol{u}_0$ is determined by solving $0_{3\times1} = \boldsymbol{K}^{(2)}_{WBC}(\lambda)\boldsymbol{u}(r,\theta_0)$. So, $\boldsymbol{w}(r,\theta_0)$ can be assembled as $\boldsymbol{w}(r,\theta_0)^T = [\boldsymbol{u}(r,\theta_0)^T \quad \boldsymbol{\varphi}(r,\theta_0)^T]$. Knowing $\boldsymbol{w}(r,\theta_0)$, $\boldsymbol{w}(r,\theta_1)$ is determined by simply using Eq. (19). Then, the components of equations and for each λ, and its derivatives in order to r and θ, in a material (m) and at a given angle (θ), inside m, can be determined using equation , being the angle θ_m substituted by θ. The components of equations and have to be standardized, because if $\boldsymbol{w}(r,\theta_0)$ is a solution so is $c\boldsymbol{w}(r,\theta_0)$, where c is any constant. In this work, this standardization was performed by finding the maximum value of the components in the angle range encompassing the whole corner and dividing all the components by that value. Having the singularity components (λ) and the stress (f) and displacement (g) functions near the singularity, the stress and displacement can be described as:

$$\sigma_{ij} = \sum_{k=1}^{n} H_k r^{\lambda_k - 1} f_{ij}(\lambda_k, \theta) \tag{32}$$

$$u_j = \sum_{k=1}^{n} H_k r^{\lambda_k} g_j(\lambda_k, \theta) \tag{33}$$

being n the number of singularity exponents (λ), which depends on the interface corner's geometry and materials. H_k is the ISSF or GSIF, which is a scalar value related to the singularity component k. The ISSF can be determined in different ways. For example, Qian and Akisanya [19] used a line integral encircling the interface corner to determine the ISSF. In the current work, the ISSF was determined by extrapolating it to the corner from values near the corner, similarly to the method used by Klusák et al. [44]. This method requires a n number of points at different angles (θ) and at a fixed radius (r) to determine a n number of ISSF, e.g., if there are two singularity components λ_1 and λ_2, two different angles are needed. Therefore, $\boldsymbol{H}$ can be determined at r using the following equation:

$$\begin{bmatrix} r^{\lambda_1-1}f_{\theta\theta}(\lambda_1,\theta_{n+1}) & \cdots & r^{\lambda_n-1}f_{\theta\theta}(\lambda_n,\theta_{n+1}) \\ \vdots & \ddots & \vdots \\ r^{\lambda_1-1}f_{\theta\theta}(\lambda_1,\theta_{n+n}) & \cdots & r^{\lambda_n-1}f_{\theta\theta}(\lambda_n,\theta_{n+n}) \end{bmatrix} \begin{bmatrix} H_1 \\ \vdots \\ H_n \end{bmatrix} = \begin{bmatrix} \sigma_{\theta\theta}(r,\theta_{n+1}) \\ \vdots \\ \sigma_{\theta\theta}(r,\theta_{n+n}) \end{bmatrix} \tag{34}$$

where $\sigma_{\theta\theta}$ is extracted from the RPIM simulations. The solution of Equation is obtained for several different r, and it is then extrapolated to $r = 0$ mm, from an r interval where it is stable, to obtain $\boldsymbol{H}$ at the interface corner.

4.2. Numerical modelling

To perform the numerical analysis, eight different discretizations were created, one for each different L_O, but the discretisation near the interface corners was the same regardless of L_O. The dimensions of the region that is discretized in the same manner are displayed in Fig. 4**a**, along with the number of nodes in that region. Also, the radial part of that region is shown in Fig. 4**b**. The overall dimensions of the joint are the same as the experimental joints, shown in Fig. 1. The left boundary was considered fixed ($U_x = U_y = U_z = 0$), while δ was imposed at the right boundary. The RPIM analysis was then performed using the authors' own MATLAB program. Additionally, a script to apply the equations of section 3.2 was developed to perform the ISSF analysis from the RPIM results. This script also allows to predict the maximum load (P_m) values based on the ISSF at the interface corner. All RPIM simulations assumed small strains and plane strain conditions, with 16 nodes per influence domain, and the shape function parameters $\gamma = 1.03$ and $p = 1.42$. It is also important to note that the influence domains near the interface have to be treated differently. A solution similar to the solution of reference [45] was adopted.

5. Results and discussion

5.1. Experimental results

Initially, the experimental data from the tensile tests is presented and analysed to serve as the basis for validating the ISSF technique that

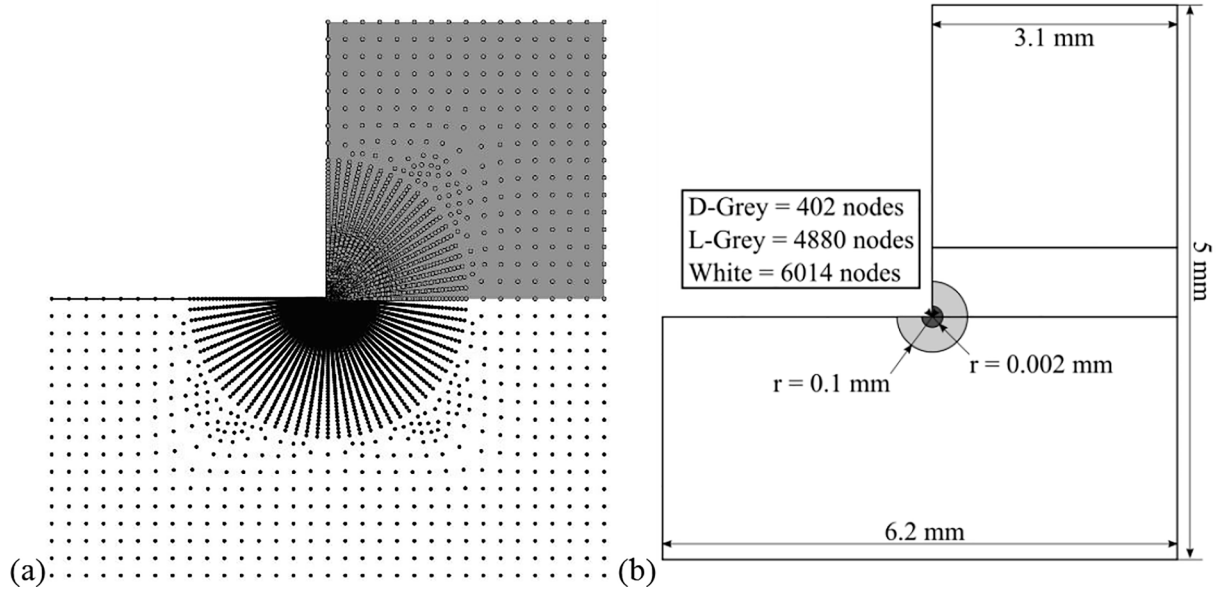

Fig. 4. (a) Discretization in an area of 1 × 1 mm^2 around the interface corner (b) Details of the discretization in the area around the interface corner.

constitutes the primary purpose of this work. It should be initially mentioned that all failures were cohesive in the adhesive layer, which obliges to identify, after failure, a visible and homogeneous layer of adhesive on both adherends. Thus, no signs of interfacial (adhesive) or interlaminar failures were detected. In the particular case of interfacial failures, these are typically linked to poor fabrication, which would render the results not valid for the purpose of this work.

The analysed experimental data is collected in Fig. 5, in the form of a P_m-L_O plot, including each L_O data point's minimum and maximum value. There is a marked L_O effect on P_m, translated by a regular increase of P_m with L_O. This tendency is documented in the literature notwithstanding the adhesive type, and it is closely related to the higher shear bonding area joining the two adherends [37]. Between adhesive types, brittle adhesives like the Araldite® AV138 perform well for short L_O but worse for high L_O due to the marked stress concentrations at the overlap edges [46]. In this case, the SLJ show a non-proportional improvement of P_m with L_O. For instance, the relative (%) P_m improvement between $L_O = 10$ and 40 mm is only 28.79%, while reaching 94.13% between $L_O = 10$ and 80 mm (limit L_O tested). The absolute P_m difference between the limit L_O was 13.1 kN. This behaviour is precisely related to the inability of this brittle adhesive to deal with the increasing peak stresses developing in the joint. These adhesive characteristics were reported in section 2.2, leading to a major performance depreciation for large L_O, quantified by the reduced P_m over the bonded area given by $L_O \times B$. The aforementioned stresses are not presented here due to being over addressed in the literature [47] and report on both peel (through-thickness normal) and shear stresses highly increasing at the overlap edges as L_O increases, while the central region is not transferring loads between the adherends. In particular, peel stresses are especially harmful to the adhesive at the overlap edges while quickly vanishing for the inner overlap. On the other hand, the shear stress gradient is less evident, but shear peak stresses are also found at the overlap edges, compared to a lighter loaded inner overlap [47]. In subsequent sections, these experimental results will be used for ISSF validation by direct P_m comparison.

5.2. ISSF analysis

After the numerical simulations have been completed, the ISSF analysis could be initialized. Firstly, the corner geometry was discretized. Fig. 6 presents a scheme of the joint example studied in this work, in this case, a SLJ.

The corner geometry necessary for this criterion consists of the angles formed between the materials where the corner is located. The

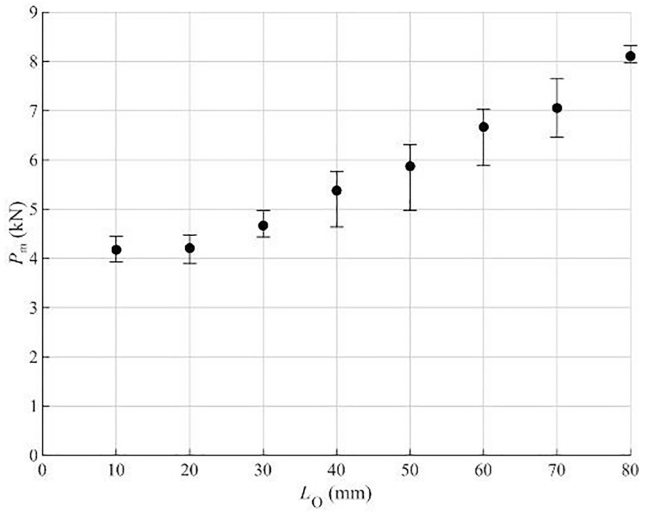

Fig. 5. P_m-L_O plot resultant from the experimental data.

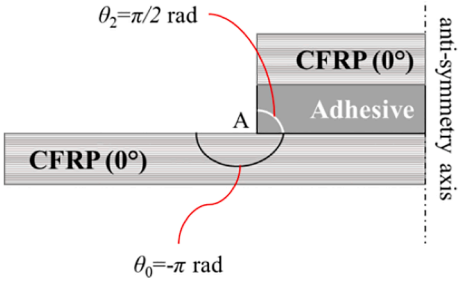

Fig. 6. SLJ corner geometry.

starting points are the corner tip (point A) and the horizontal line where the adhesive and the CFRP are in contact, intercepting the corner tip (point A). This geometry is then defined by three angles, considering counterclockwise as positive. The first angle corresponds to the CFRP ($\theta_0 = -\pi$ rad), while the third angle represents the adhesive ($\theta_2 = \pi/2$ rad), as shown in Fig. 6. The angle θ_1 is related to the horizontal line described before, being equal to 0 rad. This analysis is similar to other multi-material corners. At this stage, the CFRP and adhesive properties are also essential to compose matrix $\boldsymbol{C}$ from Eq. (8). Next, the stress singularity exponents λ can be obtained, resorting to Eq. (29). Since this equation presents the terms cos and sin, it can be considered periodic, originating an infinite number of solutions. However, only the solutions comprised in the interval $0 < \lambda < 1$ are treated in the present study since they represent singular solutions. Therefore, three exponents λ were found: $\lambda_1 = 0.6055$, $\lambda_2 = 0.7347$ and $\lambda_3 = 0.9866$. In the present study, a plane-strain analysis was carried out. Thus, the exponent λ_2 was not considered since it corresponds to an anti-plane solution. The first phase of the criterion was finished by finding two new angles necessary to perform the procedure of the next phase. The angles chosen were $\theta_4 = \pi/4$ rad and $\theta_5 = -3\pi/4$ rad. These were not randomly chosen and intended to allow a stress singularity determination based on the nodes. One angle (θ_4) is in the descending part of the $\sigma_{\theta\theta}$ curve and the other (θ_5) in the ascending part of the same curve.

Advancing in the ISSF criterion, the next stage was the determination of the stress singularity components, i.e., the ISSF values designated H_1 and H_2. Since a planar analysis was considered, only two singular exponents λ were found. Thus only two stress singularities are considered (H_1 and H_2). In order to exemplify the H determination process, the case $L_O = 50$ mm is considered. This process consists of solving the system from Eq. (34). The matrix on the left side of the equation was completed by determining the $f_{\theta\theta}$ functions from Eq. (30), while the right side corresponds to the tangential numerical stresses obtained from the RPIM simulation described in section 3.3. The unknowns of the expression are H_1 and H_2. Nonetheless, these parameters cannot be directly determined for the corner tip since $r = 0$ mm. Therefore, they were firstly obtained for several r in the interval $0 < r < 0.1$ mm. Then, H_n (n = 1 or n = 2) were extrapolated from the values between 0.01 and 0.02 mm to the corner tip ($r = 0$ mm). The extrapolation interval was chosen for its linear stability in the H-r curves and its proximity to the corner tip. Fig. 7 shows the H_1-r curves and extrapolations for the case considered ($L_O = 50$ mm). Only the H_1 component is presented since it is the most significant.

The graph also presents the H_1-r curves and extrapolations for other L_O. These were determined by imposing H_1 at $r = 0$ mm as the H_1 determined for the $L_O = 50$ mm case. The procedure described for this case was performed for each L_O. From the analysis of the H_1-r curves, an oscillation in the values between $0 < r < 0.01$ mm is perceptible. This behaviour is due to the numerical approach (RPIM) used. Since the nodes in this interval are closer to the corner tip, the stresses are influenced by the higher concentration of influence domains and their overlapping, thus influencing the H_1 determination.

A comparison between the numerical and the analytical stresses was carried out to validate the presented H estimations. The numerical

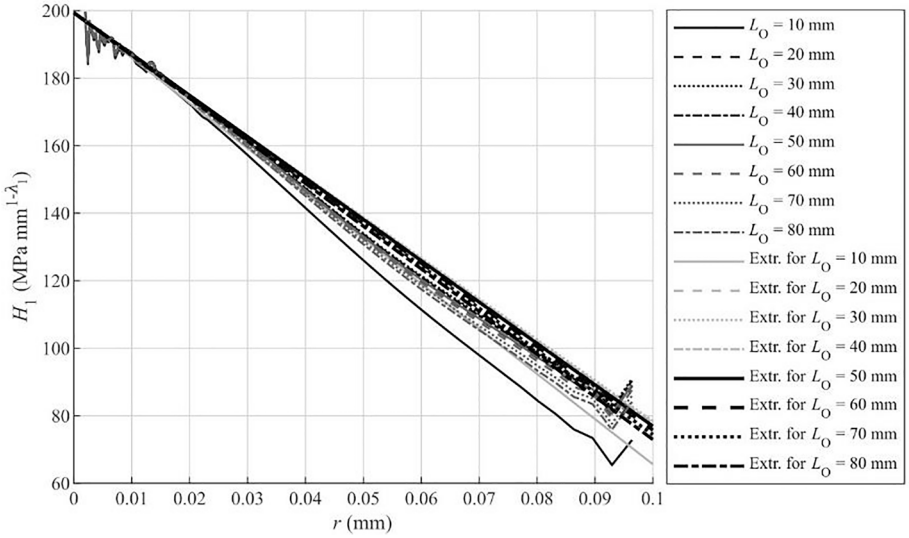

Fig. 7. H_1-r curves and extrapolations for the $L_O = 50$ mm case.

stresses were obtained from the RPIM simulations, while the analytical ones result from Eq. (32). A specific r was chosen ($r = 0.0022$ mm), where H_1 would be the same for all L_O, to evaluate the similarity between the stresses. Then, these were determined for all the angles comprised by the geometry of the SLJ considered. The obtained results are presented in Fig. 8. The two components from equation were also plotted separately to demonstrate the more significant influence of the first singularity component in the corner evaluation. Once again, some fluctuations are observed in the numerical stresses due to the RPIM approach and its dependence on the influence domains.

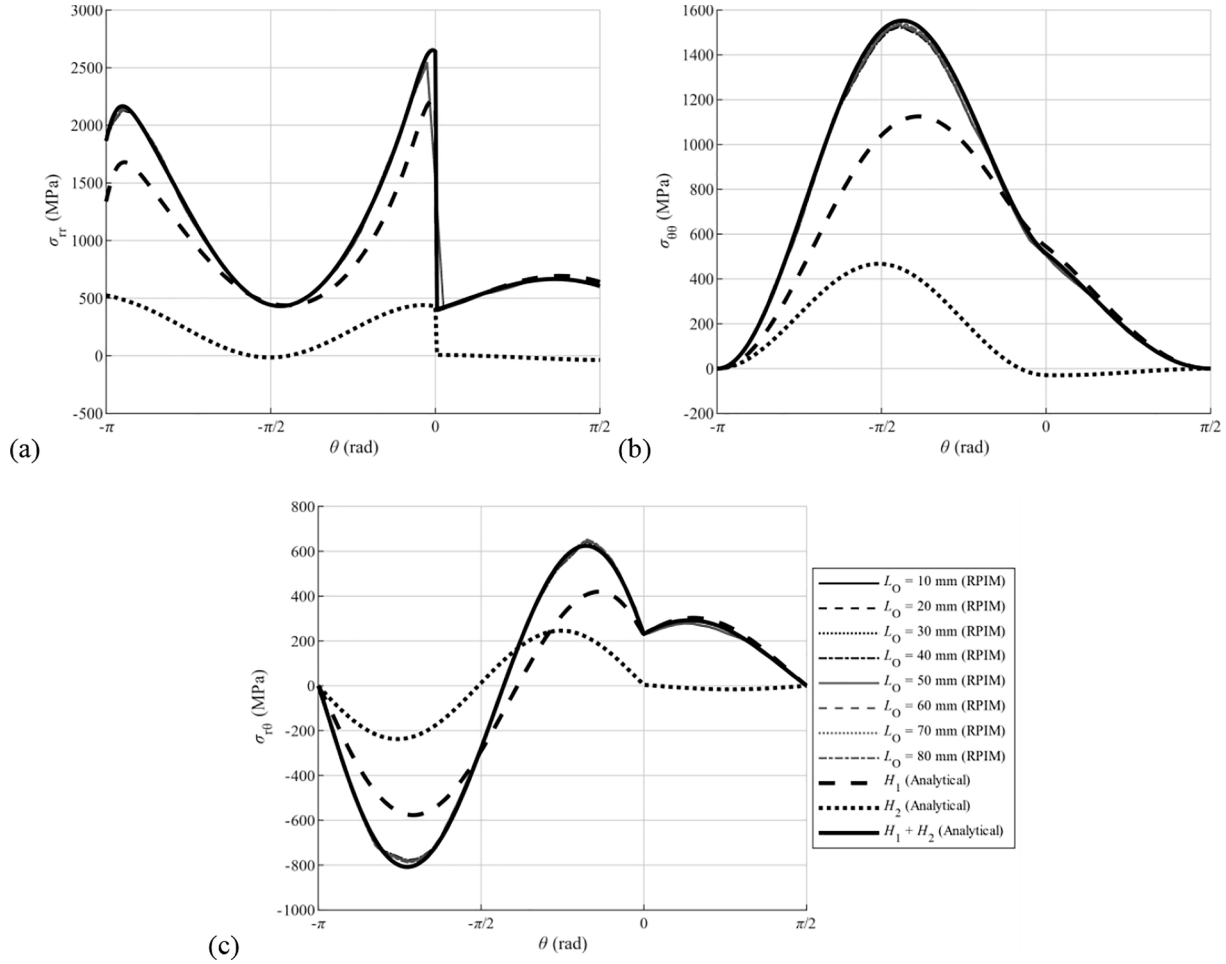

Fig. 8. Comparison between numerical and analytical stresses and between stress singularity components being (a) σ_{rr}, (b) $\sigma_{\theta\theta}$ and (c) $\sigma_{r\theta}$.

5.3. Joint strength prediction

The final step of this work consisted of predicting P_m and respective comparison with the results extracted from the experimental data. In that regard, it was necessary to determine H_c. Currently, there are no standardized experimental methods to determine H_c. With that in mind, a formulation relying on a combination of experimental and numerical data was implemented in this work. The proposed method consists of performing numerical simulations with the experimental P_m by each joint of different L_O as the imposed natural boundary conditions. Then, by the process described in section 4.2, the H_n values were determined and used as the H_{nc} values (n = 1 or n = 2) for each L_O. The procedure and results presented in section 4.2 exemplify this method for the L_O = 50 mm case. Initially, H_1 was determined, resorting to an RPIM simulation where the experimentally determined P_m for the L_O = 50 mm joint was used as the imposed load. The attained result was 199.37 MPa $mm^{1-\lambda}$, as perceptible in Fig. 7, and it was used as the H_{1c} for this L_O. The H_{1c} were determined for all the L_O this way, resulting in the values presented in Table 3. The H_{2c} values can be determined during the same procedure.

Finally, these H_{1c} were used to extrapolate the strength predictions for the other L_O. The same strategy was implemented for all L_O, originating the P_m predictions presented in Fig. 9, where each curve contains the strength prediction for that L_O and the extrapolations for the other L_O.

In general, P_m increases are smaller than those demonstrated in the experimental results. The only exception to this rule is the P_m increase between L_O = 10 and 20 mm. In fact, the experimental P_m increase is considerably smaller than those predicted with the different H_{1c}. Nonetheless, this deviation to the behaviour detected between the other L_O can be ignored since, as explained in section 4.1, the experimental P_m for L_O = 10 mm is anomalous concerning the proportionality of the experimental P_m-L_O curve. The most accentuated differences are verified between L_O = 70 and 80 mm, where the experimental P_m increase was 1051.24 N and the predictions varied between 332.25 and 455.52 N. On the other hand, between L_O = 60 and 70 mm, the discrepancies are much smaller, with a few prediction cases that even surpass the experimental P_m increase.

Another particularity from the obtained results is that, when predicting P_m for an L_O larger than the L_O used to determine H_{1c}, the result is generally an underprediction. However, two special cases break this law. The first is related to the same problem observed for the P_m prediction increases, i.e., when predicting the strength of the L_O = 20 mm and the L_O = 30 mm joints using L_O = 10 mm to obtain H_{1c}, the outcome is an overprediction. Once again, this is due to the incongruous L_O = 10 mm experimental P_m value. The second case is when L_O = 60 mm was used to predict P_m of the L_O = 70 mm joint, which resulted in a slight overprediction, with an error of 0.1%. As a matter of fact, all the P_m predictions attained using L_O = 60 mm present marginally higher results than the P_m predictions reached when using L_O = 70 mm. The contrary behaviour is also true, i.e., predicting P_m of an L_O smaller than the L_O used to determine H_{1c} originates over predictions, with the same two exceptions described.

Regarding the fluctuations between experimental and predicted P_m, it is safe to affirm that the higher the difference between the L_O used to obtain H_{1c} and the predicted joint L_O, the higher the percentual deviation in the results. The highest percentual deviation found was when L_O = 80 mm was utilised to predict P_m for L_O = 20 mm (37.10%), confirming the previous statement. However, if an L_O is used to predict P_m of a joint with an L_O that does not differ in more than 20 mm (±20 mm) from that L_O, the deviations decrease considerably. In this situation, the case where L_O = 40 mm was used to predict P_m for L_O = 20 mm revealed the higher discrepancy (14.11%). Considering the same situation, the majority of the other cases presents percentual deviations inferior to 10%. As mentioned before, all P_m predictions attained with L_O = 60 mm and L_O = 70 mm present incredibly similar results, with fluctuations below 1%.

Table 3
H_{1c} values for each L_O.

L_O used to determine H_{1c} (mm)	H_{1c} (MPa.$mm^{1-\lambda}$)
10	180.62
20	172.34
30	179.91
40	194.73
50	199.37
60	211.95
70	209.44
80	224.45

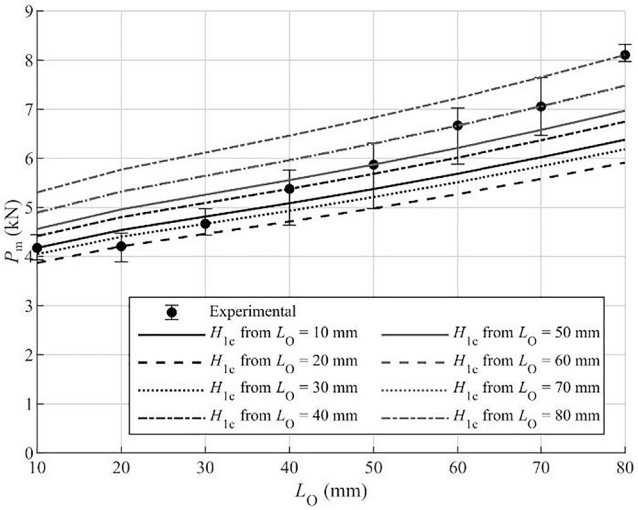

Fig. 9. P_m prediction graph for all the L_O.

6. Conclusions

The present study aimed to validate the use of the ISSF criterion in meshless methods. Firstly, SLJ composed of CFRP and bonded with a brittle adhesive were experimentally tested to collect the average P_m. Also, to evaluate the influence of L_O in the final results, eight different L_O were tested, between 10 and 80 mm. Then, the ISSF criterion was implemented. This implementation allowed concluding that, for the geometry and material combination applied in this work, three singularity exponents λ characterize the bi-material interface corner. However, one of those λ corresponded to an anti-plane solution, reason for excluding it from the analysis since a plane strain condition was implemented. Regarding H_{1c}, necessary for the P_m prediction, an alternative to the usually complex methods that have already been investigated is implemented. It consists of numerically simulating the joints, considering the experimentally determined P_m as the imposed loads. For this, the RPIM was used, intending to fulfil the primary objective of this work. These simulations were then used to determine the H_1 values that were considered the H_{1c} for each L_O. The proposed method showed some variance depending on which L_O is used, except when comparing the H_{1c} obtained with L_O = 60 and 70 mm, which were very similar. The results showed P_m increases between L_O generally smaller than those verified experimentally. Also, when predicting P_m of an L_O larger than the L_O used to determine H_{1c}, the result was an underprediction. The only exceptions to these patterns were the L_O = 10 mm case, which revealed unsatisfactory results due to an anomaly in the experimental data, and the L_O = 60 and 70 mm cases, where the P_m predictions attained with L_O = 60 mm were slightly higher than those of L_O = 70 mm, but incredibly similar (percentual deviations below 1%). With this in mind, when applying this methodology, it is recommended to only predict P_m of

joints with a L_O larger than the L_O used to determine H_{1c}. However, given the simplicity of the applied method, the results are auspicious. In that sense, it can be concluded that the ISSF criterion can be applied to meshless methods, to composite materials and to different corner geometries.

7. Declarations

Funding

This work has been funded by the Ministério da Ciência, Tecnologia e Ensino Superior through the Fundação para a Ciência e a Tecnologia (from Portugal), under project fundings 'MIT-EXPL/ISF/0084/2017', 'POCI-01–0145-FEDER-028351', and 'SFRH/BD/147628/2019'. Additionally, the authors acknowledge the funding provided by the Associated Laboratory for Energy, Transports and Aeronautics (LAETA), under project 'UIDB/50022/2020'.

7.2. Data availability statement

The raw data required to reproduce these findings cannot be shared at this time as the data also forms part of an ongoing study. The processed data required to reproduce these findings cannot be shared at this time as the data also forms part of an ongoing study.

Declaration of Competing Interest

The authors declare that they have no known competing financial interests or personal relationships that could have appeared to influence the work reported in this paper.

References

[1] Degano I, Soriano S, Villa P, Pollarolo L, Lucejko JJ, Jacobs Z, et al. Hafting of Middle Paleolithic tools in Latium (central Italy): new data from Fossellone and Sant'Agostino caves. PLoS ONE 2019;14(6):e0213473.
[2] Petrie EM. Handbook of adhesives and sealants. U.S: McGraw-Hill; 2000.
[3] Borsellino C, Calabrese L, Valenza A. Experimental and numerical evaluation of sandwich composite structures. Compos Sci Technol 2004;64(10-11):1709–15.
[4] Li T, Wang L. Bending behavior of sandwich composite structures with tunable 3D-printed core materials. Compos Struct 2017;175:46–57.
[5] Elamin M, Li B, Tan KT. Impact damage of composite sandwich structures in arctic condition. Compos Struct 2018;192:422–33.
[6] He W, Liu J, Wang S, Xie De. Low-velocity impact response and post-impact flexural behaviour of composite sandwich structures with corrugated cores. Compos Struct 2018;189:37–53.
[7] Volkersen O. Die Nietkraftverteilung in zugbeanspruchten Nietverbindungen mit konstanten Laschenquerschnitten. Jahrb Dtsch Luftfahrtforsch 1938;15:41–7.
[8] Campilho RD. *Strength prediction of adhesively-bonded joints*. 2017, Boca Raton, U.S.: CRC Press.
[9] da Silva Lucas FM, das Neves Paulo JC, Adams RD, Wang A, Spelt JK. Analytical models of adhesively bonded joints—Part II: Comparative study. Int J Adhes Adhes 2009;29(3):331–41.
[10] Goland M, Reissner E. The stresses in cemented joints. J Appl Mech 1944;66: A17–27.
[11] Hart-Smith LJ. Adhesive-bonded single-lap joints, in NASA Contract Report, NASA CR-112236; 1973.
[12] Ramalho LDC, Campilho RDSG, Belinha J, da Silva LFM. Static strength prediction of adhesive joints: a review. Int J Adhes Adhes 2020;96:102451.
[13] Campilho RDSG, Banea MD, Neto JABP, da Silva LFM. Modelling adhesive joints with cohesive zone models: effect of the cohesive law shape of the adhesive layer. Int J Adhes Adhes 2013;44:48–56.
[14] Anderson TL. *Fracture mechanics: fundamentals and applications*. 2017, Boca Raton, U.S.: CRC press.
[15] Rice JR. A path independent integral and the approximate analysis of strain concentration by notches and cracks. J Appl Mech 1968;35(2):379–86.
[16] Rybicki EF, Kanninen MF. A finite element calculation of stress intensity factors by a modified crack closure integral. Eng Fract Mech 1977;9(4):931–8.
[17] Jones S, Stier B, Bednarcyk BA, Pineda EJ, Palliyaguru UR. *Verification, Validation, and Limits of Applicability of a Rapid Bonded Joint Analysis Tool*. in *AIAA Scitech 2020 Forum*. 2020.
[18] Irwin GR. Analysis of stresses and strains near the end of a crack traversing a plate. J Appl Mech 1957;24(3):361–4.
[19] Qian ZQ, Akisanya AR. Wedge corner stress behaviour of bonded dissimilar materials. Theor Appl Fract Mech 1999;32(3):209–22.
[20] Wu Zhixue, Tian Shuai, Hua Yajun, Gu Xiang. On the interfacial strength of bonded scarf joints. Eng Fract Mech 2014;131:142–9.
[21] Galvez P, Noda N-A, Takaki R, Sano Y, Miyazaki T, Abenojar J, et al. Intensity of singular stress field (ISSF) variation as a function of the Young's modulus in single lap adhesive joints. Int J Adhes Adhes 2019;95:102418.
[22] Delale F. Stress singularities in bonded anisotropic materials. Int J Solids Struct 1984;20(1):31–40.
[23] Chen Hua-Peng. Stress singularities in anisotropic multi-material wedges and junctions. Int J Solids Struct 1998;35(11):1057–73.
[24] Pageau Stephane S, Biggers Sherrill B. A finite element approach to three-dimensional singular stress states in anisotropic multi-material wedges and junctions. Int J Solids Struct 1996;33(1):33–47.
[25] Stroh AN. Steady State Problems in Anisotropic Elasticity. 1962. 41(1-4): p. 77-103.
[26] Yao S, Zappalorto M, Pan W, Cheng C, Niu Z. Two dimensional displacement and stress fields for tri-material V-notches and sharp inclusions in anisotropic plates. Eur J Mech A Solids 2020;80:103927.
[27] Ting TCT, Chyanbin Hwu. Sextic formalism in anisotropic elasticity for almost non-semisimple matrix N. Int J Solids Struct 1988;24(1):65–76.
[28] Barroso A, Mantič V, París F. Singularity analysis of anisotropic multimaterial corners. Int J Fract 2003;119(1):1–23.
[29] Barroso A, Marín JC, Mantič V, París F. Premature failures in standard test specimens with composite materials induced by stress singularities in adhesive joints. Int J Adhes Adhes 2020;97:102478.
[30] Leguillon Dominique. Strength or toughness? A criterion for crack onset at a notch. Eur J Mech-A/Solids 2002;21(1):61–72.
[31] Liu G-R, Gu Y-T. An introduction to meshfree methods and their programming. Dordrecht, The Netherlands: Springer Science & Business Media; 2005.
[32] Wang Rongqiao, Zhang Long, Hu Dianyin, Liu Chunhui, Shen Xiuli, Cho Chongdu, et al. A novel approach to impose periodic boundary condition on braided composite RVE model based on RPIM. Compos Struct 2017;163:77–88.
[33] Ramalho LDC, Sánchez-Arce IJ, Campilho RDSG, Belinha J. Strength prediction of composite single lap joints using the radial point interpolation method. Compos Struct 2021;259:113228.
[34] Campilho RDSG, de Moura MFSF, Domingues JJMS. Modelling single and double-lap repairs on composite materials. Compos Sci Technol 2005;65(13):1948–58.
[35] Oliveira JJG, Campilho RDSG, Silva FJG, Marques EAS, Machado JJM, da Silva LFM. Adhesive thickness effects on the mixed-mode fracture toughness of bonded joints. J Adhesion 2020;96(1-4):300–20.
[36] Campilho RDSG, de Moura MFSF, Domingues JJMS. Stress and failure analyses of scarf repaired CFRP laminates using a cohesive damage model. J Adhes Sci Technol 2007;21(9):855–70.
[37] De Sousa CCRG, Campilho RDSG, Marques EAS, Costa M, da Silva LFM. Overview of different strength prediction techniques for single-lap bonded joints. Proc Inst Mech Eng, Part L: J Mater: Des Appl, 2017. 231: p. 210-223.
[38] Wang Shaoluo, Liang Wei, Duan Liming, Li Guangyao, Cui Junjia. Effects of loading rates on mechanical property and failure behavior of single-lap adhesive joints with carbon fiber reinforced plastics and aluminum alloys. Int J Adv Manuf Technol 2020;106(5-6):2569–81.
[39] Belinha J. Meshless methods in biomechanics: Bone tissue remodelling analysis, vol. 16. Switzerland: Springer; 2014.
[40] Liu GR. A point assembly method for stress analysis for two-dimensional solids. Int J Solids Struct 2002;39(1):261–76.
[41] Wang JG, Liu GR. On the optimal shape parameters of radial basis functions used for 2-D meshless methods. Comput Methods Appl Mech Eng 2002;191(23-24): 2611–30.
[42] Stroh AN. Steady state problems in anisotropic elasticity. J Math Phys 1962;41 (1–4):77–103.
[43] Mantič V, Barroso A, París F. Singular Elastic Solutions in Anisotropic Multimaterial Corners: Applications to Composites. In: Mathematical Methods and Models in Composites. World Scientific; 2013. p. 425–95.
[44] Klusák J, Profant T, Kotoul M. Various methods of numerical estimation of generalized stress intensity factors of bi-material notches. Appl Comput Mech 2009;3(2).
[45] Ramalho LDC, Sánchez-Arce IJ, Campilho RDSG, Belinha J. Strength prediction of composite single lap joints using the critical longitudinal strain criterion and a meshless method. Int J Adhes Adhes 2021;108:102884.
[46] Nunes SLS, Campilho RDSG, da Silva FJG, de Sousa CCRG, Fernandes TAB, Banea MD, et al. Comparative failure assessment of single and double-lap joints with varying adhesive systems. J Adhes 2016;92(7-9):610–34.
[47] Barbosa NGC, Campilho RDSG, Silva FJG, Moreira RDF. Comparison of different adhesively-bonded joint types for mechanical structures. Appl Adhes Sci 2018;6(1): 15.